DEVELOPMENT OF A SCALABLE PHOTOCHEMICAL REACTOR FOR SYNTHESES OF FINE CHEMICALS

by

KONSTANTIN NIKOLAYEVICH LOPONOV

Submitted for the Degree of Doctor of Philosophy

School of Engineering, University of Warwick

February 2011

Dedicated to my parents,

Evgeniya Ivanovna Loponova and Nikolay Yemelianovich Loponov

SUMMARY

This study is in the area of sustainable chemical technology and is ultimately aimed at developing a novel generic approach towards efficient, clean, safe and scalable synthesis of important intermediates for pharmaceutical applications and catalysis using non-thermal activation of chemical bonds. Current study is focused on molecular activation by light, specifically addressing the class of singlet oxygen reactions.

A laboratory-scale annular recirculating photoreactor and a scalable microreactor unit were designed, assembled and tested in oxygenation of α-pinene and stereoselective oxygenation of homoallylic alcohols by the photogenerated singlet oxygen. Efficiencies of light utilization and the quantum yields of the reactions for different sources of light in various lamp-reactor geometries were quantified using actinometry. It was shown that optimal thickness of the reaction layer, high intensity of light and elevated oxygen pressures in continuous gas-liquid segmented flow are crucial for both safe and efficient oxygenation. This study proved the viability of a novel concept of compact reactors with embedded light emitting diodes. Finally, a methodology of efficient oxyfunctionalization of allylic compounds was developed.

Following the developed methodology, the applicability of functional nanomaterials based on pure and dye-modified porous silicon as heterogeneous photosensitizers of singlet oxygen was studied in detail. It was demonstrated that the photosensitizing efficiency of all the samples is much lower than that of conventional dye photosensitizers. Low activity of the novel photosensitizers was attributed to quenching of the photogenerated singlet oxygen by the surface quenching groups of porous silicon, low quantum yield of photoluminescence in the case of pure porous silicon and to thermodynamically favorable quenching of the photoexcited porphyrin states due to energy/electron transfer to silicon nanocrystals in the case of dye modified porous silicon.

ACKNOWLEGEMENTS

First of all I would like to show my deepest gratitude to my supervisor Professor Alexei Lapkin for the opportunity to work and study in his group as a PhD student. Prof. Lapkin guided me through the dissertation project never accepting less than my best efforts. His wise advice and ideas during our discussions made significant contribution towards completion of my thesis. Especial thanks to Prof. Lapkin's inestimable help and support in all the difficult situations I met during this time.

Great thanks to my colleagues Professor Dmitry Kovalev, Professor Andrei Malkov, Dr. Bernhard Goller, Dr. Sergej Polisski, Dr. Victor Sans, Dr. Xiaolei Fan, Dr. Gazi Aliev, Dr. Mikhail Kabeshov for their help during this project and fruitful discussions.

I am indebted to my parents Nikolai Yemelianovich Loponov and Yevgenia Ivanovna Loponova, who are my first teachers, who gave me desire for learning and basic principles I still use in everyday life. Many thanks to them for staying with me during this time, for believe in me and for supporting me. Without them this thesis would not have been possible.

I am grateful to my wife Maria Vladimirovna Sotenko for her love, help and support during these years, and to my daughter Slava for happiness she brings into my life every day.

DECLARATION

Signature of the author:

Konstantin N. Loponov

TABLE OF CONTENTS

LIST OF SYMBOLS AND ABBREVIATIONS

CR	chemical reaction
CT	charge transfer
EET	electronic energy transfer
FTIR	Fourier transform infrared
HPLC	high pressure liquid chromatography
HPS	high pressure sodium lamp
IC	internal conversion
ID	inner diameter
IR	infrared
ISC	intersystem crossing
LED	light emitting diode
LPS	low pressure sodium lamp
MH	metal halide lamp
NMR	nuclear magnetic resonance
nCT	non-charge transfer
OD	outer diameter
PL	photoluminescence
pCT	partial charge transfer
SCE	saturated calomel electrode
SON	a variation of the high pressure sodium lamp
SOX	sodium oxide lamp (low pressure sodium lamp)
UV	ultraviolet
UV-A	near UV spectral region (315-400 nm)
VIS	visual
VR	vibrational relaxation
ACHA	aromatic chiral homoallylic alcohol
Ac_2O	acetic anhydride
Ce:YAG	*Ce*-doped yttrium-aluminum garnet
DMAP	4-dimethylaminopyridine
DNA	deoxyribonucleinic acid
DPBF	1,4-diphenylisobensofurane
ETFE	ethyltetrafluoroethylene
e-v	electronic-to-vibrational deactivation

F113	1,1,2-trichloro-1,2,2-trifluromethane (Freone 113)
M	organic molecule
PDMS	polydimethylsiloxane
PSi	porous silicon
PSi^*	electronically excited *PSi*
Py	pyridine
PyTPP-SiO₂	silica gel beads covalently modified with monopyridyltriphenylporphyrin
R	molecule of reagent
RB	Rose Bengal
Rg	rare gas
R6G	rhodamine 6G
S_i	*i*-th singlet energy level (*i*=0, 1, ...)
Si-C₆₀	fulleropyrrolidine-*SiO₂* hybrid
scCO_2	supercritical CO_2
TG	Tentagel resin beads
T_i	*i*-th triplet energy level (*i*=1, 2, ...)
TMS	tetramethylsilane
TPP	5,10,15,20-tetraphenyl-21*H*,23*H*-porphine
TPP(OH)₄	5,10,15,20-tetrakis(4-hydroxyphenyl)-21*H*,23*H*-porphine
TPP(OC_3H_5)₄	5,10,15,20-tetrakis(4-allyloxy)-21*H*,23*H*-porphine
t-RNA	transfer ribonucleic acid
A	total area under graph of intensity *vs.* wavelength
A_i	area of $\Delta\lambda_i$ interval of the emission spectrum of *Xe* or metal halide lamp
A_R	illuminated area of the photoreactor
B_i	area of peak corresponding to *i*-th compound obtained from NMR spectra
C_0	initial concentration
C	velocity of light in vacuum
$c_{an}(t)$	concentration of Fe^{2+} in analysed solution after dilution of aliquot V_1 to V_2
c_F, c_S	concentrations of ferrioxalate and sensitizer, correspondingly
$c_{Fe^{2+}}$	concentration of Fe^{2+}
$c_R(t)$	concentration of Fe^{2+} in reactor
$c_T(t)$	concentration of Fe^{2+} in tank

$c_\Sigma(t)$	an overall concentration of Fe^{2+} in the photochemical rig
c'_{in}, c'_{out}	inlet and outlet concentrations for a photoreactor
c_{in}, c_{out}	inlet and outlet concentrations for tank
D_i	i-th value of optical density
D_i^1	corrected values of the optical density
$D(t)$	optical density
E	energy of a single photon
E_C	electrostatic interaction energy
E_{ex}	energy related to excitation wavelength
E_{ISC}	energy difference between T_2 and S_1
E_{OX}	oxidation potential
$E_{RED}^{O_2}$	reduction potential of O_2
E_T	triplet state energy
E_Δ	energy of $O_2(^1\Delta_g)$ state
E_Σ	state energy of $O_2(^1\Sigma_g^+)$
e	charge of electron
F	Faraday constant
$F_A(\lambda)$	absorption spectrum of the acceptor molecule
$F_E(\lambda)$	emission spectrum of the excited donor molecule
f_S^T	efficiency of T_1-state formation during O_2 quenching of S_1
f_S^Δ	efficiency of $^1O_2$ production during O_2 quenching of S_1
H	Henry constant
h	Plank constant
I	intensity of transmitted light
I_a	intensity of light absorbed by photosensitizer inside the reactor
I_a^F	intensity of light absorbed by ferrioxalate actinometer inside the reactor
I_{ai}^F	intensity of photons from the range of wavelengths $\Delta\lambda_i$ absorbed by the ferrioxalate actinometer
I_C	current in the circuit
I_{ex}	intensity of excitation
I_0	intensity of incident light (intensity prior to absorption)
J_a	flux of photons

k_D	first order $^1O_2$ decay constant
k_d	overall rate constant of complex deactivation
k_{diff}^+ , k_{diff}^-	diffusion-controlled rate constants of encounter complex formation and dissociation
k_F	fluorescence constant
k_{fi}	probability of electron transition per unit time from the ground to the excited state due to absorption of photon
k_G	rate constant of $^1O_2$ generation
k_G'	rate constant of O_2^- generation
k_{IC}	internal conversion constant
k_{ISC}	intersystem crossing constant
k_R	ibimolecular reaction rate constant of R with $^1O_2$
k_r	rate constant of radiative decay
k_R'	overall bimolecular rate constant for physical quenching and chemical reaction of $^1O_2$ with R
k_{R_i}	constant of reaction rate from i-th state
k_{R1}	rate constant
$k_{CT}^{^1\Sigma}, k_{CT}^{^1\Delta}, k_{CT}^{^3\Sigma}$	rate constants for charge-transfer-induced triplet-sensitized formation of $O_2(^1\Sigma_g^+)$, $O_2(^1\Delta_g)$ and $O_2(^3\Sigma_g^-)$
$k_{IC}^{^1\Sigma}, k_{IC}^{^1\Delta}, k_{IC}^{^3\Sigma}$	decay rate constants of pCT complexes
k_Q^{Δ}	rate constant of $O_2(^1\Delta_g)$ quenching
k_Q^{Σ}	rate constant of $O_2(^1\Sigma_g^+)$ quenching
k_S^Q	rate constant for O_2 quenching of an excited singlet state
k_T^Q	rate constant for O_2 quenching of an excited triplet state
$k_T^{^1\Sigma}, k_T^{^1\Delta}, k_T^{^3\Sigma}$	overall rate constants for triplet-sensitized formation of $O_2(^1\Sigma_g^+)$, $O_2(^1\Delta_g)$ and $O_2(^3\Sigma_g^-)$
k_{XY}^{Δ}	rate constant of $O_2(^1\Delta_g)$ quenching by a single terminal bond X-Y
k_{XY}^{Σ}	rate constant of $O_2(^1\Sigma_g^+)$ quenching by a single terminal bond X-Y
$k_{\Delta E}^{^1\Sigma}, k_{\Delta E}^{^1\Delta}, k_{\Delta E}^{^3\Sigma}$	rate constants for non-charge-transfer-induced triplet-sensitized formation of $O_2(^1\Sigma_g^+)$, $O_2(^1\Delta_g)$ and $O_2(^3\Sigma_g^-)$
l	length of the photometric cell, light pathlength in the photoreactor
m	multiplicity

N	sum of all the N_i of the emission spectrum
N_A	Avogadro constant
N_i	intensity of the photons emitted by $\Delta\lambda_i$ interval of the lamp emission spectrum
N_{LED}	number of LEDs in the lamp
N_{XY}	number of terminal X-Y bonds per quencher molecule
n	a formal reaction order with respect to O_2 pressure
$n_{al}(t)$	amount of Fe^{2+} taken with the aliquot V_1
n_i	amount (mol) of Fe^{2+} taken with the aliquot V_i after Δt_i minutes illumination
n_m	total amount (mol)of Fe^{2+} in photocatalytic plant at t_m minutes
$n_T(t)$	amount of Fe^{2+} in the tank of the annular recirculating photoreactor rig
n_m^1	amount (mol) of Fe^{2+} left in photocatalytic plant after taking the aliquot
$n_{\xi i}$	amount (mol) of Fe^{2+} taken with aliquot ξ_i
$n\pi^*$	$n-\pi$ excited triplet states
$^1O_2$	singlet oxygen, or $O_2(^1\Delta_g)$
O_2^-	superoxide ion
$O_2(^1\Delta_g)$	first singlet electronic state of molecular oxygen
$O_2(^1\Sigma_g^+)$	second excited singlet electronic state of molecular oxygen
$O_2(^3\Sigma_{g^-})$	ground triplet electronic state of molecular oxygen
P	oxygen pressure
P_{in}	supplied power
P_{hv}	power of the absorbed light
P_{hv}^0	total emitted power output of the lamp
$\{P_i\}$	products
P_{LED}	output power of a single LED
P_0	1 bar of O_2 pressure
$p_S^{O_2}$	fractions of singlet states quenched by oxygen
$p_T^{O_2}$	fractions of triplet states quenched by oxygen
Q	heat
$\overline{\mathrm{R}}$	ideal gas constant
$\vec{\mathrm{R}}_j$	radius vector of the j-th nuclei
R_0	initial concentration of reagent

r_C	rate of $^1O_2$ consumption in physical quenching and reaction
r_D	rate of $^1O_2$ quenching by solvent
r_G	rate of $^1O_2$ photogeneration
$r_{Fe^{2+}}$	rate of generation of Fe^{2+} in the annular photoreactor
$\vec{r}_i$	radius vector of i-th electron
r_R	rate of reaction
r_{0i}	initial reaction rate at P_i pressure
r_0^R	initial reaction rate in reactor
r_0^T	initial rate of accumulation of the product in tank
S_M	minimal sum of squared residuals
T	temperature
t	time
u_G	flowrate of gas phase (apparent flowrate of gas)
u_G^0	actual volumetric flowrate of O_2
u_L	flowrate of liquid phase
V_j	volume of reaction solution after taking j-th aliquot
V_R	volume of reactor
V_T	volume of reaction mixture in tank
V_0	initial volume of reaction mixture
V_1	volume of sample taken for analysis from initial aliquot ξ_0
V_2	volume of sample obtained after dilution of aliquot V_1
V_Σ	V_R+V_T
X_P	mole fraction of product
X_R	mole fraction of reagent
Z_j	atomic number of j-th nuclei
$<D>_i$	average value of optical density for i-th aliquote
$<P_{LED}>$	average output power of a single LED
$<\Delta U>$	average voltage drop on a single LED
α	efficiency of indirect $O_2(^1\Delta_g)$ generation during O_2 quenching of T_1
β	efficiency of direct formation of $O_2(^1\Delta_g)$ during O_2 quenching of T_1
β_L	liquid holdup
γ	linear absorption coefficient
ΔE	excess energy

$\Delta E_{S\text{-}T}$	S_1-T_1 energy gap
ΔG_{CET}	free-energy change of complete electron transfer
Δn_m	amount (mol) of Fe^{2+} generated in photocatalytic plant for Δt_m minutes
ΔU	potential
$\Delta\lambda_i$	interval of spectral resolution
$\Delta\lambda_j$	interval of wavelengths; λ_j and λ_{j+1} represent the wavelengths with known quantum yields of Fe^{2+} formation
ε	molar extinction coefficient
ε_S, ε_F	molar extinction coefficients of sensitizer and ferrioxalate
η	overall efficiency of the annular recirculating reactor
η_{LR}	efficiency of the lamp-reactor geometry
η_{PL}	efficiency of power-to-light conversion
$\Theta(\lambda)$	quantum yield of Fe^{2+} formation at the emitted wavelength
$\Theta(\Delta\lambda_j)$	quantum yield of Fe^{2+} generation under illumination by photons from $\Delta\lambda_j$ interval
λ	wavelength of light
$\hat{\mu}$	molecular transition dipole operator
$\hat{\mu}_e$	electronic transition dipole operator
μ_{fi}	matrix element of transition dipole moment
$\hat{\mu}_n$	nuclei transition dipole operator
ν	frequency of light
ξ_i	volume of i-th aliquot taken from photocatalytic plant
$\pi\pi^*$	π - π excited triplet states
τ	residence time in the reactor
τ_D	total lifetime of $^1O_2$
τ_d	lifetime of $^1O_2$ in solvent
τ_q	deactivation time of $^1O_2$ by the surface of Si nanocrystals
τ_Δ	lifetime of $O_2(^1\Delta_g)$
τ_Σ	lifetime of $O_2(^1\Sigma_g^+)$
τ_T	total residence time in the reactor operated in gas-liquid segmented flow
Φ	overall quantum yield
Φ_Δ	overall efficiency of $O_2(^1\Delta_g)$ formation during O_2 quenching of T_1 states
$\phi_{^1O_2}$	quantum yield of $O_2(^1\Delta_g)$ sensitization

ϕ_R	quantum yield of a photochemical process
ϕ_{R_i}	quantum yield of chemical reaction from *i*-th state in comparison with physical processes
ϕ_T	triplet quantum yield
ϕ_T^0	triplet quantum yield in the absence of O_2
$\psi_e(\vec{r},\vec{R})$	electronic wave function
Ψ_f	an overall wave function of the final state
Ψ_i	an overall wave function of the initial state
ψ_s	spin wave function
$\psi_v(\vec{R})$	vibrational wave function
Ω	spectral overlap integral

LIST OF FIGURES

LIST OF TABLES

LIST OF PUBLICATIONS

K. Loponov, B. Goller, A. Moskalenko, D. Kovalev, A. Lapkin, Efficiency of Porous Silicon Photosensitizer in the Singlet Oxygen-Mediated Oxidation of Organic Compounds, J. Photochem. Photobiol. A: Chem., 211 (2010) 74-77.

B. Goller, S. Polisski, A. Moskalenko, K. Loponov, D. Kovalev, Photoexcited Silicon Nanocrystals as Multifunctional Spin-Flip Activator, ECS Transactions, 16 (2008) 337-344.

1. INTRODUCTION

One of the main topics in synthetic organic chemistry is development of clean, efficient and highly selective methods for organic synthesis. Successful implementation of these methods often depends on the combination of clean synthesis methods with an appropriate reactor technology. In conventional synthetic methods of organic chemistry molecular activation, required to initiate a reaction is provided by heat. Control over a reaction path is attained by an appropriate choice of reaction conditions, such as starting substrate structure, solvent, catalyst, and concentrations of reagents [1]. An alternative method of molecular activation is using non-thermal energy, for example the energy of photons, *i.e.* photochemistry.

Photochemical synthesis is usually cleaner, more efficient and requires much less aggressive methods than conventional syntheses because absorption of light provides most and sometimes all of the energy required to initiate a reaction [1, 2]. Photochemical reactions can be performed at very low temperatures, in the solid or liquid state or under gas-phase conditions, with spin-selective direct excitation or sensitization. In thermal excitation processes, all three forms of energy, electronic, vibrational, and rotational, are raised to higher levels. In contrast, photoexcitation raises only the electronic energy level which leads to higher selectivities. Moreover, selectivity can be controlled by specific excitation of particular functional groups in a molecule. For example, photo-cleavage has become one of the most effective methods for removing protecting groups [3]. Among the successfully realized industrial photochemical processes are production of halogenated hydrocarbons and alkane sulphates in free radical reactions [4, 5]. In the fine chemical syntheses and pharmaceuticals production photochemical reaction steps offer shorter routes in many synthetic schemes, *e.g.* synthesis of vitamins A, D, dydrogesterone and fragrances [4].

However, the use of photochemistry is limited by concerns about efficiency, scalability, heat and mass transfer, and safe operation of the processes (*e.g.* explosions caused by excess heat) [4, 5]. Indeed, synthetic organic photochemical reactions are usually performed in fixed volume batch reactors irradiated by immersed single tungsten, sodium, or mercury vapour discharge lamps. The majority of the photons is then absorbed within a short radius of the lamp according to the Lambert-Beer law (1.1), and therefore, the amount of solution that can be effectively irradiated by the light source is scale-dependent.

$$I = I_0 \exp(-\gamma l) \tag{1.1}$$

Where I_0 and I are the incident and transmitted light intensities, respectively, l is the distance travelled by light in the medium, and γ is the linear absorption coefficient.

In the case of the free-radical mechanism, the radicals formed near the light source may recombine faster than diffuse to react further with other species. This process generates excess heat instead of a productive reaction, thus reducing quantum efficiency of the overall process [4-6]. Many photochemical processes require long irradiation times, which can lead to decreased yields due to decomposition of the product, caused by unfavourable photochemical reactions. In most cases, it takes considerable effort to transform a successful lab-scale reaction to its industrial counterpart [4-6].

During the last decade, microstructured reactors attracted much attention as a new type of reactors in organic synthesis due to the unique features of microchannels, such as short molecular diffusion distances, excellent heat-transfer characteristics, laminar flow and large surface-to-volume ratios [7, 8]. Small dimensions of the microreactors allow safe exploitation of explosive processes due to quenching of radicals on the walls or internal structures of microchannels. Furthermore, once optimized, the process can be easily

scaled up by the use of a multiparallel approach or 'numbering up' of the identical microreactor units. In the case of photochemical reactions microreactors provide large specific illuminated area and high spatial uniformity of the illumination due to penetration of light through the entire reactor depth [9]. The energy from the light source is then fully utilised for the reactions. Although microstructured reactors are successfully examined in the wide range of applications of organic chemistry, surprisingly small number of studies has so far been done on the applications of microreactors in photochemistry [5, 9-21].

Another major drawback of synthetic photochemistry is the use of costly and inefficient light sources, which produce a considerable part of the emission band in the useless infrared region (IR) and, therefore, have to be cooled [22]. When monochromatic light is needed for selective excitation, glass filters or filter solutions can be applied to separate the spectral part of the emission or to band-filter one part of the emission spectrum. These filter processes are always accompanied by a severe loss in photon flux. Light emitting diodes (LEDs) with the advantages of high photon flux, availability in different wavelengths and long lifetime look very promising as compact monochromatic light sources for microengineered reaction systems [16, 23].

Reactions of singlet oxygen ($^1O_2$) with organic substrates are of much current interest due to their importance in many chemical and biological photooxidation processes including photodynamic therapy of cancer [24-26]. The most frequently used method of $^1O_2$ generation in solution is photosensitized energy transfer from the photo-excited states of dissolved organic dye molecules to O_2. Conventionally, photosensitized reactions are conducted in a homogeneous solution [19]. However, a homogeneous process has some disadvantages with respect to separation of a sensitizer from the reaction mixture, and thus, the sensitizer is not reusable. In order to overcome such

drawbacks, immobilized photosensitizers have been employed: Rose Bengal (RB) on Merrifield polymers and Amberlite [27, 28], *Ru* (II) complexes on Sephadex [29], phthalocyanine derivatives on zeolites [30], porphyrin loaded polystyrene beads [31] and so on [32]. However, the efficiency of such immobilized systems is ussually less than that of the corresponding homogeneous photosensitizers. It is therefore useful to develop a highly effective heterogeneous photosensitizer system.

Recently, it has been discovered that porous silicon nanostructures (*PSi*) may also be used as a $^1O_2$ photosensitizer [33, 34]. Kovalev *et al.* investigated the process of energy transfer from excitons confined in *Si* nanocrystals to O_2 and demonstrated that photoexcitation of *PSi* suspended in O_2-saturated benzene leads to 1,4,-diphenylisobensofurane (*DPBF*) bleaching. Latest study reported the development of a practical recirculating laboratory scale reactor with a 524 nm LED lamp [23]. The efficiency of the reactor in $^1O_2$ generation was tested using *DPBF* decomposition in O_2-saturated suspensions of *PSi* in CH_2Cl_2. Based on the obtained data it was concluded that the proposed method of $^1O_2$ generation should give reasonable production yields in the reactions of synthetic interest. However, the data reported earlier leave doubt over the specific mechanism of *DPBF* photobleaching mediated by *PSi* and do not provide direct comparison between the sensitising efficiency of *PSi* with that of the conventional organic dye photosensitizers.

Oxyfunctionalization of allylic substrates by $^1O_2$, for which O_2 and light serve as natural sources, is a highly versatile synthetic method [35]. For example, terpene-derived chiral ligands such as bipyridines, phosphinopyridine, and pyridine *N*-oxide (**Figure 1.1**) proved to be successful in a number of metal-based and metal-free catalytic transformations including allylic oxidation, allylation of aldehydes and reduction of ketones and ketimines

[36-41]. The key step in the synthesis of these catalysts is oxygenation of α-pinene to pinocarvone by $^1O_2$. Another possible application of pinocarvone in synthesis of antimalarial peroxides was recently demonstrated [42]. Generally, the process of oxygenation by $^1O_2$ involves bubbling O_2 through the illuminated reaction mixture in a batch photoreactor and requires up to two days for completion on a several grams scale. Scaling up this protocol is limited by the available equipment due to inefficient light utilisation and, in particular, by the hazard associated with the use of O_2-saturated organic solutions. The scope of the catalytic systems based on the terpene-derived chiral ligands may be further increased with the employment of microstructured reactors.

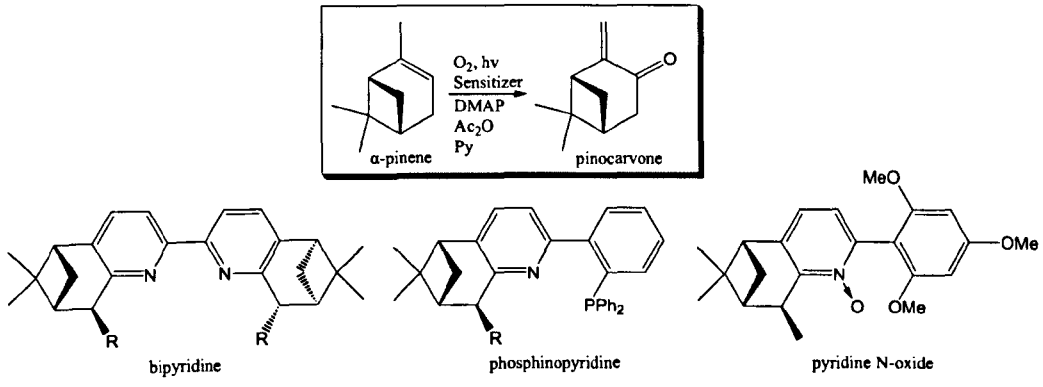

Figure 1.1. Photochemical step for converting pinene to pinocarvone and terpene-derived chiral ligands. *DMAP* is 4-dimethylaminopyridine, Ac_2O is acetic anhydride, *Py* is pyridine.

One other example is stereoselective oxygenation of aromatic chiral homoallylic alcohols (*ACHA*) which remains largely unexplored except for few scattered preliminary reports [43]. Successful development of this process may be employed in the syntheses of important natural products, such as the antibiotic showdomycin, or pseudouridine (**Figure 1.2**), isolated from *t-RNA*, and will revolutionise the synthesis of unnatural nucleobases, that are of key importance in chemical biology as a tool for studying and modulation of biological processes, for the preparation of artificial bio-analogue systems, and for the

quest to extend the genetic alphabet (by creating a stable and replicable third base pair) [44-47].

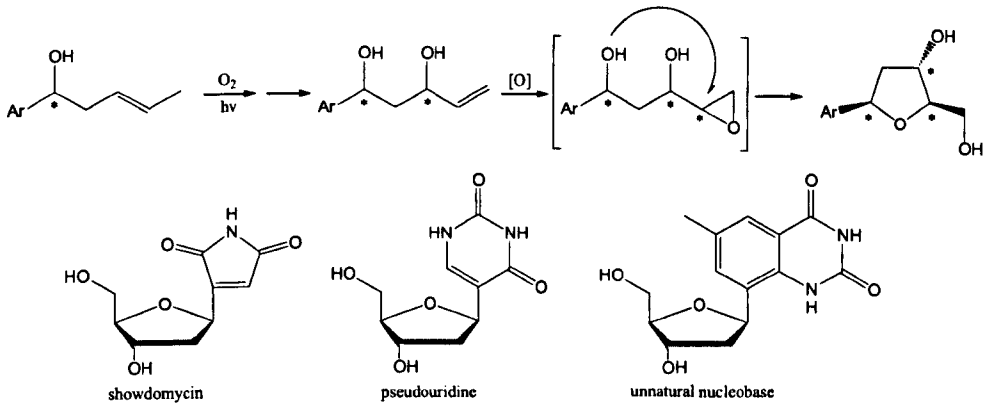

Figure 1.2. Functionalisation of *ACHA* and possible important products.

The aim of this work is to develop a novel generic approach towards clean organic synthesis, exploiting reactivity of photogenerated $^1O_2$ and the novel reaction engineering concept of multifunctional structured reactors with the embedded LEDs in oxyfunctionalization of allylic substrates, important for pharmaceutical applications and catalysis.

The specific objectives are:

- to develop a scalable multifunctional structured photoreactor unit for efficient oxyfunctionalization of allylic compounds by photosensitized $^1O_2$;
- to optimise conditions for homogeneous oxygenation of α-pinene to pinocarvone by $^1O_2$ in the multifunctional structured photochemical reactor;
- to determine the fundamental principles of optimal scaleable photochemical reactors;
- to demonstrate the generic applicability of the developed approach on a stereoselective oxygenation of *ACHA*;
- to study the applicability of novel heterogeneous $^1O_2$ photosensitizers based on *PSi* nanoassemblies in oxygenation of the allylic substrates.

2. LITERATURE REVIEW

2.1. INTRODUCTION TO PHOTOCHEMISTRY

2.1.1. Absorption of light

The quantum theory of light absorption is based on several approximations, principally, the Born-Oppenheimer approximation, the perturbation theory, and the electrical dipole transition assumption. According to this theory, a probability of an electron transition per unit time from the initial vibrational state of the ground electronic level to vibrational state of an excited electronic state due to absorption of photons of energy $h\nu$ is proportional to the square of transition dipole moment [48, 49]:

$$k_{fi} \sim \left| \mu_{fi} \right|^2 \tag{2.1}$$

where $\mu_{fi} = \langle \psi_f \,|\, \hat{\mu} \,|\, \psi_i \rangle$, Ψ_i and Ψ_f are the overall wave functions of the initial and final states respectively, $\hat{\mu}$ is molecular transition dipole operator which is determined by the following equation:

$$\hat{\mu} = \hat{\mu}_e + \hat{\mu}_n = -\sum_i e\vec{r}_i + \sum_j eZ_j\vec{R}_j \tag{2.2}$$

where $\hat{\mu}_e$ and $\hat{\mu}_n$ are electrons and nuclei transition dipole operators, e is charge of electron, Z is atomic number, $\vec{r}_i$ and $\vec{R}_j$ are radius-vectors of the i-th electron, and j-th nuclei, respectively.

The motion of electrons in the molecule is much faster than the nuclear motion due to the mass difference. The Born-Oppenheimer approximation considers electrons moving in the potential field of static nuclei. This assumption results in factorizing the entire wavefunction into nuclear (vibrational, rotational) and electronic components [49]. The overall wave function is the product of the vibrational ψ_e, electronic ψ_v and spin ψ_s wave functions:

$$\psi = \psi_e \psi_v \psi_s \tag{2.3}$$

where $\psi_e = \psi_e(\vec{r}, \vec{R})$ is a function of all electronic coordinates, $\vec{r}$, and depends parametrically on the nuclear coordinates, $\vec{R}$, and $\psi_v = \psi_v(\vec{R})$ depends only on the nuclear coordinates, $\vec{R}$.

Incorporation of (2.2) and (2.3) into transition dipole moment yields the following expression for the probability of transition:

$$\mu_{fi} = \langle \psi_e^f \psi_v^f \psi_s^f \mid \hat{\mu}_e \mid \psi_e^i \psi_v^i \psi_s^i \rangle + \langle \psi_e^f \psi_v^f \psi_s^f \mid \hat{\mu}_n \mid \psi_e^i \psi_v^i \psi_s^i \rangle \tag{2.4}$$

As dependence of ψ_e on the nuclear coordinates is usually rather weak it is neglected in the expression (2.4), which allows writing the following factorisation:

$$\mu_{fi} \approx \langle \psi_e^f \mid \hat{\mu}_e \mid \psi_e^i \rangle \langle \psi_s^f \mid \psi_s^i \rangle \langle \psi_v^f \mid \psi_v^i \rangle + \langle \psi_e^f \mid \psi_e^i \rangle \langle \psi_s^f \mid \psi_s^i \rangle \langle \psi_v^f \mid \hat{\mu}_n \mid \psi_v^i \rangle \tag{2.5}$$

Term $\langle \psi_e^f \mid \psi_e^i \rangle$ in factorization (2.5) is equal to zero because electronic wave functions of different states are orthogonal. Remaining is the product of three terms: electronic transition moment integral, spin overlap integral and vibrational overlap integral (also called the Franck-Condon factor) (from left to right):

$$\mu_{fi} \approx \langle \psi_e^f \mid \hat{\mu}_e \mid \psi_e^i \rangle \langle \psi_s^f \mid \psi_s^i \rangle \langle \psi_v^f \mid \psi_v^i \rangle \tag{2.6}$$

Spin overlap integral determines spin-allowed transitions [50]. Most organic molecules under normal conditions are in the singlet ground state S_0 in which electrons with opposing spins are paired in molecular orbitals. Electrons in triplet states T_i have parallel spins. Singlet-to-triplet transitions have transition moments equal to zero. Such a transition is called a forbidden transition. Only spin-conserving (singlet to singlet and triplet to triplet) transitions during absorption (or emission) are allowed. Electronic transition moment is related to the symmetry of orbitals. The allowed electronic transitions are ones which have a transition moment different from zero. Vibrational overlap integral (Frank-Condon factor) is linked to Frank-Condon principle [49], which

states that a more significant overlap between two vibrational wave functions of two electronic states during an electronic transition leads to an increase in probability of the transition. After the electronic transition the intermediate excited state is in nonminimal energy geometry and therefore it returns extremely rapidly to the lowest vibrational state of the new electronic state *via* vibrational relaxation (VR), with a release of the excess energy to the environment as heat. Rotational contributions have been neglected in the above derivation as they are strongly suppressed in liquids or solids and can contribute only in gas phase. The above consideration can be extended to the light emission and interactions between light absorbing and emitting molecules (energy transfer).

Weaker magnetic dipole and electric quadrupole electronic transitions along with the incomplete validity of the factorization of the total wave function into nuclear, electronic and spin wave functions mean that the selection rules are not strictly observed [49]. For any given transition, the value of μ_{fi} is determined by all of the selection rules; however spin selection is the largest contributor, followed by electronic selection rules. The Franck-Condon factor only weakly modulates the intensity of transitions with a factor in the order of 1 to the intensity of bands determined by the other selection rules. Extinction coefficient ε of spin and orbitally allowed electronic transition is $10^3 - 10^5$ L mol^{-1} cm^{-1}; for spin-allowed but orbitally-forbidden transition ε is in the order of 10^0 to 10^3 L mol^{-1} cm^{-1}; spin-forbidden but orbitally-allowed electron transition shows the lowest values of ε from 10^{-5} to 10^0 L mol^{-1} cm^{-1} [51].

2.1.2. Degradation of photoexcited states

During the very short period (~ 10^{-15} s) required for excitation an electron is promoted from ground state S_0 to higher energy levels S_i. The molecule within this period does not

undergo changes in nuclear position or in the spin state of the promoted electron. The following processes can occur after photoexcitation [49, 50]:

- nonradiative deactivation ($AB^* \rightarrow AB$ + *energy dissipation*);
- radiative deactivation or luminescence ($AB^* \rightarrow AB + h\nu$);
- ionization ($AB^* \rightarrow AB^+ + e^-$);
- intramolecular energy transfer ($ABC^* \rightarrow AB^*C$);
- photochemical reaction ($A^* \rightarrow B$ or $A^* + B \rightarrow C$);
- intermolecular energy transfer ($AB^* + CD \rightarrow AB + CD^*$).

These processes include photocatalysis and photosensitization. All possible energy transformations between different excited states of a molecule are depicted in Jablonski's diagram (**Figure 2.1**) [49-51]. If a molecule is excited to any state higher than first excited singlet S_1 it returns to that state very rapidly (~ 10^{-12} s) owing to VR (vertical wavy arrows), in which vibrational (thermal) energy is dissipated nonradiatively in collisions with other molecules, and internal conversion, IC (horizontal wavy arrows). IC is also fast (~ 10^{-14} – 10^{-12} s) nonradiative transition from the low vibrational level of high electronic state S_{i+1} to vibrational level of low electronic state S_i of the same overall electronic and vibrational energy. Radiative decay from S_i states ($i > 1$) is very unlikely for polyatomic molecules.

Direct promotion from the ground state S_0 to any triplet state has very low efficiency (ε ~ 10^{-5} L mol^{-1} cm^{-1}) as such transitions are forbidden by spin selection rule, and a triplet state can be initiated from an excited singlet state by the intersystem crossing, ISC, (horizontal wavy arrows). ISC is a nonradiative transition from the low vibrational level of the first excited site S_1 to vibrational level of the first triplet electronic state T_1 of the same overall electronic and vibrational energy. This process is slower (~ 10^{-11} – 10^{-6} s)

than IC and results in spin inversion. ISC must also occur when triplet excited states return to singlet ground states *via* nonradiative path. A prominent factor in the rate of ISC is spin-orbit coupling, which depends on the structure of the triplet state and strongly increases with nucleus mass ($\sim Z^4$). Therefore, the presence of a heavy element in a molecule, *e.g.*, *Br*, promotes ISC. The extent of spin-orbit coupling and the rate of ISC decrease with increasing separation of the orbitals containing the unpaired electron. Spin-orbit coupling also increases with the degree of ionic character of the singlet state.

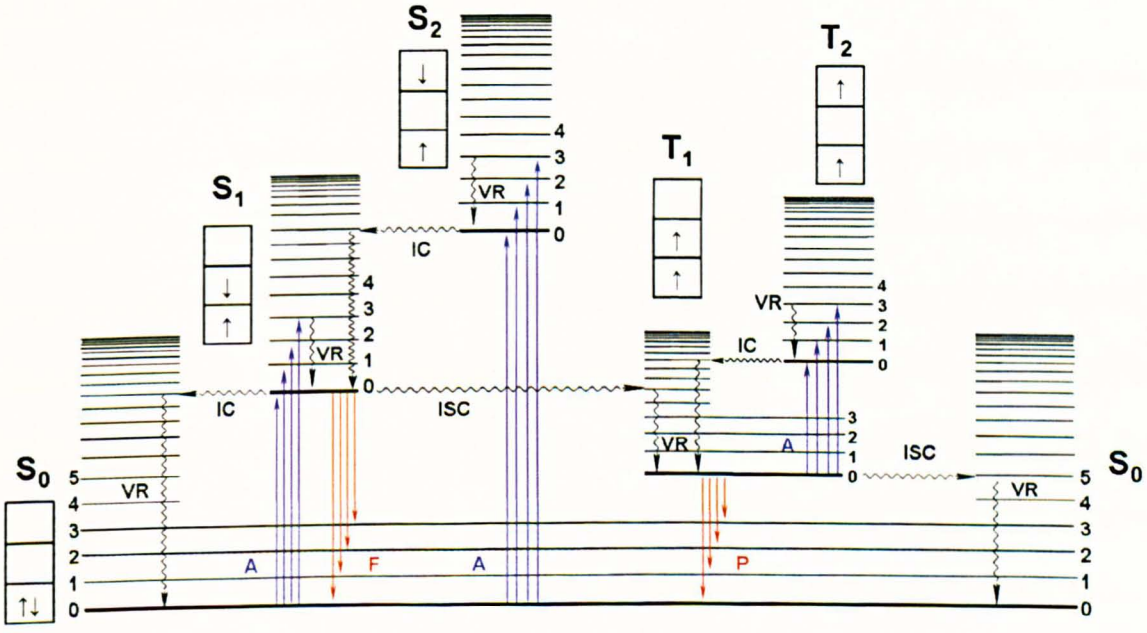

Figure 2.1. Jablonski's diagram [51]. A-absorption, F-fluorescence, P-phosphorescence, IC-internal conversion, ISC-intersystem crossing, VR-vibrational relaxation, S_i and T_i are singlet and triplet energy levels correspondingly.

The S_1 and T_1 excited states can decay to the ground state by emission of light (luminescence) *via* a radiative transition. The rate of emission can be very fast ($k = 10^5$-10^9 s^{-1}) for transitions between electronic states of the same multiplicity, but is much slower ($k = 10^3$-10^5 s^{-1}) between states of different multiplicities. The two processes are known as fluorescence and phosphorescence, respectively.

The excited states frequently go through physical and chemical quenching. Physical quenching is a process in which the photoexcited state of a molecule is deactivated by transferring its energy to another molecule during collisions. This process is termed 'quenching' if the focus is on the initially excited species or 'sensitization if the newly created excited state is of interest. Chemical quenching is the removal of the excited states through a photochemical reaction.

2.1.3. Classification of photochemical reactions

Three types of conceptual frameworks for classification of photochemical reactions may be employed [1]. First we can employ a purely phenomenological classification based on reaction types. This approach recognises that only a small set of truly distinct reaction types occurs and that the majority of photochemical reactions can be successfully classified in terms of this set. Second, photoreactions may be classified in terms of the typical reactions of chromophores, the light absorbing units of molecules. Finally, the third approach considers photoreaction mechanisms and classifies reactions of individual chromophores on the basis of a small set of general mechanisms. From the standpoint of photochemistry as a synthetic tool the concept of phenomenological reaction types is probably the most useful.

Three typical routes for photochemical reactions are depicted below:

- dissociation ($AB^* \rightarrow A + B$);
- reaction with other species ($AB^* + C \rightarrow AC + B$ or $AB^* + C \rightarrow ABC$);
- isomerization ($AB^* \rightarrow BA$).

These groups are further divided into cis-, trans- isomerisation, fragmentation, reductive additions to multiple bonds, electrocyclic reactions, sigmatropic reactions and

cycloaddition (cycloelimination) reactions. Almost all known photoreactions can be classified in terms of these six types. Only reductive addition to multiple bonds and cycloaddition reactions are intermolecular in the sense that two molecules are involved and one of them is electronically excited while another is in its ground state. The other reaction types are intramolecular in nature.

2.1.4. Quantum yield of photochemical reactions

Not every excited molecule undergoes a photochemical reaction due to the existing competitive radiative and nonradiative processes. The efficiency of a photochemical reaction is reflected by the quantum yield, ϕ_R [50]:

$$\phi_R = \frac{r_R}{I_a} \tag{2.7}$$

Where r_R is volumetric reaction rate, corresponding to a given reactant or product and I_a is the volumetric rate of photons absorption by the reactant (intensity of the absorbed light).

As photochemical processes are chains of sequential events, the overall quantum yield, Φ, is the result of these events combined. This parameter is especially useful if these processes cannot be separated. The overall quantum yield accounts for all primary and secondary processes leading to the formation of a product of interest. When $\Phi < 1$, the product is most likely to be formed by the primary reaction. When $\Phi > 1$, secondary reactions are involved and if $\Phi >> 1$, then multistep chain processes occure. If the constants of the intermolecular processes are known, it is possible to calculate the yield of a chemical reaction from i-th state, ϕ_{R_i} in comparison with physical processes:

$$\phi_{R_i} = \frac{k_{R_i}}{\sum_i k_{R_i} + k_F + k_{IC} + k_{ISC}} \tag{2.8}$$

where k_{R_i} is the constant of reaction rate from *i*-th state, k_F is fluorescence constant, k_{IC} is IC constant, k_{ISC} is ISC constant.

2.1.5. Parameters influencing photochemical reactions

2.1.5.1. Radiation wavelength

If a molecule contains different chromophores absorbing at different wavelengths (different conformers can also act as different chromophores) then change of radiation wavelength may dramatically change the result of photochemical transformations [50]. For example, different absorption spectra of cis- and trans- isomer allow the possibility of "pumping" the light specifically into one isomer and thereby driving the isomerisation towards the non-absorbing component [1]. Wavelength-selective cleavage of photolabile protecting groups is another example of photochemical transformations sensitive to wavelength [3].

2.1.5.2. Radiation intensity

Radiation intensity of a light source affects the irradiation time required to obtain the 100 % conversion [50]. The increase in radiation intensity leads to decrease in reaction time due to the increase in reaction rate. The decrease in time may be even exponential, indicating that the reaction mechanism changes with the intensity of incident light. An increased irradiance also increases the probability that multiphoton excitation will occur and causes changes in the reaction rate.

2.1.5.3. Temperature

Photochemical reactions normally have a low energy of activation, and therefore exhibit little temperature dependence [50]. However, some excited molecules will take a different reaction path depending on their particular excited state and subsequent reaction steps are

very sensitive to the effect of temperature. This can lead to a decrease in the yield of the desired product. Temperature also affects photocatalytic processes (e. g., involving TiO_2) and interactions with surrounding molecules.

2.1.5.4. Solvent

Continuum surrounding of an excited molecule can interact with molecules producing several effects [50]:

- the solvent molecule compete with dissolved molecules for the radiation and this often limits the radiation received by the solute molecule;
- solvent molecules can physically quench the excited molecules;
- solvents can affect hydrogen abstraction or serve as contributor of hydrogen;
- solvents vary in polarity which influence the type and the rate of reaction.

Photochemical transformations involve several transition states with significantly different dipole moments. These states interact with the solvent to different extents. As any such interaction depends on the solvent density, supercritical liquids with tunable density can be applied to change selectivity towards certain products [5, 52].

2.1.5.5. State of matter

Gaseous, liquid, and solid state studies give different results for the same reaction because the physical principles governing these reactions are different in each state [50]. In the solid state (polymers, *etc*) everything is determined by the available molecular conformations. Micelles are another example of a system with predefined organization, which may fundamentally change photochemical processes. The kinetics of a photochemical reaction in the gaseous state is controlled by the frequency of collisions. In solution, photochemical reactions are controlled by diffusion of reactants. Thus, reactions

carried out in the gas phase will be affected by temperature, whereas in the liquid state, temperature and viscosity of the reacting mixture will have the greatest influence on the results.

2.1.5.6. Influence of heavy atoms

The presence of a heavy atom in a structure of a photoexcited molecule increases the ISC rate due to break down of spin-selection rules [50]. This increases the population of triplet states. Due to the long life of these states the probability of chemical reaction is also increased.

2.1.5.7. Sensitizers

Direct photoexcitation of an organic molecule may result in a reaction from S_1 or T_1 leading to different products [1, 50]. The outcome depends on the competition between the rate of reaction from S_1 and the ISC from S_1 to T_1. For molecules which do not possess an efficient $S_1 \rightarrow T_1$ conversion, photosensitization of T_1 by an electronic energy transfer mechanism can be applied to populate T_1. Efficient population of T_1 requires a photosensitizer which itself forms triplets efficiently, and which can efficiently transfer triplet excitation. Thus, most good photosensitizers possess a high ISC efficiency, a relatively long triplet lifetime, and a high value of spectral overlap integral Ω [50]:

$$\Omega = \int_0^\infty F_E(\lambda) F_A(\lambda) d\lambda \qquad (2.9)$$

Where $F_E(\lambda)$ is the emission spectrum of the excited donor; $F_A(\lambda)$ is the absorption spectrum of the acceptor. This integral imposes restrictions on both the emission and the absorption spectra.

2.1.6. Mechanisms of photochemical reactions

Mechanisms of photochemical reactions can be discussed within several levels of detail [53]. The most basic level is to recognize the processes that are associated with bond breaking and bond forming. These processes can be further described by depicting the orbitals that are involved. Orbital symmetry and/or stereoelectronic effects can be recognized in this way. Photochemical reactions can also be described by potential energy diagrams (developed on the basis of computational approaches), representing transitions between the excited states, and aiming to trace the path from excitation to a product. Several excited states may be involved, each with its own potential energy surface, so there are several energy plots representing these surfaces. Two-dimensional representations can depict progress in one structural change, such as a twist about a bond or a bond breaking. Alternatively, the reaction progress may be viewed as a composite of all the structural changes that take place among reactant, excited state, and the product. **Figure 2.2** shows transitions between excited states and the ground state surface of the products for a hypothetic molecule.

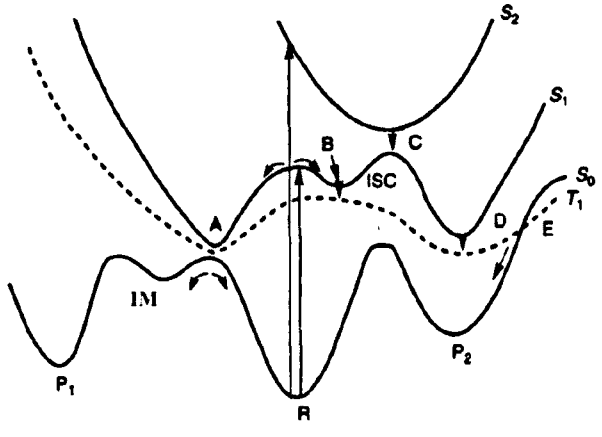

Figure 2.2. A schematic representation of a potential energy profile and transitions between excited states leading to a photochemical reaction products for a hypothetic molecule. Adopted from [53].

The diagram shows excitation to both S_1 and S_2 (the first and second singlet excited states). Molecules drop to the S_1 surface at point C. Singlet excited molecules return to the ground state at point A and may return to reactant or proceed to product P_1 *via* intermediate *IM*. ISC occurs at points B or D and provides the T_1 excited state, which gives product P_2.

2.2. MOLECULAR SINGLET OXYGEN: PHYSICAL AND CHEMICAL PROPERTIES

2.2.1. Introduction

The ground electronic state of O_2 is triplet (the group theoretical symbol is $^3\Sigma$) and contains two unpaired *p*-electrons [54-56]. Chemical reactions between singlet organic molecules and O_2 to form new singlet organic molecules are forbidden by spin selection rule [34]. Thus, the triplet multiplicity of O_2 is the reason why most reactions between O_2 and organic substances do not occur at room temperature, *i.e.*, they are kinetically inhibited. In general, consideration of spin-conservation restrictions answers fundamental question concerning stability of organic life in the ambience of O_2 normally present in atmosphere.

The two lowest electronically excited states are the $^1\Delta$ and the $^1\Sigma$ singlet states with spin pairing of the two electrons and lie 94 and 157 kJ mol^{-1} above the $^3\Sigma$ ground state respectively [57, 58]. The first excited state, $O_2(^1\Delta)$, is commonly being referred to as "singlet oxygen", or $^1O_2$.

The interest that $^1O_2$ has attracted in various scientific fields, *e.g.*, molecular physics, photochemistry [24], biology [25] and medical sciences [26] stems from its chemical properties. Because of its singlet multiplicity there is no spin restriction for reactions of $^1O_2$ with singlet organic molecules which makes it extremely reactive. This allows us to use $^1O_2$ as a powerful oxidant in bleaching and disinfection reactions (*e.g.* H_2O treatment *via* photodynamic inactivation of viruses and cells [59, 60], and as a reagent in organic synthesis (oxygenation reactions with aromatics, steroids, vitamins, amino acids, proteins, etc). It is responsible for natural photodegradation processes (photodegradation of dyes and polymers) and is also involved in the modification of biological structures (lipid

peroxidation and photohemolysis) [61, 62]. An important example of the medical applications of $^1O_2$ is the photodynamic therapy of cancer [26]. Of particular interest is the role played by $^1O_2$ in cell life cycle. It is acknowledged that the presence of $^1O_2$ initiates "controlled" cell death or apoptosis [63].

2.2.2. Sources of singlet oxygen in solution

2.2.2.1. Direct absorption by oxygen ground state

It was demonstrated that $^1O_2$ can be generated with very low efficiency *via* direct absorption of *Nd*:YAG (*Nd*-doped yttrium-aluminum garnet) laser irradiation by O_2-saturated Freon solutions at high pressures [54, 64, 65]. In addition it was shown that it is also possible to produce $^1O_2$ by irradiation of aerated vibrationally excited H_2O at 600 nm with quantum yield of $\sim 3\times10^{-5}$.

2.2.2.2. Generation by oxygen/organic molecule contact complex

The influence of dissolved O_2 on the UV-VIS absorption spectra of organic molecules is a well known phenomenon [54, 64, 65]. The additional absorption bands such as enhancement of $S_0 \rightarrow T_1$ transition of the organic molecule, M, were observed in O_2-saturated solutions. More intense absorption was also seen at shorter wavelengths which was attributed to charge transfer (CT) transitions within a $^3(M..O_2)$ contact complex:

$$M + {}^3O_2 = {}^3(M..O_2) + h\nu \rightarrow {}^3(M^{\delta+}..O_2^{\delta-})$$

The effect was discovered by comparing the absorption spectra of O_2-free and O_2-saturated aromatic compounds such as benzene, toluene, or *o*-, *m*-, or *p*-xylenes. Moreover, it was also demonstrated by picoseconds laser flash photolysis studies that irradiation of $^3(M..O_2)$ contact complexes produces $^1O_2$ with relatively high quantum yields (0.69 in cyclohexane and 0.20 in acetonitrile) [66, 67].

2.2.2.3. Microwave generation of singlet oxygen

$^1O_2$ ($^1\Sigma$ and $^1\Delta$) can be produsedby a microwave discharge passed through O_2 in a gaseous flow system [54, 64]. O and O_3 are also formed as byproducts and can further be removed by reaction with Hg vapour. $O_2(^1\Sigma)$ is rapidly quenched to give $O_2(^1\Delta)$ when the emerging gases are bubbled through solution, containing oxidizable substrates [68].

2.2.2.4. Chemical production of singlet oxygen

Among the reactions used to form $^1O_2$ are reactions of hydrogen peroxide with hypochlorite or hypobromite, reaction of potassium superoxide with water, and thermal decomposition of linear polyacene endoperoxides or of the ozonide of triphenyl phosphate [54, 64, 68-70].

2.2.2.5. Sensitized production by pulsed radiolysis

A high yield of excited states can be formed when a high energy electron beam is passed through liquid hydrocarbons, for example through benzene [54, 64]. Since the lifetimes of singlet and triplet states of benzene are only a few nanoseconds, quenching by dissolved O_2 does not produce much $^1O_2$. However, in the presence of a triplet energy acceptor, *e.g.* 10^{-2} mol L^{-1} naphthalene, energy transfer from triplet benzene occurs to give triplet naphthalene which is quenched by O_2 producing $^1O_2$ [71].

2.2.2.6. Photosensitized production

The most frequently used method of $^1O_2$ generation in solutions is photosensitization or energy transfer to O_2 from the photoexcited states of a sensitizer, which are formed by the absorption of light [54, 56, 64]. Photosensitization of $^1O_2$ is highly favoured in nature. Energy-transfer quenching of triplet states in organic molecules by O_2 is spin-allowed in contrast to all the competing deactivation processes. The excitation energies of both

$O_2(^1\Sigma)$ and $O_2(^1\Delta)$ levels are lower than the energy of many organic triplets, and in most cases, the energy difference is small enough to make the process fast and long enough to make it irreversible. Due to rapid diffusion of O_2 in many media and its high concentration in atmosphere, hardly any intermolecular process is able to compete with quenching of excited states by O_2. Therefore, any excited state that is sufficiently long lived to allow for intermolecular interactions is likely to be quenched by O_2, and $^1O_2$ photosensitization is observed in virtually any chemical system where light is absorbed in the presence of O_2. In many cases, energy transfer results in the formation of both $O_2(^1\Sigma)$ and $O_2(^1\Delta)$. However, the spin-allowed deactivation of $O_2(^1\Sigma)$ occurs with extremely high rate constants with unit efficiency in any medium and all the $O_2(^1\Sigma)$ is recovered as $O_2(^1\Delta)$.

2.2.3. Mechanism of singlet oxygen sensitization

2.2.3.1. Mechanism of $\pi\pi^*$ triplet sensitizing of singlet oxygen

Photosensitized generation of $^1O_2$ during O_2 quenching of $\pi\pi^*$ triplet states can be generally described by a mechanism shown in **Figure 2.3** [72]. The photoexcited sensitizer in T_1 state and $O_2(^3\Sigma)$ first form an excited encounter complex $^m(T_1\ ^3\Sigma)$ with multiplicities m = 1, 3, and 5 with a diffusion controlled rate constant k^+_{diff} [54, 56, 72-79]:

$$T_1 + {}^3\Sigma \underset{k^-_{diff}}{\overset{k^+_{diff}}{\rightleftharpoons}} {}^m(T_1\ {}^3\Sigma) \xrightarrow{k_d} \qquad (2.10)$$

Then, the formed encounter complexes $^{1,3}(T_1\ ^3\Sigma)$ either dissociate back with the rate constant k^-_{diff} or deactivate with an overall rate constant of complex deactivation k_d calculated from the experimentally obtained overall rate constant k_T^Q of triplet-state quenching by O_2:

$$k_d = \frac{k^+_{diff} k_T^Q}{k^-_{diff} - k_T^Q} \qquad (2.11)$$

Here $k_{diff}^{-} / k_{diff}^{+} = 1$ mol L^{-1}, and $k_{diff}^{-} = 2.7 \times 10^{10}$ s^{-1} [74, 79].

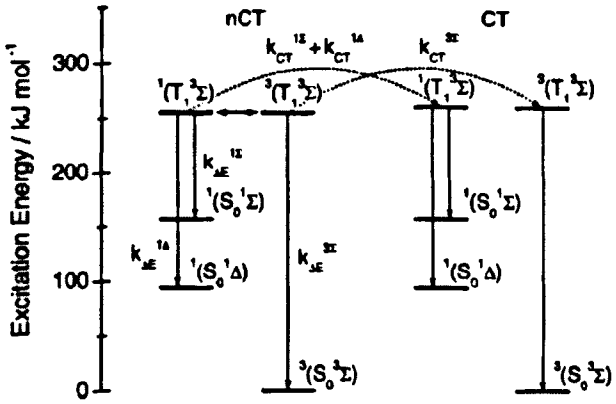

Figure 2.3. Mechanism of $\pi\pi^*$ triplet sensitization *via* both $^{1,3}(T_1\ ^3\Sigma)$ nCT and pCT complexes decay by IC to yield $O_2(^1\Sigma)$, $O_2(^1\Delta)$, and $O_2(^3\Sigma)$ and the sensitizer ground state S_0. Adopted from [72].

Rotation of the O_2 within the solvent cage of encounter complexes in the case of non-charge transfer pathway (nCT) is fast enough to allow for a completely established ISC equilibrium between isoenergetic states of the excited complexes $^m(T_1\ ^3\Sigma)$. The $^5(T_1\ ^3\Sigma)$ complex has no direct product channel. Deactivation process of $^{1,3}(T_1\ ^3\Sigma)$ nCT encounter complexes leading to formation of $O_2(^1\Sigma)$, $O_2(^1\Delta)$, and $O_2(^3\Sigma)$ occurs by IC (which is the rate-limiting step in the nCT channel) to lower complex states of the same multiplicity, *i.e.*, $^1(T_1\ ^3\Sigma) \rightarrow {}^1(S_0\ ^1\Sigma)$, $^1(T_1\ ^3\Sigma) \rightarrow {}^1(S_0\ ^1\Delta)$, and $^3(T_1\ ^3\Sigma) \rightarrow {}^3(S_0\ ^3\Sigma)$ with rate constants $k_{\Delta E}^{1\Sigma}$, $k_{\Delta E}^{1\Delta}$, and $k_{\Delta E}^{3\Sigma}$ expressed by equations (2.12-2.14) [73]:

$$k_T^{1\Sigma} = \alpha k_d \tag{2.12}$$

$$k_T^{1\Delta} = \beta k_d \tag{2.13}$$

$$k_T^{3\Sigma} = (1 - \Phi_\Delta) k_d \tag{2.14}$$

Here α is efficiency of indirect formation of $^1O_2$ *via* the very short-lived upper excited $O_2(^1\Sigma)$, which can be determined from the time resolved spectroscopic observation of

$O_2(^1\Sigma)$, β is efficiency of direct formation of $^1O_2$, $\beta = \Phi_\Delta - \alpha$, Φ_Δ is the overall efficiency of $^1O_2$ formation during O_2 quenching of T_1 states.

The nCT pathway is controlled *via* an energy gap relation given by the empirical polynomial [74]:

$$\ln\left(\frac{k_{\Delta E}^{P}}{m}\right) = 9.05 + (9\times10^{-3})\Delta E - (1.2\times10^{-4})\Delta E^2 + (1.2\times10^{-7})\Delta E^3 + (9.1\times10^{-11})\Delta E^4 \quad (2.15)$$

Here ΔE is an excess energy between the states which has to be released as heat ($\Delta E = E_T - E_\Sigma$, $E_T - E_\Delta$, and E_T for $k_{\Delta E}^{^1\Sigma}$, $k_{\Delta E}^{^1\Delta}$, and $k_{\Delta E}^{^3\Sigma}$ correspondingly), and m is multiplicity. This excess energy relation is independent of solvent polarity and holds true for sensitizers with negligible CT interactions (E_{OX}>1.8 V *vs* sulphur calomel electrode, SCE) and ΔE < 220 kJ mol^{-1}.

In the case of easily oxidizable molecules an alternative decay route of $^{1,3}(T_1\ ^3\Sigma)$ nCT complexes proceeds *via* formation of $^{1,3}(T_1\ ^3\Sigma)$ partial charge transfer (pCT) exciplexes. Significant noncovalent binding interactions slow O_2 rotation and inhibit ISC between $^1(T_1\ ^3\Sigma)$ and $^3(T_1\ ^3\Sigma)$ pCT complexes. The formation of pCT complex is rate determining in the pCT channel and operates with rate constants $k_{CT}^{^1\Sigma}$, $k_{CT}^{^1\Delta}$ and $k_{CT}^{^3\Sigma}$, which can be found from equations (2.16-2.18) [73]:

$$k_T^{^1\Sigma} = k_{\Delta E}^{^1\Sigma} + k_{CT}^{^1\Sigma} \quad (2.16)$$

$$k_T^{^1\Delta} = k_{\Delta E}^{^1\Delta} + k_{CT}^{^1\Delta} \quad (2.17)$$

$$k_T^{3\Sigma} = k_{\Delta E}^{^3\Sigma} + k_{CT}^{^3\Sigma} \quad (2.18)$$

Rate constants of pCT complexes formation depend on the strength of CT interactions and can be quantified by free-energy change of an ion pair formation, ΔG_{CET}, calculated

for complete electron transfer from the T_1 excited sensitizer to O_2. The fit function (2.19) describes the correlation between k_{CT}^{P}/m and ΔG_{CET} [73]:

$$\log(k_{CT}^{P}/m) = \log(c^{P}/m) + c_1 - c_2(\Delta G_{CET} - E_C) \tag{2.19}$$

where $c^{1\Sigma}/1$=0.67, $c^{1\Delta}/1$=0.33, and $c^{3\Sigma}/3$=1.00 are statistical weights of $O_2(^1\Sigma)$, $O_2(^1\Delta)$, and $O_2(^3\Sigma)$ formation. Constants c_1 and c_2 are specific for each type of compounds. For aromatic compounds c_1=7.65, and c_2=-0.23 mol kJ^{-1}. ΔG_{CET} can be expressed by the Rehm-Weller equation [75]:

$$\Delta G_{CET} - E_C = F(E_{OX} - E_{RED}^{O_2}) - E_T \tag{2.20}$$

Here, E_T is sensitizer triplet energy, E_{OX} is sensitizer oxidation potential, $E_{RED}^{O_2}$ is the reduction potential of O_2 (-0.78 V *vs.* SCE in acetonitrile [76]), F is the Faraday constant, E_C is electrostatic interaction energy. Excited pCT complexes then decay by rapid IC ($k_{IC}^{1\Sigma}$, $k_{IC}^{1\Delta}$, and $k_{IC}^{3\Sigma}$) to lower-lying pCT complexes, and all the species involving the sensitizer ground state S_0 dissociate to give S_0 and $O_2(^1\Sigma)$, $O_2(^1\Delta)$, and $O_2(^3\Sigma)$.

The data set shown in **Figure 2.4** includes 127 rate constants determined in CCl_4 for derivatives of naphthalene, biphenyl, fluorene, several ketones, fullerenes, porphyrins and metalloporphyrins, and other homocyclic and heterocyclic aromatics of variable molecular structure and size [74]. This relationship demonstrates that E_T and E_{OX} of the triplet sensitizer are the most important parameters determining $k_T^{1\Sigma}$, $k_T^{1\Delta}$ and $k_T^{3\Sigma}$ and therefore an overall efficiency of $^1O_2$ sensitization during O_2 quenching of $T_1(\pi\pi^*)$ states. These data can be used for optimization of the $^1O_2$ photosensitization ability of many molecules, including those used in biological and medical applications, such as the photodynamic therapy of cancer.

The nCT path dominates for sensitizers with $\Delta G_{CET} \geq 50$ kJ mol^{-1} *i.e.*, on the left-hand side of the surface in **Figure 2.4**. These sensitizers are characterized by rather small overall rate constants $k_T^Q \leq 3\times10^9$ M^{-1} s^{-1} and values of $\Phi_\Delta \geq 0.9$ if $E_T \geq 165$ kJ mol^{-1}. The additional quenching *via* the pCT channel becomes important only in the exothermic range and dominates for sensitizers with $\Delta G_{CET} - E_C \leq -25$ kJ mol^{-1}, *i.e.*, on the right border of the calculated surface. As soon as the pCT channel participates, rate constants k_T^Q strongly increase and values of Φ_Δ decrease; however, $\Phi_\Delta \geq 0.25$ holds true as long as the sensitizer is still photochemically stable. Increase in solvent polarity also results in an increase of k_T^Q, and in a decrease in Φ_Δ.

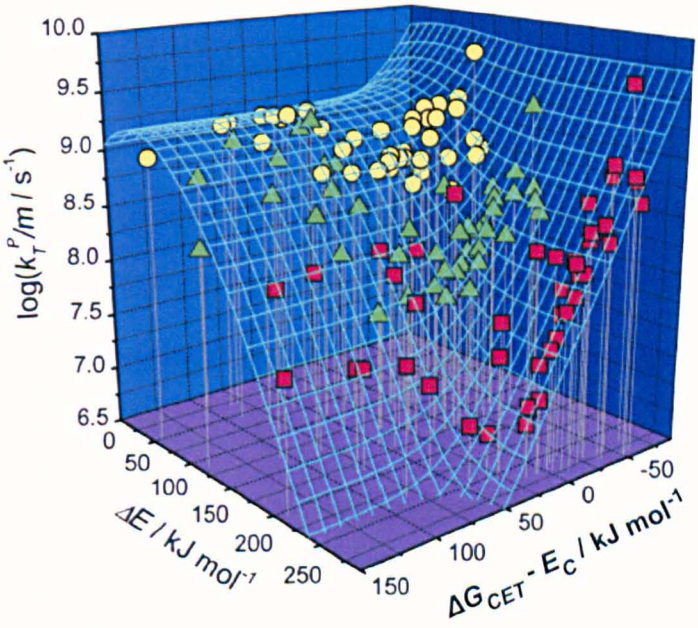

Figure 2.4. Dependence of multiplicity-normalized rate constants k_T^P / m for formation of $O_2(^1\Sigma)$ (yellow circles), $O_2(^1\Delta)$ (green triangles), and $O_2(^3\Sigma)$ (red squares) on the excess energy ΔE and the free energy for formation of an ion pair in CCl_4 for a data set comprising 46 aromatic triplet ($\pi\pi^*$) sensitizers. For clarity reasons, equation (2.19) was approximated using $c^P/m = 1$ for formation of all three O_2 product states. Adopted from [74].

2.2.3.2. Mechanism of $n\pi^*$ triplet sensitizing of $^1O_2$

It was found that quenching for both $T_1(n\pi^*)$ and $T_1(\pi\pi^*)$ sensitizers proceeds *via* nCT and pCT deactivation channels, each capable of producing $O_2(^1\Sigma)$, $O_2(^1\Delta)$, and $O_2(^3\Sigma)$. However, very different energy gap relations determine the deactivation of $n\pi^*$ and $\pi\pi^*$ sensitizers (**Figure 2.5**, *a*) [54, 56, 72-79]. The distinctions in electronic configurations lead to different sterical structures of $^{1,3}(T_1\ ^3\Sigma)$ complexes: supra-supra structure of $^{1,3}(T_1(\pi\pi^*)\ ^3\Sigma)$ complexes and four-center structure of $^{1,3}(T_1(n\pi^*)\ ^3\Sigma)$ complexes (**Figure 2.5**, *b*). In the former case only small structural changes are estimated for the deactivation of the complexes *via* IC, and therefore, a steep dependence on the energy excess is observed. Contrary to $\pi\pi^*$ sensitizers, the large structural changes accompanying the IC of $^{1,3}(T_1(n\pi^*)\ ^3\Sigma)$ complexes lead to displacement of the electronic states. This displacement results in weaker ΔE dependence in the energy gap law. Rate constants of the pCT deactivation channel are also much less dependent on ΔG_{CET} than it was found for $T_1(\pi\pi^*)$ sensitzers due to much weaker CT interactions since the substituents used in these studies to shift oxidation potential of benzophenone were bound to aromatic rings, but not to the excited carbonyl group.

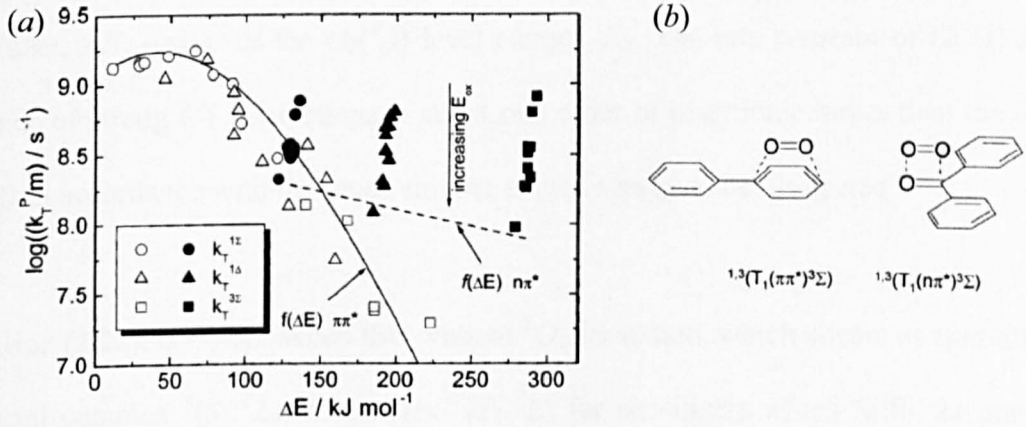

Figure 2.5. Triplet $n\pi^*$ sensitizing of $^1O_2$. (*a*) Dependence of $\log(k_T^P/m)$ on ΔE and E_{ox}. Open symbols correspond to $\pi\pi^*$-excited triplets, solid symbols to $n\pi^*$-excited benzophenone derivatives. (*b*) Structures of $^{1,3}(T_1(\pi\pi^*)\ ^3\Sigma)$ and $^{1,3}(T_1(n\pi^*)\ ^3\Sigma)$ complexes for biphenyl and benzophenone, respectively. Adopted from [77].

2.2.3.3. Mechanism of singlet sensitizing of singlet oxygen

Quenching of S_1 state by O_2 is more complex than quenching of T_1 since at least one and often two excited triplet states can exist below the S_1 state [54, 56, 72-79]. Furthermore, fluorescence quenching is a diffusion-controlled process under ambient conditions for most molecules, obscuring the variation of the actual deactivation rate constants and their dependences on molecular parameters.

Equations (2.21)-(2.24) display the four IC processes, which have been identified to be the most important. The different routes of IC lead from the initially formed excited complex $^3(S_1\ ^3\Sigma)$ to the product complexes $^3(T_1\ ^3\Sigma)$, $^3(T_1\ ^1\Delta)$, $^3(T_2\ ^3\Sigma)$, and $^3(S_0\ ^3\Sigma)$, which further dissociate to the respective components [56, 72]:

$$S_1 + O_2(^3\Sigma) \xrightarrow{K_{diff}} {}^3(S_1\ ^3\Sigma) \xrightarrow{K_I} \begin{cases} {}^3(T_1\ ^1\Delta) \longrightarrow T_1 + O_2(^1\Delta) & (2.21) \\ {}^3(T_1\ ^3\Sigma) \longrightarrow T_1 + O_2(^3\Sigma) & (2.22) \\ {}^3(T_2\ ^3\Sigma) \longrightarrow T_2 + O_2(^3\Sigma) & (2.23) \\ {}^3(S_0\ ^3\Sigma) \longrightarrow S_0 + O_2(^3\Sigma) & (2.24) \end{cases}$$

Reaction (2.21) is O_2-enhanced ISC with $^1O_2$ formation for sensitizers which fulfil the energetic conditions $T_2 >> S_1$ and the difference between S_1 and T_1 energy levels of a sensitizer, $\Delta E_{S\text{-}T}$ exceeds the $O_2(^1\Delta)$ level energy, E_Δ. The rate constant of (2.21) in the absence of strong CT interactions is about one order of magnitude larger than the one of (2.22) in accordance with the much smaller excess energy to be dissipated.

Reaction (2.22), is O_2-enhanced ISC without $^1O_2$ formation, which occurs as spin-allowed IC from complex $^3(S_1\ ^3\Sigma)$ to complex $^3(T_1\ ^3\Sigma)$ for sensitizers which fulfil the energetic conditions $T_2 >> S_1$ and $\Delta E_{S\text{-}T} < E_\Delta$. Only very small values of rate constant for O_2 quenching of an excited singlet state, $k_S^Q \approx 2\times10^8\ M^{-1}\ s^{-1}$ are found in the absence of strong CT interactions and energy transfer. However, the increase in CT interactions

enhances the rate constant of $^3(S_1\ ^3\Sigma) \rightarrow {}^3(T_1\ ^3\Sigma)$ deactivation, similarly to the IC $^3(T_1\ ^3\Sigma) \rightarrow {}^3(S_0\ ^3\Sigma)$ in the T_1 state quenching by O_2 [56].

The contribution to efficiency of $^1O_2$ production during quenching of S_1 by O_2, f_S^{Δ}, depends markedly on the position of T_2 relative to S_1. For many 9- and 9,10-substituted anthracene derivatives, T_2 lies closely above S_1. This leads to temperature-dependent fluorescence quantum yields, which are explained by the activation-controlled ISC leading to radiationless deactivation in the triplet state $S_1 \rightarrow T_2$, where the activation energy E_{ISC} is interpreted as energy difference between T_2 and S_1. Once the complex $^3(T_2\ ^3\Sigma)$ is formed, very fast subsequent dissociation occurs, yielding O_2 and the T_2 state of the anthracene derivative, which then dissipates excess energy $T_2 \rightarrow T_1$ by IC without forming $^1O_2$. These results indicate that the quenching process (2.23) *via* $^3(T_2\ ^3\Sigma)$ becomes dominant for molecules with T_2 lying below S_1, *i.e.* when the process (2.23) becomes exothermic.

The process (2.24) begins to compete with the reactions (2.21)-(2.23) in the exothermic range ($\Delta G_{CET} \leq -30$ kJ mol^{-1} in acetonitrile) contributing to an increase of k_S^Q to diffusion-controlled values and to a reduction of f_S^T (efficiency of T_1-state formation during O_2 quenching of S_1), *i.e.* strong CT interactions in the intermediately formed exciplexes, $^3(S_1\ ^3\Sigma)$, lead directly to the ground-state S_0 *via* fast IC without $^1O_2$ formation.

Thus, excess energies and CT interactions direct the different deactivation routes in fluorescence quenching by O_2 similarly to the case of T_1-state quenching by O_2. The S_1-T_1 and S_1-T_2 energy gaps determine the possible competition between (2.21)-(2.23). Together with the strength of CT interactions in the excited $^3(S_1\ ^3\Sigma)$ complex, quantified by ΔG_{CET},

which strongly influences the contribution of the process (2.24), they finally determine the values of k_S^Q and f_S^Δ.

2.2.4. Singlet oxygen quantum yield

The overall quantum yield of photosensitized $^1O_2$ formation, $\phi_{^1O_2}$ is given by (2.25) [56, 72]:

$$\phi_{^1O_2} = p_S^{O_2} f_S^\Delta + \phi_T p_T^{O_2} \Phi_\Delta \tag{2.25}$$

where $p_S^{O_2}$ and $p_T^{O_2}$ are the fractions of S_1 and T_1 states quenched by O_2, and ϕ_T is the triplet quantum yield in the presence of O_2. The efficiency of $^1O_2$ formation *via* T_1 quenching is given by the product $\phi_T \Phi_\Delta$. Triplet sensitization is the major process of $^1O_2$ generation for most compounds. Complete quenching by O_2 occurs already in air-saturated solutions ($[O_2] \approx 2\times10^{-4}$ M) because of the long lifetimes of $\pi\pi^*$ triplet states. Triplet sensitizers with strong ISC, negligible CT interactions, and $E_T > E_\Sigma$ demonstrate large quantum yields $\phi_{^1O_2}$ due to formation of $^1O_2$ *via* two channels ($^1\Sigma$ and $^1\Delta$). Phenalenone is such a sensitizer with $\phi_{^1O_2}$ approaching unity in most of the air-saturated solvents ($\phi_T = 1.00$, $E_{OX} = 1.96$ V *vs SCE* in acetonitrile, $\Delta G_{CET} - E_C = 78$ kJ mol^{-1}, and $E_T = 186$ kJ mol^{-1} [56]). However, increasing CT interactions lead to lower values of Φ_Δ and thus to a decrease in $\phi_{^1O_2}$. Reducing the quantum yield ϕ_T diminishes the efficiency of triplet sensitization as well.

Singlet sensitization is the dominant way of $^1O_2$ formation for strongly fluorescing compounds with negligible quantum yields of ISC in the absence of O_2 ($\phi_T^0 \approx 0$). The direct contribution of S_1 to $\phi_{^1O_2}$ is expressed by the term $p_S^{O_2} f_S^\Delta$. The efficiency of fluorescence quenching $p_S^{O_2}$ is mostly not larger than 0.20 in air saturated liquids, if the

S_1-state lifetime is not much longer than about 10 ns. Compounds with T_2-S_1 > 20 kJ mol^{-1} and $\Delta E_{S\text{-}T} > E_\Delta$ are efficient $^1O_2$ sensitizers. Quenching of fluorescence contributes also indirectly because T_1 is populated by O_2 enhanced ISC with efficiency $p_S^{O_2} f_S^T$ (f_S^T is efficiency of T_1-state formation during O_2 quenching of S_1). The overall quantum yield of ISC in the presence of O_2 is $\phi_T^0(1-p_S^{O_2}) + p_S^{O_2} f_S^T$ and $\phi_{^1O_2}$ is expressed by equation (2.26) in the case of negligible IC.

$$\phi_{^1O_2} = \phi_T^0(1-p_S^{O_2})\Phi_\Delta + p_S^{O_2}(f_S^\Delta + f_S^T\Phi_\Delta) \tag{2.26}$$

For strongly fluorescent compounds with negligible CT interactions fulfilling the above energetic requirements, for example, rubrene, $f_S^T = 1$ and $f_S^\Delta = 1$ hold true. $\phi_{^1O_2}$ strongly depends on concentration of O_2 in solution and may approach 2 at high O_2 partial pressures, when $p_S^{O_2}$ reaches unity. Increasing of CT interactions reduce f_S^T, f_S^Δ and Φ_Δ and, consequently, the overall quantum yield of $^1O_2$ formation. The decrease in $\phi_{^1O_2}$ is greater in polar solvents due to the enhancement of CT interactions.

2.2.5. Quenching of $^1\Delta$ and $^1\Sigma$ excited states of oxygen and their lifetimes in solution

Five main deactivation processes may compete in quenching of $^1O_2$, [56]. These are, in the order of increasing rate constants: radiative processes, electronic-to-vibrational deactivation (*e-v*), CT quenching and chemical reactions (CR) (both often of comparable magnitude), and electronic energy transfer (EET).

Efficiency of the first process is negligible if nonradiative processes are observed. Contribution of the second process, deactivation by *e-v* energy transfer, is predominant for the molecules with oxidation potential $E_{OX} \geq 1.9$ V *vs SCE* in acetonitrile and can be estimated using the bimolecular rate constant k_Q^Δ for *e-v* deactivation, which is given by

the sum of the rate constants k_{XY}^{Δ} (see **Table 2.1**) for *e-v* deactivation by each individual terminal *X-Y* bond of the quencher molecule:

$$k_Q^{\Delta} = \sum_{XY} N_{XY} k_{XY}^{\Delta} \tag{2.27}$$

Here N_{XY} is the number of terminal *X-Y* bonds per quencher molecule. Lifetime τ_{Δ} of $O_2(^1\Delta)$ in a mixture of liquids can be estimated by (2.28), where $[i]$ is the molar concentration of the component *i*:

$$\tau_{\Delta} = (\sum_{i} k_{Q,i}^{\Delta}[i])^{-1} \tag{2.28}$$

This equation can be applied for pure solvents and homogeneous liquid mixtures of several components. In the case of CS_2 and perhalogenated solvents τ_{Δ} is additionally reduced by quenching of $O_2(^1\Delta)$ by O_2. Deviations from real τ_{Δ} may also result if a strongly deactivating *X-Y* bond, such as *O-H*, is sterically hindered, as k_{XY}^{Δ} were derived for freely accessible *X-Y* bonds.

Table 2.1. Rate constants k_{XY}^{Δ} and k_{XY}^{Σ} of quenching of $O_2(^1\Sigma)$ and $O_2(^1\Delta)$ by bonds X-X in the liquid phase [56].

X – Y	k_{XY}^{Δ}, $M^{-1} s^{-1}$	k_{XY}^{Σ}, $M^{-1} s^{-1}$	X – Y	k_{XY}^{Δ}, $M^{-1} s^{-1}$	k_{XY}^{Σ}, $M^{-1} s^{-1}$
O – H	2900	1.5×10^9	C – D	10.4	3.3×10^7
N – H	1530	4.7×10^8	C = S	0.351	1.6×10^6
$C - H_{ar}$	494	1.1×10^8	$C - F_{ar}$	0.625	1.5×10^6
C – H	309	1.0×10^8	C – F	0.049	5.6×10^5
O – D	132	2.7×10^8	C – Cl	0.181	1.6×10^5
$C - D_{ar}$	21.7	5.3×10^7			

Any experimental quenching rate constant exceeding the value estimated according to (2.28) can be attributed to an additional deactivation pathway competing with *e-v* quenching. Among the three possible mechanisms, CT and CR may compete in any situation, whereas EET is possible only for quenchers with low triplet energies (*i.e.*, $E_T \leq$ 94 kJ mol^{-1}) then *e-v*, CT, and CR are negligible.

In the same way, the rate constants k_{XY}^{Σ} for *e-v* deactivation of $O_2(^1\Sigma)$ by the individual *X-Y* bonds from **Table 2.1** can be used for estimation of the rate constant k_Q^{Σ} for the overall *e-v* deactivation of $O_2(^1\Sigma)$ by a given quencher. Lifetime of $O_2(^1\Sigma)$, τ_Σ, can be estimated from the same rate constant, k_Q^{Σ}, if we apply an equation similar to (2.28). Very small values of $\tau_\Sigma \leq 1$ ns (except perhalogenated solvents and CS_2) are generally obtained. The chemistry of $O_2(^1\Sigma)$ has not yet been discovered, despite significant efforts. Thus, any experimental value exceeding the rate constant for *e-v* quenching can be attributed to CT, unless the E_T of quencher is lower than 157 kJ mol^{-1}. In the latter case, EET and diffusion controlled quenching are expected. CT and *e-v* deactivation lead to quantitative formation of $O_2(^1\Delta)$ and the quencher ground state, whereas EET leads to the formation of $O_2(^3\Sigma)$ and the triplet state of sensitizer.

2.2.6. Optimization of singlet oxygen sensitizers

The highest yields of $^1O_2$ generation are obtained when $^1O_2$ is formed due to quenching of both S_1 and T_1 by O_2 [56]. In this case Q_Δ can be as high as 2, *i.e.*, two molecules of $^1O_2$ are formed per photon absorbed. However, this situation is rare, since quenching processes compete with both intra- and intermolecular deactivation pathways. The efficiency of $O_2(^1\Delta)$ formation during O_2 quenching of S_1 approaches 2 when five conditions are simultaneously met: (i) the energy gap between S_1 and T_1 exceeds 94 kJ mol^{-1}, (ii) no second triplet state lies below S_1, (iii) the S_1 state is quantitatively quenched by O_2, (iv) the O_2 quenching process leads to quantitative formation of the T_1 state, and (v) the subsequent quenching of T_1 leads to quantitative formation of $^1O_2$. However, conditions (iii) and (iv) contradict each other. Efficient fluorescence quenching with diffusion controlled rate constant k_S^Q was found only for sensitizers with moderate to strong CT interactions, which reduce efficiency of the T_1-state population during quenching. However, sensitizers with negligible CT interactions have values of $k_S^Q <<$

k_{diff}. As a consequence, the quantum yield close to 2 is only obtained in nonpolar solvents at very high O_2 partial pressures (9,10-dicyanoanthracene is an example [56]), where the danger of combustion increases with hydrocarbon solvents.

Under normal conditions in O_2-saturated solutions $^1O_2$ is most efficiently formed *via* sensitization from triplet states. The maximum yield of unity in this case is achieved if the following five conditions are met: (i) the triplet energy of sensitizer must be larger than 94 kJ mol^{-1} (optimally larger than 157 kJ mol^{-1}, to allow for competitive formation of $O_2(^1\Sigma)$); (ii) the triplet state is quantitatively formed *via* intramolecular ISC; (iii) the triplet state is quantitatively quenched by O_2 (this is commonly observed for most $\pi\pi^*$-excited triplets, where almost complete quenching occurs already in air-saturated solutions unless other quenchers are present at very high concentrations), as opposed to $n\pi^*$-excited triplets, which often react chemically; (iv) Franck-Condon factors are favourable for energy transfer and unfavourable for enhanced internal conversion (this is observed for all $\pi\pi^*$-excited aromatic hydrocarbons, as opposed to $n\pi^*$-excited ketones); (v) CT interactions are negligible. This is fulfiled in nonpolar solvents at high sensitizer oxidation potentials and low triplet energies.

To obtain the maximum amount of usable $^1O_2$, it is also important to minimize its deactivation by the the surrounding media, in particular by the sensitizer. Deactivation of $^1O_2$ by the sensitizer can be both chemical (leading to modifications in the sensitizer, which, in most cases, reduce its $^1O_2$ sensitization ability) and physical (leading to formation of O_2 and the sensitizer ground state). Chemical reactions occur mainly with electron-rich aromatic rings, dienes, or double bonds, and with amines and sulphides. Significant physical quenching can occur *via* (i) diffusion-controlled EET, if the sensitizer triplet energy is only a few kJ mol^{-1} higher than 94 kJ mol^{-1}, or (ii) CT, if the oxidation

potential of the sensitizer is sufficiently low. Thus, a high sensitizer oxidation potential favours $^1O_2$ formation both by increasing its efficiency of production and by minimizing its physical and chemical deactivation. It is also important to mention that no aggregation of ground-state sensitizer molecules occurs, and that no formation of exciplexes occurs. Such interactions can reduce both the triplet yield and Φ_Δ. In these cases the $^1O_2$ yield decreases with the increasing sensitizer concentration.

2.2.7. Porous silicon as a singlet oxygen sensitizer

Recently, it was discovered that *H*-terminated porous silicon nanostructures, *PSi,* may also be used as $^1O_2$ photosensitizers [33, 34, 72, 80-87]. *PSi* may be produced by chemical synthesis (see for example, [88] and links therein), electrochemical etching of bulk *Si* crystals [89] or chemical etching of metal grade silicon powder [23, 90]. Bulk *Si* is a very poor light emitter due to its indirect band gap structure. However, at nanoscale, quantum size effects lead to an increase in the energy of excitons and the probability of their radiative recombination. Therefore relatively high photoluminescence (PL) quantum yields can be achieved [91, 92]. The indirect band-gap structure of *Si* nanocrystals is the reason for very slow recombination rate of excitons (in the order of 10s of μs at room temperature). Statistically 75% of photoexcited excitons persist at room temperature in their triplet states [93, 94]. Due to the long lifetime of excitons confined in *Si* nanocrystals the energy of photons is stored in electronic form and can then be transferred to other substances [95]. Moreover, the band-gap energy of *Si* nanocrystals can easily be adjusted from the bulk *Si* band-gap (1.1 eV) up to about 2.5 eV, simply by varying the size of nanocrystals, controlled by the preparation procedures [93]. Therefore, by choosing the proper nanocrystals size, the energy of excitons can be tuned to match the singlet-triplet splitting energy of a certain acceptor, *e.g.* O_2. A large surface area (up to about 500 $m^2 g^{-1}$), mesopore-range porous structure (*ca.* 7 nm pore size [96]) and good

dispersibility of hydrophobic *Si* nanocrystals in organic solvents allow good accessibility of the surface of *Si* nanocrystals for different molecules. It should also be mentioned that contrary to most conventional photosensitizers *PSi* efficiently absorbs all photons with energies higher than the nanocrystals band-gap. Therefore, a broad range of light sources can be used for excitation.

Excitons photogenerated in *PSi* were proven to be quenched by O_2 forming $^1O_2$ in gaseous environment, in organic solvents and in water [80, 81, 83]. Quenching of excited molecules reduces the emission intensity with the same strength over the whole spectral range [72]. However, in the case of *PSi*, PL suppression spectra demonstrate two peaks. The maximum suppression level of PL appears at 1.63 eV (excitation energy of $O_2(^1\Sigma)$) [80]. This fact indicates that resonant energy transfer with formation of $O_2(^1\Sigma)$ is the most effective quenching process. Subsequent *e-v* energy transfer deactivates $O_2(^1\Sigma)$ very rapidly and completely to $O_2(^1\Delta)$, identified by the corresponding emission spectrum at 0.98 eV [82, 97]. The channel of direct $O_2(^1\Delta)$ formation is inhibited due to large excess energy to be distributed simultaneously by multiple phonon emission in the nanocrystals. The five-fold suppression of PL at 1.63 eV was taken as an indirect measure of the $^1O_2$ photosensitization efficiency of 80%. However, this result actually means only an 80% quenching efficiency. The second peak in the PL suppression spectrum appears at about 2 eV (620 nm) and indicates possibly electron transfer quenching with the formation of superoxide radical-anion O_2^- [81].

Bleaching of 1,3-diphenylisobenzofuran (*DPBF*) (chemical scavenger of $^1O_2$) in the presence of photoexcited *PSi* was demonstrated, both in a spectroscopic cell and in a recirculating laboratory scale reactor [23, 33]. The bleaching rate increased with the amount of *PSi* immersed. However, bubbling the solution with N_2 to remove O_2 led only

to about 50% suppression of photobleaching. This result was explained by direct interactions between triplet excitons and *DPBF via Type-II* oxidation reaction [85]. Contrary to oxidation by the photosensitised $^1O_2$ (*Type I* pathway), this process occurs *via* direct interaction between sensitizer and substrat leading to proton or electron transfer which results further in the formation of free radicals or free-radical ions [54, 98, 99]. The radicals produced from the photosensitizer can react with O_2 to generate reactive oxygen species such as O_2^-, while radicals produced from the substrate may initiate free radical chain reactions. Both pathways can lead to degradation of *DPBF*.

Thus, the suitability of nanocrystalline *PSi* as a pure sensitizer of $^1O_2$ is still not fully proven. The data reported earlier leave doubt over the specific mechanism of photobleaching and do not provide direct comparison between the sensitizing efficiency of *PSi* with that of conventional organic dye sensitizers.

2.2.8. Singlet oxygen in organic synthesis

2.2.8.1. Singlet oxygen addition to unsaturated and aromatic compounds

Most reactions of $^1O_2$ with the unsaturated hydrocarbons can be divided into four major groups according to their pathways (**Figure 2.6**, *a-d*) [35]. The electron-rich olefins give preferably 1, 2-dioxetanes by the [2+2] cycloaddition (*a*) [100-102], conjugated dienes and naphthalene derivatives react preferably by [4+2] cycloaddition to form endoperoxides (*b*), [102, 103], unactivated olefins with allylic hydrogen atoms undergo Schenk ene reaction to form allylic hydroperoxides (*c*) [99] (*X* denotes CR_2, *NR* or *O*), and phenols and naphthols containing bulky groups in positions 2 and 4 of the ring go through 1,4-addition with the formation of hydroperoxide ketones (*d*) [102].

The allylic hydroperoxides that result from Schenk reaction were proven to be synthetically useful intermediates (**Figure 2.6**, *e*) [104, 105]. While the reduction leads to allylic alcohols, the reaction with *Ti* (IV) complexes has been utilized to prepare epoxy alcohols from simple olefins in a one-pot operation [106, 107]. Finally, dehydratation [108] provides a convenient access to synthetically useful 2-cycloalkenones and other α, β -unsaturated carbonyl compounds as enones with silicon ($R_1 = SiR_3$) [109] or tin substituents ($R_1 = SnR_3$) [110] at the *a-C* atom.

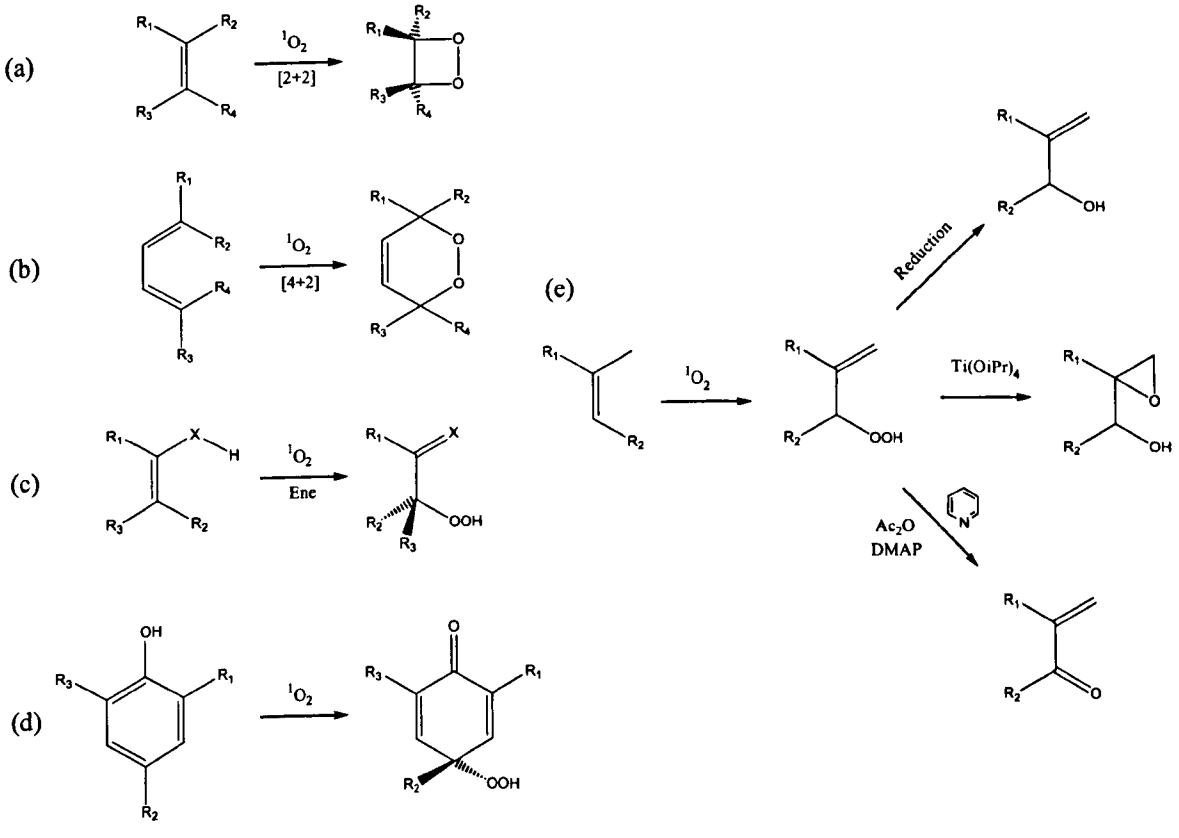

Figure 2.6. Reactions of $^1O_2$ [35, 102]. (*a*) 1,2-addition to olefins to form 1,2-dioxetane-type products; (*b*) 1,4-addition to conjugated dienes to form endoperoxides; (*c*) ene type reaction of unactivated olefins with allylic hydrogen atoms to form allylic hydroperoxides (*X* denotes CR_2, *NR* or *O*); (*d*) addition to phenol derivatives containing bulky groups in positions 2 and 4 of the ring to form hydroperoxide ketones; (*e*) synthetic applications of the allylic hydroperoxide.

2.2.8.2. Regioselectivity of ene reaction

Since $^1O_2$ is a highly reactive oxidant that undergoes reactions with a wide variety of substrates, selectivity in its transformations is mandatory for synthetic utility [35]. A central problem of Schenck reaction is that of regioselectivity. When a given substrate has several allylic hydrogen atoms, abstraction can take place at all possible sites leading to complex mixtures of isomeric products. Several empirical rules were proposed to allow *a priori* determination of regioselectivity of reactions with a variety of substrates. The *"cis* effect" describes the finding that *H* abstraction takes place preferably at the more substituted side of the double bond (**Figure 2.7**, *a*). The "gem effect" applies to gem-substituted olefins for which abstraction at the geminal position predominates (**Figure 2.7**, *b*, $X = C(O)R, SO_xR, CN, SiR_3, SnR_3, Ph$).

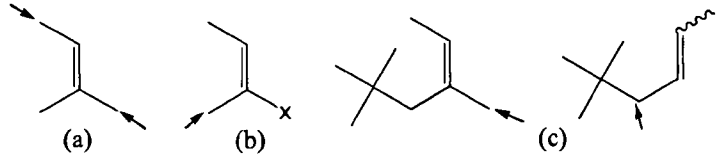

Figure 2.7. Regioselectivity of Schenck reaction [35]. (*a*) *cis* effect; (*b*) gem effect; (*c*) large group nonbonding effect.

The "large group nonbonding effect", the least general of the regioselectivity rules, describes the preferred site of abstraction for highly substituted olefins (**Figure 2.7**, *c*). Nevertheless, while some progress has been made recently in controlling regioselectivity of Schenck reaction, it is important to emphasize that the complexities of regioselectivity also influence stereoselectivity of this reaction.

2.2.8.3. Stereoselectivity

Owing to the inherent lack of stereochemical features in the linear diatomic $^1O_2$ molecule, stereoselectivity in Schenck reaction is directed by the substrate [35]. The presence of two diastereotopic faces (**Figure 2.8**) in a given chiral substrate allows for two diastereomeric

transition states of different energies in the attack of $^1O_2$. In the product-forming step, hydrogen abstraction takes place either at the neighbouring alkyl group or directly at the stereogenic center. In the latter case the stereochemistry of the resulting double bond reflects the π-facial selectivity of the initial $^1O_2$ attack (**Figure 2.8**). In the case when R^1 = *H*, the *E* isomer of the two possible products generally prevails for steric reasons.

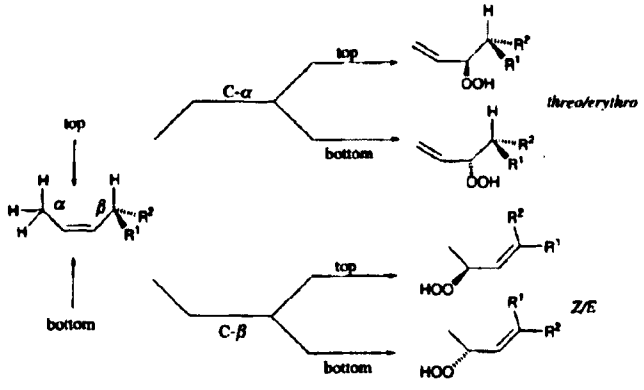

Figure 2.8. Stereochemical possibilities for chiral substrates in Schenck reaction. Adopted from [35].

The factors governing π-facial selectivity can be divided into four distinct types. In the case of steric control nonbonding repulsion between substrate and reagent makes one π-face of the double bond more preferable for the attack by $^1O_2$ than the other. This type of interaction is present in all types of substrates and shows little or no solvent dependence. The stereocontrol factor is the most important for rigid systems (cyclic and polycyclic substrates), which cannot adjust their conformations to minimize steric interactions. Thus, repulsive interactions between the substrate and $^1O_2$ can be modulated by stereoelectronic and electronic factors. The first factor describes those cases in which one face of a substrate displays a higher π-electron density due to special features of the overall geometry of the substrate molecule, for instance orbital distortion. In contrast, the second factor describes specific interactions between a substituent of the substrate and the incoming $^1O_2$ enophile. This includes attractive hydrogen bonding interactions and electrostatic attractions and repulsions. Ene reactions with $^1O_2$, which are controlled

primarily by electronic factors, are highly sensitive to solvent polarity. Since the product-forming step involves abstraction of an allylic hydrogen atom, which must not only be present in the substrate molecule but also aligned correctly, conformational factor may play a dominant role in some cases. This factor becomes important in cyclic systems, in which allylic hydrogen atoms may be accessible only on one π-face of the substrate. Since the most suitable geometry for effective hydrogen atom abstraction requires a perpendicular arrangement of the *C-H* bond with respect to the plane of the double bond, subtle conformational features may be decisive factors.

The most important substrate classes are summarized in **Table 2.2** with respect to type, sense, extent, and scope of stereocontrol in Schenck reaction [35]. One can see from these data that effective stereocontrol has not yet been achieved for cyclic systems (especially for monocyclic substrates) due to low levels of π-facial selectivity. Nonbonding repulsion and conformational effects play a major role in such systems. In common, too many effects are involved in Schenck ene reaction of cyclic substrates to reduce the experimental data to some simple rules. Polycyclic systems in many cases give very high levels of diastereoselectivity but only if the substrate already bears very special structural features. This is true for many natural products such as monoterpenes and steroids. Thus, incorporating into a synthetic sequence a potentially stereoselective Schenck reaction for a cyclic substrate is problematic. However, repulsion of $^1O_2$ by functional groups may be a useful approach for controlling *anti* attack in preparation of ene products of synthetic utility from simple cyclic alcohols or carboxylic acids.

Open-chain systems demonstrate relatively low sensitivity of $^1O_2$ to sterical effects and weak dependence on the conformational arrangements. In these highly flexible substrates, electronic effects such as hydrogen bonding and electrostatic repulsion play an important

role and override any possible sterical effects. Moreover, perpendicular arrangement of hydrogen atom to the plane of double bond (optimal for abstraction) can be readily achieved due to insignificance of conformational effects. The high sensitivity to solvent effects demonstrates the importance of electronic effects in oxygenation. Since the list of non-polar solvents includes very common ones such as CCl_4, $CHCl_3$, and aromatic hydrocarbons, this is not a major drawback for synthetic applications.

Table 2.2. Substitute-dependent π-facial selectivity in Schenck reaction. (a) Major selectivity-determining effects as defined above [35].

Substrate class	Type	Stereocontrol extent	Sense	Scope
Monocyclic olefins	Steric, conformational	Low	Anti	General
Bi- and polycyclic olefins	Steric	Moderate to high	Anti	Limited
Functionalized cyclic olefins	Steric, stereoelectronic	Low to high	Anti	Limited
Acyclic allylic alcohols	Electronic	High	Threo	General
Acyclic allylic ethers and esters	Steric	Low	Threo, erythro	General
Acyclic allylic amines	Electronic	High	Threo	General
Diacylated acyclic allylic amines	Steric, electronic	High	Erythro	?
Acyclic allylic halides, sulfoxides, and sulfones	Electronic	High	Erythro	?

The Schenck reaction of acyclic allylic alcohols and amines constitutes a very general and efficient method for the diastereoselective preparation of highly oxyfunctionalized, threo-configurated target molecules. The only prerequisite for the substrate structure is the presence of a substituent located *cis* with respect to the chiral center, which allows for efficient differentiation in the energies of the different conformers through 1,3-allylic strain. Furthermore, simple diacylation of the allylic amines can be used to prepare efficiently the *erythro* product. Other hetero substituents, for example sulfinyl, sulfonyl, and halogen groups have erythrodirecting propensity, but for these substrates it is still

necessary to define the scope and limitations. The substrate-directed Schenck reaction of olefins with an adjacent, heteroatom substituted chiral centre is a very versatile and mild method for the predicted stereoselective oxyfunctionalization of acyclic substrates.

The operative mechanistic features to perform selective oxyfunctionalizations for practical applications are highly diverse and complex so it is difficult to predict and rationalize the chemo-, regio-, and stereoselectivity of photooxygenations. Nevertheless, $^1O_2$ can be utilized in a highly stereoselective manner in the Schenck reaction for the preparation of a variety of valuable oxyfunctionalized target molecules.

2.3. PHOTOCHEMICAL ENGINEERING TECHNOLOGY

2.3.1. Introduction

Photochemical synthesis has some advantages over thermal, catalytic and other methods of producing chemical compounds, namely, selective activation of individual reactants, specific reactivity of electronically excited molecules, low thermal load on the reaction system, exact control of radiation in terms of space, time and energy [111]. In spite of these advantages there are only few examples of practical applications of photochemistry due to several reasons, including: (i) absorption characteristics - many reaction systems are ruled out for photoreactions because of low light absorption and hence low photonic efficiency; (ii) internal light filters - photoreactions may be rapidly terminated if products with competing absorptions are formed; (iii) scale up problems - scalability of reactors and light sources often leads to losses in light utilization, non-uniformity of illumination of reactors, and heat and mass transfer problems; (iv) investment costs - photochemical production plants may incur high unit capital costs if the space-time yield is low as a result of limitations imposed by the power of the lamps; (v) electricity costs - light is more expensive than heat because considerable losses occur in the production of electrical energy and its conversion into usable light energy (the overall efficiency for this process is at best only about 9 %).

Selection of the light source for photochemical transformations on a laboratory scale is based on spectral overlap between reagent absorption range and lamp emission spectrum (*i.e.* quantum yield of product formation is maximal at lamp output wavelength interval). In the case of a commercial process to this should be added efficiency of light source (in terms of watt output light power per watt of consumed power) and lifetime to be economically viable.

Most of the commertially realized photochemical processes are radical chain reactions with quantum efficiences >> 1. Therefore they often do not require any optimisation of reactor configuration (lamp-reactor geometry). Contrary, for the processes with quantum efficiency < 1 the lamp-reactor geometry becomes one of the most important features of the photochemical reactors. This geometry (which depends on the choice of reactor and of the source of light) determines light distribution and, therefore, efficiency of light utilisation inside the reactor (amount of the absorbed photons to the total amount of light emitted by the lamp).

2.3.2. Artificial sources of light

2.3.2.1. Thermoluminescence lamps

Incandescent filament lamps generate light by passing an electric current through a thin tungsten filament wire until it is extremely hot [112-115]. The higher the filament temperature the greater will be the visible light output (thermoluminescence) in lumens per watt of electric power input. The glass envelope of incandescent filament lamps is usually filled by nitrogen or argon to reduce evaporation of the tungsten filament. In a coloured incandescent lamp the envelope is coated either internally or externally with a filter. All coloured incandescent lamps operate at reduced efficiency. For example, in the case of blue lamps more than 90% of light is filtered out due to low proportion of blue light in the spectrum (**Figure 2.9**, *a*).

Incandescent light bulbs generally have efficiencies near or below 35 lm W^{-1}. For example, an ordinary 100 W incandescent lamp having a total light output of 1200 lm has an efficacy of just 12 lm W^{-1}. Only a small quantity of the electrical energy supplied to an incandescent lamp is converted to visible light, and by far the greatest proportion is dissipated as useless heat (about 95% heat and 5% light). A higher filament temperature

increases lamp efficacy, but at high filament temperatures tungsten evaporation is more rapid and leads to a shorter lamp lifetime. Moreother, the temperature of a tungsten filament cannot be increased indefinitely, as the bulb will melt if the lamp efficacy approaches 40 lm W^{-1}. Lifetime for this type of lamps is typically about 750-4000 hours.

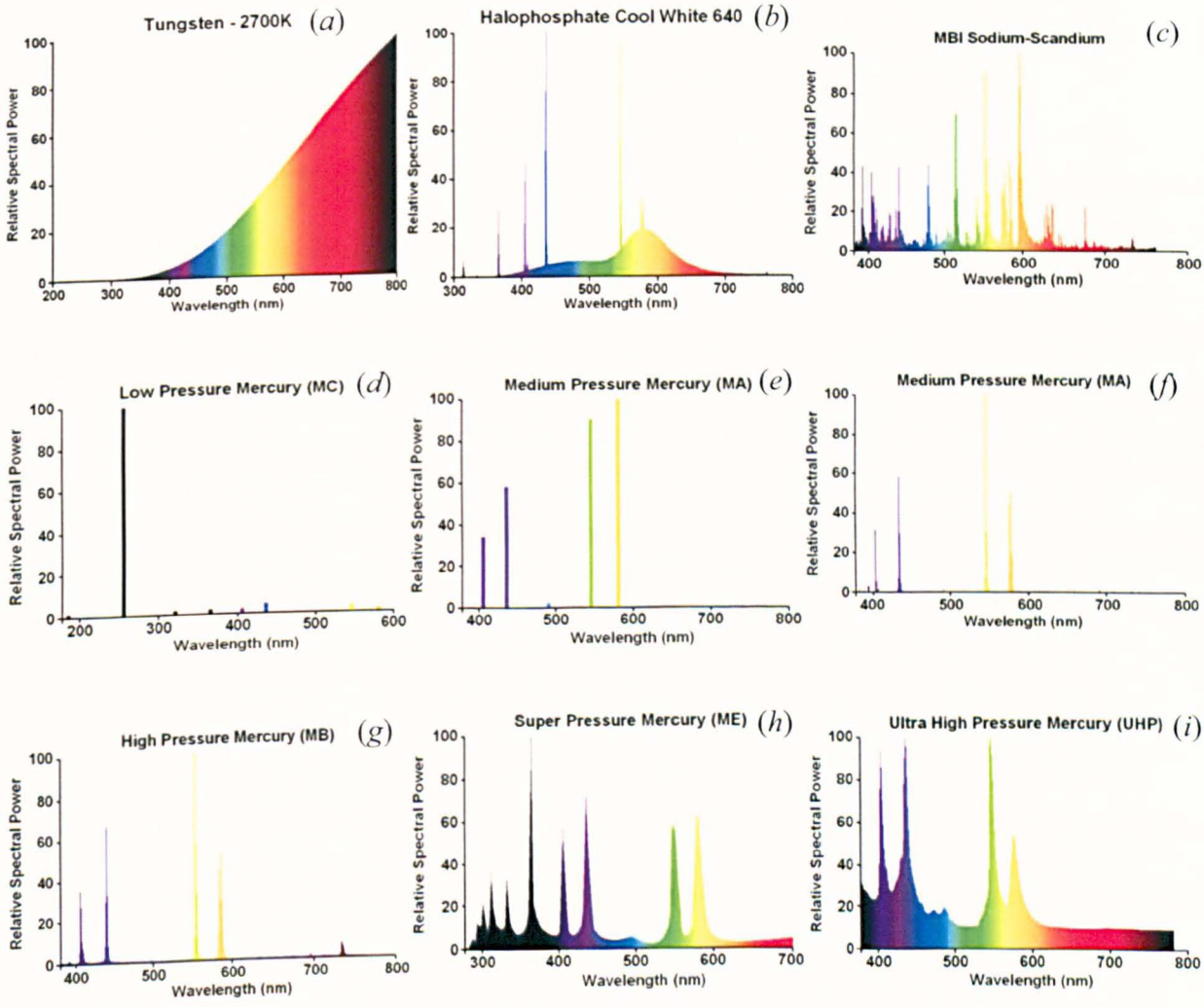

Figure 2.9. Emission spectra of different sources of light. (*a*) Tungsten filament lamp, (*b*) mercury fluorescent lamp, (*c*) metal halide lamp; (*d*)-(*i*) spectra of emitted radiation from mercury discharge lamps at varying tube pressures. Sourced from [116].

In the tungsten-halogen lamps the quartz envelope is closer to the filament than the glass used in conventional light bulbs and contains iodine [113-115]. Heating the filament to a higher temperature causes tungsten atoms to evaporate and combine with the halogen gas. These heavier molecules are then deposited back on the filament surface. This recycling

process increases lifetime of the tungsten filament and enables the lamp to produce more light per unit of energy. A typical tungsten halogen lamp will provide about 50 % greater light output and about twice the lifetime of a conventional tungsten lamp of an equivalent wattage (2000-6000 hours).

2.3.2.2. Discharge lamps

A discharge lamp consists essentially of a glass, quartz or other suitable material tube, containing a gas and, in most cases, a metal vapour [115]. The passage of an electric current through this gas/vapour produces light or UV radiation. The nature of the filling, the pressure developed and the current density determine the characteristic radiation produced by the arc. In most lamps the arc tube is enclosed within an outer glass or quartz jacket. This affords protection, can be used for phosphor or diffusing coatings, control of UV radiation emission and, by a suitable gas filling, can control the thermal characteristics of the lamp.

All discharge lamps include some mechanism for production of electrons from the electrodes within the lamp. The commonly used methods are thermionic emission (hot cathode) and field emission (cold cathode), and in both cases emissive material such as barium oxide is often contained within the electrode to lower its work function and, hence, reduce energy loss. All discharge lamps also require a special fixture and ballast for each type and wattage.

A low pressure mercury lamp contains mercury vapour at pressures of about 0.1 Pa and emits mainly at 253.7 and 184.9 nm with about 40 % and 10 % efficiency correspondingly [112, 114, 117]. Lifetime of this source of light is normally about 8000 hours. Low pressure mercury lamps are often used for disinfection and purification of

water, air or surfaces and sometimes are called germicidal lamps. There are cold and hot cathode as well as cooled induction or electrodeless (excited by microwaves) low pressure mercury lamps. When the inner side of the low pressure mercury lamp tube is covered by an amalgam of *Hg* with another element such as *In* or *Ga* (*amalgam* lamp), these lamps have 2–3 times the UV output for the same length as the standard low pressure mercury lamp. Lifetime is also increased twice (16000-20000 hours).

The interior surface of the low pressure mercury fluorescent lamp tube is coated with a fluorescent powder, the phosphor (blend of metallic and rare-earth phosphor salts), which converts the UV light produced by the discharge into visible light [50, 114, 115]. The colour and spectral composition of radiated light will depend upon the phosphor used. Spectrum of a fluorescent lamp with the most widespread halophosphate phosphor ($Ca_{10}(PO_4)_6(F,Cl)_2$:*Sb*, *Mn*) is shown in **Figure 2.9**, *b*. Another example of widely used fluorescent lamps (known as Black light source) with an added fluorescent layer (for example $SrB_4O_7F:Eu^{2+}$) which emits in the UV-A spectral region (315-400 nm). The efficacy of fluorescent tubes ranges from about 16 lm W^{-1} for a 4 W tube with an ordinary ballast to as high as about 100 lm W^{-1} for a 32 W tube with a modern electronic ballast, commonly averaging 50 to 67 lm W^{-1} overall.

A medium pressure mercury lamp contains mercury vapour at pressures ranging from 50 to several hundreds kPa and emits mostly in 200-1000 nm region with the most intense lines approximately at 218, 248, 254, 266, 280, 289, 297, 303, 313, 334, 366, 406, 408, 436, 546, and 578 nm [112, 117, 118].

A high-pressure mercury lamp consists of a pure fused silica arc tube, enclosed within a borosilicate outer envelope [113-115, 119]. The arc tube containing a controlled quantity

of mercury sufficient to produce a pressure of ca. 8 MPa or higher emits lines over a background continuum between about 200 and 1400 nm (**Figure 2.9,** *g-i*) [116, 117]. The outer envelope is filled to a pressure of 0.25-0.65 atm with either nitrogen or a nitrogen-argon mixture. Phosphors similar to those used for fluorescent lamps can be used to give these a colour closer to natural light. Mercury vapour lamps have the longest life of this class of bulbs (10000 to 24000 hours) and efficiences of about 60 lm W^{-1}.

By adding suitable metals (sodium, thallium, gallium, scandium and others) in the form of halides (usually iodides) with lower excitation potentials to the mercury high pressure arc tube, it is possible to increase the light output [113, 115, 119]. Thus, no phosphor is needed to produce a colour approaching that of a cool white fluorescent lamp with more green and yellow than in a mercury vapour lamp emission (**Figure 2.9**, *c*). These sources of light are known as high-pressure mercury-metal halide lamps. The metal halide lamps have efficiency of up to 125 1m W^{-1}.

A low pressure sodium lamp (LPS), also known as a sodium oxide lamp (SOX), consists of a long arc tube of glass construction, known as 'ply tubing', filled with low-pressure 'Penning mixture' gas (*Ne* and 1% *Ar*) to start the gas discharge [113, 115, 119]. The lamp also contains a small quantity of metallic sodium, which provides a pressure of about 0.66 Pa in the lamp when operating. The arc tube is coated with the outer vacuum envelope of glass covered by an IR reflecting film (*In*, *Sn*, *Bi* oxides, or gold). LPS lamps produce a virtually monochromatic yellow light, which consists of two radiation lines (resonant doublet) at 589.0 and 589.6 nm (**Figure 2.10**). The lines are close to the maximum spectral sensitivity of the eye (555 nm) and the lamp is therefore efficient for outdoor lighting such as street lights. Lifetime for modern LPS lamps is usually rated around 18000 hours while efficacies of up to 200 lm W^{-1} are typical.

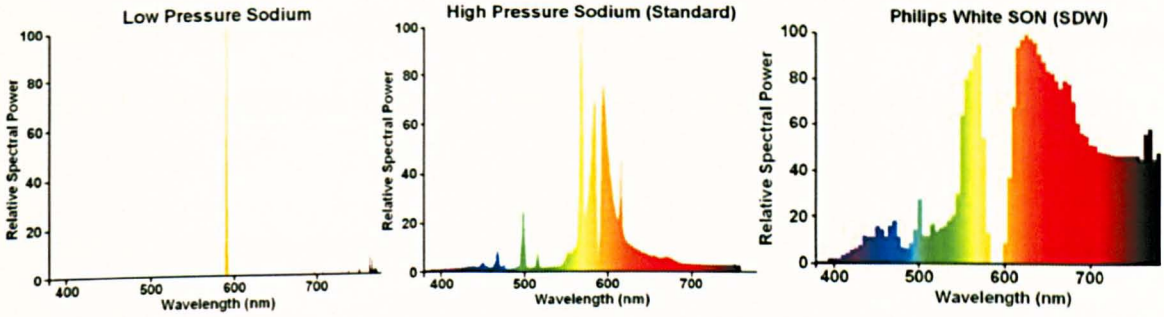

Figure 2.10. Emission spectra of sodium sources of light. From the left to the right: low pressure sodium lamp; high pressure sodium lamp; high pressure sodium white SON lamp (Philips) (adopted from [116]).

Most high pressure sodium lamps (HPS) have an arc tube containing metallic sodium doped with mercury and *Ne-Ar* mixture or *Xe* [113-115]. Sodium is added in a quantity which provides approximately 100 times higher sodium vapour pressure when operated, compared to that of LPS. The mercury vapour adjusts the electrical characteristics, and acts to reduce thermal conductivity and power loss from the arc. *Ar* or *Xe* aid starting. The arc tube is sealed into an evacuated outer jacket. The sodium *D*-line, broadened due to a high pressure of sodium is the main emission line in these lamps (**Figure 2.10**). Efficiency of HPS lamps is about 100-160 lm W^{-1}.

Different variations of the high pressure sodium lamp exist. These lamps operate at higher sodium pressures (10-100 kPa) than the typical HPS lamp (about 10 kPa). However, they have higher cost, shorter lifetime, and lower light efficiency. **Figure 2.10** demonstrates the emission spectrum of Philips white SON lamp.

A *Xe* arc lamp is an intense source of UV, visible and near-IR radiation produced by electrical discharge in *Xe* under high pressure [50, 112, 114]. The lamp consists of a glass

or fused quartz arc tube with tungsten metal electrodes at each end. For stability, these arc lamps should be operated near rated power on a well-regulated power supply.

Xe arc lamps come in two distinct varieties: pure *Xe*, which contain only *Xe*, and xenon-mercury, which contain both *Xe* and a small amount of mercury. Pure *Xe* arc lamps have a "near daylight" spectrum (**Figure 2.11**, *a*). They are not as efficient as high pressure discharge lamps due to strong near-IR lines around 820-1000 nm and normally demonstrate an output of 13 lm W^{-1} for the 75 W size, 13-20 lm W^{-1} for 150 W sizes, 35-40 lm W^{-1} in 1-1.6 kW sizes, and around 45-51 lm W^{-1} in 10-20 kW sizes. *Xe-Hg* arc lamps have a bluish-white spectrum and extremely high UV output. They are more efficient than *Xe* ones but less efficient than ordinary general purpose mercury lamps. All arc lamps have limited lifetime, typically a few hundred hours.

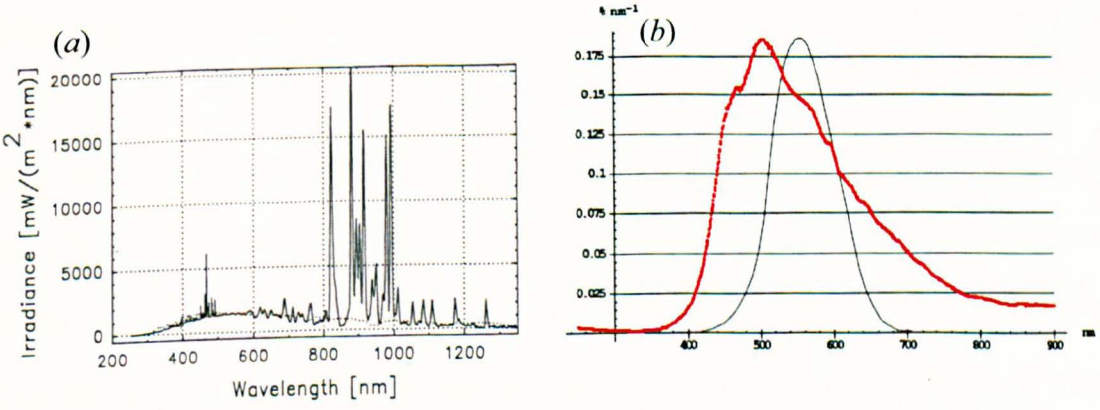

Figure 2.11. Emission spectra of *Xe* arc lamp (*a*) (sourced from [120]) with dotted line solar spectrum, and sulfur induction lamp (*b*), red curve; black curve represents eye sensitivity function (sourced from [121]).

The induction lamps are also referred to as the 'electrodeless lamps' [113, 115]. They consist of a tube, containing the radiation-producing element, and a microwave generator, which excites the elemental spectra. A mercury induction lamp operates from a separate dedicated electronic control gear. The current induced in the mercury vapour gives rise to

emission of UV radiation in a similar manner to that in a conventional low pressure mercury lamp and the phosphor can also be applied on the inside of the lamp envelope. Efficiency can reach 80 lm W^{-1} for 100 W bulbs (Osram Endura lamp). The lamp lifetime is typically about 60000 h [113, 115].

Another less known highly efficient full-spectrum electrodeless source of light is a sulfur induction lamp [121, 122]. The lamp consists of 35 mm fused-quartz bulb containing several milligrams of sulfur and rare gas at low pressure. The bulb is enclosed in a microwave-resonant wire-mesh cage. A magnetron pumps the 2.45 GHz microwaves radiation inside the bulb. The bulb is rotated continuously at high rpm to prevent it from melting. The output light generated by S_2 dimers of sulfur plasma with a peak at 510 nanometers is low in IR and UV components and mimics sunlight better than any other artificial light source (**Figure 2.11**, *b*).

The sulfur lighting technology was developed in the early 1990s, but had a commercial failure by the late 1990s. The first prototype lamps were 5.9 kW units, with a system efficiency of 80 lumens per watt. The first production models were 1.4 kW with an output of 135000 lumens. The design life of the bulb is approximately 60000 hours. However, the design life of magnetrons is currently only about 15000 to 20000 hours. Since 2005, these lamps are again being manufactured for commercial use. The later models are able to eliminate bulb rotation by using circularly polarized microwaves to spin the plasma instead. *Se* or *Te* as the light-generating medium and different additives such as $CaBr_2$, *InBr*, *LiI* and *NaI* can be used to modify the output lamp spectrum.

An excimer lamp is an incoherent source of UV radiation capable of producing quasi monochromatic radiation from the near UV (λ = 354 nm) to the vacuum UV (λ = 126 nm)

[118]. The operation of the excimer lamps relies on the radiative decomposition of excimers or exciplexes created by various types of discharges in rare gases, halogens, or rare gas-halogen mixtures with fill pressure of about 30 kPa. Some of the commercially available wavelengths are 126 nm filled with Ar_2, 146 nm filled with Kr_2, 172 nm filled with Xe_2, 222 nm filled with *KrCl*, and 308 nm filled with *XeCl*, with the efficiencies of 5-15 %. The pulsed *Xe* excimer (Xe_2) lamps may have up to 40 % efficiency. Good efficiencies are also obtained with *XeBr* at 291 nm and with *XeI* at 253 nm. Other wavelengths, produced with much lower efficiencies, are 207 nm (*KrBr*), 253 nm (*XeI*), 259 nm (Cl_2), and 341 nm (I_2) (see **Table 2.3**). Typical output spectra of excimer lamps are shown in **Figure 2.12**. Similar to mercury fluorescent lamp, different phosphors can be used to transform the UV radiation into visible light of various output spectra.

Table 2.3. Peak wavelengths (nm) obtained in dielectric barrier discharges with mixtures of rare gas (*Rg*) and halogen (sourced from [118]).

	X_2	Ne	Ar	Kr	Xe
Rg_2	-	-	126	146	172
F	157	108	193	249	354
Cl	259	-	175	222	308
Br	291	-	165	207	283
I	341	-	-	190	253

2.3.2.3. Electroluminescent devices

A light-emitting diode (LED) is an optoelectronic semiconducting device which generates light under the action of an electric field *via* electroluminescence [113, 123-131]. LED contains a *p-n* junction, through which an electric current is sent. In the heterojunction, the current generates electrons and holes, which release their energy portions as photons when they recombine. LED devices emit light preferentially in one direction *via* built-in reflecting structures. The emission bandwidth of a LED is typically some tens of

nanometres (*e.g.* 40 nm) or even > 100 nm. Semiconducting materials with a bandgap of 1.65-3.2 eV are capable of producing visible light by electroluminescence.

To operate LEDs, the current supply is needed to be stabilized as current rises exponentially with the increasing voltage. It can be achieved by operation with a current source itself, or by using a simple series resistance for connecting to a constant voltage supply. The optical output power is proportional to the operation current, except if the induced increase in temperature decreases the quantum efficiency. The operation voltage is largely determined by the bandgap energy of the material, and thus by the emission wavelength; red LEDs may be operated with less than 2 V, while blue ones require voltage of the order of 4 V.

Aluminium gallium arsenide (*AlGaAs*) is most commonly used in near-IR LEDs and laser diodes. Shorter wavelengths in the red spectral region are achieved with gallium arsenide phosphide (*GaAsP*) and aluminium indium gallium phosphide (*AlInGaP*). The internal quantum efficiency of a LED can be close to 100 % for emission wavelengths around 650 nm, whereas high efficiencies are much more difficult to achieve at shorter wavelengths of *e.g.* 620 nm. Gallium nitride (*GaN*) is usually used in UV LEDs while indium dopped gallium nitride (*InGaN*) is suitable for blue and violet LEDs. Despite high defect densities in these materials, internal quantum efficiencies of 70 % and higher are achieved. Longer wavelengths (green and yellow) are obtained by increasing the indium content, but the efficiency drops sharply as the wavelength is increased (see **Table 2.4**). Typical LED output spectra are represented in **Figure 2.12**.

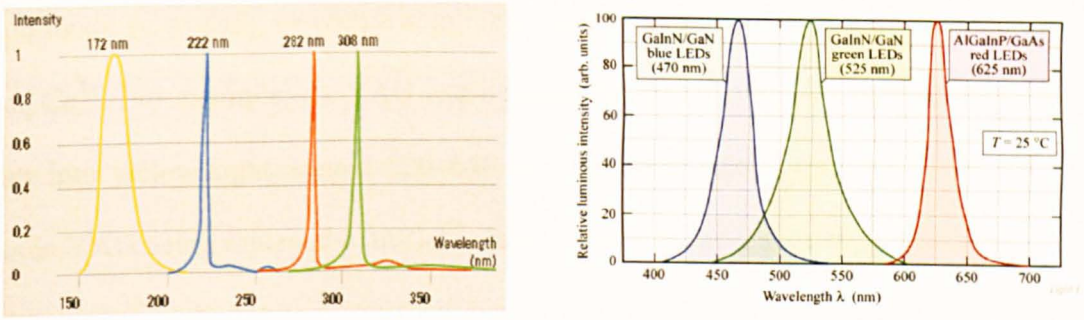

Figure 2.12. Typical emission spectra of eximer sources of light (left) (adopted from [131]), and LEDs (right) (adopted from [132]).

The technologically most difficult spectral region (in the visible range) is that of green–yellow–orange light. LEDs based on *GaAsP* have a lower efficiency than *e.g.* red LEDs. Zinc selenide (*ZnSe*) and zinc selenide telluride (*ZnSeTe*) have been developed for green emission, but the lifetimes and efficiencies are not satisfactory for lighting purposes. Various other materials, including both modified II-VI alloys and oxychalcogenides such as *LaCuOS*, are also under consideration.

Table 2.4. Typical semiconductor materials and emission wavelengths of LEDs (sourced from [123]).

Material	Typical emission wavelengths, nm
GaN	360
InGaN / GaN, ZnS	450–530
GaP:N	565
AlInGaP	590–620
GaAsP, GaAsP:N	610–650
InGaP	660–680
AlGaAs, GaAs	680–860
InGaAsP	1000–1700

White light can be generated either by mixing the outputs of red, green and blue LEDs, or by using a single UV LED to pump a combination of red, green and blue phosphors, or single blue LED and some phosphor, which converts part of the blue light into light with longer wavelengths. In the latter case the conversion is normally done either with another

semiconductor (*e.g. ZnS*), or with a scintillator crystal containing rare earth ions such as Eu^{2+} or Ce^{3+}. For example, *Ce*:YAG can be used for converting blue light around 440–460 nm into yellow light around 520–640 nm. Modified hosts, *e.g.* with some of the yttrium in YAG being replaced with Gd^{3+}, lead to shifts in the emission ranges of Ce^{3+}.

A more recent development was made in the area of LEDs based on organic and polymeric semiconductors, called organic light-emitting diodes and polymeric light-emitting diodes respectively [133, 134]. Such LEDs have one or several semiconducting layers of organic molecules (or polymer layers) situated in-betweeen electrodes. When potential is applied holes and electrons recombine near the emissive layer (metal having low work function). Even biological materials can be used for preparation of organic layers. For example, *DNA* molecules can exhibit highly efficient electroluminescence. Such materials have a potential for cheap mass fabrication of large and mechanically flexible devices. They therefore appear to be promising for future photochemical applications. However, further research and development are required for improving the efficiency and particularly the lifetime of such devices.

LED based on inorganic semiconductors are the most long-lived illumination devices as their lifetimes can exceed 100,000 hours. The luminous efficacy can be well over 100 lm W^{-1}, *i.e.* even better than that of fluorescent lamps.

Despite the obvious benefits there are some disadvantages arising from using of LEDs as a source of light. The cost per watt of output power of an LED is still fairly high. Although an LED produces less heat than an incandescent lamp with the same output power, adequate heat sinking is necessary to prevent overheating, which would decrease the lifetime. The operation current needs to be electronically stabilized, which can reduce

the overall power efficiency. However, fast progress is being made to reduce these costs, mainly by increasing the output power of the LED chips. The higher cost may be offset by reduced electricity consumption and the long lifetime. Also, advanced cooling arrangements can make it possible to generate much higher optical power.

2.3.3. Photochemical Reactors

2.3.3.1. Batch photoreactor with the external source of light

Photochemical reactors can be classified based on operation conditions (batch or continuous operation) and configuration (internal or external source of light). Batch photoreactors are characterised by the uniform distribution of concentration of reagents and products inside the reaction vessel due to agitation. In the case of continuous reactors, concentration gradient is formed along the flow during operation.

A batch photoreactor with the external source of light is the simplest type of a photoreactor configuration constituted of a stirred vessel with a lamp positioned outside (**Figure 2.13**, *a*) [135]. A disadvantage of this geometry is an inhomogeneous light distribution through the solution due to the exponential decay of intensity with distance travelled by light, leading to inefficient photons utilisation. Another problem, which is general for all batch reactors, is in inefficient heat exchange with the surroundings.

2.3.3.2. Batch photoreactors with the internal source of light

An immersed well photoreactor is one of the most widespread reactor types used in routine laboratory photochemical synthesis [136]. Consisted of a lamp within a cooling jacket (which can be used at some extent as a heat exchanger for keeping the reaction at a certain tempeature) immersed in the reaction vessel (**Figure 2.13**, *b*), this type of a photoreactor demonstrates better performance than those with the external sources of

light, owing to improved light utilisation. However, the light intensity also falls-off very rapidly with increasing the distance from the lamp due to absorption by the reactants and divergence of the light rays. Therefore, the volume of the reaction mixture which can be irradiated efficiently is limited by the length of a source of light and its intensity. One of the large-scale designs of this type of photoreactors was used for photonitrosation by Toray (**Figure 2.13**, *c*) [4, 137, 138]. The photoreactor consisted of a tank with multiple immersed lamps. The main problems of this design are the optimisation of conjoint geometry of the light sources to avoid dark zones inside the tank and heat management.

2.3.3.3. Continuous flow photoreactors with the internal source of light

This type of photochemical reactors is represented by photoreactors with a single lamp or optic fibre placed in the middle of the reactor tube (annular tubular photoreactor) [139] and photoreactors with several sources of light (lamps or optic fibres) situated inside the reactor tube in parallel [140-142] (**Figure 2.13**, *d, e*). Among the benefits of these reactors are an improved heat transfer (owing to inbuilt heat exchanger) and uniform light distribution. Laminar flow at low flowrates causes some problems with mass transfer which are partially eliminated by applying different baffles across the reactor [143-147]. Annular flow reactors are also limited in scale up by the maximum length of a single light source and its photon flux, but this can be overcome to some extent by placing several reactors in series [4, 148] or in parallel [149, 150] (**Figure 2.13**, *f, g*).

An interesting design of the continuous flow reactor with the internal source was patented by Meissner [151] (**Figure 2.13**, *h*). He proposed to use gas-filled glass or quartz hollow bodies placed in the reaction medium. The gas in the hollow bodies is stimulated by an external microwave radiation, such that the light is produced directly within the medium thus increasing the light utilisation.

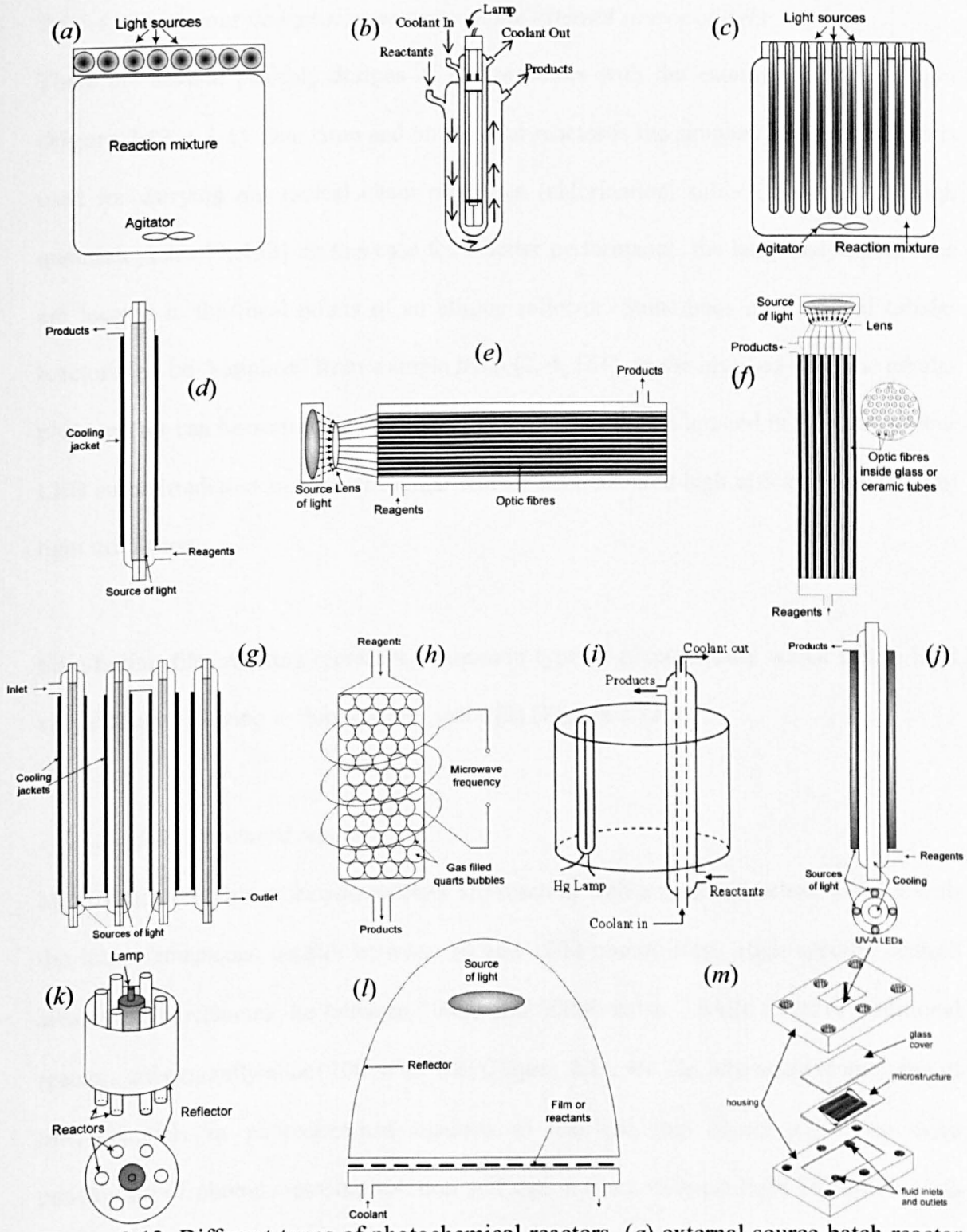

Figure 2.13. Different types of photochemical reactors. (*a*) external source batch reactor [135]; (*b*) immersed well reactor [136]; (*c*) multi-lamp immersed well reactor [4]; (*d, e*) internal source tubular reactors [4, 140, 142, 152]; (*f*) internal source tubular reactors, connected in parallel [149, 150]; (*g*) internal source tubular reactors, connected in series [4]; (*h*) packed bed reactor [151]; (*i*), (*j*) and (*k*) external source tubular reactors [2, 4, 23, 153, 154]; (*l*) film reactor [2]; (*m*) microstructured reactor (adopted from [21]).

2.3.3.4. Continuous flow photoreactors with the external source of light

There are several possible designs of photoreactors with the external sources of light (**Figure 2.13**, *i, j, k*). One lamp and one tubular reactor is the simplest geometry which is used for carrying out radical chain processes (chlorination, sulfooxidation) with high quantum yields [4, 153]. In this case for a better performance, the lamp and reactor tube are located in the focal points of an elliptic reflector. Sometimes even several tubular reactors can be "supplied" from a single lamp [2, 4, 154]. In the inversed case one tubular photoreactor can be surrounded by several lamps. This design applied in [23] where four LED strips irradiated an annular tubular reactor demonstrated high efficiency in terms of light utilisation.

Film/falling film reactors represent a common type of photoreactors which utilise light very efficiently owing to thin reaction space [2] (**Figure 2.13**, *l*).

2.3.3.5. Microstructured reactors

Microstructured photochemical reactors are reactors with a narrow reaction channel with the inner dimensions usually between 10 and 1000 micrometers. High specific surface areas of microchannels lie between 10000 and 50000 $m^2 m^{-3}$, while those of traditional reactors are generally about 100 $m^2 m^{-3}$ [8] (**Figure 2.13**, *m*). The advantage in applying of microchannels in photochemical reactors is that the thin layers allow extensive penetration of photons into the solution and thus a more efficient light utilisation. This allows using highly concentrated solutions of reagents as well as less powerful sources of light.

The large specific phase interfaces give rise to high heat exchange rates with heat exchange coefficient values in the order of 10 kW m^{-2} K^{-1} which are significantly higher

than that for traditional heat exchangers [8]. This high heat-exchanging efficiency allows fast heating and cooling in reaction mixtures within the microstructures, whereby reactions under isothermal conditions with exactly defined residence times can be carried out. In addition to heat transport, mass transport is also considerably improved. Due to the small dimensions the diffusion times are very short, thus the influence of mass transport on the speed of a reaction can be considerably reduced. The outcome is higher selectivity, yield, and product quality. The hazard potential of strongly exothermic or explosive reactions can also be drastically reduced. Higher safety is also achieved in reactions with toxic substances or higher operating pressures.

The flow in the microchannels is laminar, directed, and highly symmetric. In addition, the multiphase flows often exhibit high order between the phases (capillary, low slug or segmented flow) due to the dominance of surface and interface forces, as well as tailor-made active areas.

One of the most important benefits of microreactors is scalability of a photochemical process. Once optimized on a single microreactor chip the process then can be transferred on a larger scale by numbering up of the chips. However, in spite of all these advantages not a single photochemical process was realized on a commertial scale in microreactors so far and all the photochemical transformations in microreactors are still carried out on a laboratory scale. The reason of this undevelopement is probably due to high costs of the equipement. Moreover, utilization of light is far from perfect. Furthermore, problems associated with distribution of reagents and products, efficient cooling, monitoring the reaction, fouling of microchannels and control over the system in the complex connected microstructured reactors are still need to be resolved.

2.3.4. Photochemical transformations in microstructured reactors

2.3.4.1. Liquid phase (homogeneous) photochemical reactions

Jensen et al. described for the first time the application of microstructured reactor for photochemical reactions [5]. They applied the microfabricated reaction modules with the online UV detection in two configurations: coupling individually packaged chips, and monolithic integration of the two functions. First configuration with a single inlet, a single outlet, and a serpentine shape rectangular channel of 500 μm in width, and 250 μm depth was realized by timed deep reactive ion etching of a silicon substrate followed by anodic bonding to a Pyrex wafer. Detection chip with a straight channel of 50 μm depth was fabricated from quartz substrates and a photo-definable epoxy. For the monolithic configuration, the authors designed a sandwich structure of a silicon wafer between two quartz wafers with the reaction channel of 500 μm wide and 500 μm depth (**Figure 2.14**, *a*). Quartz wafers were bonded to patterned silicon wafers at room temperature using a Teflon-like polymer CYTOP. Inbuilt miniature UV lamp with peak wavelength at 365 nm was applied in the both cases. The authors studied the formation of pinacol from benzophenone and isopropanol as a model reaction.

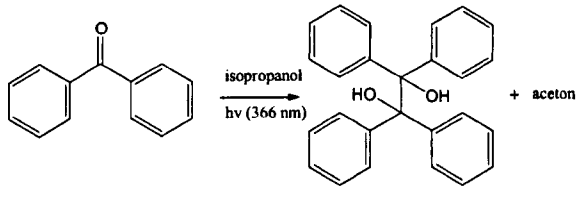

Technical reaction data, such as the dependence of the flow rate on conversion and quantum-yield values were determined based on online analysis of the reaction mixture. It was shown that the extensive penetration of light through the solution causes a highly efficient light utilisation in the microstructures.

The photochemical [2+2]-cycloaddition reaction of cyclohex-2-enone with vinyl acetate was examined by Fukuyama et al. using a Mikroglas Dwell Device [155], which is made

of Foturan glass and has a channel 500 μm deep, 1000 μm wide, and 1.4 m long (**Figure 2.14**, *b*) [7, 10].

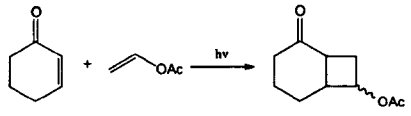

The device was equipped with water cooling heat exchanger, allowing keeping the reactor under a controlled temperature (20 °C). The reaction mixture was introduced to inlet at a flow rate of 0.5 mL h^{-1} (residence time 2 hrs), and the reactor was irradiated using a 300-W high-pressure mercury lamp located 1 cm from the reactor. The desired [2+2] cycloaddition product was obtained in 88 % yield. The reaction using a flow rate of 1.0 mL h^{-1} *via* two serially connected microreactors gave a similar result. The authors obtained 2.9 g of the desired product in 85 % yield after continuous operation for 45 hours. When the identical reaction was run in batch mode using a 10 mL Pyrex flask with the same light source, the cycloaddition product was obtained in 8 and 22 % yields after irradiation of 2 and 4 hrs, respectively. Thus, the microflow system dramatically shortened the reaction time, and increased the yield.

The same group successfully carried out the Barton reaction (nitrite photolysis) of a steroidal substrate, to give a key intermediate for the synthesis of an endothelin receptor antagonist in a stainless-steel microreactor covered by a Pyrex glass plate (Dainippon Screen Mfg.) [7, 11]. It was shown that a 15 W black light (peak wavelength: 352 nm) as the light source suffices for the Barton reaction. Similar conversions were achieved using UV-LED light (peak wavelength at 365 nm, 35 mW×48 pieces) instead of black light lamp [156]. When the reaction was carried out in a microreactor having a microchannel of 1000 μm width, 107 μm depth, and 2.2 m length at a flow rate of 1.0 ml h^{-1} (residence time: 12 min) (**Figure 2.14**, *c1*), the desired oxime was obtained in 71% yield.

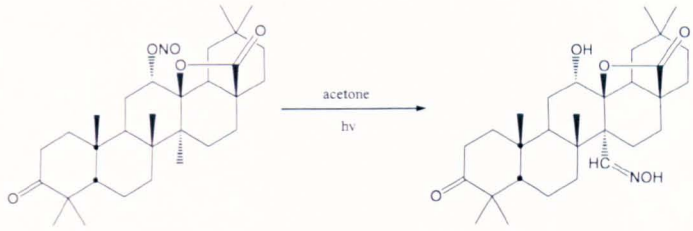

Multi-gram scale production was attained using two serially connected, multi-lane microreactors with extended channel lengths (1000 μm wide, 500 μm deep, 0.5 m long, 16 lanes, with a total holdup volume of 8 mL) and eight 20 W black lights (**Figure 2.14**, *c2*). After continuous operation for 20 hours, 3.1 g of the desired product was obtained (60 % isolated yield).

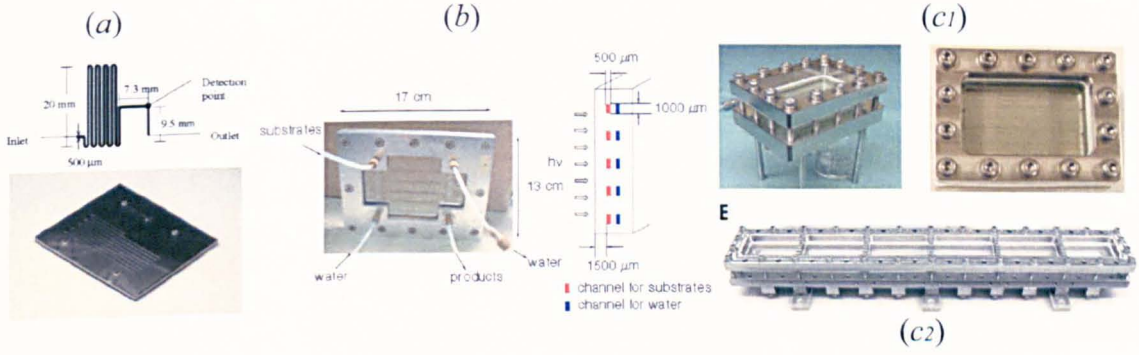

Figure 2.14. Microstructured reactors used for continuous homogeneous liquid phase synthesis. (*a*) microreactor applied in monolithic configuration of reaction module with online UV detection unit used by Jensen et al. (adopted from [5]); (*b*) Mikroglas Dwell Device microreactor (adopted from [10]); (*c1*) Dainippon Screen Mfg. microreactor, (*c2*) two serially connected Dainippon Screen Mfg. microreactors (adopted from [11]).

Finally this group carried out a continuous reaction using a PC-controlled automated photo-microreactor station, manufactured by Dainippon Screen Mfg. Co. Ltd. [156]. This automated system employed one set of a Type B microreactor and six small (15 W) black light lamps. After continuous operation for 40 h, we obtained 5.3 g of the desired product (61% isolated yield).

Maeda et al. examined the intramolecular photocycloaddition of a 1-cyanonaphthalene derivative in microreactors made of polydimethylsiloxane (*PDMS*) by photolithography [12]. Pyrex glass spin-coated by a positive type photoresist was irradiated by a tungsten lamp through a contacted photomask. The development and wet-etching by an $HF–NH_4F$ aqueous solution gave a template having a protruded curve line. The *PDMS* was molded by the template, and was attached to another flat *PDMS* plate. Finally, capillary tubes (diameter of 100 μm) were inserted. The obtained channels of 300 μm width and 50 μm depth, had the lengths of about 45 and 202 mm. *Xe* lamp with UV filter used as irradiation source. Flow rates in range of 0.03–0.05 mL h^{-1} were applied. By using the microreactors and flow system, both the efficiency and regioselectivity increased compared with those under batch conditions.

Interesting design was proposed by Hook *et al.* who constructed and optimized several compact flow reactors to perform organic photochemistry in continuous flown on a large scale [157]. Although the devices used for this reaction are better described as flow reactors than microreactors, similar cycloadditions have been performed in a glass microreactor with microchannels of only 500 μm depth with high efficiency [10]. The reactors were constructed from commercially available or customized Vycor glass immersion well equipment combined with UV-transparent, solvent-resistant fluoropolymer tubing (0.7 mm internal diameter, 150 and 176 m length, or 2.7 mm i. d., 37 and 49 m length) **(Figure 2.15)**. The reactors were assessed using the [2+2] photocycloaddition of malemide **1** and 1-hexyne forming the cyclobutene product **2** and the intramolecular [5+2] photocycloaddition of 3,4-dimethyl-1-pent-4-enylpyrrole-2,5-dione **3** to form the bicyclic azepine **4 (Figure 2.15)**. The reagents were introduced to inlet at 8 mL min^{-1}. The photochemical reactors were shown to be capable of producing

685 g of cyclobutene product and 175 g of bicyclic azepine in a continuous 24 h processing period at 80 % and 84 % yield correspondingly.

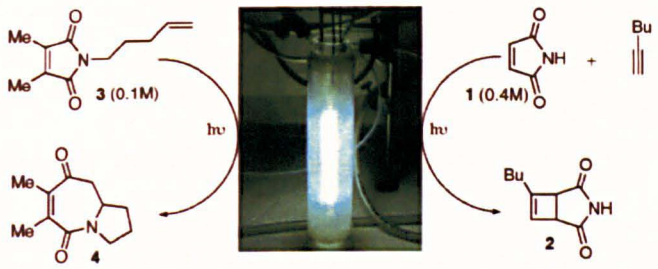

Figure 2.15. Vycor continuous flow photochemical reactor and schemes of carried out photocycloaddition reactions (adopted from [157]).

2.3.4.2. Gas-liquid interface photochemical reactions

Wootton et al. demonstrated $^1O_2$ mediated synthesis of ascaridole from α-terpinene with conversion of 85 % in a microstructured reactor [13].

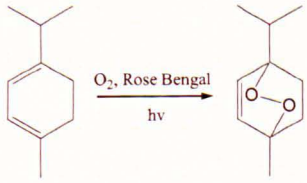

The glass microchip (5 cm × 2 cm) with two inlets and a serpentine channel (total length of 50 mm, depth and width of 50 μm and 150 μm respectively) was made using direct-write laser lithography, wet chemical etching and thermal bonding techniques (see **Figure 2.16**, *a*). The serpentine section of the chip was irradiated by the microscope overhead tungsten lamp (20 W) at a distance of 10 cm from the reactor surface. A solution of Rose Bengal (*RB*) sensitiser and α-terpinene in methanol was introduced into inlet "A" **Figure 2.16**, *a*) of the reactor chip at a flow rate of 1 μL min^{-1}. Pure O_2 was introduced into inlet "B" of the reactor chip at a flow rate of 15 μL min^{-1}. In this example, light penetration through the liquid layer also played an important role as the dissolved *RB* photosensitizer possesses a large extinction coefficient and all of the light is absorbed over a rather short

distance. In addition, due to the small volumes involved, the hazard potential of this process was greatly reduced.

Further, Ehrich, and Jahnisch et al. reported that a falling-film microreactor can also be used for photochemically induced gas–liquid reactions, such as the photochlorination of toluene-2,4-diisocyanate [8, 14].

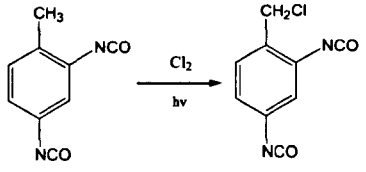

A falling-film microreactor consisted of 32 parallel microchannels (each 66 mm long, 600 microns wide and 300 microns deep) was developed by the Institut fur Mikrotechnik (IMM, Mainz) (see **Figure 2.16**, *b1*, *b2*). The authors carried out the reaction under continuous operation using both a nickel and an iron reaction plate. They demonstrated that with similar conversions a significant increase in selectivity is observed in the falling-film microreactor compared to conventional batch system. The application of a nickel plate showed the highest selectivity, while the iron plate exhibited catalytic activity that favoured ring substitution (side reaction). The advantage of microstructured reactors in this case, in terms of selectivity and space–time yield, stems also from the better penetration of photons and the higher mass-transfer rates in the thinner liquid films. Chlorine radicals are located over the total film volume and high local radical concentrations, which lead to recombination, are avoided. In a conventional reactor, the radical concentration near the light source is high while, in contrast, it is very low at the centre of the reactor. As a result the selectivity of the desired side-chain chlorinated derivatives decreases, since without photochemical induction chlorination prefers to take place at the aromatic core.

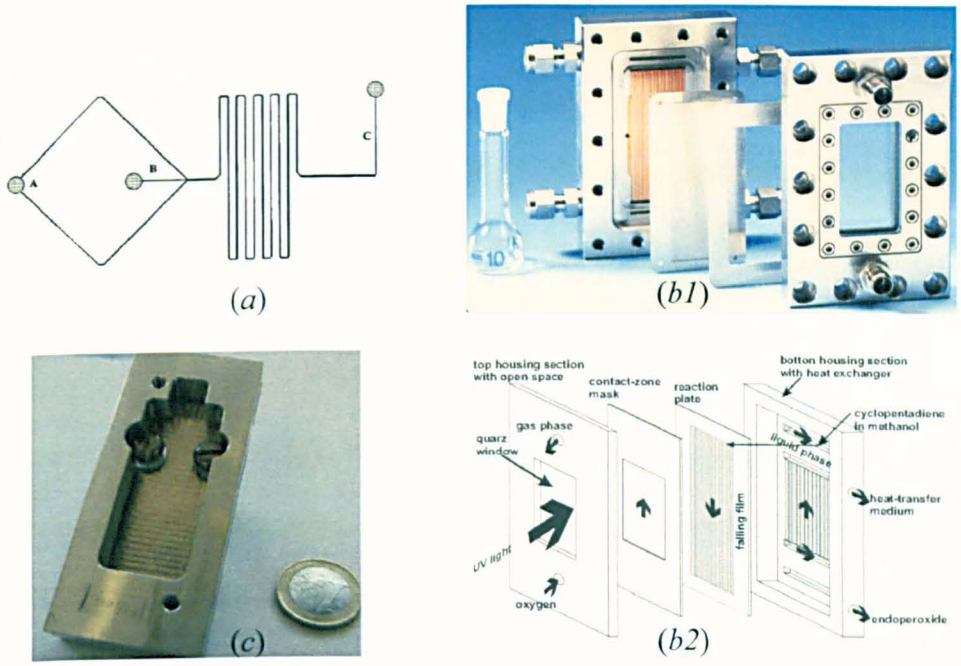

Figure 2.16. Microstructured reactors applied in gas-liquid photochemical synthesis. (*a*) schematic of reactor chip for α-terpinene photooxidation, A and B are liquid and gas inlets correspondingly, C is outlet (adopted from [13]); (*b1*, *b2*) falling-film microreactor (adopted from [8, 14]); (*c*) borofloat glass microreactor (adopted from [16]).

Jahnisch et al. also showed that the falling-film microreactor is suitable for the continuous photochemical oxygenation in the presence of $^1O_2$ [15]. The authors investigated the photooxygenation of cyclopentadiene in methanol using *RB* as a $^1O_2$ photosensitiser to generate 2-cyclopenten-1,4-diol.

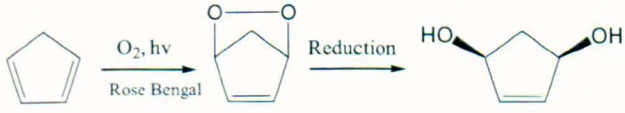

As the liquid reactants flowed downwards they contacted with a cocurrent O_2 flow (15 L h^{-1}) and the entire mixture was irradiated using a *Xe* lamp. The explosive endoperoxide, which appears as an intermediate, was reduced with thiourea to give 2-cyclopenten-1,4-diol, which is of pharmaceutical importance. With active cooling of the system the authors demonstrated an overall product yield of 20%. Unfortunately, no data relating to volumetric throughput was disclosed.

Recently Meyer et al. compared performance of a 40 mL immersed well reactor and a 270 μL borofloat glass microreactor (Little Things Factory GmbH) with semicircular 1 mm wide and 500 μm deep channels in a model photosensitized citronellol oxygenation in the presence of $Ru(^{t}bpy)_3Cl_2$ sensitizer [16] (**Figure 2.16**, *c*).

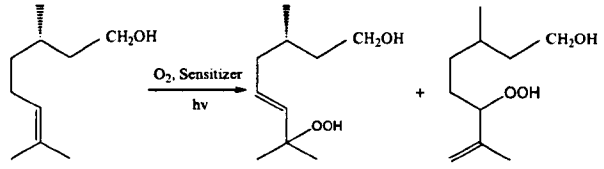

LED arrays with peak wavelength of 468 nm were applied as a source of radiation (2×15 and 4×10 LEDs with specific output powers of 6.15 and 3.0 mW cm^{-2} for immersed well and microstructured reactor respectively). Direct comparison of the space-time yields (amount of product per reactor volume per time) after 20 min reaction time demonstrated about one order of magnitude higher performance of a microreactor compared with an immersed well reactor. This study has demonstrated what the photosensitized citronellol-oxidation can successfully be transferred into a microreactor. The employment of LED's as irradiation source exemplified the high potential within chemical technology for light driven processes, however, quite low photonic efficiencies were obtained (0.022 and 0.048 for the immersed well and microstructured reactors correspondingly) probably due to low LEDs specific output powers.

2.3.4.3. Liquid-liquid interface photochemical reactions

Ueno et al described photocyanation of pyrene across an oil/water interface using two types of polymer microchannel chip [17]. The chips (channel depth of 20 μm, width of 100 μm and 350 mm total length) with two and three inlets were fabricated on the basis of photolithography and an imprinting method, with micromachined silicon templates being used for imprinting (**Figure 2.17**, *a*). An aqueous *NaCN* solution (nucleophile) and a propylene carbonate solution of pyrene (electron donor) and 1,4-dicyanobenzene (electron acceptor) were brought separately into a Y-structured microchannel chip with

the same flow velocity by pressure driven flow. Irradiation by a high-pressure *Hg* lamp resulted in the formation of 1-cyanopyrene in the oil phase (**Figure 2.17**, *b*). The results demonstrated that the interfacial photochemical reaction of pyrene proceeded successfully along the water/oil solution flow in the microchannel. Under optimum conditions by using a three-layer channel chip (water/oil/water phases), absolute 1-cyanopyrene yields as high as 73 % were attained with a reaction time of 210 s. As characteristics of an interfacial photoreaction in a microchannel chip, furthermore, it was demonstrated that the yield was proportional to the contact time between the two fluids. The reaction yield in such systems can be controlled by the flow rate, the channel geometry, and the channel length. As at flow rates slower than 0.2 μL min^{-1} stable oil/water stream in the microchannel was not formed, the authors proposed further optimisation of the total channel length as another way to improve the reaction yield.

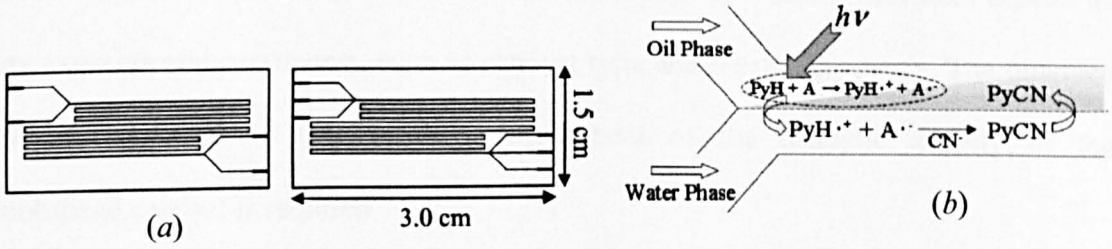

Figure 2.17. (*a*) Schematic drawings of channel designs: two- and three-layer channel chips. (*b*) Photocyanation reaction of pyrene in a microchannel. *A* represents 1,4 dicyanobenzene, *PyH* is pyrene. Adopted from [17].

2.3.4.4. Liquid-solid interface photochemical reactions (supported systems)

Gorges et al. constructed a photocatalytic microreactor with immobilized titanium dioxide as photocatalyst [21]. The microstructured device was manufactured using a low temperature ceramic green body in which 19 microchannels with a cross-section of 300 μm × 200 μm were milled by precision computer numerical control machining. The micromachining followed a calcination step in order to obtain the ceramic substrate from the structured green body. This substrate was then subjected to the deposition of a

titanium film (approximately 5 μm thick) by physical vapour deposition and subsequently to the deposition of the photocatalytic TiO_2 film by anodic spark deposition. Following the deposition of the catalyst, the microstructure was sealed with a glass top using epoxy glue, and mounted in stainless steel housing (**Figure 2.18**, *a*). Illumination was carried out with an array of 11 UV-A LEDs with the peak emission wavelength of 385 nm and total incident light intensity of 1.6 mW cm^{-2}. The authors tested the microreactor for the degradation of the model substance 4-chlorophenol.

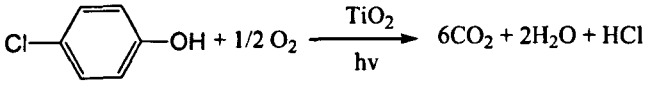

They demonstrated that there is no mass-transfer limitation for the employed operating conditions, and therefore the measured kinetic data really reflect the intrinsic kinetics of the photocatalytic reaction. Quite low photonic efficiencies were obtained compared with those in suspension systems (0.02-0.03 % versus 0.7-1.1 %). These efficiencies depend on many experimental parameters, such as catalyst type and reactor geometry. The obtained values clearly indicate that further improvement of the catalytic activity of the immobilized catalyst is required.

Takey et al. fabricated a TiO_2 modified microchannel chip and applied it to a photocatalytic redox-combined synthesis of L-pipecolinic acid from L-Lysine [18] (**Figure 2.18**, *b*).

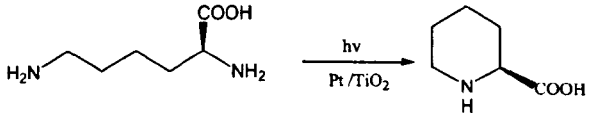

The chip was composed of two Pyrex glass substrates (0.7 mm thick). Branched microchannels (770 μm width, 3.5 μm depth) were fabricated by photolithography – wet etching techniques. A TiO_2 thin film of 300 nm thickness composed of approximately 100 nm diameter TiO_2 particles was prepared on another substrate *via* a sol–gel method from titanium tetra-n-butoxide ethanol solution as a starting material. *Pt* (0.2 wt% of the TiO_2

film) as a reduction site was loaded by photodeposition from 0.5 mM H_2PtCl_6 aqueous-ethanol solution. The two substrates were thermally bonded at 650 °C for 4 h. A high-pressure mercury lamp with UV transmitting filter was used as a light source (110 mW cm^{-2}). The conversion rate obtained in the chip was 70 times larger than that in a cuvette using TiO_2 nanoparticles with almost the same selectivity and enantiomeric excess. These results indicate that the photocatalytic redox-combined system may be successfully integrated into the microchannel and applied in photocatalytic synthesis.

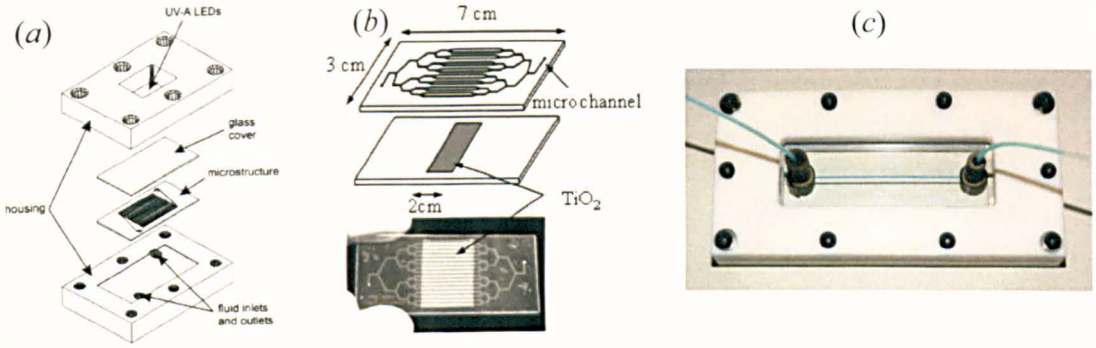

Figure 2.18. Photocatalityc microreactors with TiO_2 coated microchannels. (*a*) Ceramic body microreactor (adopted from [21]); (*b*) Pyrex glass microreactor (adopted from [18]); (c) strait channel microreactor (adopted from [9]).

Matsushita et al. studied degradation and reduction of organic compounds, and amine *N*-alkylation in microreactors made by micromilling of quartz which has a straight microchannel of 500 μm width, 10–500 μm depth, and 50 mm length [9, 19]. The bottom and side walls of the microchannel were coated with a photocatalytic TiO_2 layer in anatase form by using the sol-gel process. Particles of *Pt* were loaded on the TiO_2 layer for the study of photocatalytic *N*-alkylation of amines by using a photodeposition method. The microchannel was covered with a quartz plate (see **Figure 2.18**, *c*). UV light emitting diodes (365 and 385 nm with 0.30 and 0.67 mW output correspondingly) were chosen as a source of light.

Photodegradation of chlorophenols, bisphenol A, and dimethylformamide was examined in a microreactor of 100 μm depth. Photonic efficiencies of 0.28 and 0.01 with 365 and 385 nm UV LEDs were obtained in the case of dimethylformamide degradation.

The authors also demonstrated photocatalytic reduction of benzaldehyde in three alcohol media: methanol, ethanol, and 2-propanol. The reaction yields benzylalcohol and ketone corresponding to the alcohol media. The highest efficiency of the reaction to yield 10.7% of benzylalcohol was obtained within the irradiation time of 60 s. The efficiency is slightly lower in methanol and the lowest when 2-propanol is employed as a solvent.

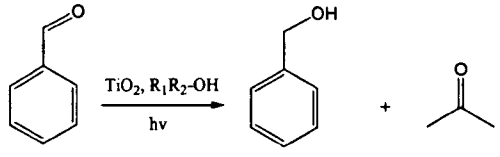

Photoreduction of *p*-nitroacetophenone was carried out with nitrogen or O_2-saturated ethanol solutions. Sample solutions were introduced into a microreactor of 100 μm depth and irradiated with an array of 365 nm UV LEDs. The reduction extent increased with increasing the irradiation time and reached 92.5 % at the irradiation time of 120 s. The photonic efficiency of the photoreduction was calculated to be 0.69 %. Photoirradiation of the solution purged with O_2 did not yield any detectable *p*-aminoacetophenone due to electron transfer from excited TiO_2 to O_2 molecules.

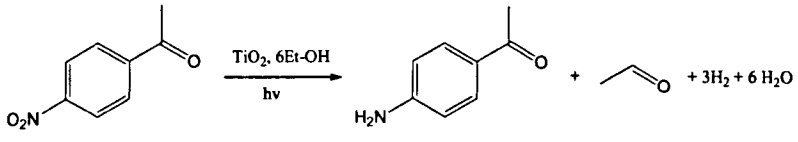

The *N*-alkylation of benzylamine and aniline in ethanol was studied in the photocatalytic microreactor of 300 μm depth with immobilized Pt/TiO_2 excited with 365-nm UV-LEDs. The reaction proceeded within only 150 s to yield 85% of *N*-ethylbenzylamine from benzylamine and 34 % of *N*-ethylaniline from aniline. The photonic efficiency of the *N*-alkylation of benzylamine was calculated to be 0.35%.

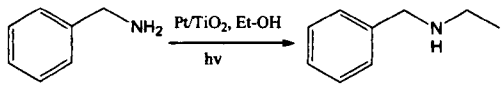

In contrast to the results obtained in batch reactors, the authors also successfully demonstrated *N*-alkylation reaction of aromatic amines by using the microreactor with immobilized pure TiO_2. The *N*-alkylation in ethanol proceeded within only 150 s to yield 43% of *N*-ethylbenzylamine with *Pt*-free TiO_2.

Another supported system was developed by Kitamura et al [20]. They applied silica gel beads of 10 μm in diameter covalently modified with metal-free monopyridyltriphenylporphyrin *via* a silane coupling reagent (*PyTPP-*SiO_2) which were introduced into a polystyrene microchannel chip. The microchip with a 2.3 cm total length dam-structured channel (450 μm width, 130 μm deep and 6 mm length for accommodating *PyTPP-*SiO_2 particles; 450 μm width, 130 μm deep and 2.3 mm length for the flow space) was fabricated by an imprinting method using Teflon substrates as templates. The number of the *PyTPP-*SiO_2 particles introduced into the microchannel chip was estimated as 8×10^8.

The microchip was applied to photodecomposition of phenol under 300 W high pressure *Hg* lamp irradiation (1.0 M $CuSO_4$ solution filter, $\lambda > 330$ nm was used). The authors demonstrated that photodecomposition yield of phenol in the microchannel is dependent on the solution flow rate. At 0.5 μL min^{-1} the decomposition yield was as high as 93% with the reaction time of 42 s, while that in a bulk aqueous *PyTPP-*SiO_2 suspension was 73% with the reaction time of 2 hrs. In the microchannel chip experiments, furthermore, the yield increased with decreasing the thickness of the solution flow layer above the *PyTPP-*SiO_2 particles. These results demonstrated again high potential of the microstructured reactors towards highly efficient photochemical transformations.

Carofiglio et.al recently compared oxygenation of α-terpinene in a gas-liquid flow using dissolved fullerene (C_{60}) with that performed employing solid-supported C_{60} in a custom-made microreactor [158]. The microreactor was built as follows: a layer of thiolene, acting as a negative resist, was poured between two glass plates covered by mask containing the desired microfluidic network and cured under UV light illumination. The uncured adhesive was flushed away with acetone, leaving the microfluidic channels. The assembled microreactor consisted of three zones: gas and liquid inlets, mixing zone and catalytic chambers for inclusion of solid supported sensitizers of $^1O_2$ (**Figure 2.19**, *a*). Authors also invented the inbuilt reversible press-fit interconnects for connecting the microreactor to a flow system. The microreactor was kept at -5 °C by ice/*NaCl* bath or by water bath at 10 °C. A 300-W tungsten halogen lamp (light intensity 19000 lux) was placed 25 cm away from the microreactor. In homogeneous conditions a 97 % conversion of α-terpinene was achieved at 1 mL h^{-1} flowrate of the reaction mixture (α-terpinene 1.0 mmol, C_{60} 0.012 mmol and n-tetradecane 0.5 mmol as internal standard for gas chromotography analysis in 10 mL of toluene). O_2 was introduced at a flowrate of 2 mL h^{-1}. However, only 51 % of ascaridol was obtained which was attributed to decomposition of product. In heterogeneous reaction authors applied solid-supported photosensitizer prepared by nucleophilic addition of C_{60} to the primary amino groups of Tentagel resin beads (*TG-*C_{60}). The reactor contained 14.3 mg of *TG-*C_{60} corresponding to 0.45 mg of C_{60} (0.6 mmol). A 97 % conversion was obtained at similar flowrates of gas and liquid.

The microreactor was also tested in photooxidation of l-methionine methyl ester to the sulfoxide by $^1O_2$ in D_2O with the *TG-*C_{60} and functionalized fulleropyrrolidine-SiO_2 hybrid (*Si-*C_{60}). For *TG-C60*, under the irradiation of the tungsten lamp, an increase of the total residence time from 32 to 102 seconds rises the conversion of methionine from 38 to 85 %. The *Si-*C_{60} demonstrated a quantitative conversion of methionine at a total

residence time of 33 seconds. A 5×3 array of white LED (18000 lux) was also employed in oxygenation. A 95% conversion of methionine was achieved for a 42 seconds total residence time.

2.3.4.5. Oxygenation in supercritical CO_2

Recently it was demonstrated that supercritical CO_2 (scCO_2) can also be employed as a solvent for oxygenation in a continuous flow [159]. Although the reactor described in this work is not a microreactor, the work itself is worth mentioning. The authors performed oxygenation of α-terpinene and cytronellol by $^1O_2$ in a tubular sapphire continuous photoreactor (internal diameter of 7.8 mm, the wall thickness of 1.2 mm, the total volume of 5.7 mL, and irradiated volume of 4.1 mL) (**Figure 2.19**, *b*). Two arrays of four composite white LEDs (1000 lumen each, composed of a cluster of six individual diodes) were mounted on two aluminum heat sinks. The arrays were situated at a distance of about 0.5 cm from the sapphire reactor and cooled by two 5 cm diameter fans. Liquid CO_2 was pumped at 2.0 mL min^{-1}, α-terpinene with the dissolved tetra(pentafluorophenyl)porphine sensitizer was pumped at 0.2 mL min^{-1}, and O_2 was introduced at a rate of two molar equivalents to organic reactant at 140 bar. 8 h run yielded 96 mL of ascaridol with about 0.5% of α-terpinene.

The reactor was also tested in the oxidation of citronellol. In this case authors met problems of solubility of tetra(pentafluorophenyl)porphine and products of citronellol oxidation in sc(CO_2). The problem of photosensitizer solubility the difficulties associated with second phase formation were overcome using downflow configuration. A 100 % conversion of citronellol with distribution of products 1:0. was overcome by addition of equimolar concentration of dimethyl carbonate to citronellol, while 92 was achieved during the single-pass at 0.1 mL min^{-1}, 1.0 mL min^{-1} of CO_2, and two equivalents of O_2 at

180 bar. The reaction was performed for approximately 4 h converting 12 mL of citronellol. Selectivity of 97.6 % towards Rose Oxide (mixture of cis and trans isomers) was achieved after treatment by Na_2SO_3 and acidification step in aqueous *HCl*. Space-time yield for the sapphire reactor was found to be about 70 mmol L^{-1} min^{-1} which is nearly two orders of magnitude higher than that obtained earlier in a microreactor [16]. The proposed approach to oxygenation using scCO_2 as a solvent looks promising although insolubility of reagents or products in scCO_2 should be considered in each case.

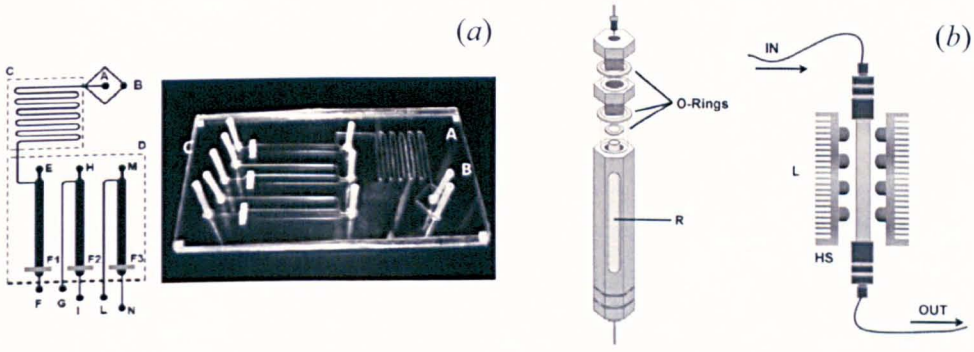

Figure 2.19. Microreactor with the inbuilt photocatalytic chambers (*a*). (A) is O_2 inlet, (B) is solution inlet, (C) is mixing zone, (D) is micro-chamber zone, (E, H, and M) are photocatalyst feed ports, (F, G, I, L, N) are outlet/connection ports, (F1, F2, F3) are paper filter restrains. Adopted from [158]. (*b*) Sapphire tube reactor. (R) is reactor mounted in the reactor housing, L are two LED arrays, HS is aluminum heat sink. Sourced from [159].

2.3.5. Industrial photochemical processes

2.3.5.1. Chlorination, sulfochlorination, sulfoxidation

In practice, radical chain reactions with high quantum yields (for example, chlorination) are frequently conducted without any great attempt being made to optimize utilization of the light [4, 111]. An example of industrial chlorination is the production of monochloroalkanes from a C_{11-14} *n*-paraffin refinery cut by Phillips Petroleum [153]. The production unit consists of two pairs of Vycor tubes (7.5 x 150cm) and a water-cooled 7.5

kW mercury lamp. A cylindrical reflecting shield of polished aluminium reduces dissipation of light to the surroundings. The plant has a production capacity of some 27 tonnes of chloroparafin per day, corresponding to about l0000 t/a.

Photochlorination of benzene to produce γ-hexachlorocyclohexane (insecticide) was developed by Ethyl Corporation with a 15 % yield [4, 111, 160]. The photochemical reactor comprises 18 connected annular flow tubular segments with the lamps surrounded by the reaction solution. Two 40 W fluorescent lamps are located at the centre of each segment. The photochlorination of toluene to benzyl chloride, benzylidene dichloride, and benzotrichloride was developed in a series of four lead-lined photoreactors at 80-110 °C.

Photochemical sulfoxidation (so-called light-water process) for the manufacture of surfactants was evolved as an industrial process at Hoechst with the total capacity of ca. 50000 t/a [2, 4, 111, 161]. O_2 serves in this process as an oxidizing agent instead of chlorine used in the conventional sulfochlorination. The primary sulfoxidation product (peroxysulfonic acid) is trapped by water inside an immersed well photochemical reactor before it can undergo radical decomposition. Compared to conventional sulfochlorination the light consumption of sulfoxidation is very high. About 0.2 kWh of electrical energy is required for lamp operation in the production of 1 kg of alkanesulfonate [161]. This means that only ca. 1600 t/a can be produced with one 40 kW mercury lamp.

2.3.5.2. Photonitrosation (oximation)

Photonitrosation of cyclohexane, *i.e.* the light induced reaction of nitrosyl chloride with cyclohexane to form cyclohexanone oxime (production of caprolactam or monomer of Nylon 6) was conducted by Toray in a large production plant on a 160000 t/a scale [2, 4,

111]. Each immersed reactor with a capacity of 10000 t/a needed 50 *Tl* doped 60 kW high pressure mercury lamps, in total 48 MW of electric power for lamps operation.

Another industrial application of photonitrosation is the production of lauryllactam, the monomer of Nylon 12, developed by Aquitaine-Organico. The photochemical plant comprises several photoreactors, each containing 27 immersed lamps of 60 kW power consumption each with a total capacity of 8000 t/a.

2.3.5.3. Photooxygenation

Synthesis of ascaridole discovered by Schenck (reaction of α-terpinene with $^1O_2$) was carried out on a technical scale after 1945 [4, 111, 162, 163]. At that time, ascaridole had some significance as an anthelmintic, and previously it could only be obtained from natural oil of *chenopodium*. The first chemical pilot plant used solar radiation for the synthesis and was sponsored by the Marshall Plan. Air was passed into ordinary glass carboys containing α-terpinene in ethanol, with chlorophyll from the leaves of stinging nettles as the sensitizer. This solar chemical production process was later abandoned because of the discontinuance of the pharmacological use of ascaridol due to its significant side effects.

The ene-reaction with $^1O_2$ is being used by two perfumery manufacturers, Symrise (former Dragoco and Haarmann & Reimer) and Firmenich, for the production of Rose Oxide fragrance from citronellol [4, 111, 164-166]. They produce 60-100 t/a of the chemical each year, using high pressure vapour lamps (mercury and sodium).

Another example of commercial $^1O_2$ use is the synthesis of 1,2-dioxetanes. Once stabilized, these compounds are triggered enzymatically to decomposition with

chemiluminescence emission and therefore, can be used for bioanalysis (immunoassay, gene expression studies, *DNA* sequencing, identification of infectious agents, etc.) [167]. The commercial synthesis of stabilized 1,2-dioxetanes is realized by Lumigen Inc [168-170] using polymer *RB*, a merrifield polymer to which *RB* is immobilized and halogen lamp as a source of light [171]. This reusable heterogeneous sensitizer has been patented and sold under the tradename Sensitox TM.

2.3.5.4. Vitamin D_3 and dydrogesterone synthesis

Synthesis of vitamin D_3 is one of the oldest non-radical industrial photoreactions [2, 4, 111]. Vitamin D_3 is produced from cholesterol extracted from wool grease. The cholesterol is converted to 7-dehydrocholesterol in four steps. Then photochemical ring opening of 7-dehydrocholesterol gives previtamin D_3 which on heating to 50-80°C undergoes a hydrogen shift to give the final vitamin D_3. The energy consumed in the photochemical step (40 kW mercury lamps irradiation) is ca. 80 kWh per kg of vitamin D_3. One of the largest manufacturers of vitamin D_3 is Philips-Duphar in Netherlands. In analogy to the mentioned above photochemical transformation of 7-dehydrocholesterol, irradiation of the pregnadiene derivative gives the retrosteroid which is cleaved by *HCl* in alcohol to form the sexual hormone dydrogesterone [2, 4, 111].

2.3.5.5. Radioactively labeled aldosterone production

The functionalization of saturated carbon atoms by photolysis of nitrites (Barton reaction) is used by an American company New England Nuclear in the multistep production of tritium-labeled aldosterone on a small scale for use as a medical diagnostic aid [4].

2.3.5.6. Photoisomerization of vitamin A acetate

Synthesis of vitamin A acetate, performed on an industrial scale at BASF, affords a mixture of two stereoisomers, the all-trans and the 11-cis form [4]. Only the all-trans isomer is suitable for use in pharmaceuticals and animal feeds. A very mild photochemical method has been developed at BASF for converting 11-cis- into all-trans-vitamin A acetate: it consists in irradiating the stereoisomeric mixture with visible light in the presence of a coloured sensitizer such as *Zn*-tetraphenylporphine or chlorophyll.

2.3.5.7. Photocatalytic oxidation

Semiconductor photocatalysts, namely polycrystalline TiO_2, in the allotropic phases of both anatase and rutile are used for both domestic and industrial water purification applications [172]. UV illumination with energy of photons greater than the semiconductor bandgap produces electron-hole pair which can participate in reduction-oxidation reactions involving electron acceptor or donor species adsorbed on the surface of the catalyst particles. Photocatalytic air or water treatment decomposes pollutants, nuisance colour, taste and odour compounds, bacteria, and viruses to harmless by-products (mineralisation process) [173, 174].

Treatment of water can be accomplished by adding a powdered form of TiO_2 to the water, or it can be immobilized on a substrate. Polluted air streams purification is often more efficient than liquid waste water treatment due to the fast gas phase kinetics. This fact has led some people to utilize air stripping of pollutants from liquid phase for treatment in the gas phase. In the process of air streams treating, TiO_2 must be dispersed in a matrix with a high surface area to allow the gas to pass over it and react under UV irradiation.

Several companies intensively promote photocatalytic purifiers to the market. Purifics is such an industrial water treatment company specializing in photocatalysis [175]. They developed a Photo-Cat process. This industrial process is based on a patented closed loop TiO_2 photocatalyst slurry process. The technology is comprised of sets of modular photocatalytic racks, each containing a number of individual cells. Depending on the concentration of the contaminants and the throughput required, the racks are linked together in a serial and/or parallel mode. The catalyst is continuously separated from the purified water and reintroduced into the inlet stream. Air Oasis [176], Biozone PureWare [177], and Multi-Tech [178] are just several examples of air purifier manufacturers that flooded the market.

2.4. INFERENCE

Present literature review clearly demonstrated that photochemistry is a very powerful tool of synthetic chemistry which is still under utilized in industrial applications due to complexity of scale up processes and high cost of running the equipment. Application of the microstructured photochemical reactors opened up new horizons for highly selective and safe process operation due to improved mass and heat transfer as well as more efficient light utilization in microstructures. Moreover, scale up can be easily achieved by numbering up of the base units. Rapid development of microfabrication techniques enables to obtain multifunctional microstructured units at low cost. Recent studies clearly stated that LEDs are very promising efficient compact sources of light suitable for microengineered reaction systems owing to narrow width of the emission band, availability in different wavelengths and easy manufacturing of the compact arrays. Fast progress is being made to reduce the cost and increase the output power of the LED chips.

Photochemical Schenk ene reactions of olefins with $^1O_2$ open new routes for synthesis of terpene-derived chiral ligands as well as for oxyfunctionalisation of chiral homoallylic alcohols to obtain fine chemicals. For further development of products it is important to elaborate an efficient and convenient approach for oxygenation of allylic substrates by $^1O_2$ which can be used further for scale up the syntheses. It is desirable also to develop an efficient heterogeneous photosensitiser to resolve the problem of separation of a homogeneous sensitizer from the reaction mixture. *PSi* in the form of colloids or nanoporous films may be promising candidate on this role. Therefore the present study is devoted to development of a scalable photoreactor and determining the applicability of *PSi* as a $^1O_2$ sensitizer and support for dye sensitizers.

3. EXPERIMENTAL

3.1. CHEMICALS

In this work the following chemicals were used: α-pinene (ACROS Organics, 97 %), α-terpinene (ACROS Organics, 90 %), diphenylisobensofurane (*DPBF*) (Sigma-Aldrich, 97 %), pyridine (*Py*) (ACROS Organics, 99 %), 4-dimethylaminopyridine (*DMAP*) (Fisher Scientific, peptide synthesis grade), acetic anhydride (Ac_2O) (Sigma-Aldrich, 99 %), 5,10,15,20-Tetraphenyl-21*H*,23*H*-porphine (*TPP*) (ACROS Organics), 5,10,15,20-Tetrakis(4-hydroxyphenyl)-21*H*,23*H*-porphine ($TPP(OH)_4$) (Sigma-Aldrich, 95 %), 5,10,15,20-Tetrakis(4-allyloxy)-21*H*,23*H*-porphine ($TPP(OC_3H_5)_4$) (Sigma-Aldrich, 90 %), Rose Bengal (*RB*) (ACROS Organics), CH_2Cl_2 (Fisher Scientific, 99.99 %), ethanol (Fisher Scientific, 99.99 %), 1,1,2-trichloro-1,2,2-trifluromethane (*F113*) (Riedel-de Haen, 99.7 %), C_6F_6 (Sigma-Aldrich, > 99.5 %), CCl_4 (Sigma-Aldrich, > 99.5 %), 0.1 M *HCl* (Sigma-Aldrich, 99 %), $NaHCO_3$ (Sigma-Aldrich), Na_2SO_4 anhydrous (ACROS Organics, 99 %), $CDCl_3$ (ACROS Organics, 99.8 %), 1,10 phenanthroline (Sigma-Aldrich, 99+ %), sodium acetate (Sigma-Aldrich, ACS reagent), H_2SO_4 (98 % analytical grade, Fisher Scientific), $H_2PtCl_6 \cdot H_2O$ (Sigma-Aldrich, 99.995 %), $AlCl_3$, 0.5 M in tetrahydrofuran (Sigma-Aldrich), tolyene (Sigma-Aldrich, H_2O < 0.005%, 99.7 %), methanol (Sigma-Aldrich, H_2O < 0.01 %, 99.5 %), O_2 (BOC Gases), N_2 (oxygen-free, BOC Gases). Water was purified by a ELGA water filter (18 MOm). Potassium ferrioxalate $K_3Fe(C_2O_4)_3 \cdot 3H_2O$ was prepared according to Hatchard and Parker's procedure [179] from $K_2C_2O_4$ (Fisher Scientific, analytical grade) and $FeCl_3$ anhydrous (ACROS Organics, 98 %). Porous silicon (*PSi*) powders and modified *PSi* powders were prepared as described in Chapter **3.3.6**.

3.2. EQUIPMENT

3.2.1. Immersed well photochemical reactor

A standard quartz batch immersed well photochemical reactor (Photochemical reactors) consists of a light source **1** surrounded by a cooling jacket, which is immersed into the reaction media (**Figure 3.1**, *a* [136]). Inlet **2** and outlet **3** are for circulation of a cooling liquid and **4** and **5** are designed for O_2 inlet and outlet. Total reactor volume is 300 mL. Medium pressure *Hg* lamp with a nominal power 125 W (model 3010) has an overall length 260 mm, discharge length 30 mm and diameter 12 mm and produces predominantly 365-366 nm radiation with smaller amounts also in the UV region at 254, 265, 270, 289, 297, 302, 313 and 334 nm (**Figure 3.1**, *b*). Significant amounts of radiation are produced in the visible region at 405-408, 436, 546 and 577-579 nm. Total light output, J measured by ferrioxalate actinometry in a quartz immersion well reactor is 7×10^{18} photons s^{-1}.

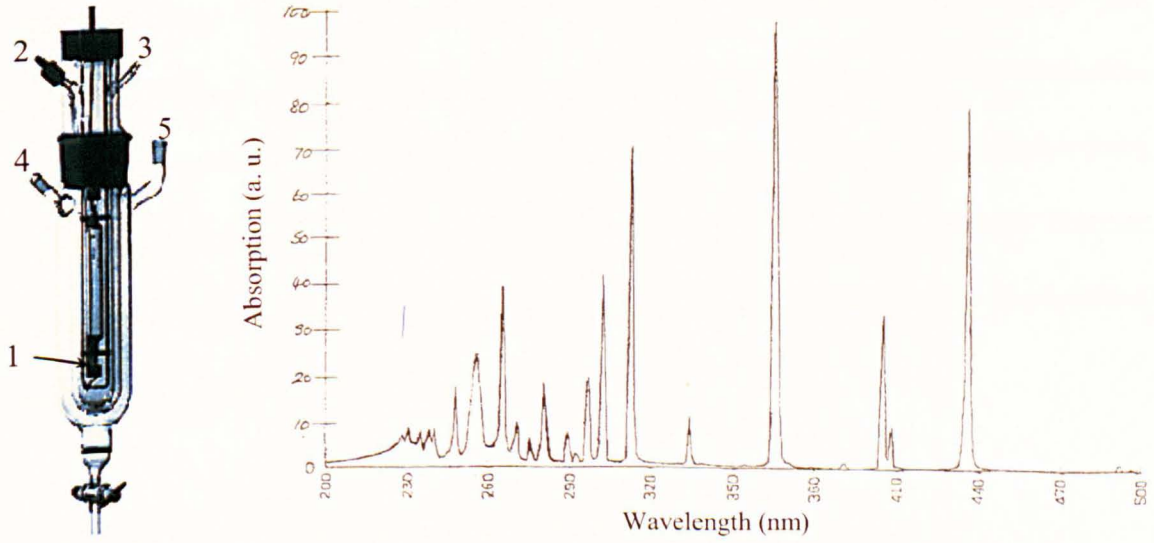

Figure 3.1. Immersed well batch reactor (*a*) [136]. 1-light source (125 W *Hg* medium pressure lamp) immersed in the reactor, 2-gas inlet, 3-cooling fluid inlet, 4-cooling fluid outlet, 5-gas outlet. Emission spectrum of the 125 W medium pressure *Hg* lamp (obtained from Photochemical reactors) (*b*).

3.2.2. Annular recirculating photochemical reactor rig

3.2.2.1. General description

The recirculating photochemical reactor rig (**Figure 3.2**) consists of the thermostated Pyrex annular continuous photochemical reactor **1** (1.5 mm thickness of annular space and a total reactor volume of 9.5 mL, see **Figure 3.3**, *a*) connected to the gas-liquid separator **3** from one side and to reservoir **4** from another, producing closed loop for circulation of liquid. Similar reactor was used in the work of Lapkin *et al.* [23]. The photorector was surrounded by LED strips, actinic fluorescent tubes or illumiated from one side by a *Xe* lamp **2** (see next section and **Figure 3.3** for details). A valve-less rotary piston dispensing pump **6** (Ismatec Ltd) was used for the liquid flow. Gases flow rates were controlled by mass flow controllers **9** (Bronkhorst Hi-Tech). Liquid and gas were mixed in a T-piece at the inlet into the reactor and directed upwards, establishing slug annular flow. A solution of reactants in the liquid reservoir was continuously stirred using a magnetic stirrer **5** (SB161, Stuart) during the reaction. The gas vent line from the gas-liquid separator was equipped with a heat exchanger **8** to reduce solvent loss, connected to a Haake thermostat DC30 (Thermo Electron Corporation), kept at -7 °C by circulating ethylene glycol-water mixture (1:1). Haake thermostat DC10 **7** (Thermo Electron Corporation) was used to control temperature of the reactor by circulating thermostated water through the inner reactor tube.

3.2.2.2. Light sources and lamp-reactor geometry

Three different light sources in different geometries were used in the experiments with the annular recirculating reactor: custom-built LED lamp made of 10 strips, 24 LED's each, 240 LED's in total (Farnell, peak wavelength at 524 nm), mounted onto a dark plastic case providing a 15 cm long illumination zone surrounding the photoreactor, a custom made fluorescent lamp assembled usung two U-shaped 420 nm actinic fluorescent

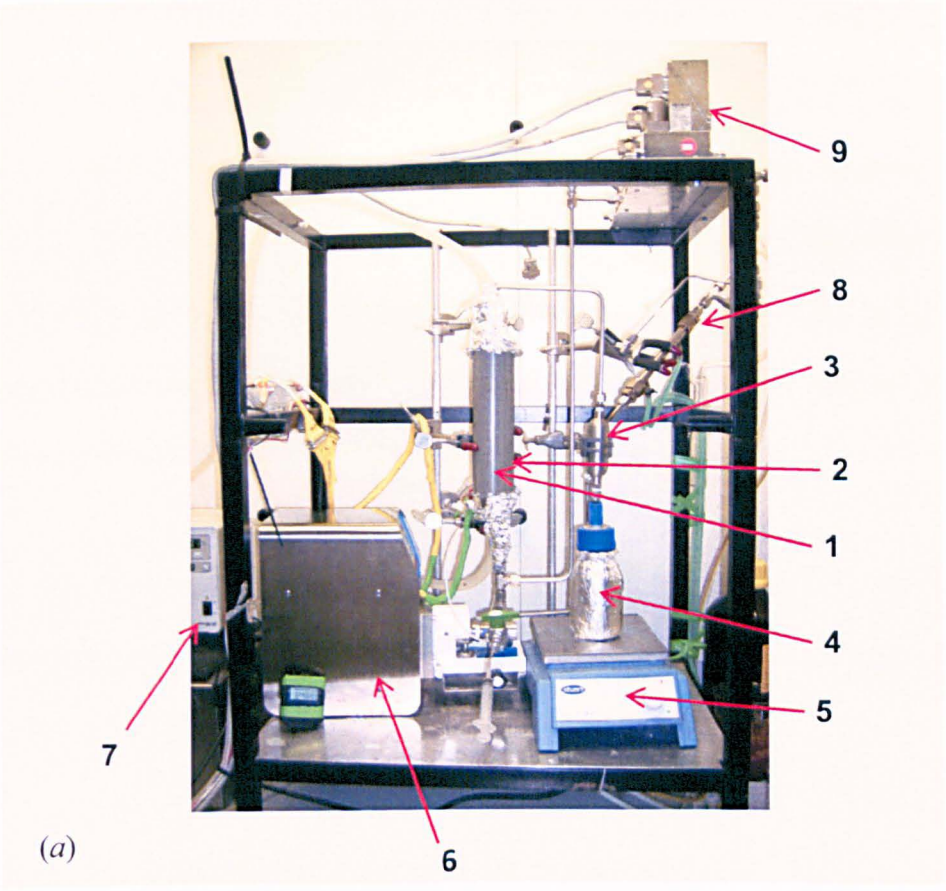

Figure 3.2. Recirculating photochemical reactor test bench, (*a*) photo, and (*b*) scheme. 1-Pyrex glass annular continuous photochemical reactor, 2-lamp, 3-gas-liquid separator, 4-reservoir, 5-magnetic stirrer, 6-Ismatec pump, 7-Haake thermostat DC10 (coolant water), 8-ethylene glycol cooled condenser (connected to Haake thermostat DC30), 9-O_2 and N_2 mass flow controllers.

bulbs of 24 W and 25.6 cm length each, (Catalina Aquarium) surrounded by aluminium cylindrical reflector, and a *Xe* 75 W short-arc lamp (Osram XBO75WL2, 9 cm bulb length) in a rectangular case (Photon Technology International) with 3.5 cm illuminated reactor length (see **Figure 3.3**, *b*, *c* and *d* correspondingly). Illuminated surfase areas of the annular photoreactor and the corresponding reaction volumes as well as the amounts of photons absorbed in these volumes (obtained from the actinometry data, see **Appendix A**) are shown in **Table 3.1** for all lamp-reactor geometries.

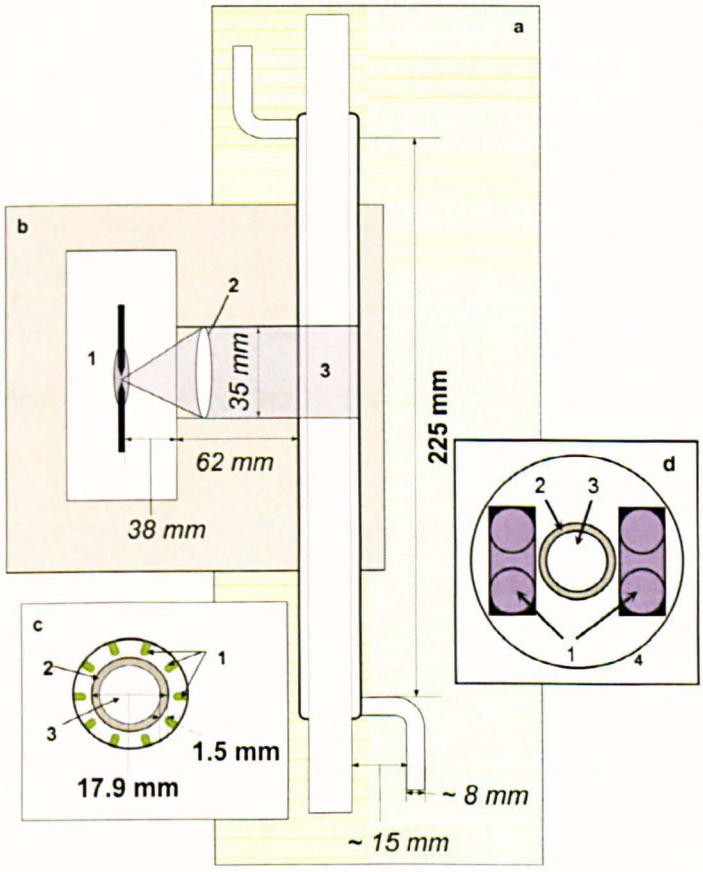

Figure 3.3. Annular photoreactor (*a*) and lamp-reactor geometry for (*b*)-75 W *Xe* arc lamp (1-lamp, 2-lens, 3-illuminated zone); (*c*)- 1.44 W 524 nm LED array cross-section (1-10×24 LEDs per strip, illuminated length is 15 cm) (*d*)-48 W Actinic fluorescent 420 nm (1-U-tube bulb ×2, 24 W each, illuminated length is 23 cm), 2-annular space of reactor, 3-heat transfer fluid, 4-reflector.

The LEDs were powered using a 60 V power supply *via* Supertex CL2 LED drivers and 1.2 kΩ resistors. The electrical design of the LED lamp is depictured in **Figure 3.4**. The actinic fluorescent lamp was powered using 128 W solid state electronic ballast. The *Xe* arc lamp was powered by the arc power supply LPS-220 (Photon Technology International). Emission spectra of all the lamps used with the annular photoreactor as well as the absorption spectra of the dye photosensitizers are shown in **Figure 3.5**.

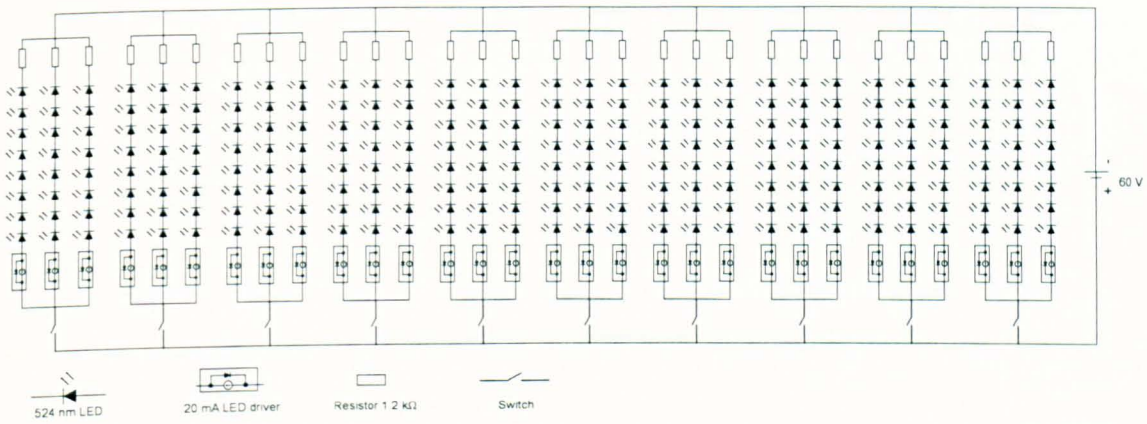

Figure 3.4. Electrical design of the 240 LEDs lamp (10 strips of 24 LEDs each, 524 nm peak wavelength).

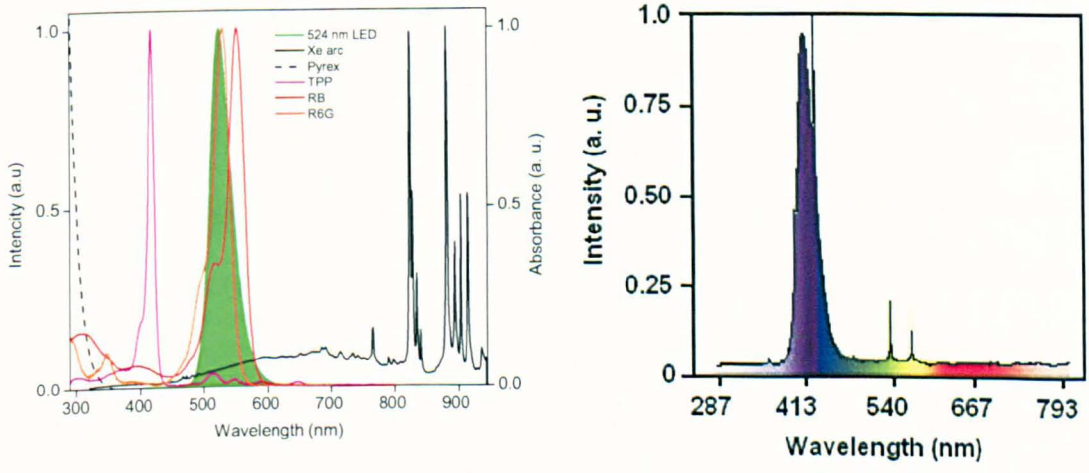

Figure 3.5. Emission spectra of light sources and absorption spectra of dye photosensitizers. (*a*) Green peak corresponds to the 524 nm LED, black line-to the *Xe* arc, violet line is tetraphenylporphine (*TPP*) in CH_2Cl_2, red line is Rose Bengal (*RB*) in ethanol, and orange line is Rodamine 6G (*R6G*) in ethanol (sourced from[180]). (*b*) A 420 nm actinic fluorescent lamp emission spectrum (sourced from [181]).

Table 3.1. Lamp-reactor geometry parameters. A_R is illuminated area, cm^2, V_R is illuminated reactor volume, mL, and J_a is flux of the photons absorbed by photosensitizer during oxygenation, Einstein s^{-1}, measured by ferrioxalate actinometry.

Lamp	A_R	V_R	J_a
420 nm Actinic	111.91	11.0	6.3×10^{-6}
524 nm LED	76.30	9.5	4.4×10^{-6}
Xe arc	15.00	3.0	6.8×10^{-7}

3.2.3. Microreactor rig

3.2.3.1. General description

Microreactor rig (**Figure 3.6**) consists mainly of a microreactor chip **1** pressed to a stainless steel heat exchanger **2** by two plastic flangeless fittings (two 1/4'-28 PPS nuts and two Tefzel ferrules with stainless steel lock rings, Upchurch Scientific) which serve at the same time as connections for ethyltetrafluoroethylene (*ETFE*) tubings (1/16" OD, 0.75 mm ID, Upchurch Scientific) to the inlet **9** and outlet **10**. Reaction mixture was pumped from reservoir **3** through the microreactor by the HPLC pump **4** (Knauer S100, 10 mL pumphead). Haake thermostat DC10 **7** (Thermo Electron Corporation) was used to control temperature of the reactor by circulating thermostated water through the heat exchanger. A source of light **2** (524 nm or 416 nm LED arrays (5×9 LED), 75W *Xe* arc or 250 W metal halide lamp were used) was attached to the top of the microreactor. The microreactor chip (**Figure 3.7**) was made from a *Si* wafer (*n*-type, 75 mm in diameter) using photoresist mask for stain etching of the meandering channel (width×height=500×240 μm, length=199.5 cm, V = 240 μL). A Pyrex 7740 glass plate cover (77.5×40×2 mm) with two round holes for inlet and outlet was attached by anodic bonding. Fabrication of *Si* wafer and anodic bonding were done in the collaborating research labs in St. Petersburg, Russia. The heat exchanger (**Figure 3.7**) was fabricated by Cawkwell Engineering, UK using micromachining. Briefly, stainless steel plate with the countercurrent channels (35 channels for each inlet, width×height=500×500 μm, length of

each channel is 97.75 cm, and 500 μm space between the channels), two drilled inlets and four outlets is covered by the stainless steel sheet, sealed with the o-ring in-between and assembled together with the bolts inbuilt into the metal base.

The microreactor rig allows two different modes of operation (continuous and recirculating, see **Table 3.2**) with easy switch from one mode to another by valve **11**. Each mode of operation makes it possible to use two different approaches towards saturation of the reaction mixture by O_2: bubbling O_2 through the reaction mixture and segmented gas-liquid flow. In the case of continuous O_2 bubbling through the reaction mixture the mixture in the reservour **3** was continuously saturated by O_2 and agitated by magnetic stirrer **4**. The flow of O_2 was set at 30 mL min^{-1} by a low flow metering valve **8** (Swagelok). For reduction of solvent loses the reservoir **3** was equipped by condenser **5** connected to a Haake thermostat DC30 (Thermo Electron Corporation). The condenser was kept at -7 °C by circulating ethylene glycol-water mixture (1:1). O_2 bubbling was started 1 hour before each experiment. After 1 hour the lamp was switched on and the reaction mixture was pumped through the illuminated microreactor at different flowrates. Aliquotes were collected directly from the outlet of the microreactor or from the reservour in the cases of continuous and recirculating modes correspondingly. Back pressure regulators **12** (2.8 and 5.2 bars, Upchurch Scientific) and relief valve **13** set at 2.5 or 5 bars (Swagelok) were used in experiments at elevated O_2 pressures.

In the case of segmented gas-liquid flow O_2 was supplied *via ETFE* tubings (1/16" OD, 0.75 mm ID, Upchurch Scientific) attached to a *ETFE* tee connection (0.5 mm through holes, Upchurch Scientific) and the established two-phase gas-liquid flow entered the illuminated microreactor. Aliquotes were collected directly from the outlet of the

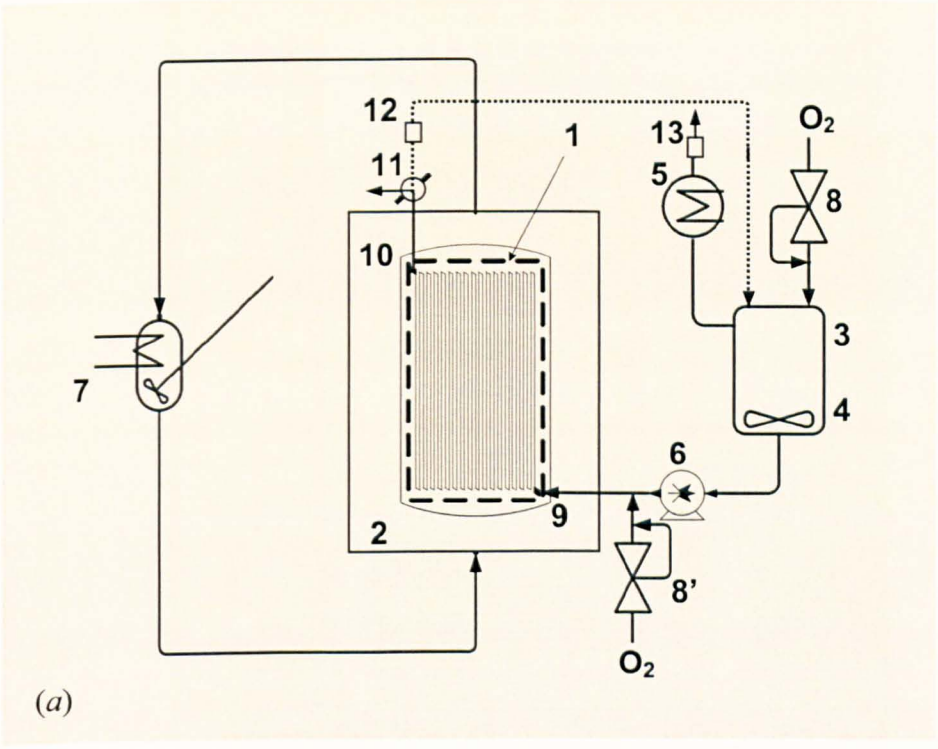

(*a*)

(*b*)

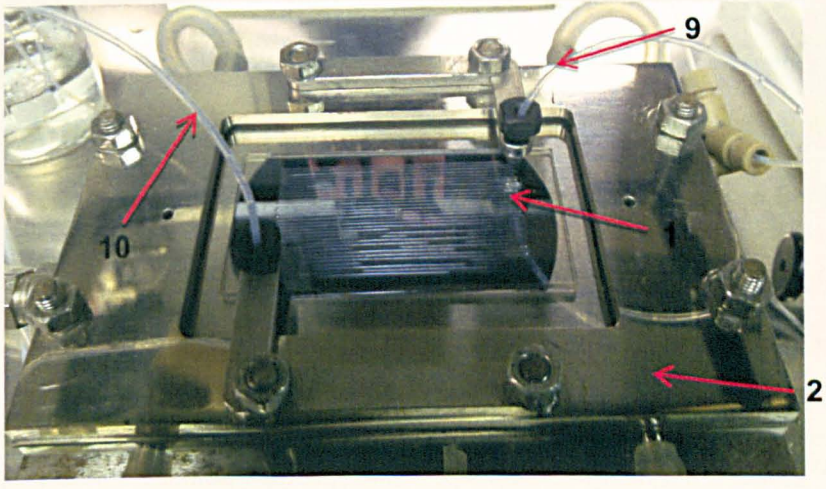

Figure 3.6. Microstructured photochemical reactor rig (*a*) scheme and (*b*) photo. 1-anodically bonded glass-to silicon microstructured photoreactor with 5×9 LED array, 2-heat exchanger, 3-reservoir, 4-magnetic stirrer, 5-ethylene glycol cooled condenser (connected to thermostat), 6-HPLC pump, 7-thermostat (coolant water), 8 and 8'-O_2 metering valves, 9-inlet, 10-outlet, 11-switch valve, 12-back pressure regulator, 13- relief valve.

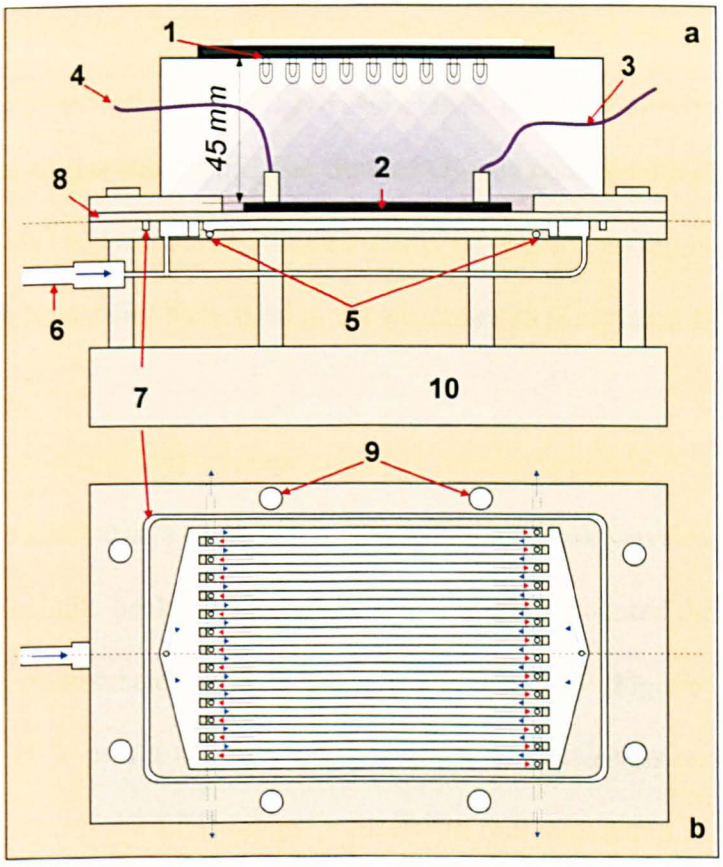

Figure 3.7. Crossections of heat exhchanger, (a)-vertical, (b)-horisontal. 1-LED array, 2-microreactor, 3-microreactor inlet, 4-microreactor outlet, 5-heat exchanger outlets, 6-heat exchanger inlet, 7-groove with o-ring, 8-stainless steel sheet, 9-assembly holes, 10-base.

Table 3.2. Modes of operation and types of O_2 saturation used in the microreactor rig.

Mode of operation	*Lamp*	*O_2 saturation type*	*Scheme*
Recirculating	416 nm LED	Bubbling O_2 in tank	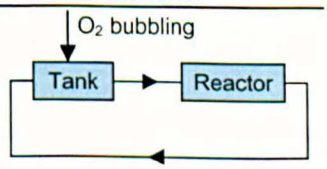
	Metal halide	Segmented gas-liquid flow	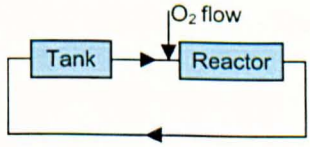
Continuous	416 nm LED 524 nm LED *Xe* arc	Bubbling O_2 in tank	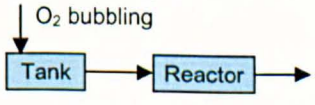
	416 nm LED	Segmented gas-liquid flow	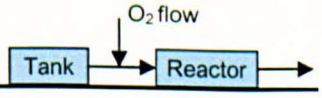

microreactor or from the reservour in the cases of continuous and recirculating modes correspondingly. Different patterns of a segmented gas-liquid flow were obtained.by varying flowrates of gas and liquid. The flow of O_2 was controlled by low flow metering valve **8'** (Swagelok) and measured volumetrically. Back pressure regulators **12** (7, 17, 34, 51 bar, Upchurch Scientific) were used in the experiments at elevated O_2 pressures.

3.2.3.2. Light sources and lamp-reactor geometry for microreactor

Two custom built LED arrays of 45 LEDs (5×9) (Farnell, peak wavelength at 524 nm and Roithner Laser Technik, peak wavelength at 416 nm) were mounted onto metal cases and fixed above the microreactor at a distance of 4.5 cm (see **Figure 3.7**). LEDs were powered using a 60 V power supply *via* Supertex CL2 LED drivers and 1.2 kΩ resistors. The electrical design of the LED lamps is similar to that depictured in **Figure 3.4**. A *Xe* 75 W short-arc lamp (Osram XBO75WL2, 9 cm bulb length) in a rectangular metal case (Photon Technology International), powered by arc power supply LPS-220 (Photon Technology International) was mounted at a distance of 9.2 cm above the microreactor. A double-ended (FC2 ends/base) 250 W aquarium metal halide lamp (2.5 cm length of discharge tube, 10000 K, with UV cut glass bulb, *i*Quatix) was mounted onto a rectangular metal box with two built-in cooling fans and downwards looking glass IR filter window. The distance between the lamp and the microreactor was 11.3 cm. The lamp was powered by a 250 W magnetic ballast (Mark 3, MaxiBright). The illuminated surface area of the microreactor was 9.98 cm^2 and reaction volume was 240 μL. The emission spectra of lamps are depictured in **Figure 3.8**. Amounts of photons absorbed in the microreactor during oxygenation obtained from the actinometry data (see **Appendix A**) are shown in **Table 3.3** for all sourses of light.

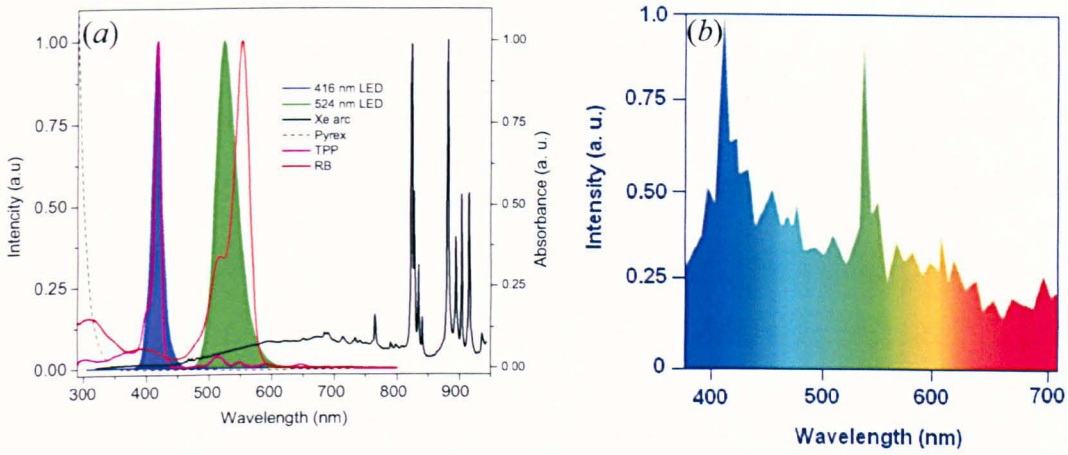

Figure 3.8. Emission spectra of light sources and absorption spectra of dye sensitizers. (*a*) 416 nm LED (violet peak), 524 nm LED (green peak), *Xe* arc (black line), Rose Bengal (*RB*) (red line), tetraphenylporphine (*TPP*) (violet line), tetra-(4-hydroxy) - phenylporphine ($TPP(OH)_4$) (blue line). (*b*) Metal halide lamp (soursed from [182]).

Table 3.3. Lamp-reactor geometry parameters. A_R is illuminated area, cm^2, V_R is illuminated volume, mL, and J_a is flux of the photons absorbed by photosensitizer, mol s^{-1}, measured by ferrioxalate actinometry.

Lamp	A_R	V_R	J_a
416 nm LED	9.98	2.4×10^{-4}	4.6×10^{-7}
524 nm LED	9.98	2.4×10^{-4}	7.7×10^{-8}
Xe arc	9.98	2.4×10^{-4}	8.0×10^{-8}
Metal halide	9.98	2.4×10^{-4}	8.6×10^{-7}

3.3. PROCEDURES

3.3.1. Actinometry procedure

The intensities of absorbed light for all the light sourses were measured under flow conditions (liquid circulation through the reactor) following the Hatchard–Parker procedure [179].

3.3.1.1. Actinometry solutions

The ferrioxalate actinometer solution (0.15 M) (*a*) was prepared as follows. 36.84 g of solid $K_3Fe(C_2O_4)_3 \cdot 3H_2O$ was dissolved in 400 mL of distilled H_2O, then 50 mL of 0.5 M sulphuric acid was added and solution then was diluted to 1 L with distilled H_2O. The solution was prepared in dim light and stored in a dark place. 1,10-Phenanthroline solution (0.1 % in water) (*b*) was prepared as follows. 0.180 g of solid was dissolved in 100 mL of distilled H_2O. This solution is also light sensitive so it was also prepared in dim light and stored in the dark. Acetic buffer solution (*c*) was prepared as follows. 600 mL of 1 M CH_3COONa was mixed with 360 mL of 1 M H_2SO_4 and then was diluted to 1 L by distilled H_2O.

3.3.1.2. Calibration for actinometry

The molar absorption coefficient ε was obtained from the absorbance measurements of the known quantities of Fe^{2+} solutions (see **Appendix A**). These calibration solutions were prepared using methods described in [179]. To each 20 mL flask varying amounts of 4×10^{-4} M Fe^{2+} in 0.05 M H_2SO_4 solution were added (0, 0.5, 1, 1.5, 2, 2.5, 3, 3.5, 4, 4.5 and 5 mL). To these were added 2 mL of solution (*b*), 5 mL of solution (*c*) and 3 mL of distilled water. The solutions were made up to 20 mL with 0.05 M sulphuric acid. Samples were left for one hour so that the complex can be formed and then were measured in a UV-VIS spectrometer at 510 nm in a 1 cm quartz cell. The solution with

zero concentration of the Fe^{2+} ions was used as the reference. All measurements were repeated three times and averaged.

3.3.1.3. General procedure

N_2 was bubbling at 30 mL min^{-1} through the solution (*a*) prior to and during each experiment. An aliquot was taken as a blank sample before each experiment. The solution was then irradiated for certain periods of time during recirculating/pumping through the reactor and aliquots were taken at the end of each period.

3.3.1.4. Aliquots preparation, analysis and data treatment

2-3 mL of irradiated potassium ferrioxalate solution (5-9 mL in the case of LED lamp in annular recirculating experiment) was sampled into a non-transparent bottle so that no further reduction of the Fe^{3+} occured. Then an aliquot V_1 of the sample (V_1=2 mL in the cases of 524 nm LED and *Xe* arc lamps with the annular recirculating reactor and V_1=1 mL in all the other cases) was put into a 20 mL flask (V_2). To this flask, 2 mL of the solution (*b*) and 1 mL of the solution (*c*) were added. Then the mixture was made up to 20 mL by distilled water, thoroughly mixed and left in a dark place for one hour, providing enough time for the Fe^{2+}-phenanthroline complex formation. Absorbance of samples was measured on UV-VIS spectrometer Shimadzu UV-1601 at 510 nm using a 1, 0.5 and 0.1 cm quartz cells. The sample taken before exposure to light was used as the reference. All measurements were repeated three times and averaged.

3.3.1.5. Calculation of the intensities of light absorbed inside the photoreactors

At every time t_i when an aliquot is taken, the amount of Fe^{2+} in the tank of the annular recirculating photoreactor rig, $n_T(t)$ is equal to $n_T(t)=c_T(t)V_T$ mol, where $c_T(t)$ is concentration of Fe^{2+} in tank, V_T is the volume of actinometer in the tank. The amount of

Fe^{2+} taken with the aliquot V_1 for preparing the solution V_2 = 2×10^{-2} L for analysis is $n_{al}(t)=c_T(t)V_1$ mol. Therefore, concentration of Fe^{2+} in the analysed solution (mol L^{-1}) after dilution to V_2 is:

$$c_{an}(t) = \frac{n_{al}(t)}{V_2} = \frac{c_T(t)V_1}{V_2} \tag{3.1}$$

The optical density is expressed *via* Beer-Lambert law equation:

$$D(t) = \varepsilon l c_{an}(t) \tag{3.2}$$

Here ε is the molar extinction coefficient, ε=11310 L mol^{-1} cm^{-1} which was determined from the calibration graph, see **Figure A1** in **Appendix A**, l is the length of the photometric cell. In the case of the 524 nm LED lamp with the annular photoreactor the decrease of the volume of the actinometer solution due to collection of the aliquots for analysis was significant enough to be neglected. Therefore, corrected optical densities D_i^1 were used for the calculations in (3.2) (see **Appendix A**). Concentration of Fe^{2+} ions in the tank after combining (3.1) and (3.2) is then expressed as follows:

$$c_T(t) = \frac{D(t)V_2}{\varepsilon l V_1} \tag{3.3}$$

Rates of accumulation of Fe^{2+} ions in tank, $\frac{dc_T(t)}{dt}$ were found as slopes of the linear plots $c_T(t)$. In the case of microreactor $\frac{dc_T(t)}{dt} = \frac{dc_R(t)}{dt} = r_{Fe^{2+}}$ where $c_R(t)$ is concentration of Fe^{2+} in reactor and $r_{Fe^{2+}}$ is rate of generation of Fe^{2+} in reactor.

To shift from the accumulation rate of Fe^{2+} ions in tank to the actual reaction rate in the annular reactor one should take into account the dilution of photogenerated ions in the tank. The model shown in **Figure 3.1** was used for mass balance calculation in the annular recirculating rig. Volume of the connecting tubes was neglected in this consideration.

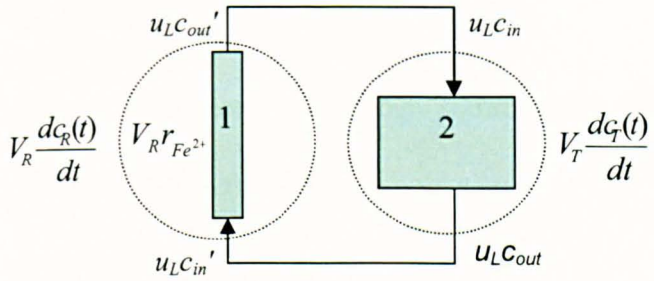

Figure 3.9. Model representing the annular photoreactor for the mass balance calculations. 1 is reactor, 2 is tank. For the abbreviations see text.

Mass balance for the tank is expressed as follows:

$$V_T \frac{dc_T(t)}{dt} = u_L(c_{out} - c_{in}) \tag{3.4}$$

Here u_L is liquid flowrate, $u_L c_{in}$ and $u_L c_{out}$ are molar flows of Fe^{2+} in and out of the tank. Similar equation for the reactor with taking into account the rate of generation of Fe^{2+} inside the annular reactor due to photochemical reaction, $r_{Fe^{2+}}$ can be obtained:

$$V_R \frac{dc_R(t)}{dt} = u_L(c_{out}' - c_{in}') + V_R r_{Fe^{2+}} \tag{3.5}$$

Mass balance for the whole photochemical reactor rig is then:

$$(V_R + V_T)\frac{dc_\Sigma(t)}{dt} = V_R \frac{dc_R(t)}{dt} + V_T \frac{dc_T(t)}{dt} \tag{3.6}$$

Here $c_\Sigma(t)$ is an overall concentration of Fe^{2+} in the photochemical rig. From the other side, a change of concentration of Fe^{2+} in the system occurs only due to reaction in the annular photoreactor:

$$(V_R + V_T)\frac{dc_\Sigma(t)}{dt} = V_R r_{Fe^{2+}} \tag{3.7}$$

Expression (3.7) can also be obtained *via* combining (3.4), (3.5) and (3.6) and keeping in mind that $c_{out}' = c_{in}$ and $c_{out} = c_{in}'$. Finally, we can obtain the equation of mass balance in the system:

$$V_R r_{Fe^{2+}} = V_R \frac{dc_R(t)}{dt} + V_T \frac{dc_T(t)}{dt} \tag{3.8}$$

If we assume that concentration does not change significantly during one cycle, *i.e.* $c_R(t) \approx c_T(t)$ we can rewrite (3.8) as follows:

$$r_{Fe^{2+}} = \left(\frac{V_R + V_T}{V_R}\right)\frac{dc_T(t)}{dt} \tag{3.9}$$

Here V_R+V_T = 250 mL in the cases of the 524 nm and Xe arc lamps and 100 mL in the case of the 420 nm actinic fluorescent lamp. Intensity of light absorbed by ferrioxalate actinometer, I_a^F (mol L s^{-1}) was calculated using the following equation:

$$I_a^F = \frac{r_{Fe^{2+}}}{\Theta(\lambda)} \tag{3.10}$$

Here $\Theta(\lambda)$ is the quantum yield of Fe^{2+} formation at the emitted wavelength. From the original Hatchard and Parker data [179] it was estimated by interpolation that $\Theta(\lambda)$=1.08, 0.58, and 1.07 at λ=416, 524 and 420 nm in the cases of 416 nm LED, 524 nm LED, and 420 nm actinic fluorescent lamp correspondingly.

To obtain the intensity of light absorbed inside the reactor during the oxygenation of allylic substrate, I_a (mol L^{-1} s^{-1}) we have to account for the amounts of light absorbed by actinometer and photosensitizer in the reactor:

$$I_a = I_a^F \frac{1-10^{-\varepsilon_S(\lambda)lc_S}}{1-10^{-\varepsilon_F(\lambda)lc_F}} \tag{3.11}$$

Here ε_S and ε_F are molar extinction coefficients of the sensitizer and ferrioxalate, c_S and c_F are concentrations of sensitizer and ferrioxalate, l is pathlength of light in the photoreactor. All the parameters used for the calculation of the absorbed light inside the annular reactor and microreactor are listed in **Table 3.4, 3.5.**

Table 3.4. Parameters used for calculation of light absorbance by ferrioxalate actinometer. I_0 is intensity of light prior to absorption.

	λ, nm	ε_F, L mol^{-1} cm^{-1}	l, cm	c_F, M	I_a^F / I_0
Annular reactor	420	110	0.3	0.006	0.316
	524	0.35	0.3	0.15	0.036
Microreactor	416	140	0.024	0.006	0.045
	524	0.35	0.024	0.15	0.003

Table 3.5. Parameters used for calculation of light absorbance by *TPP*. I_0 is intensity of light prior to absorption.

	λ, nm	ε_S, L mol^{-1} cm^{-1}	l, cm	c_S, M	I_a / I_0
Annular reactor	420	399663	0.3	8.1×10^{-4}	1
	524	10900	0.3		1
Microreactor	416	345000	0.024		1
	524	10900	0.024		0.39

Planck equation for the energy of a single photon was used for estimation of the power of the adsorbed photons:

$$E = h\nu = h\frac{c}{\lambda} \tag{3.12}$$

where h is Plank constant ($h = 6.63\times10^{-34}$ J s), ν is frequency of light, c is velocity of light in vacuum ($c = 3.00\times10^{8}$ m s^{-1}) and λ is a wavelength of light. Then the absorbed power can be found as:

$$P_{h\nu} = EN_A J_a \tag{3.13}$$

Here N_A=6.02×10^{23} mol^{-1} is Avogadro constant and $J_a = I_a V_R$. According to (3.12), energy of a single photon for 416, 420 and 524 nm wavelengths are equal to 4.8×10^{-19}, 4.7×10^{-19} and 3.8×10^{-19} J (or 287639 284900 and 228355 J mol^{-1} of photons), correspondingly. An example of calculation of the amount of absorbed photons, absorbed power and and overall efficiency in the case of the 524 nm LED lamp (240 LEDs) with the annular reactor is given in **Appendix A**.

The *Xe* arc lamp and the metal halide lamps have continuous spectra from UV to IR region. Therefore it is not possible to employ the same approach for the I_a calculation as it was used for the LED lamps because quantum efficiencies $\Theta(\lambda)$ of Fe^{2+} generation are different for the different wavelengths λ. The only possibility for estimating the number of photons in these cases is using an average quantum yield.

Let us extrapolate the values for quantum yields of Fe^{2+} generation given in [179] for several wavelengths, λ_j, on intervals $\Delta\lambda_j = \lambda_{j+1} - \lambda_j$ until the next known values at λ_{j+1} to cover the entire range of the emitted wavelengths. Then, after partition the radiation spectrum of the *Xe* arc or metal halide lamp on the smallest possible equal $\Delta\lambda_i$ intervals (intervals of spectral resolution), the rate of Fe^{2+} generation inside the reactor can be written as:

$$r_{Fe^{2+}} = \sum_{j=1}^{n} \sum_{i=j}^{j+1} I_{ai}^{F} \Theta(\Delta\lambda_j) \tag{3.14}$$

Here $\Theta(\Delta\lambda_j)$ is the quantum yield of Fe^{2+} generation under illumination by photons from $\Delta\lambda_j$ interval, I_{ai}^{F} is the intensity of photons with wavelengths from the range $\Delta\lambda_i$, mol L^{-1} s^{-1}, absorbed by the ferrioxalate actinometer. After calculating each area under this graph, $A_i = N_i\Delta\lambda_i$ we can express the particular contribution of each group of photons to the total intensity of the emitted photons:

$$I_{ai}^{F} = I_{a}^{F} \frac{A_i}{A} = I_{a}^{F} \frac{N_i \Delta\lambda_i}{\sum_i N_i \Delta\lambda_i} = I_{a}^{F} \frac{N_i}{N} \tag{3.15}$$

Where A is total area of intensity *vs.* wavelength graph in arbitral units, $A = \sum_i A_i$, I_a^F is an overall intensity of photons absorbed by the actinometer inside the reactor, mol L^{-1} s^{-1}, N_i is intensity of the emitted photons in interval $\Delta\lambda_i$ taken from the emission spectrum of lamp used, and $N = \sum_i N_i \Delta\lambda_i$. Combining (3.14) and (3.15) we will obtain (3.16):

$$r_{Fe^{2+}} = \frac{I_a^F}{N} \sum_{j=1}^{n} \sum_{i=j}^{j+1} N_i \Theta(\Delta\lambda_j) \tag{3.16}$$

Now it is possible to work out the total intensity of photons, absorbed by the actinometer inside the photochemical reactor:

$$I_a^F = \frac{r_{Fe^{2+}}}{\frac{1}{N} \sum_{j=1}^{n} \sum_{i=j}^{j+1} N_i \Theta(\Delta\lambda_j)} \tag{3.17}$$

The sum $\frac{1}{N} \sum_{j=1}^{n} \sum_{i=j}^{j+1} N_i \Theta(\Delta\lambda_j)$ or the average quantum yields calculated as integrals for the curves from the **Figure 3.10** are equal to 0.37 and 0.74 in the cases of *Xe* arc and metal halide lamps correspondingly.

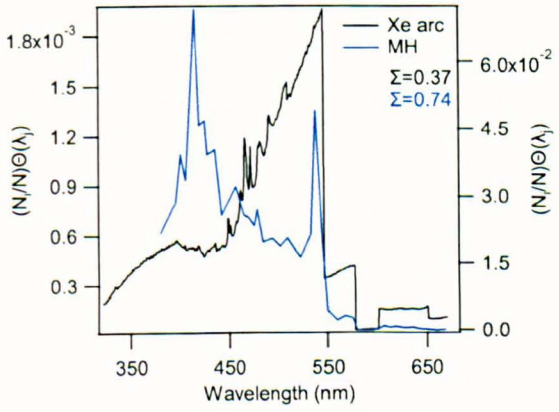

Figure 3.10. Emission spectra of *Xe* arc and metal halide lamps, corrected on quantum yields for $\Delta\lambda_j$ intervals taken from [179].

To obtain the amounts of light absorbed inside the photoreactors during oxygenation we should take into account, that Lambert-Beer equation is fulfilled only for each particular wavelength λ_i. Therefore, a modified equation (3.11) should be written as:

$$I_a = I_a^F \frac{\sum_i N_i (1 - 10^{-\varepsilon_S(\lambda_i) l c_S})}{\sum_i N_i (1 - 10^{-\varepsilon_F(\lambda_i) l c_F})} \tag{3.18}$$

where l is equal to 0.5 cm for the *Xe* arc lamp with the annular reactor and microreactor and 1 cm in the case of metal halide lamp, c_S=8.1×10^{-4} M, and c_F= 0.15 M in the case of

the annular reactor and 0.006 M in the case of the microreactor. Coefficients of extinction for *TPP* and ferrioxalate as functions of wavelength as well as the modified emission spectra of the lamps (with taking into account absorption by *TPP* and ferrioxalate) used for the calculation of sums in (3.18) are shown in **Figure 3.11** and listed in **Table 3.6**.

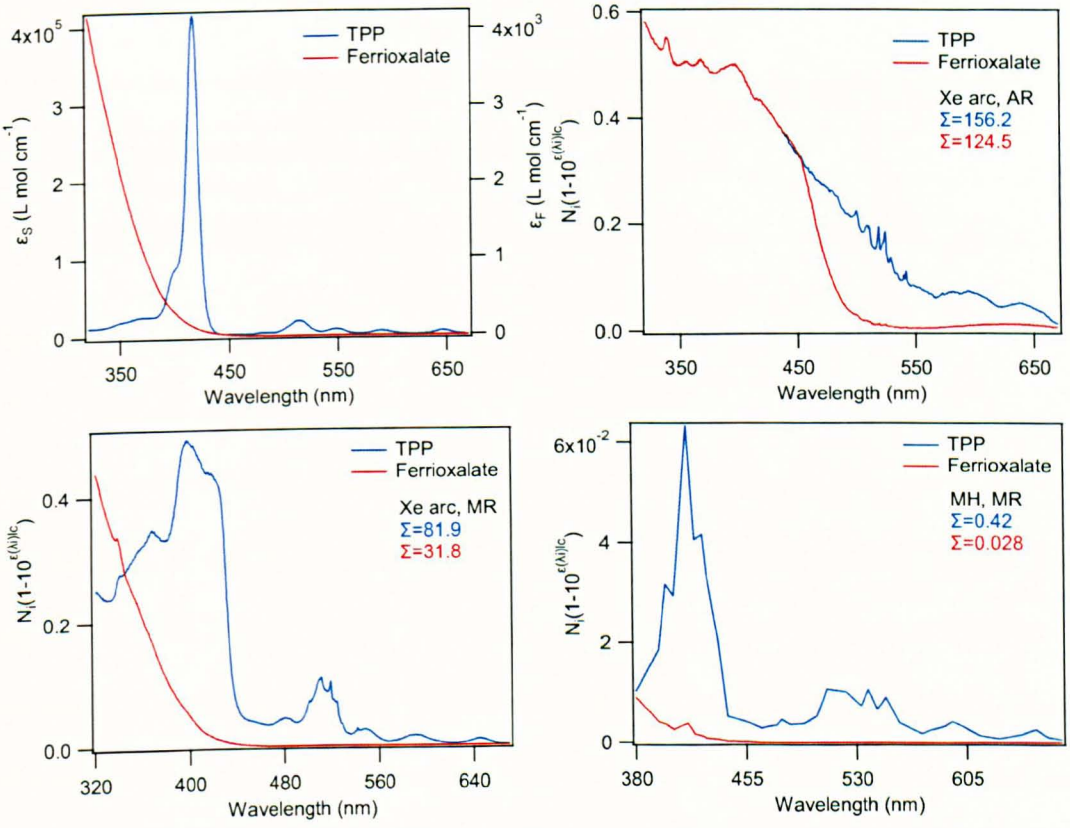

Figure 3.11. Coefficients of extinction for *TPP* and ferrioxalate as functions of wavelength (*a*). Graphs used for the calculation of sums in equation (3.18) for *Xe* arc and metal halide (MH) lamps, (*b*) with the annular reactor (AR), (*c*) and (*d*) with the microreactor (MR). Blue and red coloured sums (Σ) represent integrals of the corresponding curves.

Table 3.6. Parameters used for calculation of the amounts of light absorbed inside the photoreactors during oxygenation, I_a in the cases of *Xe* arc and metal halide lamps obtainded from Figure 3.11. MH is metal halide lamp, $\sum TPP = \sum_i N_i(1-10^{-\varepsilon_S(\lambda_i)lc_S})$, and $\sum \text{Ferrioxalate} = \sum_i N_i(1-10^{-\varepsilon_F(\lambda_i)lc_F})$.

	Lamp	ΣTPP	ΣFerrioxalate	ΣTPP/ΣFerrioxalate
Annular reactor	Xe arc	156.2	124.5	1.3
Microreactor	Xe arc	81.9	31.8	2.6
Microreactor	MH	0.42	0.028	15.0

3.3.2. Photodegradation of DPBF

3.3.2.1. General procedure

One millimolar solution of *DPBF* and 0.2 % wt of *PSi* in in 250 mL of *F113* were pumped with 40 mL min^{-1} flow rate through the annular recirculating reactor. Reactor temperature was kept at 20 °C in all the experiments. The reaction mixture was pre-saturated for 20 minutes with N_2 or O_2 depending on the experiment carried out. Then, the 524 nm LED lamp was switched on and the solution was irradiated for a period of several hours. Aliquots were taken every 15 or 30 minutes. Flowrates of gases were 30 or 50 mL min^{-1} in the case of O_2 and 30 mL min^{-1} in the case of N_2.

3.3.2.2. Preparation and analysis of samples and treatment of data

Ca. 2.5 mL of irradiated solution was filtered prior to making a sample for analysis to avoid the influence of *PSi* particles. Then 0.5 mL of sample was placed into a glass bottle and all the *F113* solvent was evaporated under air flow. Then the dry residue was dissolved in 10 mL of ethanol. Photo-degradation of *DPBF* was measured by monitoring the intensity of absorbance at 410 nm in a 1 cm quartz cell using UV-VIS spectrometer Shimadzu UV-1601. Pure ethanol was used as the reference sample. All measurements were repeated three times and averaged. The initial rates of *DPBF* photoderadation in the

tank were found as slopes of the linear fits of the experimental data (see **Appendix C** for details). Photodegradation rates inside the annular photoreactor, r_R were recalculated using the equation (3.9). Quantum yields of *DPBF* photodegradation were estimated using equation (2.7) shown in **Literature Review.**

3.3.3. Oxygenation of α-pinene to pinocarvone

3.3.3.1. Reaction mixture and general procedure

Oxygenation of α-pinene was carried out using modification of the method reported in [108]. The reaction mixture (α-pinene mix) was prepared as follows: 5.85 mL of α-pinene, 0.45 g of *DMAP*, 4.23 mL of acetic anhydride and 5 mL of pyridine were dissolved in 20 mL of solvent (CH_2Cl_2, *F113*, CCl_4, or ethanol, for details see **Table 3.7, 3.8**) inside of the light-proof reservoir. Then a sensitizer (*RB*, *R6G*, *TPP*, $TPP(OH)_4$, or different types of *PSi*) was added and the mixture was diluted by a solvent to 100 mL and mixed. In the case of *RB* and *R6G* the α-pinene mixture was diluted up to 250 mL in total by the solvent. Concentrations of sensitizers in all the experiments in the microreactor were 8.1×10^{-4} M. The reaction mixture was recirculated/pumped through the reactor. In the cases of the immersed well, the annular recirculating reactor, and the microreactor operated in continuous and recirculating modes, α-pinene mixture was saturated by O_2 *via* continuous bubbling of gas at a flowrate of 30 mL min^{-1} for 1 hr before and during each experiment. Then the lamp was switched on and aliquots were taken at different times. Liquid flowrate was 40 mL min^{-1} in the case of the annular recirculating reactor. Microreactor in a recirculating mode operated at 2 mL min^{-1}. Aliquotes were collected from the reservoir. In a segmented flow mode the microreactor was irradiated continuously while O_2 was introduced into the microchannel at various gas and liquid flowrates and pressures through a tee-connection forming the segmented gas-liquid flow. Aliquotes in this case were collected directly from the outlet of the microreactor operated

in a continuous mode and from the reservoir in the recirculating mode. All the reactors were kept at 20 °C.

Table 3.7. Concentrations of sensitizers and solvents used in oxygenation of α-pinene in the immersed well reactor.

Sensitizer	Solvent	125 W Hg
TPP	CH_2Cl_2	8.1×10^{-5} M
PSi	CH_2Cl_2	0.2 % wt
PSi	CH_2Cl_2	0.02 % wt
PSi	CCl_4	0.02 % wt

Table 3.8. Concentrations of sensitizers, and light sourses used in the oxygenation of α-pinene in the annular recirculating reactor.

Sensitizer	Solvent	524 nm LED	75 W Xe arc	420 nm actinic
PSi	CH_2Cl_2	-	0.2 % wt	-
PSi	F113	0.2 % wt	-	-
PSi^{I}	F113	0.2 % wt	-	-
PSi^{II}	F113	0.2 % wt	-	-
TPP	CH_2Cl_2	8.1×10^{-4} M	8.1×10^{-4} M	8.1×10^{-4} M
				10^{-4} M
				10^{-5} M
				5×10^{-6} M
				5×10^{-7} M
R6G	CH_2Cl_2	7.1×10^{-4} M	7.1×10^{-4} M	-
RB	Ethanol	6.0×10^{-4} M	-	-

^{1}H and ^{13}C NMR spectra were recorded using NMR spectrometer (Brooks, 300 or 400 MHz). NMR samples were prepared by using about 20 mg of sample dissolved in $CDCl_3$ solvent and chemical shifts were expressed in ppm with respect to the appropriate residual solvent peak (CH_3Cl at 7.27 ppm). Conversions of pinocarvone and byproduct X_i were calculated using the following equation:

$$X_i = \frac{B_i}{\sum_i B_i} \tag{3.19}$$

There B_i is the area of peak corresponding to *i*-th compound obtained from NMR spectra. Initial reaction rates and quantum yields of pinocarvone generation were calculated similar to that for *DPBF* oxidation.

3.3.4. Oxygenation of α-terpinene

3.3.4.1. Reaction mixture and general procedure

5.85 mL of α-terpinene and sensitizer (*TPP* or *PSi*) were dissolved in 250 mL of solvent (*CH_2Cl_2* or *F113*) inside a light-proof reservoir. The reaction mixture was recirculated in the annular recirculating rig and saturated by *O_2 via* continuous bubbling at a flowrate of 30 mL min^{-1}. *O_2* bubbling was started 1 hr prior to each experiment. Then the lamp (*Xe* arc or 524 nm LED) was switched on and aliquots were taken during the experiment at different times. Liquid flowrate was 40 mL min^{-1}. Reactor was kept at 20 °C. **Table 3.9** summarises the experimental parameters.

Table 3.9. Concentrations of sensitizers and sourses of light used in oxygenation of α-terpinene in the annular recirculating reactor.

Sensitizer	Solvent	524 nm LED	75 W Xe
PSi	F113	0.2 % wt	-
PSi	CH_2Cl_2	-	0.2 % wt
TPP	-	8.7×10^{-5} M	-

3.3.4.2. Aliquots preparation, analysis and data treatment

About 2-3 mL of irradiated reaction mixture was evaporated (filtered prior to evaporation in the case of *PSi*). The residue was dissolved in ~ 2 mL of *$CDCl_3$* and analysed by *^1H* and *^{13}C* NMR. Conversion was calculated from *^1H* NMR spectra using the equation (3.19).

3.3.5. Oxygenation of trimethylsilane (TMS) derivative of ACHA

0.2 g of *TMS* derivative of *ACHA* and $5*10^{-2}$ g of *TPP* were dissolved in 100 mL of CH_2Cl_2. The reaction mixture was recirculated in the annular reactor recirculating rig and saturated by O_2 *via* continuous bubbling at a flowrate of 30 mL min^{-1}. O_2 bubbling was started 1 hr prior to each experiment. Then the 420 nm actinic fluorescent lamp lamp was switched on and aliquots were taken during the experiment at different times. In the case of the microreactor two modes were used for oxygenation of *TMS* derivative of *ACHA*. Microreactor was illuminated by the 416 nm LED lamp when the continuous mode and continuous O_2 bubbling *via* reaction mixture were used while in the recirculating mode with segmented gas-lquid flow the reactor was illuminated by the 250 W metal halide lamp. 0.1 and 0.3 g of *TMS* derivative of *ACHA* in 100 mL of CH_2Cl_2 were used in these cases correspondingly. Conversions were calculated from ^1H NMR spectra using the equation (3.19).

3.3.6. NMR spectra

Pinocarvone. ^1H NMR $CDCl_3$ (300MHz) δ 0.74 (3H), 1.19 (d, J = 10.3Hz, 1H) 1.29 (s, 2H), 2.13 (m, 1H), 2.46 (m, 1H), 2.60 (m, 2H) 2.7 (t, J=6,1Hz, 1H), 4.95 (s, 1H), 5.91 (s, 1H) [183].

Ascaridol. ^1H NMR ($CDCl_3$, 500 MHz) δ 0.95 (3H, s), 0.98 (3H, s), 1.34 (3H, s), 1.48 (2H, m), 1.89 (1H, m), 1.99 (2H, m), 6.37 (1H, d, J = 8.5 Hz), 6.46 (1H, d, J = 8.5 Hz); ^{13}C NMR ($CDCl_3$, 125 MHz) δ 17.1, 17.2, 21.3, 25.5, 29.4, 32.1, 74.3, 79.7, 133.0, 136.3. ^{13}C NMR ($CDCl_3$, 125 MHz) 17.1, 17.2, 21.3, 25.5, 29.4, 32.1, 74.3, 79.7, 133.0, 136.3 ppm [184].

(R)-(+)-(E)-trimethyl(1-phenylpent-3-enyloxy)silane (*TMS* derivative of *ACHA*). ^{1}H NMR (400 MHz; $CDCl_3$) δ 0.0 (s, 9H), 1.60 (d, J = 5.7 Hz, 3H), 2.34-2.39 (m, 2H), 4.58 (dd, J = 7.6, 5.4 Hz, 1H), 5.21-5.48 (m, 2H), 7.17-7.31 (m, 5H).

Syn-((*1R,3S*)-(+)-*3-hydroperoxy-1-phenylpent-4-enyloxy*)*trimethylsilane* (**1**). ^{1}H NMR (400 MHz; $CDCl_3$) δ 0.0 (s, 9H), 1.74 (ddd, *J* = 14.3, 6.4, 4.9, 1H), 2.25 (ddd, *J* = 14.3, 8.7, 7.8 Hz, 1H), 4.39 (q, *J* = 7.0 Hz, 1H), 4.76 (dd, *J* = 8.7, 4.4 Hz, 1H), 5.29-5.33 (m, 2H), 5.88 (ddd, J = 17.5, 10.5, 7.1 Hz, 1H), 7.24-7.35 (m, 5H), 8.35 (s, 1H).

Anti-((*1R,3R*)-(+)-*3-hydroperoxy-1-phenylpent-4-enyloxy*)*trimethylsilane* (**2**). ^{1}H NMR (400 MHz; $CDCl_3$) δ 0.0 (s, 9H), 1.82 (ddd, *J* = 14.8, 8.7, 3.1 Hz, 1H), 1.92 (ddd, *J* = 14.8, 9.2, 3.9 Hz, 1H), 4.48-4.53 (m, 1H), 4.85 (dd, 9.2, 3.1 1H), 5.21 (dd, *J* = 10.5, 1.2 Hz, 1H), 5.27 (dd, J = 17.4, 1.2 Hz, 1H), 5.79 (ddd, *J* = 17.4, 10.5, 6.9 Hz, 1H), 7.11-7.27 (m, 5H), 8.42 (s, 1H).

3.3.7. Preparation of PSi powders

Powders of *Si* nanocrystals (*PSi*, PSi^I and PSi^{II}) were obtained by chemical etching of metallurgical grade polycrystalline *Si* powder (mean particles size of 4 μm) or by electrochemical etching of the *B*-doped *Si* (100) wafers. In the case of chemical etching the polycrystalline *Si* powder was first immersed in a solution of *HF* and water to remove surface SiO_2 layer, then HNO_3 was added gradually until the ratio of used chemicals was about 4:1:20 of $HF:HNO_3:H_2O$. The etching was finished when an efficient red-orange emission under illumination by UV light appeared. The powder was stored in air and used in oxygenation reactions with and without refreshment in *HF* vapour (PSi^I and *PSi* samples correspondingly). PSi^{II} was prepared by crushing of microporous *Si* layers obtained *via* electrochemical etching of *B*-doped (100) wafers with a typical resistivity of 2–10 Ω cm. The electrochemical etching was performed in a mixture of ethanol and *HF* (49 wt. % in water) 1:1 by volume using a *Pt* wire as cathode. The etching current density was 30–50 mA cm^{-2}. The powder was refreshed in *HF* vapour prior to use in the reactions. An average pore size of all the obtained powders was in the range of 3-7 nm, and surface area was about 160 $m^2 g^{-1}$ [90, 96].

3.3.8. Dye immobilization on the surface of H-terminated PSi

Thermal and photochemical synthesis. To solution of $TPP(OC_3H_5)_4$ (0.005 g in 100 mL of dry toluene) was added 1 g of *PSi* and the suspension was vigorously shaked for several minutes. The reaction flask was continuously stirred during reaction and N_2 bubbled through the reaction mixture. The reaction mixture was refluxed during heating at 105 °C or during irradiation by a 75 W *Xe* arc lamp from the side of the reaction flack at room temperature. The reaction was stopped after 45 hrs.

Ultrasonic synthesis. Ultrasonic synthesis was carried out in a UNIlab Workstation Glovebox (MBraun), H_2O < 1 ppm, O_2 < 1 ppm using Sonicator 3000 (Misonix Incorporated). 1 g of *PSi* was added to solution of $TPP(OC_3H_5)_4$ (0.005 g in 80 mL of dry toluene and 20 mL of dry methanol). After sonication for 20 minutes a 1 mL of a 0.05 M H_2PtCl_6 solution in methanol was added to the reaction mixture. Alternatively, 4 mL of 0.5 M $AlCl_3$ in tetrahydrofuran were added to the solution of the dye with added *PSi*. The sonication was continued during 3 hours at 18 W. Reaction temperature was about 80 °C.

The immobilized *PSi* nanoparticles were filtered using vacuum filtration assembly (Sigma Aldrich) and 47 mm diameter glass fiber filters, 0.7 μm pore size (Fisher) and washed several times by CH_2Cl_2 (3×100 mL) and 3×20 mL of acetone until disappearance of dye fluorescence in the filtrate. Then the powder was washed by 0.1 M *HCl* (10 mL), H_2O:acetone = 1:1 (20 mL) and finally by acetone (50 mL). Filtrated powders were dried on air.

3.3.9. FTIR measurements procedure

IR spectra of *PSi* samples in absorbance mode were measured in the spectral range of 400-4000 cm^{-1} using a Spectrum 100 FTIR spectrometer (Perkin Elmer). About 1 mg of

sample was mixed with 100 mg of *KBr*, grinded carefully and pressed to a pellet at pressure of 10 bar. Background was collected with a pure *KBr* tablet before measuring samples. Spectra were acquired after collection for 7 minutes with 2 cm^{-1} resolution.

3.3.10. Photoluminescent spectroscopy measurements procedure

30 mg of *PSi* powder (or 37 μM of *TPP*) were dispersed in 2 mL of solvent (CH_2Cl_2, C_6F_6 or CCl_4) and different amounts of α-terpinene were added in different experiments as specified in **Results and discussion**. PL was excited by an Ar^+ laser (energy 2.54 eV) with an excitation intensity of up to 500 mW cm^{-2}. Near-IR PL measurements aiming for detection of radiative relaxation of $^1O_2$ ($^1\Delta$-$^3\Sigma$ transition) were performed in O_2-saturated solvents using an *InGaAs* array detector coupled with a single monochromator. For measurements in the visible range a Si charge-coupled device was used. All optical spectra were corrected to the sensitivity of the respective optical setup.

4. RESULTS AND DISCUSSION

4.1. OXYGENATION OF ALLYLIC SUBSTRATES BY $^1O_2$ IN THE ANNULAR RECIRCULATING PHOTOREACTOR

4.1.1. Oxygenation of α-pinene

Oxygenation of α-pinene (0.36 M solution in 100 mL of CH_2Cl_2, *TPP* as a photosensitizer) was first carried out in a conventional immersed-well quartz photoreactor. A 53 % conversion was achieved after 7 hours of illumination by a 125 W medium pressure *Hg* lamp and continuous bubbling of O_2 through the reaction mixture (see **Figure 4.1**, *a* and **Table 4.1**). The quantum yield of pinocarvone production under these conditions was about 0.062. Complete conversion of α-pinene required several days of illumination.

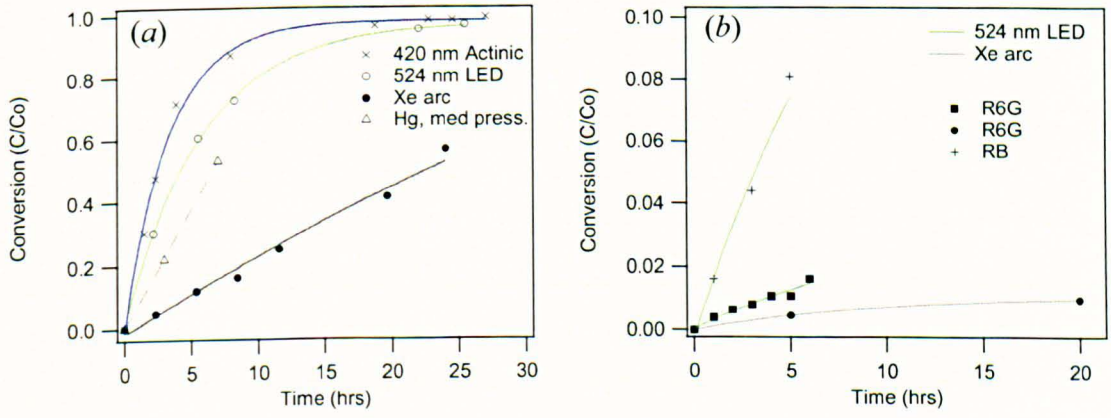

Figure 4.1. Conversion of α-pinene to pinocarvone. (*a*) Annular recirculating reactor, C_0=3.6×10^{-1} M in 100 mL of CH_2Cl_2 with 524 nm LED, 420 nm fluorescent and *Xe* arc lamps (green, violet and grey lines) 8.1×10^{-4} M of *TPP* and immersion well reactor with *Hg* lamp (dotted line), 8.1×10^{-5} M of *TPP*. (*b*) Annular recirculating reactor, C_0=1.5×10^{-1} M in 250 mL, (+) 5.95×10^{-4} M *RB* in ethanol (only intermediate peroxide was formed), (■) 7.1×10^{-4} M *R6G* in CH_2Cl_2 and 524 nm LED lamp (green lines); (●) 7.1×10^{-4} M *R6G* in CH_2Cl_2 and *Xe* lamp. The liquid flowrate in all the recirculating experiments was 40 mL min^{-1}. O_2 flow rate was 30 mL min^{-1} and T=20 °C in all the experiments.

Next, oxygenation of α-pinene was studied in an annular recirculating photoreactor. Three different sources of light and three different geometries were used: 524 nm LED, 420 nm actinic fluorescent, and 75 W *Xe* arc lamps (see **Experimental** for details). The intensity of the absorbed photons I_a (mol L^{-1} s^{-1}) for these lamp-reactor geometries was measured by ferrioxalate actinometry (see **Experimental** and **Appendix A**). The highest intensity of the absorbed photons was achieved in the case of the 420 nm actinic fluorescent lamp, followed by the 524 nm LED lamp, while the *Xe* arc lamp demonstrated the lowest performance (see **Table 4.1**).

Table 4.1. A summary of α-pinene mixture oxygenation (100 mL, 0.36 M of α-pinene in CH_2Cl_2) performed in the annular recirculating and immersed-well photoreactors with 8.1×10^{-4} M and 8.1×10^{-5} M of *TPP* correspondingly.

Lamp	I_a, Einst L^{-1} s^{-1}	r_0^T, mol L^{-1} s^{-1}	r_0^R, mol L^{-1} s^{-1}	X_P (t=7 hrs)	ϕ_R
Actinic 420 nm	5.7×10^{-4}	2.0×10^{-5}	1.8×10^{-4}	0.86	0.322
524 nm LED	4.6×10^{-4}	1.1×10^{-5}	1.1×10^{-4}	0.68	0.248
Xe arc	2.3×10^{-4}	2.1×10^{-6}	7.0×10^{-5}	0.16	0.303
Hg med. pressure	1.2×10^{-4}	7.6×10^{-6}	7.6×10^{-6}	0.53	0.065

An overall efficiency of the photoreactor (power absorbed during oxygenation, $P_{h\nu}$ to the supplied power, P_{in}) taking into account efficiency of the light source and the specific lamp-reactor geometry may be expressed as:

$$\eta = \eta_{LR}\,\eta_{PL} \tag{4.1}$$

where η_{LR} is efficiency of the lamp-reactor geometry, η_{PL} is efficiency of power-to-light conversion, $\eta_{LR} = \frac{P_{h\nu}}{P_{h\nu}^0}$, $\eta_{PL} = \frac{P_{h\nu}^0}{P_{in}}$, and $P_{h\nu}^0$ is total emitted power output of the lamp. In the case of the 524 nm LED lamp it was possible to estimate the $P_{h\nu}^0$ (see **Appendix B**) and therefore, the efficiency of lamp-reactor geometry, η_{LR}. Using the number of photons absorbed inside the photoreactor (measured by actinometry) it was found that about 70 %

of light illuminated by the lamp was used in the photoreaction (**Table 4.2**). The observed high efficiency of light utilization stems from the circular geometry of the LED lamp and the narrow radiation pattern of a single LED bulb (the off-axis angle where the intensity drops to 0.5 of the on-axis intensity is 7.5°). The origin of light losses in the system is most likely due to the reflection of light from different interfaces (air-glass, glass-liquid, and O_2 bubble-liquid interfaces). The efficiency of the power-to-light conversion, η_{PL} taking into account 30 drivers with the total power consumption of 20.9 W used for stabilization of the LED feed current, was about 3.9 %. Without the drivers the power conversion increases to 8.8%. This number is two-three times lower than that normally delivered by conventional light sources, such as *Xe* arc and fluorescent lamps, which routinely demonstrate about 20-40 % power-to-light conversion efficiency [185]. An overall efficiency of the annular recirculating reactor, η with the 524 nm LED lamp was found to be about 2.7 and 6.1 % with and without drivers, correspondingly (see **Table 4.2**).

Table 4.2. Efficiency of the lamp-reactor geometry, power-to-light conversion, and overall efficiency of the annular recirculating photoreactor for the 524 nm LED and 420 nm actinic fluorescent lamps.

Lamp	η_{LR}, %	η_{PL}, %	η, %
524 nm LED	69.1	8.8	6.1
524 nm LED & drivers	69.1	3.9	2.7
Actinic 420 nm	9.5-19	20-40[a]	3.8

Two other sources of light used with the annular photoreactor should have even lower levels of light utilization. Indeed, in the case of the 420 nm actinic fluorescent lamp in addition to reflection of light from the interfaces, about half of the total photon flux is propagated towards the direction opposite to the reactor and mostly wasted despite the

[a] Taken from ref. [184]; [b] value estimated using equation (1.1) and η_{PL} = 20-40 % [184].

reflector surrounding the bulbs. As a result, η of only about 3.8 % (an overall efficiency) was achieved in this lamp-reactor geometry (estimated efficiency of the lamp-reactor geometry for the 420 nm actinic fluorescent lamp is less than 20 % which is about three times less compared to that found in the case of 524 nm LED lamp, see **Table 4.2**). Due to the inefficient lamp-reactor geometry used with the *Xe* arc lamp only a small fraction of the total photon flux (approximately 5 % of the total flux) illuminates the reactor. However, it was impossible to estimate quantitatively the efficiency of the lamp-reactor geometry and the overall efficiency for this lamp, as the total flux of photons can be calculated only by using an integrating sphere.

The initial rates of pinocarvone accumulation in the tank and its generation inside the annular reactor follow the trend of the amount of absorbed photons: the more photons are absorbed inside the reactor, the higher are the initial rates of generation and accumulation of the product. The highest rate was achieved with the 420 nm actinic fluorescent lamp followed by 524 nm LED lamp (see **Figure 4.1**, *a*, and **Table 4.1**). The *Xe* arc lamp initiated the lowest reaction rate which is likely due to the inefficient light utilization in the non-optimal lamp-reactor geometry (only a small segment of the annular reactor was illuminated by the lamp with most of the photon flux wasted). This tendency is also reflected in the quantum yields of pinocarvone generation (**Table 4.1**). It is remarkable that quantum yields obtained in the annular photoreactor are higher compared to those found for the immersed-well reactor illuminated by a *Hg* lamp.

Two other photosensitizers of $^1O_2$ generation, *RB* and Rhodamine 6G (*R6G*), were tested in the oxygenation of α-pinene into pinocarvone. *RB* has a small absorption band at *ca.* 519 nm and the main absorption peak at 559 nm and *R6G* with an absorption peak at 529.8 nm (see **Experimental**) (quantum yields of $^1O_2$ generation are 0.8 and 0.12

correspondingly [54]). Emissions from the *Xe* arc and the 524 nm LED lamps have good overlaps with the absorption bands of both photosensitizers and, therefore, they were used for illumination of the photoreactor. One can see from the experimental data that the initial reaction rates of product generation (and therefore, quantum yields) are significantly lower compared with these mediated by *TPP* (**Figure 4.1**, *a*, *b*, **Table 4.1**, **4.3**) even taking into account the difference in the recirculating volumes of α-pinene mixtures (100 mL for *TPP* and 250 mL in the case of *RB* and *R6G*). In the oxygenation with *RB* only the product of ene reaction (an intermediate peroxide formed in α-pinene oxygenation to pinocarvone by $^1O_2$) was obtained after 6 hrs of illumination. The reason why pinocarvone was not formed under these conditions can be explained by inhibition of the step of peroxide acylation by ethanol used as a solvent due to the formation of ethyl acetate. A shorter lifetime of $^1O_2$ in ethanol compared to that in CH_2Cl_2 (1.6×10^{-5} *vs* 7.7×10^{-5} s [64]) and deactivation of *RB* due to its agglomeration [186] and binding with acetylpyridinium ion (similar to binding of *RB* with dimethylviologen [187]) may also be responsible for the observed low conversion. Low activity in the case of *R6G* stems probably from the low quantum yield of $^1O_2$ generation.

Table 4.3. A summary of α-pinene mixture oxygenation (250 mL, 0.15 M of α-pinene) performed in the annular recirculating reactor with 6.0×10^{-4} M *RB* in ethanol and 7.1×10^{-4} M *R6G* in CH_2Cl_2.

Sens	Lamp	I_a, Einst L^{-1} s^{-1}	r_0^T, mol L^{-1} s^{-1}	r_0^R, mol L^{-1} s^{-1}	ϕ_R
RB	524 nm LED	4.6×10^{-4}	6.4×10^{-7}	1.7×10^{-5}	0.037
R6G	524 nm LED	4.6×10^{-4}	1.3×10^{-7}	3.4×10^{-6}	0.007
R6G	Xe arc	2.3×10^{-4}	3.6×10^{-8}	3.0×10^{-6}	0.013

The influence of the amount of absorbed photons on the initial rate of α-pinene oxygenation was studied in more details. Several experiments with various concentrations of *TPP* (from 8.1×10^{-4} to 5×10^{-7} M) were carried out in the annular recirculating reactor

with the 420 nm actinic fluorescent lamp. It was found that low concentrations of *TPP* are correlated with the reduced initial reaction rates, which increase with the increase in the *TPP* loading. A similar behavior was mentioned in the literature for other sensitizers, see for example [16, 186]. The reaction mixture containing 5×10^{-7} M *TPP* showed a steady-state conversion at the level of about 50 % after 24 hours of illumination accompanied by a change of the reaction mixture's color from purple to brown. The observed changes are explained by the shift of the sensitizer absorption bands towards longer wavelengths due to partial protonation of *TPP* by acetic acid formed in the reaction [188, 189]. A decrease in the triplet quantum yield of the protonated *TPP* [190] as well as a smaller overlap between the shifted absorption bands of *TPP* and emission spectrum of the 420 nm. fluorescent lamp are the reasons responsible for low conversion.

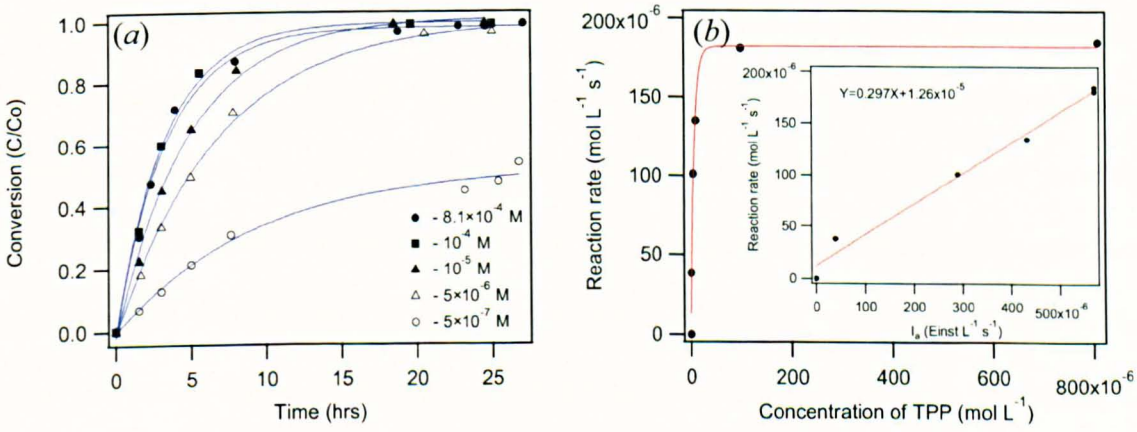

Figure 4.2. A dependence of α-pinene conversion (C_0=3.6×10^{-1} M) to pinocarvone in the annular recirculating reactor on the amount of sensitizer in 100 mL of α-pinene mixture (8.1×10^{-4} M, 10^{-4} M, 10^{-5} M, 5×10^{-6} M, and 5×10^{-7} M of TPP) (*a*). A dependence of the initial reaction rate of pinocarvone generation in the annular recirculating reactor on the amount of sensitizer added (*b*). The liquid flowrate is 40 mL min^{-1}, O_2 flowrate is 30 mL min^{-1}, and $T = 20$ ° C.

The data obtained in the experiments with various concentrations of *TPP* also revealed that the reaction rate is proportional to the amount of absorbed photons and for the fixed

intensity of incident light there is an optimum in the photosensitizer concentration which coincides with the complete absorption of incident light by the reaction layer (**Figure 4.2,** *b*). The concentrations higher than the optimum do not lead to any increase in the initial reaction rate. Moreover, an excess of a photosensitizer results in the formation of dark zones inside the volume of a reactor, which, together with poor mixing, may reduce the overall efficiency of oxygenation. This might be the main reason responsible for lower quantum yield of oxygenation in the immersed-well reactor. Indeed, concentration of 8.1×10^{-5} M TPP in the 1.8 cm thickness of the reactor space is more than enough for absorption of all the photons emitted by the *Hg* lamp. Therefore, a dark zone inside the reactor is unavoidable in this case, while agitation by the magnetic stirrer is likely to be insufficient for instantaneous homogeneous mixing. The annular recirculating reactor with the optimized geometry *i.e.* a 0.15 cm thickness of the annular space and efficient mixing provided by the well-dispersed rising bubbles of O_2 does not have such a disadvantage even at an 8-time excess in the amount of the photosensitizer over the optimum (see **Figure 4.2**). Moreover, in the case of higher concentrations of a sensitizer more photons are absorbed by the same volume of solution, which results in a higher concentration of triplet states, and hence in a higher rate of $^1O_2$ generation. Therefore, the thickness of the reaction layer is an important parameter responsible for high quantum yield, which is highest in the case of narrow reaction space and concentrations of photosensitizers high-enough for complete absorbance of all the emitted photons. It is also worth mentioning that multiple experiments on optimization of the amount of sensitizer usually done by some researchers [16, 191] may be avoided as this parameter can be calculated using Lambert-Beer law.

A variation of the reaction scale two times up and two times down revealed a decrease in the reaction rate with the increase of α-pinene concentration in the reaction mixture

(amounts of pyridine, *DMAP* and Ac_2O were altered proportionally) and decreasing solvent:reagents ratio (see **Figure 4.3**). A similar result was mentioned in [108] where a lower conversion was observed after tripling the reaction scale. This behavior is explained by stronger quenching of $^1O_2$ at elevated concentrations of pyridine and *DMAP* (*N*-containing compounds are known as efficient quenchers of $^1O_2$ [64, 192]) leading to a lower steady-state concentration of $^1O_2$ and the consecutive reduction in the reaction rate. This explanation is also supported by the developed kinetic model of the reaction, which is discussed later.

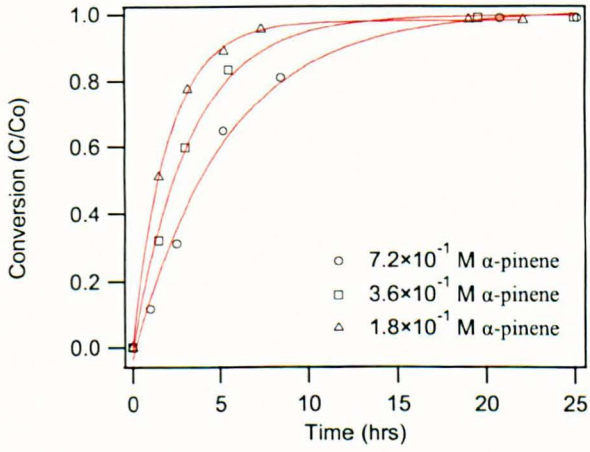

Figure 4.3. Conversion versus time-on-stream of α-pinene to pinocarvone in the annular recirculating reactor at different initial concentrations of α-pinene (1.8×10^{-1} M, 3.6×10^{-1} M and 7.2×10^{-1} M, amounts of acetic anhydride, pyridine and *DMAP* were changed proportionally, 8.1×10^{-4} M *TPP*, CH_2Cl_2 as solvent, 100 mL in total). The liquid flowrate is 40 mL min^{-1}, O_2 flowrate is 30 mL min^{-1}, T = 20 °C.

A simple kinetic model of the oxygenation inside a photoreactor was developed based on a steady-state approximation applied to the concentration of $^1O_2$ [54, 64]:

$$r_G = r_D + r_C \tag{4.2}$$

Here $r_G = I_a\phi_{^1O_2}$, $r_D = k_D[^1O_2]$, and $r_C = k_R'[R][^1O_2]$ are the rates of $^1O_2$ generation, quenching of $^1O_2$ by solvent and consumption of $^1O_2$ in physical quenching and reaction

with reagent R, correspondingly. k_D is a first order $^1O_2$ decay constant, k_R' is an overall bimolecular rate constant for physical quenching and chemical reaction of $^1O_2$ with R, I_a is intensity of light absorbed in the volume of a reactor, and $\phi_{^1O_2}$ is quantum yield of $^1O_2$ generation. The expression for the rate of reaction $r_R = k_R[R][^1O_2]$ in the annular photoreactor may then be written in terms of reagent concentration:

$$\frac{d[R]}{dt} = -I_a \phi_{^1O_2} \frac{k_R[R]}{k_D + k_R'[R]} \tag{4.3}$$

Here k_R is a bimolecular reaction rate constant of reagent R with $^1O_2$. One can see from equation (4.3) that reaction rate is proportional to the intensity of absorbed light, which corresponds to experimental observations. After taking into account equation (3.9) in **Experimental**, integration and rearrangements we obtain the solution as implicit function of product conversion, $X_P = 1 - [R]/R_0$:

$$\boxed{t = \frac{V_\Sigma}{I_a V_R \phi_{^1O_2} k_R} \left(k_R' R_0 X_P - k_D \ln(1 - X_P) \right)} \tag{4.4}$$

Here R_0 is an initial concentration of reagent; $V_\Sigma = V_R + V_T$ and V_R and V_T are volumes of a reactor and a recirculating tank, correspondingly. For detailed derivation of equation (4.4) see **Appendix E.**

By varying quantum yield of $^1O_2$ generation in the cases of different lamps with all other parameters being fixed (**Table 4.4, Figure 4.4**, *a*), and by varying quantum yield and $^1O_2$ decay rate constant at different initial concentrations of α-pinene and various amounts of absorbed light (**Table 4.5, 4.6, Figure 4.4**, *b*, *c*), the best fits of the model to the experimental data were obtained using the least squares method. I_a was extracted from the actinometry data, lifetime of $^1O_2$ in CH_2Cl_2, k_D, and rate constant for physical quenching

and chemical reaction of $^1O_2$ with α-pinene, k_R' were taken from [54, 64]. Physical quenching of $^1O_2$ by α-pinene was neglected in current consideration, *i.e.* $k_R' \approx k_R$.

Table 4.4. Parameters used in the least squares fitting of the kinetic model to the experimental data of α-pinene oxygenation in the annular recirculating reactor with different lamps.

	$I_a \times V_R/V_\Sigma$, Einst L^{-1} s^{-1}	$\phi_{^1O_2}$ *	$\phi_{^1O_2}$ [a]	R_0, M	k_R [b], L mol^{-1} s^{-1}	k_D [b], s^{-1}	S_M
420 nm Fluorescent	6.3×10^{-5}	0.65	0.5-0.8	3.6×10^{-1}	4.3×10^{4}	1.3×10^{4}	0.010
524 nm LED	4.4×10^{-5}	0.55	0.5-0.8	3.6×10^{-1}	4.3×10^{4}	1.3×10^{4}	0.008
Xe arc	6.9×10^{-6}	0.67	0.5-0.8	3.6×10^{-1}	4.3×10^{4}	1.3×10^{4}	0.005

Table 4.5. Parameters used in the least squares fitting of the kinetic model to the experimental data of α-pinene oxygenation in the annular recirculating reactor with different concentrations of α-pinene.

	$I_a \times V_R/V_\Sigma$, Einst L^{-1} s^{-1}	$\phi_{^1O_2}$ *	$\phi_{^1O_2}$ [a]	R_0, M	k_R [b], L mol^{-1} s^{-1}	k_D *,[b], s^{-1}	S_M
420 nm fluorescent	6.3×10^{-5}	0.68	0.5-0.8	1.8×10^{-1}	4.3×10^{4}	1.0×10^{4}	0.010
	6.3×10^{-5}	0.65	0.5-0.8	3.6×10^{-1}	4.3×10^{4}	1.3×10^{4}	0.010
	6.3×10^{-5}	0.68	0.5-0.8	7.2×10^{-1}	4.3×10^{4}	1.7×10^{4}	0.004

Table 4.6. Parameters used in the least square fitting of the kinetic model to the experimental data of α-pinene oxygenation in the annular photoreactor with different concentrations of *TPP* corresponding to different amounts of the absorbed photons.

	$I_a \times V_R/V_\Sigma$, Einst L^{-1} s^{-1}	$\phi_{^1O_2}$ *	$\phi_{^1O_2}$ [b]	R_0, M	k_R [b], L mol^{-1} s^{-1}	k_D *,[c], s^{-1}	S_M
420 nm Fluorescent	6.3×10^{-5}	0.65	0.5-0.8	3.6×10^{-1}	4.3×10^{4}	1.0×10^{4}	0.010
	6.3×10^{-5}	0.67	0.5-0.8	3.6×10^{-1}	4.3×10^{4}	1.3×10^{4}	0.002
	5.2×10^{-5}	0.52	0.5-0.8	3.6×10^{-1}	4.3×10^{4}	1.3×10^{4}	0.001
	4.8×10^{-5}	0.47	0.5-0.8	3.6×10^{-1}	4.3×10^{4}	1.3×10^{4}	0.003
	8.3×10^{-6}	0.85	0.5-0.8	3.6×10^{-1}	4.3×10^{4}	1.0×10^{4}	0.0001

[a] values are taken from [54], [b] values are taken from [64], [c] k_D is in the range from 1.0×10^4 to 1.9×10^4 [64], * is best fitted parameter, $S_M = \sum_{i=1}^{n}\left[X_P^{Experiment} - X_P^{Theory}\right]^2$ is minimal sum of squared residuals.

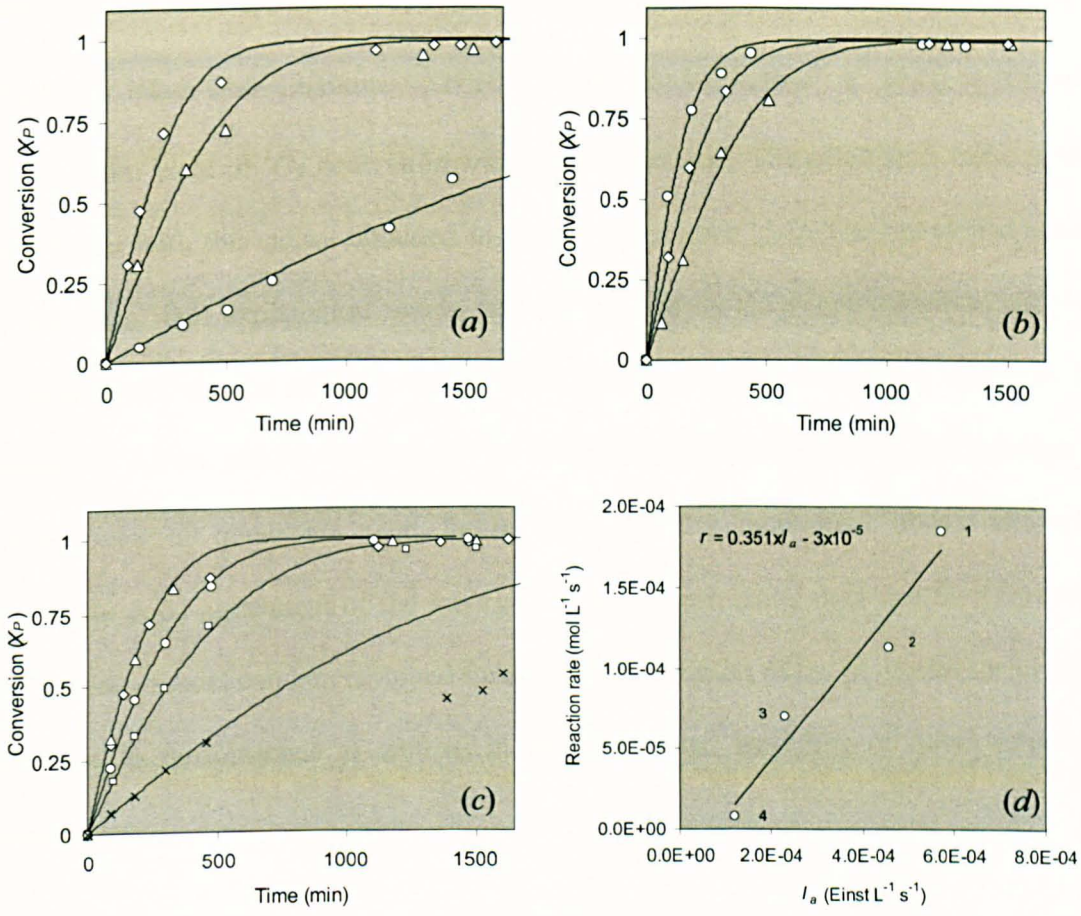

Figure 4.4. Fitting of the model to the experimental data of α-pinene oxygenation in the annular recirculating reactor using least square method; (*a*) with different lamps: ◇ 420 nm fluorescent, Δ 524 nm LED and ○ *Xe* arc lamp; (*b*) at different concentrations of α-pinene: ○ 1.8×10^{-1} M, ◇ 3.6×10^{-1}, Δ 7.2×10^{-1} M; (*c*) at different concentrations of *TPP* corresponding to different amounts of absorbed photons: ◇ 8.1×10^{-4} M, Δ 10^{-4} M, ○ 10^{-5} M, □ 5×10^{-6} M, and x 5×10^{-7} M; (*d*) is the dependence of the reaction rate on the amount of absorbed photons in the annular reactor: 1 is 420 nm fluorescent, 2 is 524 nm LED, 3 is *Xe* arc lamps and in the immersed-well reactor, 4 is medium pressure *Hg* lamp. Markers represent experimental data, lines are best fits.

Figure 4.4, *d*, shows the dependence of the initial reaction rate on the amount of absorbed photons in the annular reactor and in the immersed-well reactor with different lamps used for illumination. The data fit to a linear plot with the slope of 0.351. Applying values of

R_0, used in the experiments (3.6×10^{-1} M) and the values for k_D and bimolecular rate constant k_R' taken from literature (1.3×10^4 s^{-1} and 4.3×10^4 L mol^{-1} s^{-1} [64]) to equation (4.3), quantum yield of $^1O_2$ generation was found to be 0.65. The calculated value is also in agreement with the values obtained in the earlier studies [54]. The developed model also supports the explanation made earlier on steady-state concentration of $^1O_2$ dependence on variation of the reaction scale. Indeed, the best fits of the model to the oxygenation curves require an increase of the quenching constant with the increase in concentrations of quenchers (see **Table 4.5**). All the mentioned above examples demonstrate good agreement of the theory with the experimental data and therefore, this simple kinetic model can be employed further in optimization of the photoreactor in order to increase its performance as well as in the design and modeling of novel improved photoreactors.

4.1.2. Oxygenation of ACHA

Earlier study by our collaborators from the University of Loughborough (group of Prof. A. Malkov) carried out in the immersed-well photoreactor for 36 h under 150 W *Hg* lamp illumination demonstrated that *ACHA*s are less reactive towards oxygenation by $^1O_2$ compared to α-pinene. The reaction has poor regioselectivity due to weak electronic directing influence of hydroxyl group. Two regioisomers (two diastereoisomers each, in approximately equimolar ratios) are the main products in the reaction mixture:

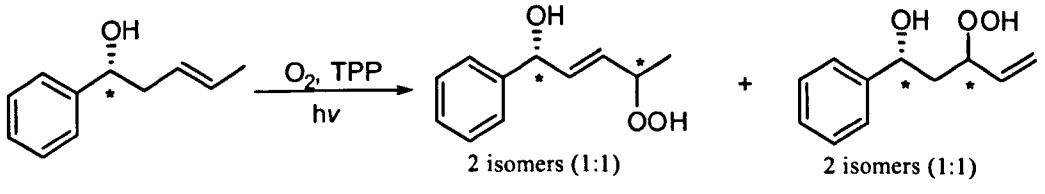

(4.5)

Following the observation that steric and stereoelectronic factors of *Si* substituents influence regio- and diastereselectivity of $^1O_2$ ene reactions [193] several silane derivatives of *ACHA* with the protecting group attached to the alcohol were studied. It

was found that oxygenation of *TMS* derivative of *ACHA* in the immersed-well reactor under 400 W sodium lamp illumination at -20 °C produced better regio- and diastereoselectivity with a clear preference toward compounds **1** and **2** with terminal double bond ((**1**+**2**):(**3**+**4**)=1:0.64 and **1**:**2**=0.54:1) compared to free alcohol (see equation (4.6)). Furthermore, the presence of *TMS* protecting group made the chromatographic separation of diastereoisomers **1** and **2**, and the mixture of **3** and **4** possible. Compound **2** is further used in a series of transformations leading to the value-added *C*-nucleosides (see **Figure 1.2** in **Introduction**). However, the overall efficiency of the oxygenation in the immersed-well reactor remaines low and has to be improved for the overall process to have a chance of being commercially interesting.

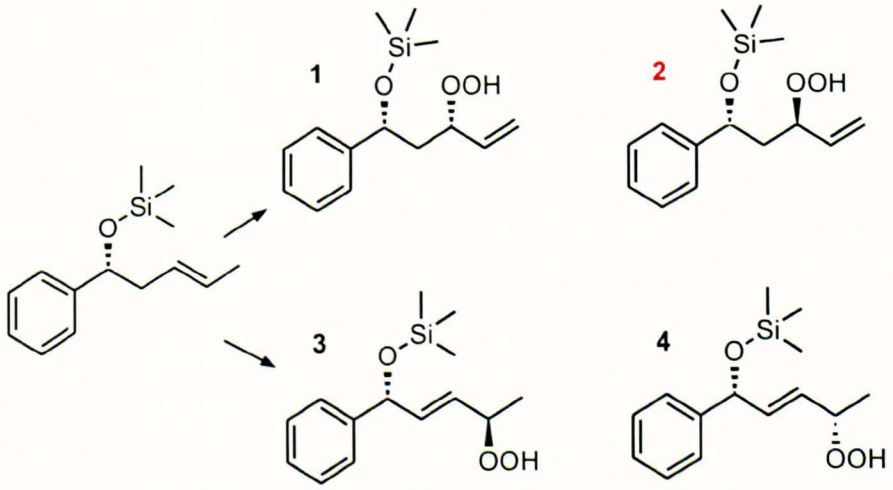

(4.6)

In order to achieve higher efficiency in the oxygenation of a *TMS* derivative of *ACHA* (C_0=8.5×10^{-3} M) the reaction was carried out in the annular recirculating photoreactor illuminated by the 420 nm actinic fluorescent lamp at 20 °C (see **Figure 4.5**). Again, a mixture of two regioisomers was obtained with a preference toward compound **2** with terminal double bond with slightly worse regio- and stereoselectivity: **((1+2):(3+4)** = 0.64:1 and **1**:**2** = 0.44:1). A lower selectivity may be explained by the partial cleavage of *TMS* group due to its hydrolysis. Product **2** was obtained with the yield of about 24 % in two days of the oxygenation in the annular recirculating reactor with a significantly lower consumption of power used for illumination due to a thinner reaction layer.

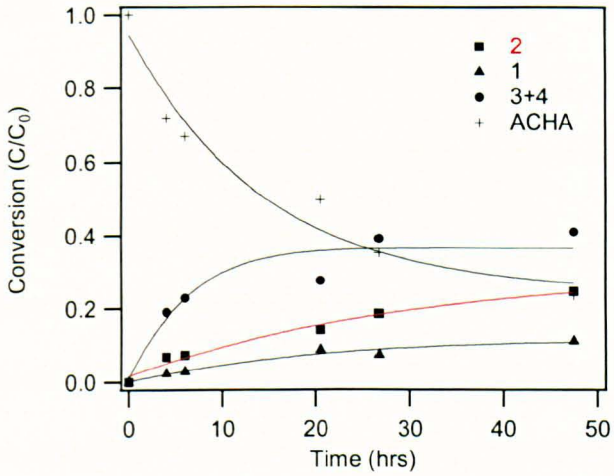

Figure 4.5. Conversion of *TMS* derivative of *ACHA* (C_0=8.5×10^{-3} M in 100 mL of CH_2Cl_2) in the annular recirculating reactor under 420 nm actinic fluorescent lamp. Concentration of *TPP* is 8.1×10^{-4} M, the liquid flowrate is 40 mL min^{-1}, O_2 flowrate is 30 mL min^{-1} and T = 20 °C.

According to equation (3.9) derived in **Experimental** the initial rate of accumulation of **2** in the tank, 1.2×10^{-8} mol L^{-1} s^{-1} (evaluated from kinetic data, **Figure 4.5**) corresponds to the initial reaction rate of 1.1×10^{-7} mol L^{-1} s^{-1} in the annular reactor. Using expression (4.3) for the rate of reaction and applying the value of R_0, used in the experiment (R_0=8.5×10^{-3}), the amount of the absorbed light (5.7×10^{-4} Einst L^{-1} s^{-1}) and values for k_D and $\phi_{^1O_2}$ taken from literature (1.3×10^4 s^{-1} and 0.6, respectively [54, 64]), the bimolecular reaction rate constant k_R was estimated to be about 4.9×10^2 L mol^{-1} s^{-1}. The obtained value is about two orders of magnitude less than that for α-pinene. Therefore, a more powerful source of light should be used in order to obtain higher productivity (mol s^{-1}) as well as utilisation of light should be improved.

4.2. OXYGENATION OF ALLYLIC SUBSTRATES BY $^1O_2$ IN THE MICROREACTOR

4.2.1. Homogeneous oxygenation of α-pinene in O_2-saturated solutions

4.2.1.1. Oxygenation in a continuous mode

Previous chapter demonstrated that reactors with narrow reaction space are superior to these with thick optical pathways due to better utilization of light in the reactions. In all the mentioned above cases the oxygenation was carried out in solutions saturated by O_2 at atmospheric pressure *via* continuous bubbling of O_2 through the reactors. It would be useful to investigate the influence of O_2 pressure on the efficiency of oxygenation. However, neither the immersed-well nor the annular recirculating reactors allow using elevated O_2 pressures. Moreover, both photoreactors have limited scale-up potentials as was mentioned in **Literature Review**. To overcome the drawbacks of the conventional photoreactors we developed a photochemical rig equipped with a glass-silicon microreactor chip with channel dimensions in the order of hundreds micrometers. The microreactor rig allows two different modes of operation, *i.e.* recirculating and continuous and two different approaches towards saturation of the reaction mixture by O_2 *i.e.* pre-saturation of the reaction mixture *via* O_2 bubbling and in-line saturation using segmented gas-liquid flow, at various pressures (1 to 60 bars), see **Experimental** for details.

Three different sources of light were used for illumination of the microreactor: the in-house assembled 524 and 416 nm LED arrays and a *Xe* arc lamp (see **Experimental** for details). The amount of the absorbed photons was estimated from the ferrioxalate actinometry data (see **Experimental** and **Appendix A**). The highest amount of photons was absorbed in the case of the 416 nm LED array, followed by the *Xe* arc lamp and the 524 nm LED array (see **Table 4.7**). The efficiency of the lamp-reactor geometry was estimated for both the LED arrays. It was found that about 7 and 21 % of light emitted by

the 524 nm and 416 nm arrays is used in the photoreaction (**Table 4.8, Appendix B**). Low efficiencies of this lamp-reactor geometry are explained by the long distance between the microreactor and the light sources. In order to achieve better values the arrays should be situated at the shortest possible distances. The overall efficiencies for the LED arrays, taking into account 5 drivers, were found to be 0.3 % and 1.6 % correspondingly while without drivers the values increase about two times. Although the estimated values of lamp-reactor geometry efficiencies are quite low, the specific (per volume of the microreactor) intensities of light absorbed inside the microreactor are of the same order of magnitude (or even higher as in the case of the 416 nm LED array) with these found for the annular photoreactor (compare **Table 4.7** and **Table 4.1**).

Table 4.7. Oxygenation of α-pinene in the microreactor illuminated by the 524, 416 nm LED arrays and *Xe* arc lamps. The reaction was carried out in the continuous mode at continuous saturation by O_2 at 1, 3.5 and 6 bar in the tank.

Lamp	P, bar	I_a, Einst L^{-1} s^{-1}	r_0^R, mol L^{-1} s^{-1}	ϕ_R
Xe arc	1.0	3.3×10^{-4}	1.4×10^{-4}	0.420
524 nm LED	1.0	3.2×10^{-4}	1.3×10^{-4}	0.404
416 nm LED	1.0	1.9×10^{-3}	3.3×10^{-4}	0.171
416 nm LED	3.5	1.9×10^{-3}	7.4×10^{-4}	0.384
416 nm LED	6.0	1.9×10^{-3}	8.5×10^{-4}	0.414

Table 4.8. Efficiency of the lamp-reactor geometry, power-to-light conversion, and overall efficiency of the microreactor with the 524 and 416 nm LED arrays.

Lamp	η_{LR}, %	η_{PL}, %	η, %
524 nm LED	6.7	8.8	0.6
524 nm LED & drivers	6.7	3.9	0.3
416 nm LED	21.4	15.3	3.3
416 nm LED & drivers	21.4	7.4	1.6

After determining the efficiencies of light utilization the microreactor was tested in the oxygenation of α-pinene using the LED arrays and the *Xe* arc lamp for illumination. The

reaction was carried out in a continuous mode at various liquid flowrates (u_L = 2.5, 2.0, 1.5, 1.0, 0.75, 0.5, 0.25, 0.1, 0.05, 0.01, 0.005 mL min^{-1}) using continuous O_2 pre-saturation of the reaction mixture *via* O_2 bubbling in the feed tank at different pressures (1, 3.5 and 6 bar). It was found that at high flowrates conversion of α-pinene increases with the decrease in the flowrate of the reaction mixture, until a stationary conversion is achieved (**Figure 4.6**). This is associated with the increase in the residence time in the reactor, $\tau=V_R/u_L$. The stationary conversion (or maximum conversion) at a given concentration of a sensitizer is determined either by the amount of α-pinene or by the amount of the dissolved O_2. Concentration of O_2 in CH_2Cl_2 saturated by O_2 at normal pressure is 8.8×10^{-3} M while in ethanol and in $CHCl_3$ the concentrations are slightly higher (9.8×10^{-3} M and 9.2×10^{-3} M respectively) [194, 195]. Therefore, consumption of all the dissolved O_2 in the reaction with 0.36 M solutions of α-pinene (about 40 times excess) corresponds to the maximum possible conversions of 2.4, 2.7 and 2.6 % in CH_2Cl_2, ethanol and $CHCl_3$, respectively. The obtained values are in good agreement with the experimental data (**Figure 4.6**). In the case of ethanol at short residence times only intermediate peroxide was obtained.

At long residence times the conversion falls down exponentially (**Figure 4.6**, *a*) which may be associated with the reduction of O_2 concentration in the reaction mixture due to diffusion of O_2 through the walls of Teflon tubing or interconnections.

The maximum conversions also correlate with the amounts of O_2 dissolved in the particular solvents at elevated pressures (see **Figure 4.6**, *c*, *d*). The saturation concentration of O_2 in CH_2Cl_2 at 3.5 bar is about 3.1×10^{-2} M [194], which corresponds to the maximum conversion of 8.5 % while at 6 bar O_2 solubility is increased up to 5.3×10^{-2} M [194] and 14.7 % conversion respectively. Similar values were obtained for $CHCl_3$

saturated by O_2 at 6 bar (5.6×10^{-2} M [194] and maximum conversion of 15.4 %). These numbers are in agreement with the experimental data (see **Figure 4.6**, *c*, *d*). Slight discrepancies between experiments and the theory may be attributed to a lower O_2 capacity of the α-pinene mixture compared to that of the pure solvents and to the faster diffusion of O_2 through the walls of Teflon tubing at elevated pressures.

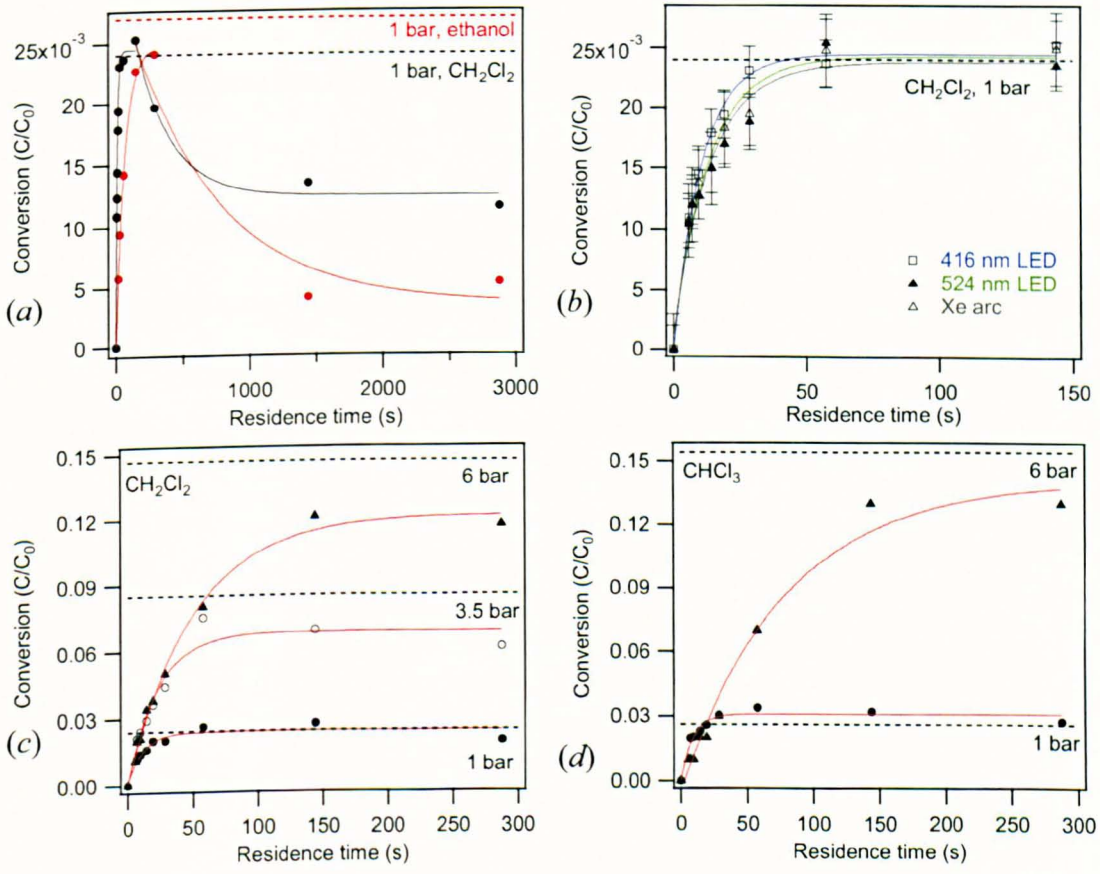

Figure 4.6. Conversion of α-pinene (C_0=3.6×10^{-1} M) to pinocarvone (to intermediate peroxide in the case of ethanol) in the microreactor in a continuous mode at continuous saturation of reaction mixture *via* O_2 bubbling (*a*) at 1 bar in ethanol with $TPP(OH)_4$ (red circles), and in CH_2Cl_2 with *TPP* (black circles) illuminated by 416 nm LED array; (*b*) at 1 bar in CH_2Cl_2 with *TPP* illuminated by Δ Xe arc lamp, ▲ 524 nm LED array, □ 416 nm LED array; (*c*) in CH_2Cl_2 and (*d*) in $CHCl_3$ with *TPP* at ▲ 6 bar, ○ 3.5 bar, ● 1 bar illuminated by 416 nm LED array. Dotted lines represent maximum conversion corresponding to consumption of all the O_2 dissolved in the particular solvent at particular pressures. Concentration of sensitizers is 8.1×10^{-4} M, T = 20 °C.

The initial reaction rates and quantum yields estimated for different O_2 pressures and sources of light are listed in **Table 4.7**. The obtained data suggest that higher conversions of α-pinene (0.36 M) may be obtained at higher O_2 saturation pressures with suitable residence times. It was estimated that 40 bars is sufficient for attaining 0.36 M concentration of O_2 in CH_2Cl_2. However, saturation of the reaction mixture by O_2 at such a high pressure involves an increased risk of explosion and therefore normally should be avoided. Therefore, due to safety reasons this experiment was not carried out.

Using the initial reaction rates at different pressures of O_2 in CH_2Cl_2 (**Table 4.7**) it was possible to estimate the formal reaction order for O_2 pressure as a slope in coordinates $\ln(r_{0i}\times r_{0j})^{-1}$ versus $\ln(P_i\times P_j)^{-1}$ (see **Figure 4.7**). It was found that $n = 0.7\pm0.2$ in the range of pressures studied.

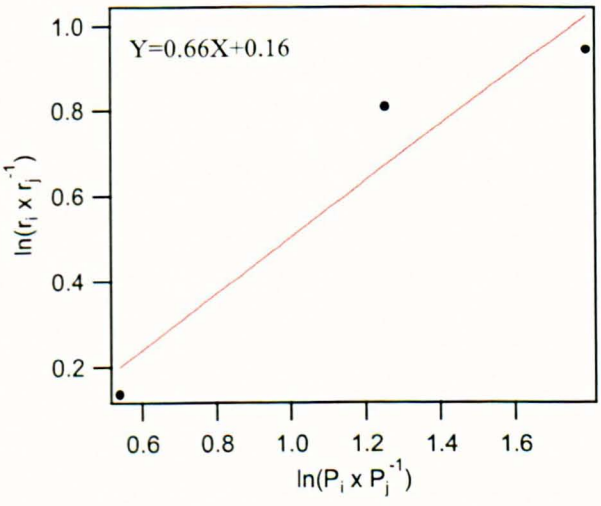

Figure 4.7. The dependence of logarithm reaction rates ratio on logarithm O_2 pressures ratio to determine a formal reaction order with respect to O_2 pressure. A slope of 0.7±0.2 of a linear fit of the experimental data in coordinates $\ln(r_{0i}\times r_{0j}^{-1})$ versus $\ln(P_i\times P_j^{-1})$. Here r_{0i} is initial reaction rate at P_i pressure.

4.2.1.2. Oxygenation in a recirculating mode

It was demonstrated above that the concentration of O_2 dissolved in CH_2Cl_2 at

atmospheric pressure is about 10^{-2} M. If concentration of a reagent is higher than the amount of available O_2 the compound will not be completely oxygenated in the continuous mode during one pass, as stoichiometry of ene reaction is 1:1. For example, in the experiments carried out with 0.36 M solutions of α-pinene about 97 % of α-pinene remained unreacted. In order to obtain 100 % conversion the reaction mixture should be re-saturated by O_2 and passed through the reactor several times in a recirculation mode.

The recirculating experiments were carried out at a flowrate of 2 mL min^{-1} using the 416 nm LED array for illumination of the microreactor and continuous saturation of the rection mixture by bubbling O_2 in the tank at 1 and 6 bar. These conditions correspond to conversions of about 1 and 2 % obtained in one pass in the continuous mode (see **Figure 4.6**, *b*, *c*) while concentration of O_2 is not depleted completely during the oxygenation. Kinetic curves obtained in both experiments are shown in **Figure 4.8**. One can see from these data that about 4-5 days is required for complete oxygenation of all the α-pinene (0.36 M) in 100 mL of the reaction mixture saturated by O_2 at atmospheric pressure. The initial reaction rate recalculated from the initial rate of the product accumulation in the tank using equation (3.9) from **Experimental** (and therefore, quantum yield) is close to that estimated earlier in the continuous mode experiment (see **Table 4.7** and **4.9**). The initial rate of reaction increases approximately three times at 6 bars of O_2 saturation pressure, similar to the experiments carried out in the continuous mode. The obtained value is in satisfactory agreement with that obtained in the continuous mode. About 2 days is required for 100 % conversion of 100 mL in the microreactor unit. The reaction order with respect to O_2 pressure was estimated using the initial reaction rates from **Table 4.9**. The obtained value of about 0.6 is close to that obtained in the continuous mode of oxygenation (0.7±0.2).

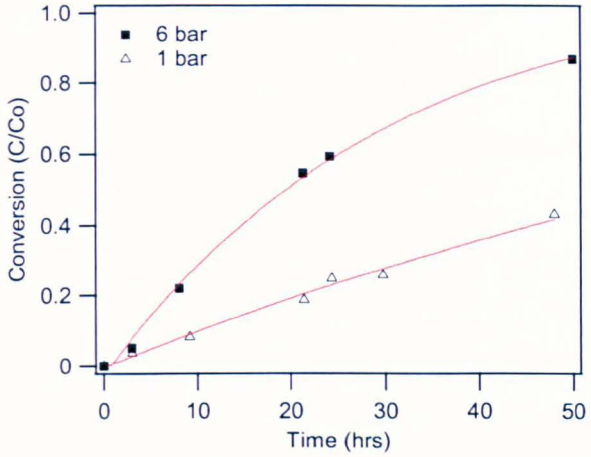

Figure 4.8. Conversion of a-pinene (C_0=3.6×10^{-1} M in 100 mL of CH_2Cl_2, concentration of sensitizers is 8.1×10^{-4} M) to pinocarvone in microreactor illuminated by the 416 nm LED array in recirculating mode at continuous saturation of reaction mixture *via* O_2 bubbling at 6 bar and at 1 bar. The liquid flowrate is 2 mL min^{-1}, T = 20 °C in all the experiments.

Table 4.9. Oxygenation of α-pinene in the microreactor illuminated by the 416 nm LED array and carried out in a recirculating mode at continuous saturation by O_2 in the feed tank at P=1 and 6 bar.

Lamp	P, bar	I_a, Einst L^{-1} s^{-1}	r_0^T, mol L^{-1} s^{-1}	r_0^R, mol L^{-1} s^{-1}	ϕ_R
416 nm LED	1.0	1.9×10^{-3}	8.9×10^{-7}	3.7×10^{-4}	0.192
416 nm LED	6.0	1.9×10^{-3}	2.6×10^{-6}	1.1×10^{-3}	0.562

4.2.2. Oxygenation of α-pinene in the gas-liquid segmented flow in microreactor

The major drawback of operating a microreactor in the recirculating or continuous modes with pre-saturation of the reaction mixtures by O_2 in a reservoir at normal and elevated pressures is the hazard of explosion of the formed O_2-organic vapor mixtures. It was reported earlier that microreactors allow safe and efficient way of carrying out gas-liquid reactions in a segmented flow including oxygenation of allylic substrates by photogenerated $^1O_2$ and gas-phase reactions at elevated O_2 pressures due to short

quenching distances in a microchannel, small volumes of gas bubbles and excellent heat exchange (see [8] and references therein). Moreother, small dimensions and meandering geometry of a microchannel provide efficient internal mixing in segmented gas-liquid flows [196, 197].

The influence of different O_2 pressures and flowrates on the conversion of α-pinene in a segmented gas-liquid flow was studied in more detail. The oxygenation was carried out at a fixed liquid flowrate (0.1 mL min^{-1}) with O_2 injected into the reaction mixture *via* a *t*-connector. The 416 nm LED array was used for illumination of the microreactor. Several different types of segmented flow were observed depending on O_2 flowrate. At low O_2 flowrates (< 0.5 mL min^{-1}) small gas bubbles were separated by liquid slugs of approximately the same length. The length of the bubbles became longer with increasing the O_2 flow rate, while the regularity of the obtained patterns (lengths of bubbles and liquid plugs) decreased. Inset in **Figure 4.9**, *a* represents a typical gas-liquid flow pattern obtained at O_2 flowrate of 700 mL min^{-1} at 6 bars. At O_2 flowrates > 15 mL min^{-1} an annular flow was observed. There are many factors crucial for the stability of segmented flow [198]. Most important among them are the configuration of gas injector, geometric changes in the channel, such as bends, and spatial variation of the surface roughness and the microchannel cross-section. In the current study a simple *t*-connector was used as an O_2 injector for the formation of gas-liquid flow inside the Teflon tubing. The obtained segmented flow was then introduced into rectangular meandering microchannel *via* tight compression fitting connection. As a consequence, variations in bubble lengths in the obtained flow were up to 30-40 % of the bubble length.

At the elevated O_2 pressures in the range of gas flowrates between 1-10 mL min^{-1} pulsations of the two-phase flow were observed. This phenomenon, known as 'pulsed

flow', was extensively studied due to its importance in operation of the industrial three-phase gas-liquid trickle-bed reactors [199, 200]. Pulsing behaviour is explained by the formation of global convective instability in a system. The conditions of the transition from trickle-flow to pulsed flow are determined by densities, viscosities and surface tensions of the gas and the liquid, as well as by the internal structure and the material of the bed (in our case by the internal structure of cartridges used in the back pressure regulator). The specially designed high-precision backpressure regulators suit better for operation of microreactors in segmented gas-liquid flow regime without the pulsations [201]. However, these regulators are rather expensive and it is therefore useful to develop some simple and cheap alternatives.

It was found that pulsations of segmented flow at high pressures of O_2 can be significantly reduced by using 1/16" Teflon tubing packed with *PSi* as a back-pressure regulator. However, further investigation of pulsed flow was not pursued, because the range of pulsed flows was outside the window of maximum performance of the microreactor.

It was found that conversion of α-pinene increased with a decrease in the flowrate of O_2 in the range of pressures studied (1-52 bar), see **Figure 4.9**, *a*. This is explained by the shortening of a total residence time, $\tau_T=V_R/(u_G+u_L)$ and smaller liquid holdup, $\beta_L=u_L/(u_G+u_L)$. The apparent O_2 flowrate, u_G can be expressed as a function of O_2 pressure from the mass balance equation (4.7), taking into account the amount of dissolved O_2 at a given gas pressure, $P \cdot H \cdot u_L$.

$$\frac{P_0}{RT}u_G^0 = \frac{P}{RT}u_G + PHu_L \qquad (4.7)$$

Here P is O_2 pressure, P_0 = 1 atm, $\overline{R}$ is ideal gas constant, T is temperature, u_G^0 and u_L are the actual volumetric flowrates of O_2 and liquid phase, H is Henry constant (H=8.8×10^{-3} M atm^{-1} for CH_2Cl_2 [194]).

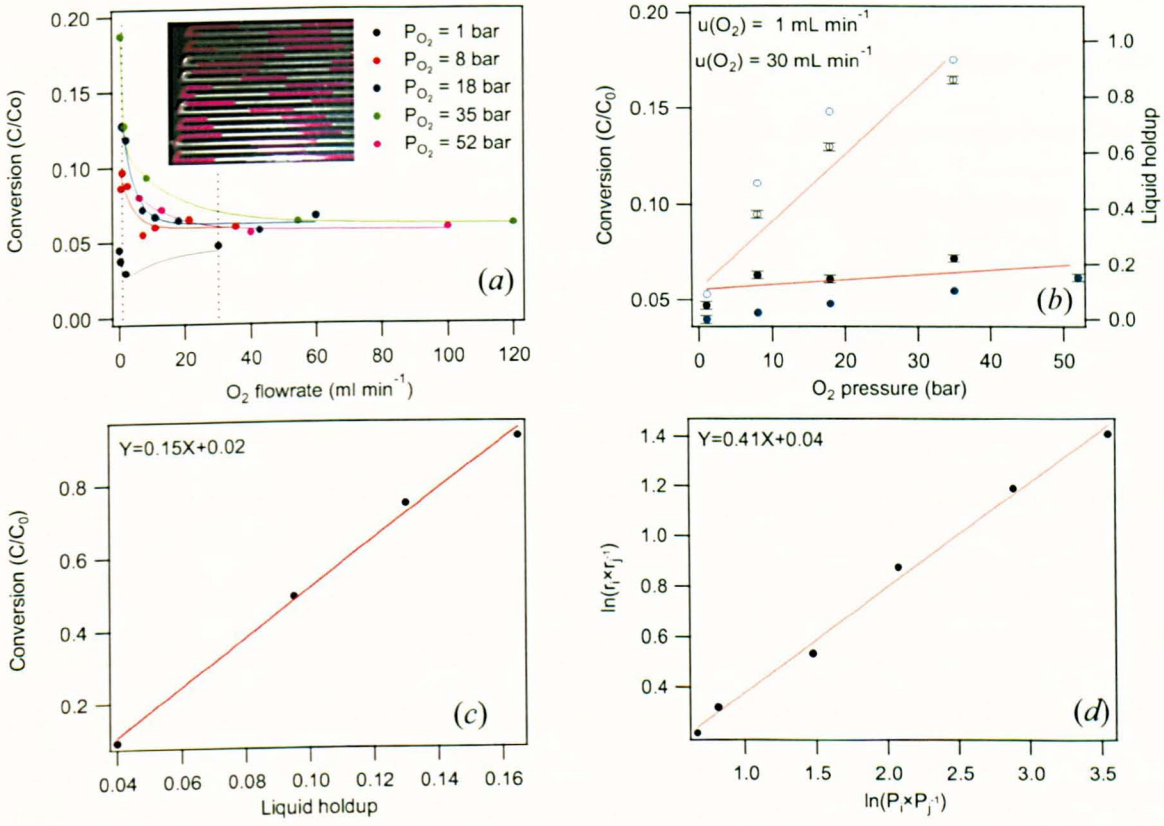

Figure 4.9. A summary of performance of the microreactor operated in a gas-liquid segmented flow mode. (*a*) Conversion of α-pinene (3.6×10^{-1} M) to pinocarvone in the gas-liquid segmented flow *vs.* actual O_2 flowrate at different gas pressures (1, 8, 18, 35, 52 bar). Vertical dotted lines are at 1 and 30 mL min^{-1}. Inset: photo of gas-liquid segmented flow in the microchannel. (*b*) Conversion and liquid holdup *vs.* O_2 pressure for the actual gas flowrates of 1 mL min^{-1} (○) and 30 mL min^{-1} (●), black circles are for conversion, blue are for liquid holdup. (*c*) The dependence of conversion on the liquid holdup. (*d*) The reaction order with respect to O_2 pressure. Solvent is CH_2Cl_2, concentration of *TPP* is 8.1×10^{-4} M, the liquid flowrate is 100 μL min^{-1}, the 416 nm LED array was used for illumination, T = 20 °C.

The conversion (and therefore, quantum yield of reaction) is proportional to O_2 pressure at low flowrates of O_2 while at the high gas flowrates it becomes virtually independent of pressure (**Figure 4.9**, *b*, **Table 4.10**) and governed by the total residence time and liquid holdup. **Figure 4.9**, *b*, *c* show that conversion of α-pinene is proportional to the liquid holdup. The formal reaction order for O_2 pressure of 0.4±0.1 extracted from the experimental data (**Figure 4.9**, *d*) is lower than that found in the homogeneous conditions (0.7±0.2) using pre-saturation of the reaction mixtures by O_2. This may indicate mass-transfer limitations due to slow diffusion of O_2 from gas bubble to the liquid media.

The region of O_2 flowrates below 1 mL min^{-1} was studied in more detail at a fixed O_2 pressure of 2 bar and different liquid flowrates in order to determine optimal conditions for oxygenation of α-pinene. A more powerful 250 W metal halide lamp was used for illumination of the microreactor. It was expected that the lamp will allow obtaining higher conversions. However, the intensity of the absorbed photons estimated using the actinometry data was found to be about 3.6×10^{-3} Einst L^{-1} s^{-1} which is only twice higher than that obtained for the 416 nm LED array (1.9×10^{-3} Einst L^{-1} s^{-1}) (see **Experimental** and **Appendix A**). Such a low value found in the case of the 250 W metal halide lamp is explained by the inefficient lamp-reactor geometry and about 1.6 times longer distance between the lamp and the microreactor. The lamp emits light in all directions and only a small part of the total flux of photons illuminates the reactor while most of the photons are wasted. An improvement in light utilization can be achieved only if the lamp is used for the illumination of several microreactors situated in a circular geometry around the lamp. This example again demonstrates the benefit of using LEDs in photochemical applications which stems from their flexibility in terms of arrangement with the reactors, together with high intensity of the emitted light and low power consumption.

The consumption of O_2 during the oxygenation of α-pinene was regulated using visual monitoring of the disappearance of O_2 bubbles inside the microchannel. It was found that for the fixed liquid flowrate at low gas flowrates the conversion of α-pinene varies in a linear manner as a function of the O_2 flowrate, *i.e.* the reaction is limited by the supply of O_2 (**Figure 4.10**, *a*). For the higher rates of O_2 flow, the α-pinene conversion reaches a maximum and then decreases due to the shortening of the total residence time. A similar behaviour was observed in a gas-liquid-solid catalytic oxidation of benzyl alcohol in a compact multichannel reactor and in the hydrogenation of methylstyrene in monolith reactors [202, 203]. The maximum of the α-pinene conversion for each particular liquid flowrate corresponds to complete disappearance of gas bubbles at the outlet of the microchannel due to consumption of O_2 in the reaction. At these conditions the microreactor operates at its maximum performance.

A decrease in the liquid flowrate results in higher conversions of α-pinene but, at the same time, the rate of reaction (or productivity, expressed in mol s^{-1}) becomes lower (see **Table 4.10**). Higher conversions are explained by the longer total residence times while a decrease in the rate of gas-liquid mass transfer and smaller gas and liquid holdups (and therefore, smaller amounts of α-pinene and O_2 available for oxygenation per unit time) lead to lower reaction rates [202-204]. It is worth mentioning that the rates of reaction are close to or even higher than these obtained in the annular and immersed-well reactors due to better light utilization in the microreactor (see for comparison **Table 4.1** and **Table 4.10**).

Figure 4.10, *b* represents the observed correlations between productivity and the amounts of available α-pinene and O_2 versus total residence time τ_T calculated for the conditions of complete consumption of O_2. These data suggest that using 5 identical microreactor units

connected in series (providing a 5-times longer single reaction channel) with independent supply of each unit by O_2 (similar to staged injection of O_2 along the length of the microchannel applied in [202]) in the regime of low conversions is more efficient in terms of productivity than the same 5 microreactors connected in parallel with the flowrates adjusted to obtain 100 % conversions in each microreactor unit.

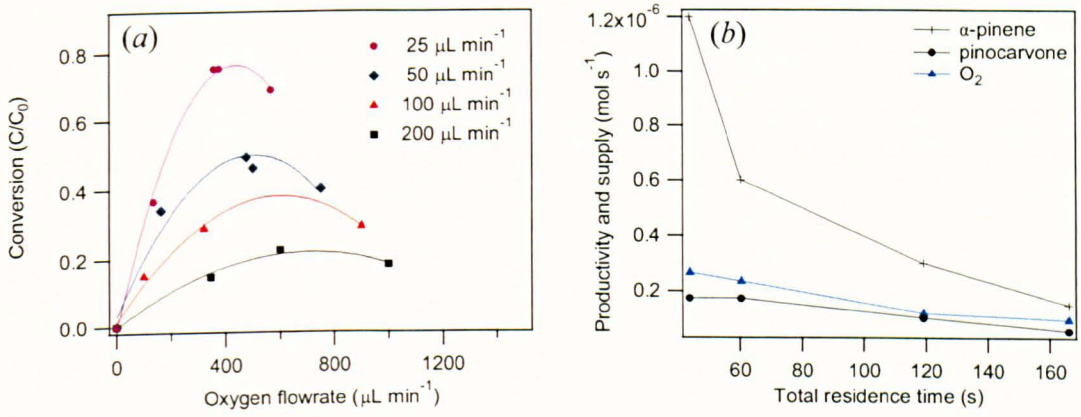

Figure 4.10. Dependence of α-pinene conversion (C_0=3.6×10^{-1} M) to pinocarvone on the flowrate of O_2 at different flowrates of the reaction mixture (*a*). Correlations of the productivity with the amounts of available O_2 and α-pinene *vs.* total residence time (*b*).

Table 4.10. Oxygenation of α-pinene carried out in the microreactor in segmented flow mode illuminated by the 416 nm LED array at different O_2 pressures with fixed flowrates of O_2 and reaction mixture (u_G=1 mL min^{-1}, u_L=100 μL^{-1} min^{-1}) and illuminated by the 250 W metal halide lamp at various u_L and fixed P. Values of u_G are taken at maximum performance of the microreactor.

Lamp	P, (bar)/ u_L, (μL^{-1} min^{-1})/ u_G, (μL^{-1} min^{-1})	I_a (Einst L^{-1} s^{-1})	r_0^R, (mol L^{-1} s^{-1})	ϕ_R
416 nm LED	1.0/100/1000	1.9×10^{-3}	1.0×10^{-4}	0.053
416 nm LED	8.0/100/1000	1.9×10^{-3}	2.4×10^{-4}	0.125
416 nm LED	18.0/100/1000	1.9×10^{-3}	3.3×10^{-4}	0.171
416 nm LED	35.0/100/1000	1.9×10^{-3}	4.1×10^{-4}	0.217
250 W MH	2.0/25/436	3.6×10^{-3}	4.9×10^{-4}	0.136
250 W MH	2.0/50/503	3.6×10^{-3}	6.2×10^{-4}	0.172
250 W MH	2.0/100/605	3.6×10^{-3}	9.5×10^{-4}	0.263
250 W MH	2.0/200/716	3.6×10^{-3}	1.1×10^{-3}	0.306

It is worth to compare different types of photoreactors in terms of productivity (in moles of α-pinene per unit of time). Productivity was calculated as $X_P(t_i) \times R_0 \times V_\Sigma \times t_i^{-1}$ or $X_P(t_i) \times R_0 \times u_L$ in the cases of the recirculating and the continuous modes of operation, respectively (see **Figure 4.11**). One can see from these data that productivity is decreasing with the increase in the residence time for the recirculating reactors while it is constant for the reactors operating in a continuous mode. Although the productivities of a single microreactor unit are 3-7 times lower than these estimated for the annular recirculating and the immersed-well reactors the quantum yields of α-pinene oxygenation are mostly similar or higher in the case of the microreactor, due to better utilization of light in the reaction.

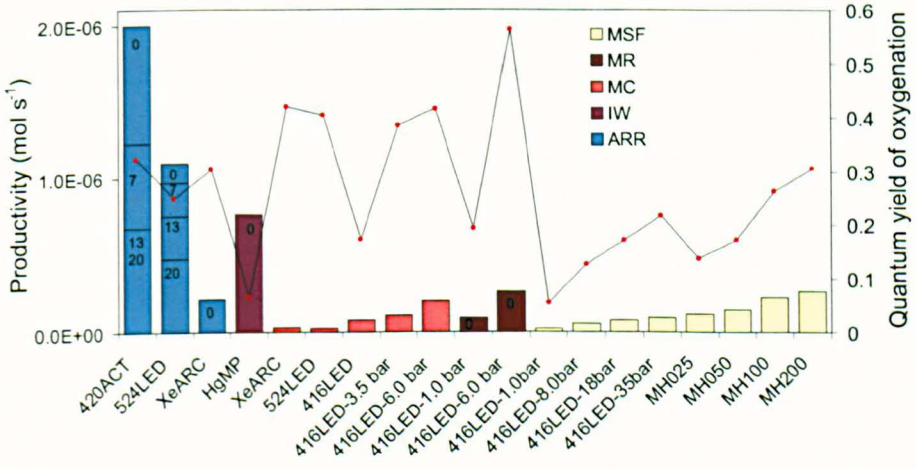

Figure 4.11. Maximum productivity of different types of photoreactors (moles of α-pinene per second) tested at different conditions (various sources of light, O_2 pressures, flowrates, modes of operation). ARR is annular recirculating reactor, IW is immersing well reactor, MR-C, MR-R and MR-SF represent the microreactor operating in a continuous, recirculating and the segmented flow modes. 420ACT is 420 nm actinic lamp, MH is metal halide lamp. Numbers represent the liquid flowrates in μL min^{-1}. Red dots represent quantum yields of α-pinene oxygenation at the specified conditions and correspond to the right axis.

4.2.3. Oxygenation of ACHA in the microreactor

Oxygenation of *TMS* derivative of *ACHA* in the microreactor was tested first in the continuous mode with continuous pre-saturation of the reaction mixture by O_2 in a tank at atmospheric pressure. The 416 nm and the 524 nm LED arrays were used for illumination of the microreactor. The initial concentration of *ACHA* (4.3×10^{-3} M) used in the experiments is two times lower than the concentration of the O_2 dissolved in CH_2Cl_2 at atmospheric pressure (8.8×10^{-3} M). Therefore, potentially, all the *ACHA* may be oxidized in the microreactor. However, only about 25 % of *ACHA* was transformed into the products **1-4**, which correspond to about 9 % conversions towards **2** under both the 524 and the 416 nm LED arrays illumination (**Figure 4.12**, *a*, *b*). This may be attributed to a low reaction rate constant (estimated value is about 4.9×10^{2} L mol^{-1} s^{-1}), low initial concentration of *ACHA* and the diffusion of O_2 through the walls of Teflon tubes at long residence times.

The oxygenation of *ACHA* was also carried out in the recirculating mode using segmented gas-liquid flow at 2 bar of O_2 pressure (4 and 1 mL min^{-1} for O_2 and liquid flows correspondingly). Temperature of the microreactor was kept at 10 °C. The 250 W metal halide lamp was applied for the illumination of the microreactor. The kinetic curves of oxygenation of *ACHA* are shown in **Figure 4.12**, *c*. It was found that the rates of product accumulation differ about 4 times for the annular recirculating reactor and the microreactor in the recirculating mode (1.2×10^{-8} and 3.4×10^{-9} mol L^{-1} s^{-1} correspondingly) while the rate of reaction is about 10 times higher in the case of the microreactor due to better light utilisation (**Table 4.11**). Reaction rates and quantum yields evaluated for the microreactor operated in the continuous mode also significantly surpass these for the annular recirculating reactor.

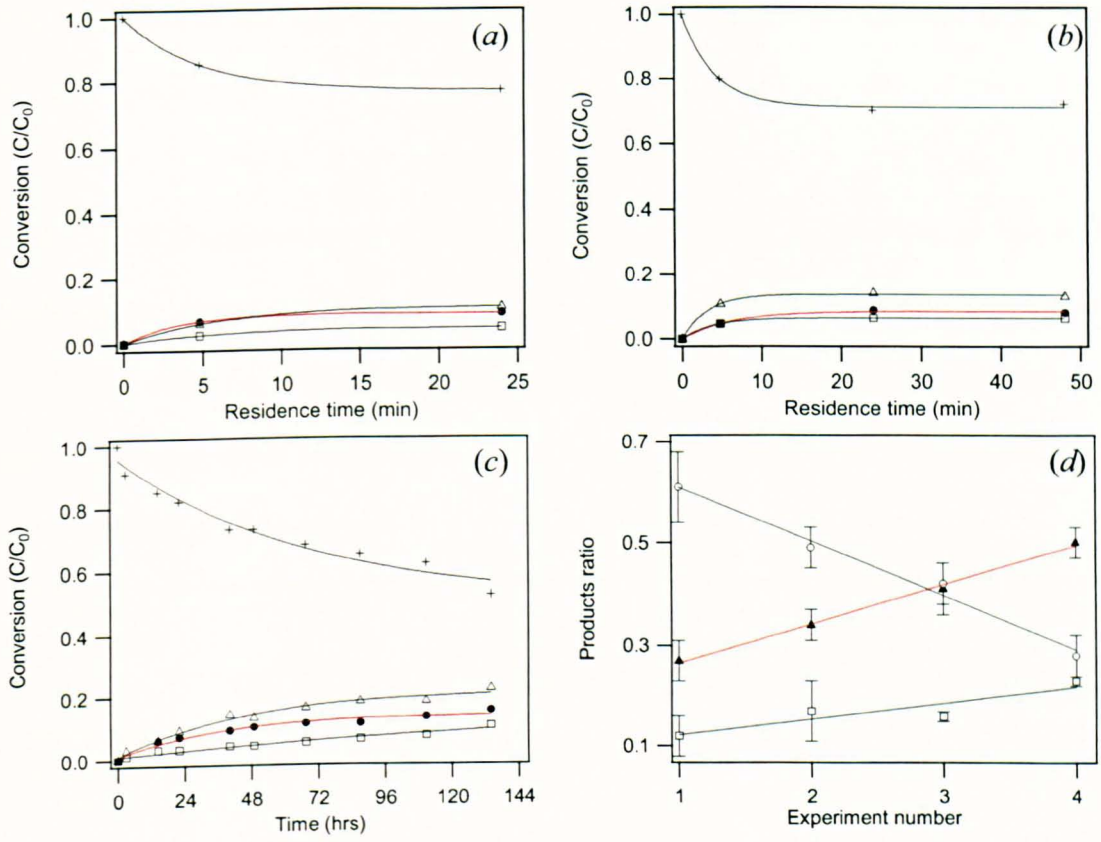

Figure 4.12. Oxygenation of *ACHA* (4.3×10^{-3} M) in the microreactor, (*a*) and (*b*) in continuous mode with O_2 presaturation of the reaction mixture under the 416 nm LED and the 524 nm LED illumination correspondingly, T = 20 °C; (*c*) in the recirculating mode and the segmented gas-liquid flow under the 250 W metal halide lamp illumination, liquid flowrate is 2 mL min^{-1}, O_2 flowrate is 4 mL min^{-1}, T = 10 °C. (*d*) The ratio of products distribution in different experiments performed. 1 corresponds to the experiment in the annular recirculating reactor with the 420 nm actinic lamp, 2, 3, and 4 correspond to the experiments (*c*), (*a*) and (*b*) respectively.

Together with the higher reaction rates and quantum yields of oxidation of *ACHA*, the microreactor operated in the continuous and the recirculating modes demonstrated better selectivity towards **2** compared to the annular reactor (**Figure 4.12**, *d*). The selectivity slightly increases in the case of the continuous mode of operation. This fact can be explained by a lower residence time spent in the reactor when probability of side

reactions, such as hydrolysis of *TMS* directing group leading to the decrease in selectivity, is less.

Table 4.11. Oxygenation of a *TMS* derivative of *ACHA* carried out in the annular recirculating reactor (u_G=30 mL^{-1} min^{-1}, u_L=40 mL^{-1} min^{-1}), in the microreactor in the continuous mode (u_L=50 μL^{-1} min^{-1}) with O_2 pre-saturation of the reaction mixture and in the recirculating mode (u_L=1000 μL^{-1} min^{-1}) in gas-liquid segmented flow (u_G=4000 μL^{-1} min^{-1}) at 2 bar of O_2 pressure.

Reactor (mode)	Lamp	I_a (Einst L^{-1} s^{-1})	r_0^T, (mol L^{-1} s^{-1})	r_0^R, (mol L^{-1} s^{-1})	ϕ_R
Annular (recirculating)	420 nm actinic	5.7×10^{-4}	1.2×10^{-8}	1.1×10^{-7}	1.9×10^{-4}
Microreactor (continuous)	416 nm LED	1.9×10^{-3}	-	9.9×10^{-7}	5.2×10^{-4}
	524 nm LED	3.2×10^{-4}	-	7.0×10^{-7}	2.2×10^{-3}
Microreactor (recirculating)	250 W MH	2.1×10^{-3}	3.4×10^{-9}	1.4×10^{-6}	6.7×10^{-4}

4.2.4. Factors influencing the efficiency of oxygenation of allylic substrates by $^1O_2$

Efficient photosensitized oxygenation of allylic compounds by $^1O_2$ in photoreactors requires complex optimisation of several main factors. These are: (i) the geometry and materials of construction of a photoreactor, (ii) intensity, spectral composition and type of the light source used, (iii) the lamp-reactor geometry used, (iv) concentration, photostability and quantum yield of a photosensitizer, (v) saturation of reaction solution by O_2, (vi) the rate of heat exchange, and (vii) potential for reuse of a photosensitizer. Summarizing all the available data it is possible to propose some simple design rules in order to develop efficient and safe photoreactors for photochemical applications and, in particular, for oxygenation of allylic compounds by photogenerated $^1O_2$.

Quantum yield of oxygenation is highest in the case of narrow reaction layers due to

better utilization of light in a reaction. The rate of reaction depends on concentration of the exited triplet states which is a function of the photosensitizer concentration and flux of photons. According to Lambert-Beer equation, the smaller the depth of a reaction layer, the higher the concentration of a photosensitizer is required for complete absorption of the incident light by the reaction layer. Therefore, the minimal depth of a microchannel is restricted by the solubility of a photosensitizer in a particular solvent. Moreover, high concentrations of photosensitizers close to the limit of their solubility may diminish concentration of $^1O_2$ in solution due to quenching. The optimal depth of the microchannel estimated for the case of 10^{-3} M *TPP* and the 416 nm LED array is in the order of 150-300 microns.

The residence time in the reactor is proportional to the length of the microchannel. A longer microchannel in a single microreactor unit provides higher conversion. Therefore an optimal packing of a meandering microchannel should provide maximum ratio of the illuminated area of a microchannel to the illuminated area of a microreactor unit.

Materials of the photoreactor and the type of assembly are also of a great significance. For example, many polymer materials as well as adhesives used in sealing of microreactor parts are not suitable as they cannot withstand elevated temperatures, pressures or organic solvents. The anodically bonded glass and glass-to-silicon photoreactors with etched densly packed meandering microchannels are simple and reliable devices which are capable of withstanding high temperatures, pressures and most common solvents.

The intensity and spectral composition of a light source used for illumination of photoreactors are also crucial for efficient oxygenation by $^1O_2$. As it was shown earlier, the rate of oxygenation is proportional to the intensity of the absorbed light. Therefore, it is necessary to use light sources of high intensity for better productivity of the photoreactor. Sources of polychromatic (white) light are useful in the case of screening a suitable photo-stable sensitizer with high quantum yield of $^1O_2$ generation. However, monochromatic sources of light matching certain absorption band of a photosensitizer are more preferable if the photosensitizer is already chosen. It is easy to obtain more than 99 % of light absorption because the amount of the absorbed photons is regulated by concentration of a photosensitizer according to Lambert-Beer relation. High internal efficiency of power-to-light conversion and long lifetime of a light source also increase the overall efficiency of a system.

The lamp-reactor geometry should also be optimized to provide the maximum possible utilization of light. The flux of photons from a light source is inversely proportional to the square of the distance from the light source. Therefore, the shortest possible distances are essential for better light utilization. The compact LED bulbs are the most suitable light sources because they can be arranged very efficiently with virtually any reactor geometry. Mono- and polychromatic high-power LED arrays (100-300 W are already commercially available, **Figure 4.13**, *a*, *b*) are ideally suited to flat microreactor units. In this case the best utilization of light is achieved in a stacking geometry (**Figure 4.13**, *c*). Specially designed LED arrays tailored to the geometry of a microchannel would give an additional improvement to the overall efficiency. High-power LED arrays require efficient cooling to increase light output and to increase stability. Therefore, heat exchangers should be integrated into the system to provide efficient cooling of the LED arrays and the microreactor units in order to keep the desired temperature of reaction and to prevent

damage of the LED arrays. Heat management will play an increasingly important role with the increasing power of LED arrays used for illumination.

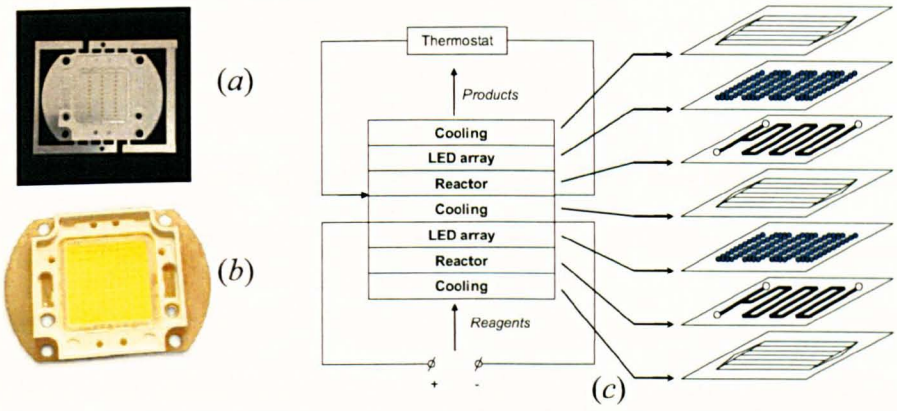

Figure 4.13. Photographic images of commercially available mono- (*a*) and polychromatic (*b*) high-power LED arrays of 100 and 300 W. A proposed scheme of a sandwich-type multilayer module comprised of several flat glass-to-silicon microreactor units with the integrated LED arrays and heat exchangers for homogeneous or heterogeneous oxygenation reactions (*c*).

A problem of saturation of the reaction mixture with O_2 is another important issue crucial for both safety and efficiency of oxygenation. Present study have shown that concentration of dissolved O_2, controlled by the nature of solvent, composition of the reaction mixture used and O_2 pressure, directly influences the rate of oxygenation. However, highly explosive hydrocarbon vapor/O_2 mixtures can form in the reservoir during saturation of the reaction mixture by O_2 *via* bubbling. The hazard of explosion significantly increases with the increase in O_2 pressure.

Oxygenation in a microreactor using gas-liquid segmented flow mode resolves this contradiction. Short quenching distances for radicals in the small volumes of gas bubbles inside a microchannel allow safe operation even at elevated O_2 pressures (in this study oxygenation of α-pinene was carried out at O_2 pressures up to 52 bar), while

a meandering geometry of microchannel provides efficient internal mixing. Establishing such reaction conditions that all O_2 fed at the reaction inlet is consumed in the reactor increases safety of oxygenation.

Oxygenation of α-pinene and *ACHA* in the microreactor in a continuous mode using segmented gas-liquid flow also revealed that operation at short total residence times is more efficient in terms of productivity and selectivity. Therefore, a long-enough reaction channel (or several microreactors connected in series) with staged injection of O_2 along the length of the microchannel is preferable in order to increase the productivity of the reactor while the microreactors connected in parralel will improve the selectivity of oxygenation.

Finally, a common drawback of all the photochemical processes using dissolved photosensitizers is that the photosensitizer is not reusable. Contrary to that, heterogeneous photosensitizers are suitable for multiple use since they can easily be separated from the reaction mixture by filtration, or can be immobilized directly onto the walls of a photoreactor. Novel heterogeneous photosensitizing nanomaterials based on *PSi* look very promising for the applications with the glass-to-silicon anodically bonded microreactors. Nanocrystals of *PSi* can be easily prepared in the form of films inside a microreactor by etching the walls of a *Si* microchannel in *HF*-containing mixtures. Therefore, the following two chapters are devoted to the investigation of the applicability of $^1O_2$ photosensitizers based on *PSi* in oxygenation of allylic compounds.

4.3. HETEROGENEOUS $^1O_2$ PHOTOSENSITIZERS BASED ON POROUS SILICON (PSi)

4.3.1. Photodegradation of DPBF

Following recent studies [23, 33] the ability of *PSi* to substitute the common dye photosensitizers in generation of $^1O_2$ was investigated in more details. As in the earlier work [23], *DPBF* was chosen as an $^1O_2$ trap. This compound easily undergoes a 1,4-cycloaddition reaction with $^1O_2$ molecules forming an endoperoxide (an overall reaction constant, $k_R' = 8\times10^8$ L mol^{-1} s^{-1} [205]), which decomposes irreversibly yielding the product 1,2-dibenzoylbenzene, equation (4.8) [33, 85].

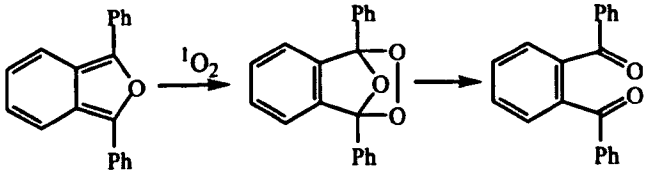

DPBF 1,2-dibenzoylbenzene (4.8)

Figure 4.14 shows results of the *DPBF* photodegradation experiments performed in the annular recirculating reactor in N_2- and O_2-saturated *F113* containing dispersed *PSi*, under dark conditions and under the 524 nm LED lamp illumination. The concentration of *DPBF* did not change without illumination either in N_2 or O_2 ambience. Also, no photobleaching of *DPBF* was observed under the LED lamp illumination in the abcence of *PSi*. A small decrease in the concentration of *DPBF* was found under irradiation of N_2-saturated suspensions of *PSi* by the LED lamp. The same effect was reported earlier, and was explained by direct electronic interaction between triplet excited states of *Si* nanocrystals and *DPBF* [23, 33, 85]. This process is also known as Type I photosensitized oxidation, taking place due to donation and acceptance of protons or electrons which results in the formation of free-radical ions. An alternative pathway of oxidation is by the photosensitised $^1O_2$ (Type II pathway) which can also lead to degradation of organic compounds [98]. Type II process is dependent on the concentration of O_2 molecules in solution. If a solution is O_2-

depleted, the shift from Type II to Type I mechanism is favourable. The observed photodegradation of *DPBF* can also be partly related to an incomplete replacement of O_2 by N_2 after bubbling of N_2, or to the presence of physisorbed O_2 on the surface of *PSi* as it was mentioned earlier [23].

When *PSi* was dispersed in an O_2-saturated solution and exposed to the LEDs illumination for several hours, a linear decrease in *DPBF* concentration was observed. This indicates stability of *PSi* photosensitizer during photodegradation of *DPBF*. In contrast to results obtained in [23] this study demonstrated that photodegradation rate of *DPBF* is independent of the O_2 flow rate. The initial rate of *DPBF* photobleaching in the reaction tank was found to be about 5.0×10^{-8} mol L s^{-1}. The reaction rate inside the annular photoreactor recalculated from this number was found to be 1.3×10^{-6} mol L s^{-1}. Despite the more than double the number of the LEDs used (240 versus 96 LEDs), or a five fold increase in the amount of absorbed photons (4.4×10^{-6} Einst s^{-1} *vs.* 8.3×10^{-7} Einst s^{-1}) the *DPBF* photodegradation rates in the current study and in [23] are nearly equal (1.3×10^{-6} mol L s^{-1} *vs.* 1.2×10^{-6} mol L^{-1} s^{-1}) (see **Figure 4.14**, *a*, *b*). This result is explained if the limiting step in the *PSi*-mediated *DPBF* photobleaching is absorption of photons and the formation of excitons in *PSi*, which is coincident with the observed zero-order kinetics of *DPBF* photodegradation.

In order to characterise performance of *DPBF* photobleaching in a particular reactor the authors used the term "quantum yield of chemical reaction" defined as a ratio of the rate of photobleaching of *DPBF* to the rate of $^1O_2$ generation [23]. However, this term corresponds to the utilisation of $^1O_2$ in the reaction but not the real efficiency of a photoreactor in the photobleaching process. For this purpose it is better to use the generally accepted overall quantum yield, especially when the mechanism of the

photobleaching process is not clear, as in the case of *PSi*.

Using the number of absorbed photons obtained from the actinometry data (see **Appendix A**) and the initial rate of *DPBF* photodegradation the overall quantum yield of *DPBF* photodegradation was found to be 3.0×10^{-3}, which is five times lower compared to 1.4×10^{-2} re-calculated using the data from reference [23]. The obtained data suggest that photobleaching of *DPBF* mediated by *PSi* is not as efficient as it was reported earlier. Moreover, the data leave doubt over the specific mechanisms involved in *PSi*-mediated photodegradation of *DPBF* which will be discussed further.

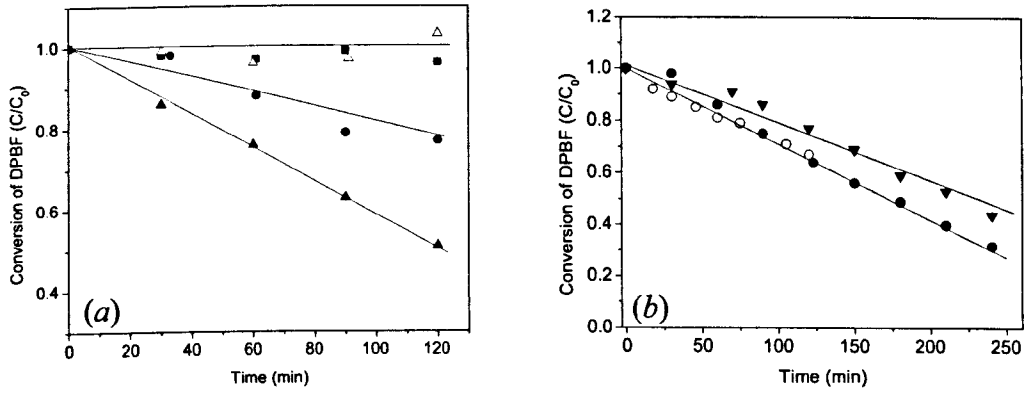

Figure 4.14. Photodegradation of 10^{-3} M solution of *DPBF* in *F113* containing 0.2 % wt dispersed *PSi* (250 mL) performed in a recirculating annular reactor and measured by monitoring of the intensity of absorbance at 410 nm in a 1 cm quartz cell. (*a*) N_2 (○, ■) and O_2 (Δ, ▲) saturated solutions under LEDs illumination (Δ, ○) and in dark (▲, ■), N_2 and O_2 flow rates are 30 mL min^{-1}; (*b*) oxygen flow rate influence on oxidation, ○ 30 mL min^{-1}, • 50 mL min^{-1}, ▼ data from ref. [23] (O_2 flowrate is 50 mL min^{-1}). Reactor temperature is 20 °C, the liquid flowrate is 40 mL min^{-1}.

4.3.2. Oxygenation of α-pinene

PSi was also tested as $^1O_2$ photosensitizer in the oxygenation of α-pinene to pinocarvone in both, batch and flow conditions. However, there was no conversion at all either in the immersed-well quartz reactor with different amounts of *PSi* (0.2 and 0.02 % wt) suspended in CH_2Cl_2 or in CCl_4 after 7 hours of illumination by a 125 W *Hg* lamp, or in the annular recirculating reactor for all the different types of *PSi* used: *PSi*, PSi^I, and PSi^{II} (see **Table 4.12**) even after 24 hours of illumination by a *Xe* arc or an LED lamp. In the experiments with *PSi* in CCl_4, and also with PSi^I, and PSi^{II} a change of color of *PSi* was observed, which was interpreted as oxidation of the *PSi* powder.

Table 4.12. A summary of α-pinene photooxidation experiments performed in the immersed-well reactor under a *Hg* lamp illumination and in the flow reactor under the LED and *Xe* lamp illumination. O_2 flow rate was 30 mL min^{-1}, T = 20 °C, the liquid flow rate was 40 mL min^{-1}.

Reactor	Lamp	Solvent	Amount of PSi, % wt.	Conversion (Time), % (h)
Immersing well	Hg med. press	CH_2Cl_2	0.2	0 (7)
		CH_2Cl_2	0.02	0 (7)
		CCl_4	0.02	0 (7)
Annular recirculating	524 nm LED	F113	0.2	0 (6)
		F113	0.2[a]	0 (24)
		F113	0.2[b]	0 (24)
	Xe arc	CH_2Cl_2	0.2	0 (23.4)

[a]-PSi^I, [b]- PSi^{II}

4.3.3. Quenching of excitons confined in PSi by organic molecules

It is known that apart from the quenching of excitons confined in *Si* nanocrystals by O_2, another possible deactivation pathway is direct quenching of excitons by various organic molecules [95, 206, 207]. Therefore, in order to clarify the reasons for the observed inefficiency of *PSi* as $^1O_2$ sensitizer it was decided first to check the quenching of *PSi* PL (suspensions of 1.1 % wt in CH_2Cl_2) by *DPBF*, α-pinene, or α-pinene reaction mixture with co-reactants during gradual addition of the corresponding compounds. In the case of

DPBF and α-pinene mixture, about 0.7 and 30 mM concentrations respectively are sufficient to quench all the excitons which would, otherwise, lead to the formation of $^1O_2$ states (see **Figure 4.15**, *a*, *b*). Since the energy of the triplet state of *DPBF* lies about 1.48 eV above the ground state and almost all photoexcited excitons in *Si* nanocrystals have energies above this value, this process is favorable [208]. Quenching of *PSi* PL by the α-pinene reaction mixture is explained by the presence of pyridine and *DMAP* in the mixture, which are known as efficient quenchers of *PSi* PL even in micromolar concentrations [206, 207].

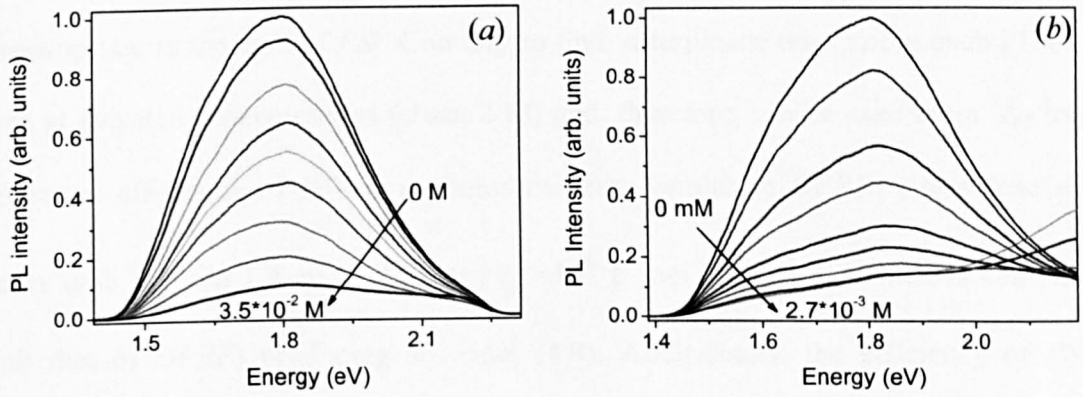

Figure 4.15. PL spectra of 0.9 % wt. *PSi* powder dispersed in CH_2Cl_2, containing various concentrations of quencher. (*a*) α-pinene reaction mixture; concentrations from top to the bottom: 0, 38, 110, 380, 940 μM, 3.3, 14, 29, 35 mM. (*b*) *DPBF*, concentrations from top to the bottom: 0, 35, 70, 100, 210, 350, 700 μM, 1.7, 2.7 mM. Note, at high concentrations of *DPBF* its PL can be clearly seen in the spectral range of higher energies. $E_{ex.}$=2.54 eV, $I_{ex.}$=500 μW cm^{-2}.

At the elevated *DPBF* concentrations (about 0.8 mM) the increase in PL intensity in the high-energy side of the spectral range is caused by *DPBF* luminescence. At high concentrations it efficiently absorbs laser light and, therefore, luminesces stronger than *PSi*. *PSi* PL quenching means that if the mM concentrations of *DPBF* are used in

photobleaching experiments (for example, in [23]), the energy of almost all excitons is directly transferred to *DPBF* molecules. This process restricts formation of $^1O_2$ and the photobleaching of *DPBF* mainly takes place *via* a Type I pathway described above. In the case of pure α-pinene it was found that it does not quench *PSi* PL even at 2 M concentrations.

4.3.4. Oxygenation of α-terpinene

In the previous chapter it was shown that *DPBF* is a very efficient quencher of excitons confined in *PSi* even at micromolar concentrations. Therefore its use as a $^1O_2$ trap is inappropriate in the case of *PSi*. Contrary to that, α-terpinene does not quench PL of *PSi* even at elevated concentrations (about 2 M) and, therefore, can be used as an $^1O_2$ trap to determine efficiency of *PSi* as a photosensitizer. Similar to *DPBF*, α-terpinene easily reacts with $^1O_2$ *via* 1,4-cycloaddition ($k_R^{'}$ =10^8 L mol^{-1} s^{-1} [209], which is comparable with that of *DPBF*) producing ascaridol (4.9). Additionally, the efficiency of *PSi* in photooxidation of α-terpinene by $^1O_2$ was compared here with that of a conventional triplet dye $^1O_2$ photosensitizer tetraphenylporphine (*TPP*).

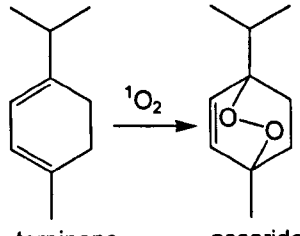

α-terpinene ascaridol (4.9)

From the NMR spectra obtained in the experiment with the conventional sensitizer *TPP* it was found that 15 % conversion of α-terpinene to ascaridol was achieved after 3.5 hours of illumination in the recirculating photoreactor (**Table 4.13**). In the case of the *PSi* sensitizer formation of ascaridol was not detected even after illumination for 24 hours. However, this does not mean that reaction does not take place at all, rather a more sensitive method of detection is required, for example, the direct measurement of $^1O_2$ PL by near-IR spectroscopy, described below. Another potential explanation of the lack of

ascaridol signal in NMR spectra is the feasibility of its sorption on the extended surface of *PSi*, especially as the reaction is very slow in the case of this sensitizer and the expected product concentrations are very small.

Table 4.13. Details of the α-terpinene photooxidation experiments performed in the annular continuous photoreactor under 525 nm LED and *Xe* arc lamps illumination. O_2 flow rate is 30 mL min^{-1}, $T = 20$ °C, liquid flowrate is 40 mL min^{-1}.

Reactor	Lamp	Solvent	Sensitizer	Comments
Annular	Xe arc	CH_2Cl_2	TPP (8.7×10^{-5} M)	Ascaridol / 3.5 hrs
recirculating	Xe arc	CH_2Cl_2	PSi (0.2 % wt)	No product / 23.4 hrs
	524 nm LED	F113	PSi (0.2 % wt)	No product / 6 hrs

In general, the rate of photooxidation depends on the bimolecular rate constant and on the steady-state concentration of $^1O_2$ in solution [54, 64]. In equilibrium the rate of $^1O_2$ generation, $\phi_{^1O_2} I_a$ equals the rate of its decay $k_D[^1O_2]$ and therefore steady state concentration of $^1O_2$ can be expressed as:

$$[^1O_2] = \frac{\phi_{^1O_2} I_a}{k_D} \tag{4.10}$$

Here $\phi_{^1O_2}$ is quantum yield of $^1O_2$ generation, I_a is the intensity of the absorbed light and k_D is the first order $^1O_2$ decay constant. In the presence of $^1O_2$ quencher R, steady state concentration of $^1O_2$ is reduced to:

$$[^1O_2] = \frac{\phi_{^1O_2} I_a}{(k_D + k_R'[R])} \tag{4.11}$$

Here k_R' is an overall rate constant for physical quenching and chemical reaction with $^1O_2$. Reduction in the steady state concentration of $^1O_2$ in solution can be detected as the decrease of $^1O_2$ PL emission intensity at 1270 nm (0.98 eV). Therefore, by using a more sensitive PL spectroscopy it is possible to monitor photooxidation of α-terpinene and compare the efficiencies of both sensitizers.

Measuring the intensity of $^1O_2$ PL during gradual addition of small amounts of α-terpinene to the suspensions of *PSi* (0.9 % wt in C_6F_6) it was found that 460 μM concentration of α-terpinene is sufficient to suppress $^1O_2$ PL almost completely (**Figure 4.16**). A decrease in $^1O_2$ PL (or, respectively, of $^1O_2$ steady state concentration) can take place either due to physical quenching or chemical reaction [56]. In the case of physical quenching, an addition of a specific amount of quencher will result in the corresponding constant level of PL suppression. On the contrary, if the chemical reaction path dominates, concentration of the reagent decreases with time, and consequently the level of $^1O_2$ PL quenching should be reduced. The corresponding experiment was done as seen in **Figure 4.17**.

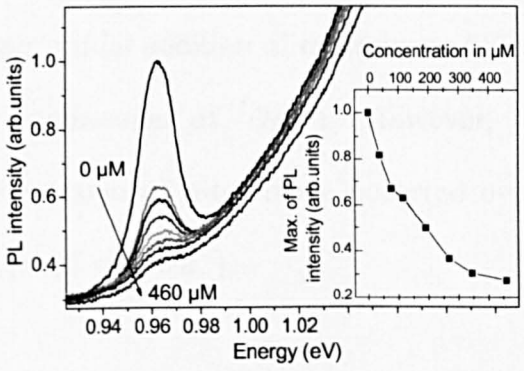

Figure 4.16. PL spectra of $^1O_2$ ($^1\Delta \rightarrow {}^3\Sigma$ decay transition) photogenerated by 0.9 % wt. of *PSi* powder in C_6F_6. α-terpinene was gradually added to the solution to obtain the following concentrations, from top to bottom: 0, 40, 75, 120, 200, 270, 350, 460 μM. Inset: evolution of the maximum of the $^1O_2$ luminescence *vs* α-terpinene concentration. The broad PL from *PSi* dangling bonds is subtracted in order to estimate the PL intensity of the $^1O_2$ emission line. $I_{ex.}$=30 mW cm^{-2}, $E_{ex.}$=2.54 eV.

Following the initial quenching of $^1O_2$ PL with 75 μM of α-terpinene, the PL intensity recovered almost completely over 40 min of illumination by an Ar^+ laser ($I_{ex.}$= 500 mW cm^{-2}). This indicates a chemical reaction between $^1O_2$ and α-terpinene. In **Figure**

4.17, *a* the PL signal without α-terpinene corresponds to the curve having the largest intensity, whereas the curve with the lowest intensity is recorded immediately after the addition of the reactant. The lines between these two limits from the bottom to the top clearly show recovery of $^1O_2$ luminescence after continuous illumination for 12, 21 and 40 minutes, respectively. This is easily seen in the inset in **Figure 4.17**, *a* showing the intensity of the $^1O_2$ PL as a function of time.

The corresponding experiment with a conventional sensitizer *TPP* is shown in **Figure 4.17** *b*. A similar ratio of the sensitizer to the reactant molecules was used (37 μM in C_6F_6). To estimate the similar amount of *TPP* we assumed that *PSi* is composed from nanocrystals with an average size of 5 nm acting as elementary absorbers. As in the case of the *PSi* sensitizer, initial addition of α-terpinene (30 mM concentration) leads to a nearly complete suppression of $^1O_2$ PL. However, in the case of the *TPP* sensitizer, complete conversion of α-terpinene occurred over 25 min using a much lower light intensity ($I_{ex.}$= 15 mW cm^{-2}).

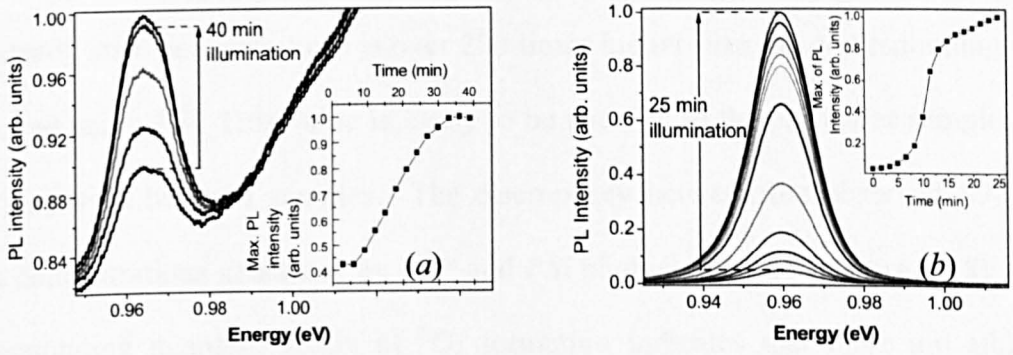

Figure 4.17. Time evolution of the $^1O_2$ PL spectra ($^1\Delta \rightarrow {}^3\Sigma$ decay transition) after initial addition of (*a*) 75 μM α-terpinene to 0.9 % wt. of *PSi* powder in C_6F_6, $I_{ex.}$= 500 mW cm^{-2}, $E_{ex.}$= 2.54 eV; (*b*) 30 mM of α-terpinene to 37 μM *TPP* in C_6F_6, $I_{ex.}$= 15 mW cm^{-2}, $E_{ex.}$= 2.54 eV. Insets: $^1O_2$ PL peak intensity as a function of time for the respective images. In the case of *PSi* the broad PL from *Si* defects was subtracted in order to estimate the *PL* intensity.

4.3.5. Factors influencing the efficiency of $^1O_2$ generation by PSi

The overall rate of $^1O_2$ generation mediated by *PSi* is a product of the intensity of absorbed light, quantum yield of long living photogenerated excitons and the efficiency of energy transfer from the photoexcited *Si* nanocrystals to O_2. Despite the high efficiency of the latter process, which is about 80 % [81], the overall efficiency of $^1O_2$ generation cannot exceed 0.05-0.1, because quantum yield of *PSi* PL (or the number of long living excitons created by light per number of absorbed photons) does not exceed this value [93]. Therefore, in the case of the *PSi* sensitizer the illumination time or intensity of light should be significantly increased to achieve the same conversion of α-terpinene to ascaridol as with *TPP*, having quantum yield of $^1O_2$ generation in the range of about 0.5-0.8 [54].

The efficiencies of $^1O_2$ formation mediated by both *PSi* and *TPP* were also directly compared. **Figure 4.18** shows that under similar illumination conditions and with a similar amount of primary absorbers in the reaction system the intensity of the emission peak from the $^1\Delta \rightarrow {}^3\Sigma$ transition of $^1O_2$ generated by *TPP* (and, therefore, $^1O_2$ steady state concentration) is over 200 times higher than the corresponding values achieved using *PSi*. This value is likely to be specific to the particular sample of *PSi* and may vary between samples. The discrepancy between the observed $^1O_2$ steady state concentrations generated by *TPP* and *PSi* photosensitizers (**Figure 4.18**) and the corresponding quantum yields of $^1O_2$ formation indicates that there are additional decay channels for $^1O_2$ in *PSi*, which are discussed below.

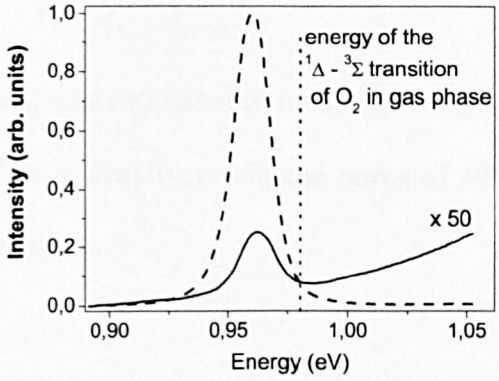

Figure 4.18. PL spectra of $^1O_2$ ($^1\Delta \rightarrow {}^3\Sigma$ decay transition) generated by 0.9 % wt. of *PSi* in CCl_4 (solid line) and 37 μM *TPP* (dashed line). Solid curve was multiplied by a factor of 50. Dotted vertical line indicates the energy of $^1O_2$ $^1\Delta \rightarrow {}^3\Sigma$ transition in the gas phase. $I_{ex.} = 15$ mW cm^{-2}, $E_{ex.} = 2.54$ eV.

As it was mentioned earlier, the steady state concentration of $^1O_2$ in the absence of added quenchers can be expressed by equation (4.10). If *TPP* is used as $^1O_2$ sensitizer, the $^1O_2$ decays mostly due to collisions with molecules of solvent, and therefore, decay constant k_D is determined only by the lifetime of $^1O_2$ in a particular solvent, τ_d. Physical quenching by *TPP* can be neglected due to its small concentration. In the case of *PSi* an additional term, given by the deactivation time of $^1O_2$ by the surface of *Si* nanocrystals, τ_q, contributes to the solvent-mediated quenching of $^1O_2$. It should be noted that the surface of *Si* nanocrystals is *H*-terminated and, due to high frequency of *Si-H* bonds oscillations, this surface can very efficiently quench $^1O_2$ molecules during collisions [56]. The total lifetime of $^1O_2$, τ_D, measured in suspensions of *PSi* (1 % wt) in C_6F_6 in the absence of other quenchers was found to be 3.9 ms [33]. Taking into account this value and the lifetime of $^1O_2$ in pure C_6F_6 (τ_d =25 ms [210]) it is possible to estimate the deactivation time of $^1O_2$ by the surface of *Si* nanocrystals, using equation (4.12):

$$\frac{1}{\tau_D} = \frac{1}{\tau_d} + \frac{1}{\tau_q} \tag{3.12}$$

Based on this equation τ_q was estimated to be about 4.9 ms. This value implies that 84 % of photogenerated $^1O_2$ is deactivated in the pores of *PSi* due to collisions with its hydrogenated internal surface.

It is worth mentioning that quenching of photoexcited excitons confined in *PSi* by O_2 may also lead to the formation of superoxide ion (O_2^-): O_2 is a very good electron acceptor and electrons can easily be donated by the excitons. Formation of superoxide ion competes with the $^1O_2$ generation and can also directly contribute to quenching of $^1O_2$ (estimated quenching constant of $^1O_2$ by O_2^- is about 10^{10} L mol^{-1} s^{-1}) [211]. This assumption explaines the appearence of an additional weak local spectral minimum at around 2 eV in the differential spectra of the PL quenching [81] and it also does not contradict the observed photodegradation of *DPBF* in the presence of *PSi*, as it is well known that *DPBF* also reacts with O_2^- *via* different routes [212, 213]. However, additional experiments have to be performed to unequivocally prove or disprove the hypothesis of O_2^- formation.

Figure 4.19 shows a general scheme of the main possible physical and chemical reaction channels in the system: *PSi* (photosensitizer), light (*hv*), solvent, molecule of reagent (*R*), and O_2. Despite simplifications the scheme can be applied for any sensitizer including *PSi*. Detailed scheme developed for dye senstizers can be found in [54].

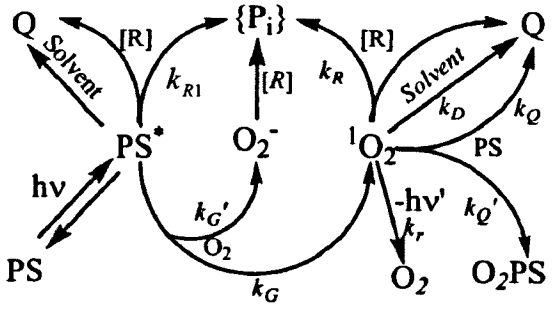

Figure 4.19. A schematic description of reaction pathways in the system containing photons, photosensitizer, solvent, O_2 and a reagent molecule (R). Details are in the text.

Electronic excitations of PSi^* in principle may be quenched by any acceptor to a different extent. Quenching by O_2 leads to $^1O_2$ or/and O_2^- with the rate constants k_G and k_G' respectively. R quenches the excited states in PSi^* physically, resulting in heat generation (Q), or chemically yielding different products $\{P_i\}$ with the rate constant k_{R1}. The generated $^1O_2$ is consumed either *via* radiative decay (k_r) or physical and chemical quenching by surrounding media (k_D), and by *PSi* with rate constants k_Q', k_Q yielding Q and oxidation of *PSi* correspondingly. Finally, oxygenation of R by $^1O_2$ with reaction constant k_R leads to the desired products of ene reaction. O_2^- quenches $^1O_2$, reacts with *PSi* and R. It is worth mentioning that different sets of products $\{P_i\}$ may be obtained in the reaction of R with $^1O_2$, O_2^- or *via* direct interaction with the photosensitizer. Also, some paths of this scheme can be more complex and could have different relative importance. For instance, in the case of *PSi* it was shown, that the contribution of degradation pathways of *DPBF* different from the $^1O_2$-mediated photooxidation plays a significant role in the total *DPBF* photobleaching process, while physical quenchng of $^1O_2$ by *H*-terminated surface is crucial in overall deactivation of $^1O_2$.

4.4. HETEROGENEOUS $^1O_2$ PHOTOSENSITIZERS BASED ON DYE-MODIFIED POROUS SILICON

4.4.1. FTIR characterization of the dye-modified PSi sensitizers

One of the key ideas of this project was to use *PSi* nanocrystals as a heterogeneous photosensitizer for generation of $^1O_2$. If successful, this approach towards generation of $^1O_2$ could be further realized in a novel design of glass-silicon photochemical microreactors with the imbedded layers of *PSi* formed by the chemical etching of the walls of the microchannel by *HF* mixtures. However, our studies clearly demonstrated that pure *PSi* nanocrystals are inefficient photosensitizers of $^1O_2$ generation due to low quantum yield of $^1O_2$ formation and due to quenching of $^1O_2$ by the *H*-terminated walls of pores.

In spite of this disadvantage *PSi* has one important feature: the *H*-terminated surface of the nanomaterial can be easily modified by immobilization of different functional molecules *via* hydrosilylation with the formation of stable *Si-C* bonds [214, 215]. Hydrosilylation of *H*-terminated *Si* and *PSi* surfaces was exploited for passivation of *Si* and *PSi* surfaces by the attached alkenes and manufacturing of bioarrays (see for example, review [216] and references therein), for the formation of the enzymatic catalytic surfaces [217] and bonding of the redox-active molecules (such as porphyrines and ferrocenes) functionalized for surface attachment for information storage devices [218, 219]. Therefore, in order to improve the photosensitizing properties of *PSi*, the functional nanomaterial can be modified by an appropriate efficient $^1O_2$ dye photosensitizer using hydrosilylation reaction with *H*-terminated *PSi* surface.

A commercially available tetra(4-allyloxy)phenylporphine photosensitizer with four terminal double bonds was chosen for this purpose. Thermal (T=108 °C), photo- (*Xe* arc

lamp illumination), and catalytic (H_2PtCl_6 and $AlCl_3$) activation were tested in this study (see **Experimental** for details).

All the samples (pure *PSi* and dye-modified *PSi* photosensitizers) were analyzed by FTIR spectroscopy (**Figure 4.20**). The spectrum of pure *PSi* powder exhibits two broad absorption bands at 2086 and 2251 cm^{-1}. First peak corresponds to the *Si-*H_x stretching modes (x=1-3), while second is assigned to the *O*-back-bonded *Si-H* species, $(O_2)SiH_2$ and $(O_3)SiH$ [217, 220]. Absorption bands at 625, 660, 840 and 880 cm^{-1} correspond to *Si-*H_x bending and rocking modes [217, 221]. The broad intensive peak with the maximum at 1073 cm^{-1} is attributed to *Si-O-R* symmetric stretching vibrations of partially oxidized *PSi* surface [222]. The modified *PSi* powders prepared *via* thermally, photo- and catalytically (H_2PtCl_6)-activated hydrosilylation of the dye to *PSi* demonstrated almost complete disappearance of *Si-*H_x absorption modes in FTIR spectra while in the case of $AlCl_3$-activated attachment of the dye to *PSi*, the *Si-*H_x bonds were left almost unchanged (see **Figure 4.20**, *a*). Absorption peak at 1606 cm^{-1} is attributed to *C=C* vibrations of the non-attached double bonds of the dye sensitizer [223]. The peak is broadened by the absorption band centered at 1626 cm^{-1} and can be related to molecular water [222, 224]. There were no distinct *Si-C* absorption bands found in FTIR spectra either at 680 cm^{-1} and in 750-870 cm^{-1} regions, nor at 1258 and 1458 cm^{-1} [215, 222, 225-228]. This fact may be explained by small IR absorption crossection and low concentration of *Si-C* bonds on the surface [229]. The differential spectra between FTIR spectrum of pure *PSi* and immobilized samples show disappearance of *Si-*H_x absorption bands at 625, 660, 840, 880, 2086 and 2251 cm^{-1} after immobilization of the dye (see **Figure 4.20**, *b*). The increase of absorption at 680, 875 cm^{-1}, and at 780 and 1458 cm^{-1} may be attributed to *Si-C* stretching and bending modes, correspondingly. The peaks situated at 805, 960-1035, 1175, and 1230 cm^{-1} are attributed to the absorption bands of the dye photosensitizer.

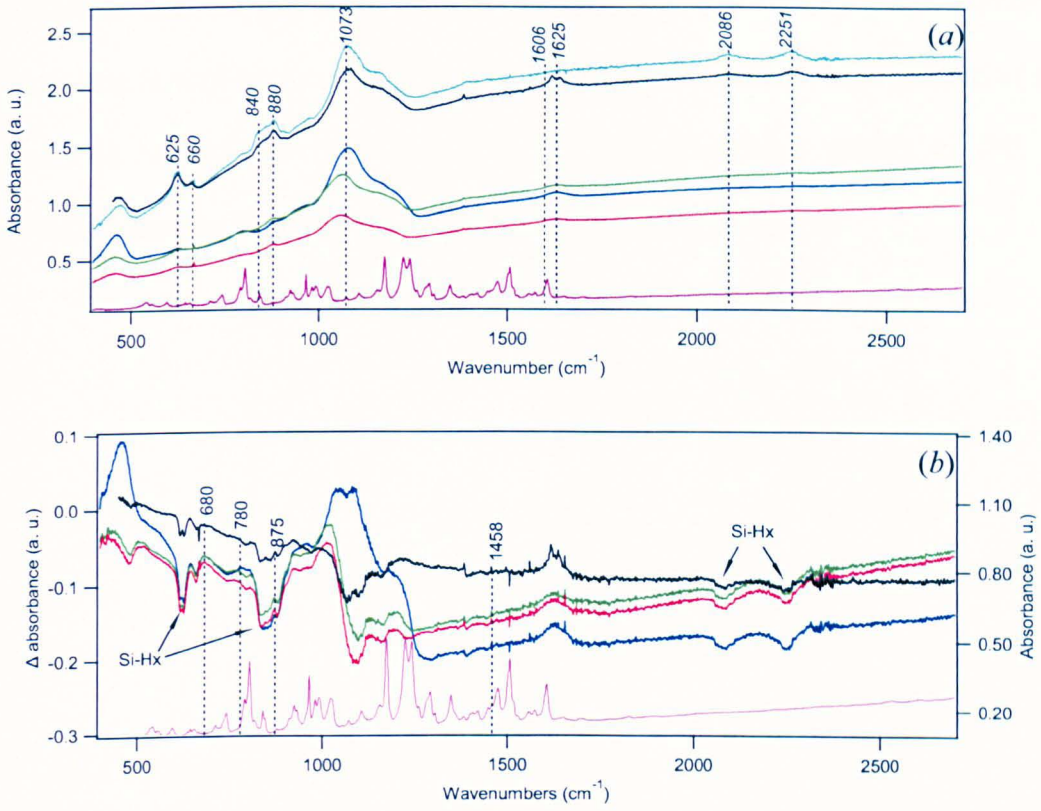

Figure 4.20. FTIR spectra of pure *PSi*, pure dye sensitizer and dye-modified *PSi* samples (*a*). Differential spectra between FTIR spectrum of pure *PSi* and immobilized samples (*b*). Photosensitizers prepared by photoactivated under *Xe* arc lamp illumination, thermally activated at T=108 °C, catalytically activated by H_2PtCl_6 and $AlCl_3$ hydrosilylation are represented by green, red, dark-blue and black curves, correspondingly. Pure *PSi* and dye sensitizer are represented by blue and violet curves, respectively. Right scale in (*b*) is for absorbance of dye.

4.4.2. Oxygenation of α-pinene mediated by the dye-modified PSi sensitizers

The *PSi* samples modified with the dye were tested in the oxygenation of α-pinene using the annular recirculating photoreactor and a simple tubular batch reactor (V_R=12 mL) under the 524 nm LED lamp illumination (I_a=4.6×10^{-4} Einst L^{-1} s^{-1}). The kinetic curves of oxygenation are shown in **Figure 4.21**. Comparison of the product accumulation rates and reaction rates inside the photoreactor with these obtained in the case of pure *TPP* photosensitizer revealed that all the immobilized photosensitizers are much less active in

the oxygenation than the free porphyrin (see **Table 4.14**). Low activity of the supported photosensitizers is well known fact [230-232] which can be related to quenching of the photogenerated $^1O_2$ by the *Si-H* and *Si-OH* surface quenching groups of *PSi*, or energy/electron transfer from the attached porphyrins to *Si* nanocrystals.

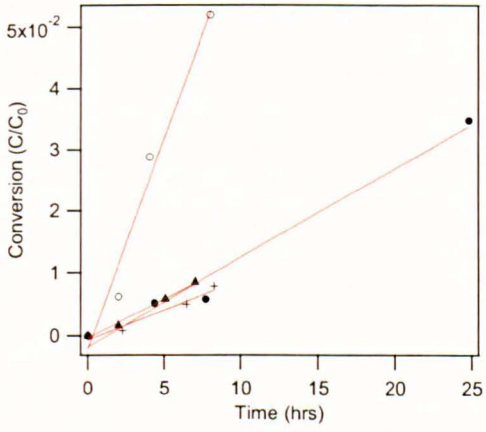

Figure 4.21. Oxygenation of α-pinene in the annular recirculating photoreactor (● and + correspond to light- and temperature-activated hydrosilylation) and in tubular batch reactor (V_R=12 mL) (○ and ▲ represent $AlCl_3$ and H_2PtCl_6 activated hydrosilylation) under the 524 nm LED lamp illumination (I_a=4.6×10^{-4} Einst L^{-1} s^{-1}).

Table 4.14. Product accumulation rates and reaction rates obtained in the annular recirculating photoreactor and a simple tubular batch photoreactor (V_R=12 mL) in the cases of *TPP* and dye-modified *PSi* prepared *via* thermal, photo, and catalytically activated hydrosilulation, *PSi-S* (*T*), *PSi-S* (*hν*), *PSi-S* (H_2PtCl_6) and *PSi-S* ($AlCl_3$), correspondingly.

	TPP	*PSi-S (T)*	*PSi-S (hν)*	*PSi-S* (H_2PtCl_6)	*PSi-S* ($AlCl_3$)
r_0^T, Mol L^{-1} s^{-1}	1.1×10^{-5}	9.6×10^{-8}	1.4×10^{-7}	1.2×10^{-7}	6.8×10^{-7}
r_0^R, mol L^{-1} s^{-1}	1.1×10^{-4}	1.0×10^{-6}	1.5×10^{-6}	1.2×10^{-7}	6.8×10^{-7}
ϕ_R	0.239	0.002	0.003	-	-

The first reason was earlier found to be responsible for low efficiency of the pure *PSi* and therefore cannot be eliminated in the case of the dye-modified *PSi* photosensitizers. The

effect of $^1O_2$ deactivation by quenching groups of the support was also reported for 2-acetonaphthone absorbed on silica and silica-immobilized porphyrins [231-233]. Therefore, this factor probably contributes to low efficiency of the dye-modified *PSi* photosensitizers.

Energy or electron transfer in the dye-semiconductor systems is driven by thermodynamics [234-236]. From the energetic diagram shown on **Figure 4.22** it is clear that both the energy transfer from the excited state of the immobilized porphyrin to the *PSi* conducting band and the electron transfer from the immobilized porphyrin to the valence bond of the *PSi* excited state are thermodynamically favorable. Direct energy transfer from the highest occupied molecular orbital of *TPP* to the conduction band of *PSi* is also possible as it was shown for the porphyrin-modified *Si* nanowires [236]. The mentioned above consideration is fulfilled for *TPP* (energy levels of a photosensitizer used in this study are very close to these of *TPP* [234, 237]) immobilized on *Si* nanoparticles with a bandgap from bulk *Si* (1.1 eV) up to *PSi* with a bandgap of 2.9 eV (which corresponds to energy difference of about 1.0-1.3 eV between conductind band of *PSi* and Fermi level [238, 239]).

In the case of energy/electron transfer the length of a spacer linking the photosensitizer to the surface can also play an important role as it was demonstrated for *Zn*-porphyrin monolayers attached to *Si*(100) surfaces and Merrifield-immobilized porphyrins [229, 230]. The authors found that photosensitizers with longer spacers between porphyrin and *Si* monocrystal exhibit slower electron-transfer rates. Also, immobilized photosensitizers with longer spacer between porphyrin and the polymer support were more efficient in oxygenation of monoterpenes. In the current study the length of each of four tethers was equal to a C_4 carbon chain spacer while the most efficient immobilized photosensitizers

were linked to Merrifield polymer by a C_{12} spacer. Contrary to that, for the silica-supported porphyrins the impact of the spacer length on activity in $^1O_2$ oxygenation was shown to be insignificant [231, 232]. The authors attributed this fact to efficient quenching of photogenerated $^1O_2$ by the silica matrix. However, quenching of $^1O_2$ cannot substitute energy transfer from the excited states. The lower impact of spacer length is better explained by a lower band gap of the Merrifield polymer compared to that of silica, making energy transfer from the excited dye molecules to silica unfavorable.

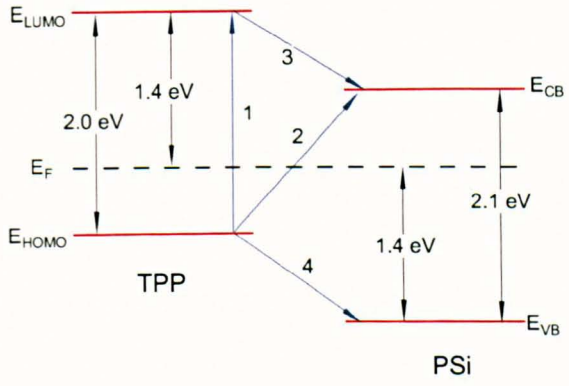

Figure 4.22. Diagram of energetic levels of *TPP* and *PSi*. E_{VB} is energy of valence band, E_{CB} is energy of conducting band, E_F Fermi level, E_{HOMO} is energy of highest occupied molecular orbital, E_{LUMO} is energy of lowest unoccupied molecular orbital, 1 is excitation of *TPP*, 2 is direct transfer, 3 is indirect transfer, 4 is electron transfer to excited *PSi*. Data for *TPP* and *PSi* energy levels were taken from references [234, 237, 238].

To avoid (reverse) undesirable energy transfer a photosensitizer with energy levels adjusted to *PSi* support (with smaller bandgap and energy of lowest unoccupied molecular orbital lower than the energy of conducting band of *PSi*) should be used. A longer spacer linking the photosensitizer to the surface of support will decrease the rate of energy/electron transfer from porphyrin to the support. As a possibility the *PSi* matrix could be oxidized prior or after dye immobilization in order to increase its band gap. However, *Si-OH* bonds are about two orders of magnitude more efficient quenchers of

$^1O_2$ [56] and therefore, oxidation will lead to a decrease of the overall efficiency. Further study is required in order to quantify the influence of the above factors discussed above and to develop an efficient heterogeneous supported photosensitizer.

CONCLUSIONS

A laboratory-scale annular recirculating photoreactor was designed, assembled and tested with a 524 nm LED, a 420 nm actinic fluorescent, and *Xe* arc lamps in different lamp-reactor geometries. Based on the actinometry data it was shown that the overall efficiency of the LED lamp is close to that of the more power-consuming actinic fluorescent lamp due to several times more efficient circular lamp-reactor geometry and the narrow radiation pattern of a single LED bulb. The reactor was tested in the oxygenation of α-pinene to pinocarvone and in the stereoselective oxygenation of homoallylic alcohol. It was shown that the reaction rate is proportional to the intensity of the absorbed photons. A comparison of the performance of the annular reactor with the conventional immersed-well photoreactor confirmed the importance of narrow reaction space for efficient oxygenation. Using a simple kinetic model a bimolecular reaction rate constant of the homoallylic alcohol oxygenation was estimated to be about two orders of magnitude lower than that for α-pinene.

A photochemical rig equipped with a glass-silicon microreactor chip and a metal plate heat exchanger was designed, assembled and tested with the 524 and 416 nm LED arrays, a *Xe* arc and a metal halide lamps. The microreactor was used in the oxygenation of α-pinene and homoallylic alcohol at different oxygen pressures in continuous and recirculating modes in the oxygen-saturated reaction mixtures and in a gas-liquid segmented flow mode. Based on the actinometry and kinetic data it was shown that the intensities of light absorbed in the microreactor, rates and quantum yields of oxygenation are close or several times higher than those found for the annular and the immersed-well photoreactors due to a better light utilization in the microreactor. The productivity of the microreactor was found to be 3-7 times lower due to the lower volume of the reactor. It was also shown that the LED arrays are comparable with the more power-consuming

sources of light in terms of intensity of the absorbed light. The microreactor also demonstrated better selectivity in the oxygenation of homoallylic alcohol due to a lower residence time in the reactor and therefore, a lower probability of side reactions.

In all the modes of operation the productivity of the microreactor increases with oxygen pressure. In the gas-liquid segmented flow mode at low gas flowrates the conversion is limited by the supply of oxygen and proportional to gas pressure and liquid holdup. At high gas flowrates it becomes virtually independent on pressure and a decrease in conversion is governed by the shortening of the total residence time and decreasing of the liquid holdup. Within the window of maximum performance, the productivity of the microreactor increases with a decrease in the total residence time (in opposite to conversion) due to higher gas and liquid holdup volumes. The estimated formal reaction order for oxygen pressure in the homogeneous oxygenation of α-pinene is about 0.6-0.7 while in the case of the segmented flow it decreases to about 0.4 indicating mass-transfer limitations at the gas-liquid interface. Based on the results obtained, a methodology of efficient oxyfunctionalization of allylic compounds was developed.

Following the developed methodology, an extensive comparative study of the photosensitizing efficiency of a proposed photosensitizer based on porous silicon and a conventional dye sensitizer tetraphenylporphine was performed. By monitoring the photoluminescence emission line of singlet oxygen it was concluded that the photosensitizing efficiency of porous silicon is much lower than that of tetraphenylporphine. This effect was mainly attributed to the low quantum yield of photoluminescence of porous silicon (in the order of the few percents) and to very efficient energy transfer from electronically excited singlet oxygen molecules to high frequency surface *Si–H* vibration modes which is crucial for deactivation of singlet

oxygen states. Efficient quenching of photoluminescence was observed due to direct energy transfer from photoexcited excitons confined in *PSi* to suitable acceptor molecules. This process, leading to alternative pathways of oxidation, is responsible for photobleaching of diphenylisobensofuran at millimolar concentrations reported in earlier studies.

In order to improve the photosensitizing efficiency of porous silicon, a commercially available tetra(4-allyloxy)phenylporphine photosensitizer with four terminal double bonds was immobilized on *H*-terminated surface of the nanocrystals *via* thermally, photo-, and catalytically activated hydrosilylation. The immobilization was proven by infrared spectroscopy. It was shown that all the immobilized photosensitizers are much less active in the oxygenation of α-pinene than the free porphyrin. Low activity of the supported photosensitizers was attributed to quenching of the photogenerated singlet oxygen by the *Si-H* and *Si-OH* surface quenching groups of porous silicon, and to thermodynamically favorable quenching of the photoexcited porphyrin states due to energy/electron transfer to *Si* nanocrystals.

FURTHER PLANS AND RECOMMENDATIONS

It is planned to build an optimized laboratory scale microreactor rig using several microreactor units each equipped with high pressure oxygen supply, flexibility of connecting the units either in series or in parallel and integration of the commercially available high power LED arrays. Design of an LED arrays tailored to the geometry of a microchannel will improve utilization of light in the microchannel and an overall efficiency of the system.

Although pure and dye-modified porous silicon demonstrated low efficiency towards oxygenation of allylic substrates, it would be useful to study the dependence of photosensitizing efficiency on the spacer length for this matrix. Surface modification of porous silicon by less efficient quenching groups such as, for example, $-CF_3$ would be another approach to increase the efficiency. It is also worth developing an efficient methodology of integration of heterogeneous photosensitizer based on different supports such as Merrifield polymer within the microchannels.

It is also interesting to study other possible approaches towards heterogeneous photosensitizing. For example, perfluoro-1,3-dimethylcyclohexane is a nontoxic, non-flammable and low volatile solvent, immiscible with most organic compounds. Oxygen is highly soluble in this solvent while lifetime of singlet oxygen is several orders of magnitude higher than that found for the most of the common solvents. Therefore, the solvent with a dissolved perfluorinated photosensitizer (for example, fluorous tetraphenylporphyrin), saturated by oxygen at elevated pressures *via* bubbling the gas in feed tank, may be used in the segmented liquid-liquid flow as a safe oxygen carrier and generator of singlet oxygen under illumination in a microchannel where the second liquid phase is a mixture of reagents.

APPENDIX A: ACTINOMETRY

1. CALIBRATION OF ACTINOMETRY

Calibration of actinometry (**Table A1** and **Figure A1**) was carried out according to Hatchard-Parker procedure [179] which is described in **Experimental** part. Molar coefficient of extinction ε=11310 L mol^{-1} cm^{-1} was extracted from the calibration curve.

Table A1. Calibration for actinometry data. D_i is the i value of optical density, $<D>$ is the average value of optical density, $c_{Fe^{2+}}$ is the concentration of Fe^{2+} ions.

Sample	$c_{Fe^{2+}}$, mol L^{-1}	D_1	D_2	D_3	$<D>$	$<D>_i - <D>_0$
0	0	0.002	0.002	0.002	0.002	0.000
1	1×10^{-5}	0.120	0.124	0.123	0.122	0.120
2	2×10^{-5}	0.274	0.269	0.266	0.270	0.268
3	3×10^{-5}	0.371	0.372	0.374	0.372	0.370
4	4×10^{-5}	0.486	0.484	0.484	0.485	0.483
5	5×10^{-5}	0.593	0.593	0.593	0.593	0.591
6	6×10^{-5}	0.708	0.707	0.705	0.707	0.705
7	7×10^{-5}	0.809	0.808	0.811	0.809	0.807
8	8×10^{-5}	0.905	0.907	0.906	0.906	0.904
9	9×10^{-5}	1.016	1.017	1.015	1.016	1.014
10	1×10^{-4}	1.175	1.175	1.173	1.174	1.172

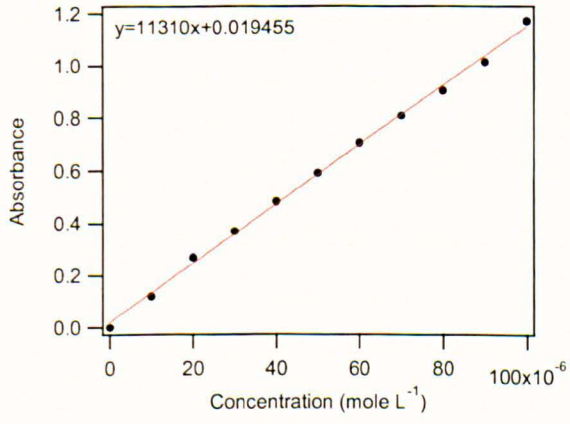

Figure A1. Calibration graph of absorbance *vs.* $c_{Fe^{2+}}$ iones measured in l = 1 cm quartz cell. Molar coefficient of extinction ε = 11310 L mol^{-1} cm^{-1}.

2. EXPERIMENTAL DATA AND PROCEDURE OF DATA CORRECTION*

Since the volume of solution in the annular recirculating reactor decreases during the experiment as aliquots are taken for analysis at every point, the optical density D should be corrected.

Assume the initial volume was V_0. Therefore, the initial quantity n_0 (in moles) of Fe^{2+} is proportional to D_0V_0 with εl as a coefficient. Than, for the blank measurement (to obtain D_0), aliquot ξ_0 was taken. Hence, at the start point the volume was $V_1 = V_0 - \xi_0$ or, in terms of the Fe^{2+} amount, $n_1^1 = n_0 - n_{\xi 0}$ mol, where $\varepsilon l n_{\xi 0} = D_0\xi_0$. After irradiation Δn_1 mol of Fe^{2+} was generated and $\varepsilon l n_1 = D_1V_1 = \varepsilon l(n_1^1 + \Delta n_1) = \varepsilon l(n_0 + \Delta n_1 - n_{\xi 0})$. Than the next aliquot ξ_1 was taken, hence the volume of solution changed as $V_2 = V_1 - \xi_1 = V_0 - \xi_0 - \xi_1$ and the Fe^{2+} amount became $n_2^1 = n_1 - n_{\xi 1}$. After the next period of irradiation the quantity of Fe^{2+} will increase by Δn_2 mol, $\varepsilon l n_2 = D_2V_2 = \varepsilon l(n_2^1 + \Delta n_2) = \varepsilon l(n_1 - n_{\xi 1} + \Delta n_2) = \varepsilon l(n_0 + \Delta n_1 + \Delta n_2 - n_{\xi 0} - n_{\xi 1})$, than the next aliquot, ξ_2 was taken and so on. Continuing this approach we can finally obtain a system of following equations (A1):

$$\varepsilon l n_0 = D_0V_0$$

$$\varepsilon l n_1 = D_1V_1 = D_0V_0 + \varepsilon l\Delta n_1 - D_0\xi_0$$

$$\varepsilon l n_2 = D_2V_2 = D_0V_0 + \varepsilon l(\Delta n_1 + \Delta n_2) - D_0\xi_0 - D_1\xi_1$$

$$\varepsilon l n_3 = D_3V_3 = D_0V_0 + \varepsilon l(\Delta n_1 + \Delta n_2 + \Delta n_3) - D_0\xi_0 - D_1\xi_1 - D_2\xi_2$$

$$\cdots\cdots\cdots$$

$$\varepsilon l n_m = D_mV_m = D_0V_0 + \varepsilon l(\Delta n_1 + \ldots + \Delta n_m) - D_0\xi_0 - \ldots - D_{m-1}\xi_{m-1} \qquad \text{(A1)}$$

On the other hand, if we neglect the volume of the aliquots and assume the volume of solution is constant we arrive to the system (A2):

$$D_1^1V_0 = D_0V_0 + \varepsilon l\Delta n_1$$

* The procedure of optical density correction was used only in the case of annular photoreactor for an LED lamp. In all the other cases the decrease in volume was small enough ($\xi_i \sim 1.5$ ml) to be neglected.

$$D_2^1V_0 = D_0V_0 + \varepsilon l(\Delta n_1 + \Delta n_2)$$

$$D_3^1V_0 = D_0V_0 + \varepsilon l(\Delta n_1 + \Delta n_2 + \Delta n_3)$$

$$\ldots\ldots\ldots$$

$$D_m^1V_0 = D_0V_0 + \varepsilon l(\Delta n_1 + \ldots + \Delta n_m) \qquad \text{(A2)}$$

Comparison of systems (A1) and (A2) leads us to the system (A3):

$$D_1V_1 = D_1^1V_0 - D_0\xi_0$$

$$D_2V_2 = D_2^1V_0 - D_0\xi_0 - D_1\xi_1$$

$$D_3V_3 = D_3^1V_0 - D_0\xi_0 - D_1\xi_1 - D_2\xi_2$$

$$\ldots\ldots\ldots$$

$$D_mV_m = D_m^1V_0 - D_0\xi_0 - \ldots - D_{m-1}\xi_{m-1} \qquad \text{(A3)}$$

After algebraic rearrangements and keeping in mind that $V_1 = V_0 - \xi_0$, $V_i = V_0 - \xi_0 - \ldots - \xi_{i-1}$ in the end we can express D_i^1 as a function of D_i:

$$D_1^1 = D_1 + (D_0 - D_1)\frac{\xi_0}{V_0}$$

$$D_2^1 = D_2 + (D_0 - D_2)\frac{\xi_0}{V_0} + (D_1 - D_2)\frac{\xi_1}{V_0}$$

$$D_3^1 = D_3 + (D_0 - D_3)\frac{\xi_0}{V_0} + (D_1 - D_3)\frac{\xi_1}{V_0} + (D_2 - D_3)\frac{\xi_2}{V_0}$$

$$\ldots\ldots\ldots$$

$$D_m^1 = D_m + (D_0 - D_m)\frac{\xi_0}{V_0} + \ldots + (D_{m-1} - D_m)\frac{\xi_{m-1}}{V_0} \qquad \text{(A4)}$$

Experimental data and corrected values of optical density are shown in **Table A2** and **Figure A2**.

Table A2. LED lamp actinometry in the annular photoreactor, experimental and corrected data. D_i is the i value of optical density, $<D>$ is the average value of optical density, D_i^l is the corrected values of the optical density, ξ is the volume of initial aliquot taken from photocatalytic plant, t is time of experiment, l is light pathway, l=1 cm, and $c_T(t)$ is concentration of Fe^{2+} in tank.

t, min	D_1	D_2	D_3	$<D>$	$<D>_i - <D>_0$	D_i^l	ξ, L	$c_T(t)$, mol L^{-1}
0	0.005	0.005	0.006	0.005	0.000	0.000	7.0×10^{-3}	0
10	0.271	0.276	0.271	0.273	0.267	0.267	9.3×10^{-3}	2.4×10^{-4}
20	0.498	0.498	0.498	0.498	0.493	0.484	7.0×10^{-3}	4.3×10^{-4}
30	0.784	0.784	0.784	0.784	0.779	0.750	9.5×10^{-3}	6.6×10^{-4}
40	1.047	1.047	1.047	1.047	1.042	0.985	7.5×10^{-3}	8.7×10^{-4}
50	1.351	1.351	1.351	1.351	1.346	1.247	9.0×10^{-3}	1.1×10^{-3}
60	1.642	1.642	1.642	1.642	1.637	1.486	7.5×10^{-3}	1.3×10^{-3}
70	1.922	1.922	1.922	1.922	1.917	1.708	7.0×10^{-3}	1.5×10^{-3}
80	2.270	2.270	2.270	2.270	2.265	1.974	5.5×10^{-3}	1.7×10^{-3}
90	2.591	2.591	2.591	2.591	2.586	2.212	5.0×10^{-3}	2.0×10^{-3}

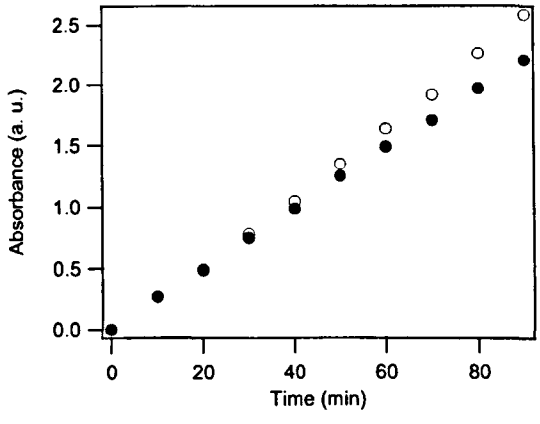

Figure A2. Absorbance of Fe^{2+}-phenanthroline complex formed from the ferrioxalate actinometer after 524 nm LED lamp irradiation *vs.* time. Hollow circles represent experimental data; filled circles show the corrected data with taking into account the change in volume due to samples collection.

Table A3. Actinic fluorescent *Xe* arc and lamps actinometry in the annular photoreactor, experimental data. D_i is the *i* value of optical density, $<D>$ is the average value of optical density, *l* is light pathway, *t* is time of experiment, and $c_T(t)$ is concentration of Fe^{2+} in tank.

Lamp	l, cm	t, min	D_1	D_2	D_3	$<D>$	$<D>_i - <D>_0$	$c_T(t)$, mol L^{-1}
Actinic	1	0	0.035	0.036	0.036	0.036	0	0
		0.5	0.492	0.490	0.493	0.492	0.456	8.1×10^{-4}
		1.5	1.431	1.432	1.431	1.431	1.395	2.5×10^{-3}
		2.5	2.143	2.149	2.141	2.144	2.108	3.7×10^{-3}
		3.5	2.587	2.587	2.583	2.586	2.550	4.5×10^{-3}
	0.15	0	0.014	0.014	0.014	0.014	0	0
		1.5	0.256	0.258	0.257	0.257	0.243	2.9×10^{-3}
		2.5	0.393	0.393	0.394	0.393	0.379	4.5×10^{-3}
		3.5	0.483	0.484	0.484	0.484	0.470	5.5×10^{-3}
Xe arc	1	0	0.024	0.023	0.023	0.023	0.000	0
		20.5	0.932	0.932	0.932	0.932	0.909	8.0×10^{-4}
		35	1.509	1.510	1.510	1.510	1.486	1.3×10^{-3}
		50	2.571	2.571	2.571	2.571	2.548	2.3×10^{-3}
		65	3.215	3.215	3.215	3.215	3.192	2.8×10^{-3}

Table A4. Actinometry of 524 nm LED, 416 nm LED, *Xe* arc, and metal halide lamps in the microreactor, measured in continuous mode. D_i is the *i* value of optical density, $<D>$ is the average value of optical density, *l* is light pathway, τ is residence time in the reactor, and $c_R(t)$ is concentration of Fe^{2+} at the outlet.

Lamp	l, cm	τ, min	D_1	D_2	D_3	$<D>$	$<D>_i - <D>_0$	$c_R(t)$, mol L^{-1}
525 nm	1	0	0.158	0.155	0.154	0.156	0	0
		4.8	0.417	0.415	0.415	0.416	0.260	4.6×10^{-4}
		24	1.406	1.406	1.405	1.406	1.250	2.2×10^{-3}
Xe	0.5	0	0.033	0.031	0.032	0.032	0	0
		0.48	0.452	0.454	0.455	0.454	0.422	1.5×10^{-3}
		0.24	0.253	0.253	0.253	0.253	0.221	7.8×10^{-4}
416 nm	0.5	0	0.033	0.031	0.032	0.032	0	0
		0.48	0.788	0.788	0.785	0.787	0.755	2.7×10^{-3}
		0.24	0.487	0.487	0.489	0.488	0.456	1.6×10^{-3}
Metal halide	1	0	0.075	0.073	0.069	0.072	0	0
		0.240	1.561	1.556	1.555	1.557	1.485	2.6×10^{-3}
		0.120	0.841	0.839	0.836	0.838	0.766	1.4×10^{-3}
		0.080	0.749	0.746	0.746	0.747	0.675	1.2×10^{-3}
		0.069	0.536	0.534	0.536	0.536	0.463	8.2×10^{-4}
		0.060	0.558	0.556	0.556	0.556	0.484	8.6×10^{-4}

3. INTENSITY OF THE ABSORBED LIGHT CALCULATION

An example of calculation using equations (3.3), (3.9-3.11), and (3.13) deduced in **Experimental** part for the annular reactor illuminated by the 524 nm LED lamp is given below. Concentration of Fe^{2+} in tank calculated for the aliquot taken after 10 minites of irradiation:

$$c_T(t) = \frac{D(t)V_2}{\varepsilon l V_1} = \frac{0.267 \times 0.02}{11310 \times 1 \times 0.002} = 2.4 \times 10^{-4} \text{ M}$$

The rate of accumulation of Fe^{2+} in tank $\frac{dc_T}{dt}$ was obtained as a slope of the linear plot $c_T(t)$ (**Figure A3**).

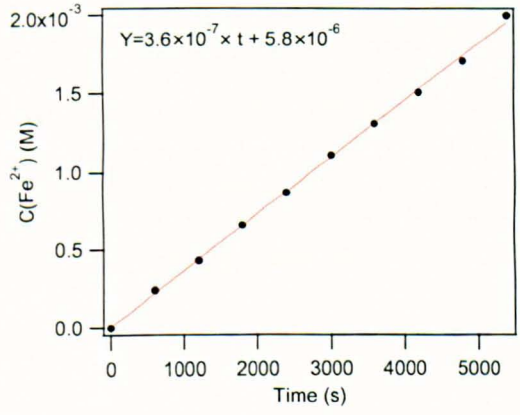

Figure A3. Concentration of Fe^{2+} ions as a function of time of illumination measured in the annular recirculating photoreactor illuminated by the 524 nm LED lamp. The rate of accumulation of Fe^{2+} in tank obtained as a slope of the c(t) plot is equal to 3.6×10^{-7} mol L^{-1} s^{-1}.

Rate of Fe^{2+} generation in the annular photoreactor:

$$r_{Fe^{2+}} = \left(\frac{V_R + V_T}{V_R}\right)\frac{dc_T}{dt} = \frac{250}{9.5} \times 3.6 \times 10^{-7} = 9.5 \times 10^{-6} \text{ mol L}^{-1} \text{ s}^{-1}$$

Amount of light, absorbed by ferrioxalate:

$$I_a^F = \frac{r_{Fe^{2+}}}{\Theta(\lambda)} = \frac{9.5 \times 10^{-6}}{0.58} = 1.6 \times 10^{-5} \text{ Einst L}^{-1} \text{ s}^{-1}$$

Amount of light, absorbed by *TPP* during oxygenation:

$$I_a = I_a^F \frac{1-10^{-\varepsilon_S(\lambda)lc_S}}{1-10^{-\varepsilon_F(\lambda)lc_F}} = 1.6\times10^{-5} \times \frac{(1-10^{10900\times0.3\times8.1\times10^{-4}})}{(1-10^{0.35\times0.3\times0.15})} =$$

$$= 1.6\times10^{-5} \times \frac{1}{0.036} = 4.6\times10^{-4} \text{ Einst } L^{-1} s^{-1}$$

Flux of the absorbed photons illuminated by the 524 nm LED lamp:

$$J_a = I_a \times V_R = 4.6\times10^{-4} \times 9.5\times10^{-3} = 4.4\times10^{-6} \text{ Einstein } s^{-1};$$

The power of the absorbed light can be found by multiplying the flux of photons on the energy of one mole of photons:

$$P_{hv} = 4.4\times10^{-6} \times 228354.9 = 0.995 \text{ J } s^{-1} = 0.995 \text{ W}$$

Summary of the calculations for the 524 nm, 416 nm actinic fluorescent, and *Xe* arc lamps in the annular photoreactor as well as for the 524 nm and 416 nm LED, *Xe* arc and metal halide lams in the microreactor are represented in **Table A5**. Equations (3.17), (3.18) and data from **Figure 3.10** and **3.11** (see **Experimental**) were used in the cases of *Xe* arc and metal halide lamps.

Table A5. Summary of the calculations for all the lamps used in current study with the annular photoreactor and the microreactor.

Reactor	Lamp	dc/dt	$r_{Fe^{2+}}$	I_a^F	I_a	J_a	P_{hv}
Annular reactor	524 nm LED	3.6×10^{-7}	9.5×10^{-6}	1.6×10^{-5}	4.6×10^{-4}	4.4×10^{-6}	0.995
	420 actinic	2.2×10^{-5}	2.0×10^{-4}	1.8×10^{-4}	5.7×10^{-4}	6.3×10^{-6}	1.811
	Xe arc	7.9×10^{-7}	6.6×10^{-5}	1.8×10^{-4}	2.3×10^{-4}	6.8×10^{-7}	-
Microreactor	524 nm LED	1.4×10^{-6}	1.4×10^{-6}	2.4×10^{-6}	3.2×10^{-4}	7.7×10^{-8}	0.018
	416 nm LED	8.9×10^{-5}	8.9×10^{-5}	8.2×10^{-5}	1.9×10^{-3}	4.6×10^{-7}	0.106
	Xe arc	4.8×10^{-5}	4.8×10^{-5}	1.3×10^{-4}	3.3×10^{-4}	8.0×10^{-8}	-
	Metal halide	1.8×10^{-4}	1.8×10^{-4}	2.4×10^{-4}	3.6×10^{-3}	8.6×10^{-7}	-

APPENDIX B: LIGHT UTILISATION AND EFFICIENCY

1. CALCULATIONS FOR 524 NM, 416 NM LED and 420 NM ACTINIC LAMPS

The output power of a single LED as a function of potential ΔU was obtained using Laser Check power meter (Coherent Inc., accuracy 5%) (**Figure B1**). The average voltage drop for a single LED, $<\Delta U>$ was obtained from the voltage drop of 240 LEDs. The obtained value was equal to 3.4 V. Using the approximated equation (B1) (see **Figure B1**) the average output power of a single LED $<P_{LED}>$ in the set of 240 LEDs was found to be about 6.0 mW.

$$P_{LED} = 7.6576\,\Delta U^2 - 38.632\,\Delta U + 48.781 \qquad \text{(B1)}$$

P_{LED} here is the output power of a single LED. The value obtained is in agreement with the manufacturer's power specification of 5.3-9.3 mW.

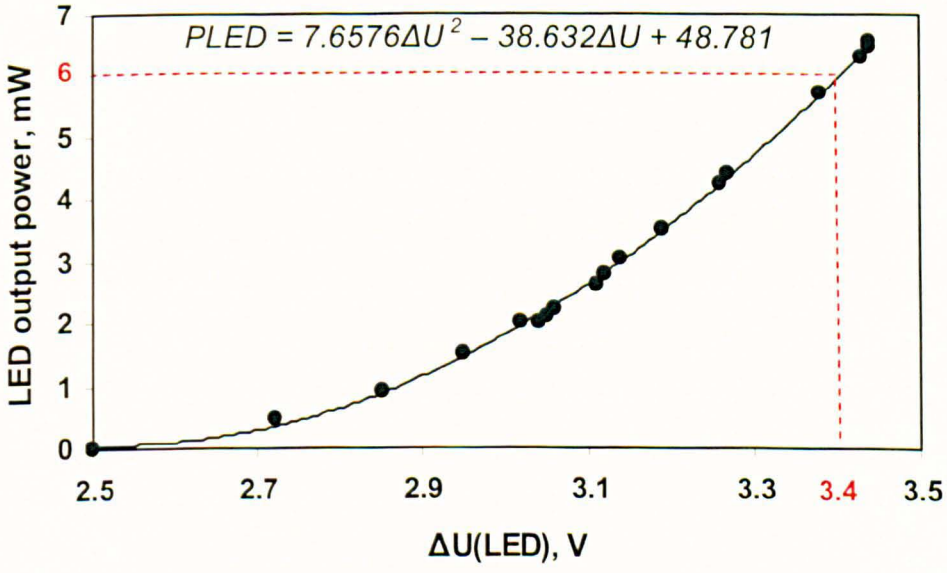

Figure B1. Output power *vs.* voltage drop for single LED measured by Laser Check powermeter.

The total output power of the set of 240 green LEDs, P_{hv}^{0} can be simply taken as a multiple of $<P_{LED}>$ on 240:

$$P_{h\nu}^{0} = 6.0 \times 240 = 1440.0 \text{ mW}$$

Efficiency of the lamp-reactor geometry, η_{LR} can be found as a ratio between the values of the power obtained by actinometry and that measured by the powermeter. In the case of the annular reactor with the 524 nm LED:

$$\eta_{LR} = \frac{P_{h\nu}}{P_{h\nu}^{0}} = \frac{995}{1440} = 0.691$$

The input power for the 524 nm LED lamp is expressed as a product of voltage drop for a single LED, current in the circuit and the number of LEDs in the lamp:

$$P_{in} = <\Delta U> \times I_C \times N_{LED}$$

The total efficiency of power-to-output light conversion, with taking into account 30 drivers (the total power consumption of 20.9 W) used for stabilization of the LED feed current:

$$\eta_{PL} = \frac{P_{h\nu}^{0}}{P_{in}} = \frac{1440}{(3.4 \times 240 \times 0.02) + 20900} = \frac{1440}{16320 + 20900} = 0.039$$

Without the drivers the efficiency of power-to-output light conversion is:

$$\eta_{PL} = \frac{P_{h\nu}^{0}}{P_{in}} = \frac{1440}{3.4 \times 240 \times 0.02} = \frac{1440}{16320} = 0.088$$

Therefore an overall efficiency of the system with taking into account drivers is:

$$\eta = \frac{P_{h\nu}}{P_{in}} = \frac{P_{h\nu}}{P_{h\nu}^{0}} \frac{P_{h\nu}^{0}}{P_{in}} = \eta_{LR}\eta_{PL} = 0.691 \times 0.039 = 0.027$$

Without taking into account the power consumed by drivers an overall efficiency is:

$$\eta = \frac{P_{h\nu}}{P_{in}} = \frac{P_{h\nu}}{P_{h\nu}^{0}} \frac{P_{h\nu}^{0}}{P_{in}} = \eta_{LR}\eta_{PL} = 0.691 \times 0.088 = 0.061$$

The efficiences of lamp-reactor geometry for the annular recirculating reactor with the 524 nm LED lamp and for the microreactor with the 524 nm and 416 nm LED arrays are summarized in **Table B1**.

Table B1. The efficiences of lamp-reactor geometry for the annular recirculating reactor with the 524 nm LED lamp and for the microreactor with the 524 nm and 416 nm LED arrays.

Reactor	Lamp	N	$\langle P_{LED} \rangle$, mW	P_{in}, W	$P^0_{h\nu}$, W	$P_{h\nu}$, W	η_{LR}, %	η_{PL}, %	η, %
Annular reactor	524 nm LED	240	6	16.32	1.440	0.995	69.1	8.8	6.1
	524 nm LED & drivers	240	6	37.22	1.440	0.995	69.1	3.9	2.7
Microreactor	524 nm LED	45	6	3.06	0.270	0.018	6.7	8.8	0.6
	524 nm LED & drivers	45	6	6.54	0.270	0.018	6.7	4.1	0.3
	416 nm LED	45	11	3.24	0.495	0.106	21.4	15.3	3.3
	416 nm LED & drivers	45	11	6.72	0.495	0.106	21.4	7.4	1.6

APPENDIX C: OXIDATION OF DPBF

1. CALIBRATION

DPBF oxidation was monitored at 410 nm. Molar extinction coefficient ε = 24088 L mol^{-1} cm^{-1} at 410 nm was obtained from the calibration data (**Figure C1**) and **Table C1**).

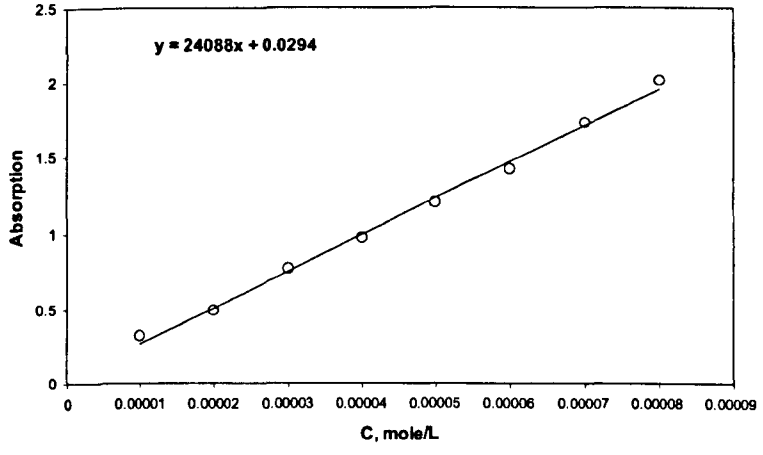

Figure C1. Calibration graph of absorbance *vs.* concentration of *DPBF* measured at 410 nm in l = 1 cm quartz cell. Molar coefficient of extinction ε = 24088 L mol^{-1} cm^{-1}.

Table C1. Calibration data of absorbance *vs.* concentration of *DPBF* measured at 410 nm in l = 1 cm quartz cell. D_i is the i-th value of optical density, <D> is the average value of optical density.

Concentration of DPBF, mol L^{-1}	D_1	D_2	D_3	<D>
1×10^{-5}	0.322	0.322	0.325	0.323
2×10^{-5}	0.480	0.496	0.497	0.491
3×10^{-5}	0.763	0.765	0.763	0.764
4×10^{-5}	0.970	0.970	0.971	0.970
5×10^{-5}	1.194	1.195	1.196	1.195
6×10^{-5}	1.416	1.418	1.42	1.418
7×10^{-5}	1.729	1.729	1.732	1.730
8×10^{-5}	2.016	2.016	2.016	2.016

2. UV-VIS ABSORPTION SPECTRA AND ABSORPTION DATA OF DPBF OXIDATION

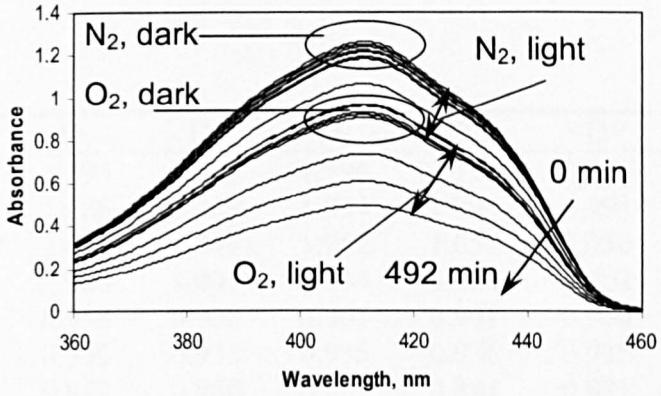

Figure C2. Absorption spectra of N_2 and O_2 saturated 10^{-3} M solution of *DPBF* in *F113* in presence of 0.2 % wt *PSi* irradiated by LED lamp and kept in dark for different times in continuous reactor. Spectra were measured in a 1 cm quartz cell. N_2 and O_2 flow rates are 30 mL min^{-1}, T = 20 °C, liquid flowrate is 40 mL min^{-1}.

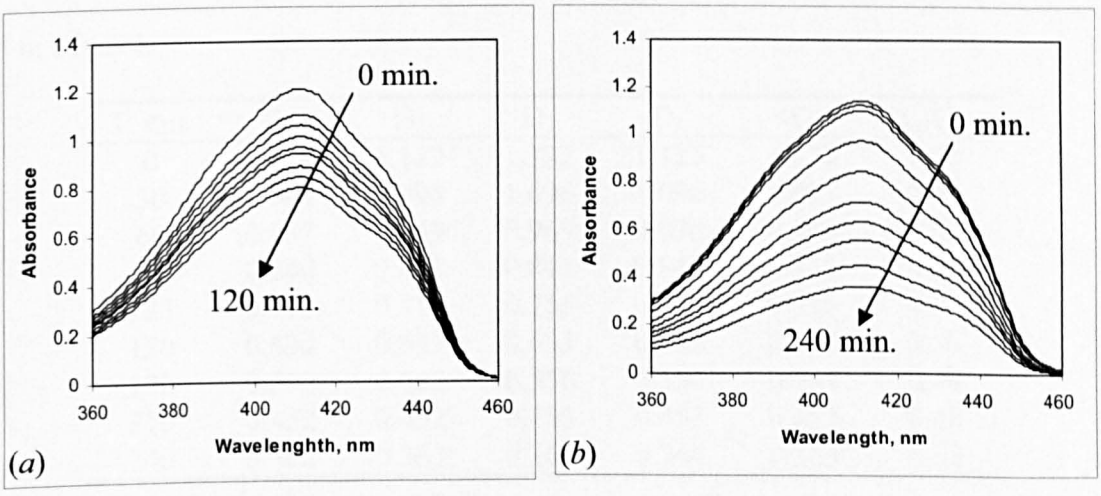

Figure C3. Absorption spectra of O_2 saturated 10^{-3} M solution of *DPBF* in *F113* in the presence of 0.2 % wt *PSi* irradiated by LED lamp for different times in continuous reactor. Spectra were measured in a 1 cm quartz cell. O_2 flow rates are (*a*) 30 and (*b*) 50 mL min^{-1}, T = 20 °C, liquid flowrate is 40 mL min^{-1}.

Table C2. Oxidation of *DPBF* in *F113* in the presence of 0.2 % wt *PSi* under different times of LED lamp irradiation in continuous reactor. O_2 flowrate is 30 mL min^{-1}, T = 20 °C, liquid flowrate is 40 mL min^{-1}. Absorbance was measured at 410 nm in a 1 cm quartz cell in ethanol.

t, min	D_1	D_2	D_3	D_4	<D>	C/C_0
0	1.194	1.195	1.196	1.198	1.196	1.00
18	1.086	1.089	1.094	1.093	1.091	0.91
30	1.048	1.049	1.052	1.052	1.050	0.88
46	1.000	1.001	1.004	1.004	1.002	0.84
60	0.958	0.958	0.961	0.961	0.960	0.80
75	0.935	0.935	0.935	0.936	0.935	0.78
90	0.882	0.880	0.881	0.881	0.881	0.74
105	0.836	0.838	0.840	0.840	0.839	0.70
120	0.795	0.797	0.791	0.797	0.795	0.66

Table C3. Oxidation of *DPBF* in *F113* in the presence of 0.2 % wt *PSi* under different times of LED lamp irradiation in continuous reactor. O_2 flow rate is 50 mL min^{-1}, T = 20 °C, liquid flowrate is 40 mL min^{-1}. Absorbance was measured at 410 nm in a 1 cm quartz cell in ethanol.

T, min	D_1	D_2	D_3	D_4	<D>	C/C_0
0	1.119	1.122	1.122	1.123	1.122	1.00
30	1.094	1.094	1.096	1.096	1.095	0.98
60	0.967	0.969	0.969	0.970	0.969	0.86
90	0.840	0.841	0.841	0.841	0.841	0.75
123	0.713	0.715	0.715	0.715	0.715	0.64
150	0.634	0.632	0.633	0.633	0.633	0.56
180	0.551	0.552	0.556	0.556	0.554	0.49
210	0.452	0.452	0.453	0.453	0.453	0.40
240	0.362	0.363	0.363	0.364	0.363	0.32

Table C4. Oxidation of *DPBF* in *F113* in the presence of 0.2 % wt *PSi* under different times of LED lamp irradiation in continuous reactor. N_2 flow rate is 30 mL min^{-1}, T = 20 °C, liquid flowrate is 40 mL min^{-1}. Absorbance was measured at 410 nm in a 1 cm quartz cell in ethanol.

	t, min	D_1	D_2	D_3	D_4	<D>	C/C_0
N_2	0	1.26	1.261	1.263	1.26	1.261	1.00
Dark	30	1.235	1.236	1.236	1.237	1.236	0.98
	61	1.219	1.22	1.222	1.222	1.221	0.97
	90	1.248	1.247	1.248	1.247	1.248	0.99
	120	1.209	1.212	1.214	1.215	1.213	0.96
N_2	0	1.209	1.212	1.214	1.215	1.213	1.00
Light	33	1.184	1.183	1.181	1.183	1.183	0.98
	61	1.060	1.059	1.063	1.063	1.061	0.88
	90	0.959	0.961	0.961	0.961	0.961	0.79
	120	0.908	0.909	0.912	-	0.939	0.77

3. DPBF OXIDATION RATE AND QUANTUM YIELD CALCULATIONS

From the data of *DPBF* oxidation it is possible to work out reaction rate and quantum yield. From the $c(t)$ plot it is possible to work out the rate of *DPBF* photobleaching in tank as a gradient of the oxidation curve (**Figure C4**).

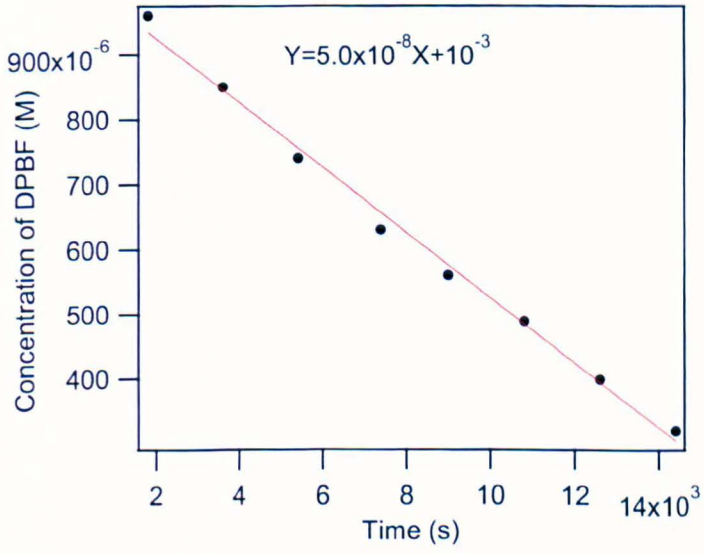

Figure C4. Influence of the oxygen flow rate on *DPBF* photooxidation. Photodegradation of 10^{-3} M solution of *DPBF* in *F113* in the presence of 0.2 % wt *pSi* measured by monitoring of the intensity of absorbance at 410 nm in a 1 cm quartz cell. O_2 flow rate is 50 mL min^{-1}, T = 20 °C, liquid flowrate is 40 mL min^{-1}.

According to equation (3.9) from **Literature Review** the obtained value (5×10^{-8} mol L^{-1} s^{-1}) corresponds to the reacton rate in the annular reactor.

$$r_R = (250/9.5)\times5\times10^{-8} = 1.3\times10^{-6} \text{ mol } L^{-1} s^{-1}$$

Overall quantum yield of *DPBF* oxidation under LED illumination can be calculated as a ratio between volumetric reaction rate r_R and volumetric number of absorbed photons I_a, obtained from the actinometry:

$$\phi_R = \frac{r_R}{I_a} = \frac{1.3\times10^{-6}}{4.6\times10^{-4}} = 0.003 .$$

APPENDIX D: EXAMPLES OF ^{1}H AND ^{13}C NMR SPECTRA

1. OXYGENATION OF α-PINENE

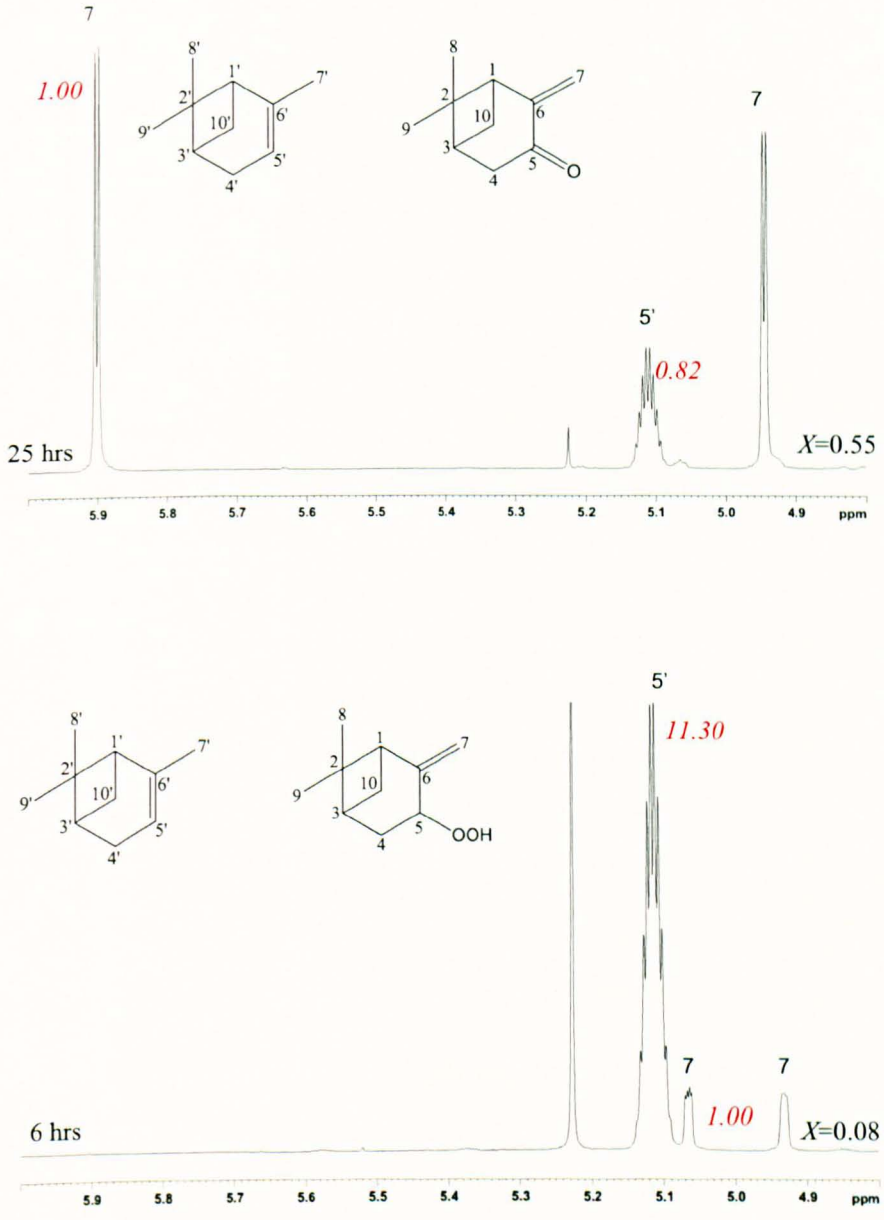

Figure D1. ^{1}H NMR spectra (in $CDCl_3$) of α-pinene oxidation in the annular recirculating photoreactor in presence of (*a*) 8.1×10^{-4} M *TPP* in CH_2Cl_2 (5.23 ppm) under *Xe* lamp illumination; (*b*) 6.0×10^{-4} M *RB* in ethanol under 524 nm LED lamp illumination. $T = 20$ °C, O_2 flowrate 30 ml min^{-1}. Relative areas of the peaks are depictured in red italic font. Conversions of the pinocarvone and peroxide, conversions X are calculated according to equation (3.19), **Experimental**. Values of the corresponding integrals are typed in red italic font.

2. OXYGENATION OF α-TERPINENE

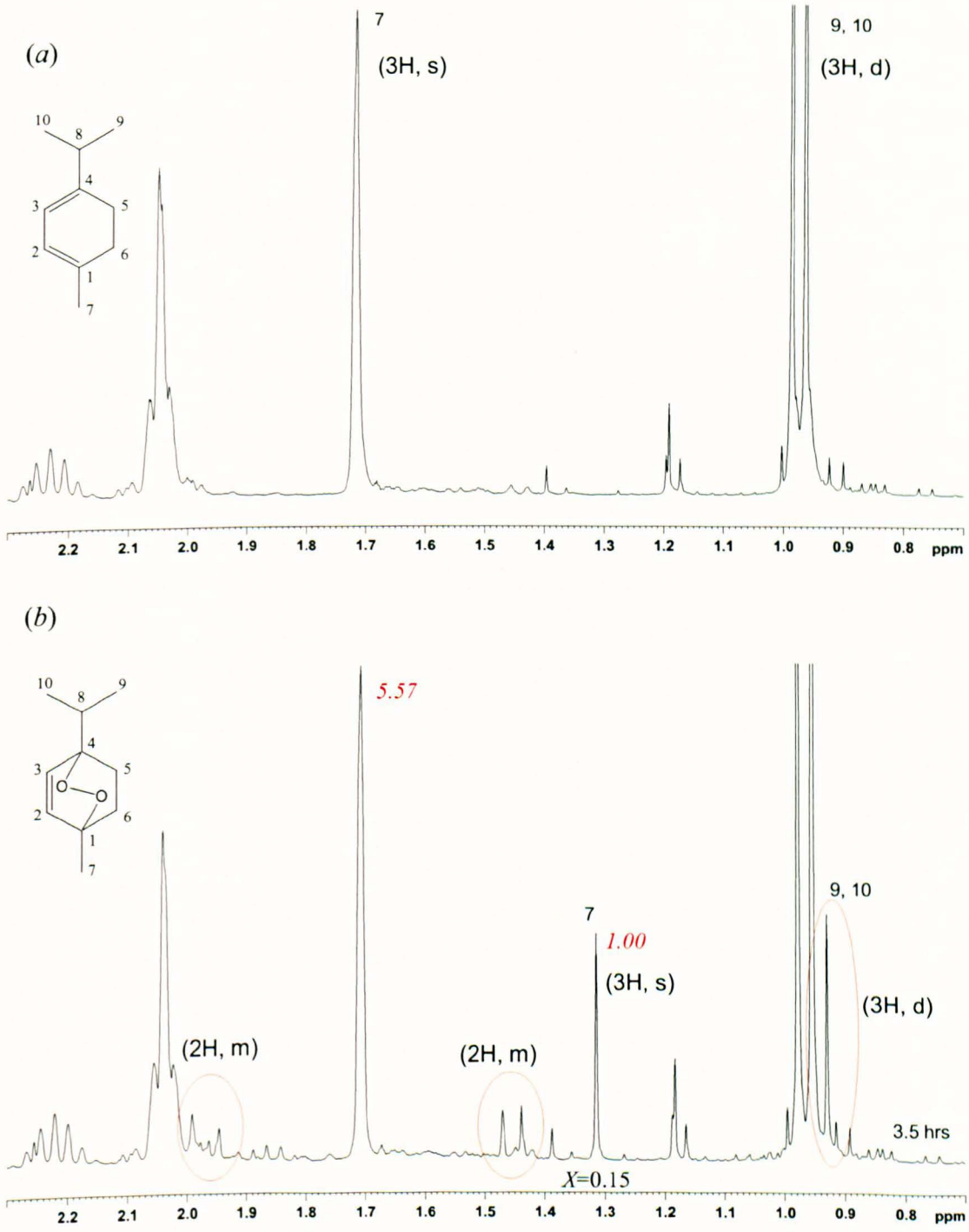

Figure D2. ^{1}H NMR spectra (in $CDCl_3$) of (*a*) α-terpinene, (*b*) α-terpinene after 3.5 hrs of irradiation under *Xe* arc lamp illumination in the annular recirculating photoreactor with 8.7×10^{-5} M *TPP* in CH_2Cl_2. T = 20 °C, O_2 flowrate 30 mL min^{-1}. Ascaridol is the main product [184]. Conversions X are calculated according to equation (3.19), **Experimental**. Values of the corresponding integrals are typed in red italic font.

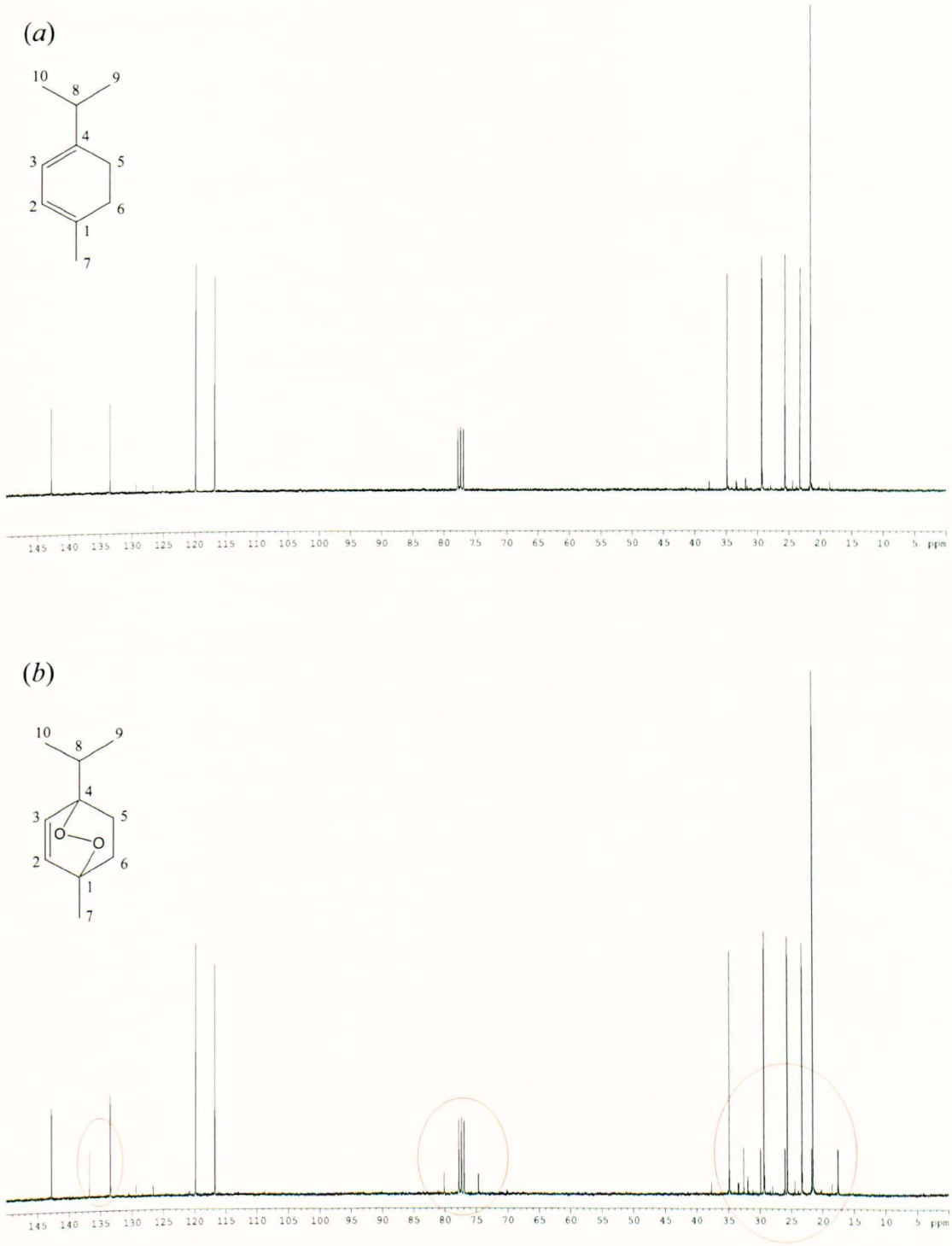

Figure D3. ^{13}C NMR spectra (in $CDCl_3$) of (*a*) α-terpinene, (*b*) α-terpinene after 3.5 hours of irradiation under *Xe* arc lamp illumination in annular recirculating photoreactor with 8.7×10^{-5} M *TPP* sensitizer. T = 20 °C, O_2 flowrate 30 mL min^{-1}. Ascaridol peaks: 17.1, 17.2, 21.3, 25.5, 29.4, 32.1, 74.3, 79.7, 133.0, 136.3 ppm [184].

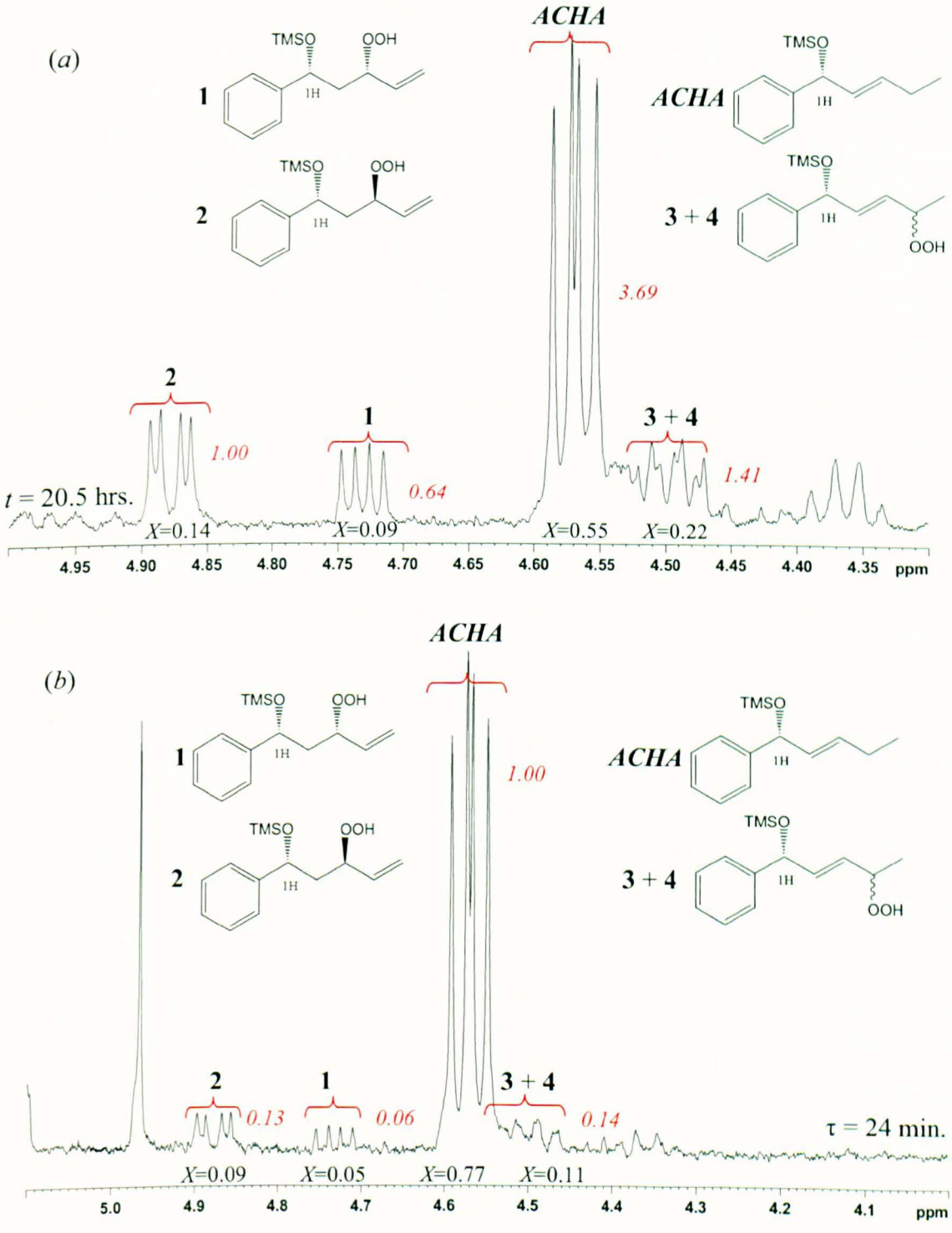

Figure D4. ^{1}H NMR spectra (in $CDCl_3$) of the *TMS* derivative of *ACHA* illuminated in the annular reactor by 420 nm actinic lamp for 20.5 hrs (*a*) and in the microreactor in continious mode at 10 μL min^{-1} illuminated by 420 nm LED array (*b*). T = 20 °C. Conversions X are calculated according to equation (3.19), **Experimental**. Values of corresponding integrals are typed in red italic font.

APPENDIX E: KINETIC MODELING

Let us propose simple kinetic model of $^1O_2$ generation and consumption inside the recirculating or batch photoreactor:

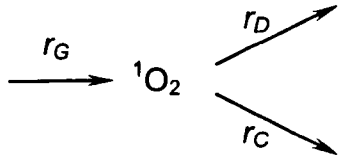

where $r_G = I_a \phi_{^1O_2}$, $r_D = k_D[^1O_2]$, and $r_C = k_R'[R][^1O_2]$ are the rates of $^1O_2$ generation, quenching of $^1O_2$ by solvent and consumption of $^1O_2$ in physical quenching and reaction with reagent R, correspondingly. k_D is first order $^1O_2$ decay constant, k_R' is an overall rate constant for physical quenching and chemical reaction of $^1O_2$ with R, I_a is intensity of light absorbed in the volume of reactor, and $\phi_{^1O_2}$ is quantum yield of $^1O_2$ generation.

In the case of quasistationary approximation the following equation holds true:

$$r_G = r_D + r_C \tag{E1}$$

Therefore, the steady state concentration of $^1O_2$ in this case can be expressed as follows:

$$[^1O_2] = \frac{I_a \phi_{^1O_2}}{k_D + k_R'[R]} \tag{E2}$$

From the other side, rate of reagent oxygenation by $^1O_2$ is expressed by equation (E3) with the rate constant k_R of chemical reaction of R with $^1O_2$:

$$\frac{d[R]}{dt} = -k_R[R][^1O_2] \tag{E3}$$

Combining the equation (E2) with the reaction rate expression (E3) it is possible to obtain the following differential equation:

$$\frac{d[R]}{dt} = -k_R[R]\frac{I_a \phi_{^1O_2}}{k_D + k_R'[R]}$$

or:

$$-\frac{\left(k_D + k_R'[R]\right)}{[R]} d[R] = I_a \phi_{^1O_2} k_R dt$$

This equation can be integrated from the initial concentration R_0 at t=0 to $[R]$ at the time t:

$$-k_D \int_{R_0}^{[R]} \frac{d[R]}{[R]} - k_R' \int_{R_0}^{[R]} d[R] = I_a \phi_{^1O_2} k_R t$$

After integration and rearrangements we obtain the solution as implicit function of reagent concentration or inverse function $t([R])$:

$$t = \frac{1}{I_a \phi_{^1O_2} k_R} \left(k_R' (R_0 - [R]) - k_D \ln \frac{[R]}{R_0} \right)$$

Finally, we can write this equation in terms of reagent conversion, $X_R = [R]/R_0$:

$$\boxed{t = \frac{1}{I_a \phi_{^1O_2} k_R} \left(k_D \ln X_R + k_R' R_0 (1 - X_R) \right)} \qquad \text{(E4)}$$

or in terms of product conversion, $X_P = 1 - X_R$:

$$\boxed{t = \frac{1}{I_a \phi_{^1O_2} k_R} \left(k_D \ln(1 - X_P) + k_R' R_0 X_P \right)} \qquad \text{(E5)}$$

In order to obtain the accumulation time in the feed tank we should apply equation (3.9) derived in **Experimental** to (E3) which lead after integration to (E6):

$$\boxed{t = \frac{V_\Sigma}{I_a V_R \phi_{^1O_2} k_R} \left(k_R' R_0 X_P - k_D \ln(1 - X_P) \right)} \qquad \text{(E6)}$$

where $V_\Sigma = V_R + V_T$ and V_R and V_T are volumes of a reactor and a recirculating tank, correspondingly.

REFERENCES

[1] N.J. Turro, G. Schuster, Photochemical Reactions as a Tool in Organic Syntheses, Science 187 (1975) 303-312.

[2] L.K. Doraiswamy, Organic Synthesis Engineering, Oxford University Press (2001) 815-855.

[3] C.G. Bochet, Wavelength-selective cleavage of photolabile protecting groups, Tetrahedron Letters 41 (2000) 6341-6346.

[4] M. Fisher, Industrial Applications of Photochemical Syntheses, Angew. Chem. Int. Ed. 17 (1978) 16-26.

[5] H. Lu, M.A. Schmidt, K.F. Jensen, Photochemical reactions and on-line UV detection in microfabricated reactors, Lab on a Chip 1 (2001) 22-28.

[6] R. Roberts, R.P. Ouellette, M.M. Muradaz, R.F. Cozzens, P.N. Cheremisinoff, Applications of Photochemistry, Lancaster, Pennsylvania: Technomic Publishing Co., Inc. (1984).

[7] T. Fukuyama, M.T. Rahman, M. Sato, I. Ryu, Adventures in inner space: microflow systems for practical organic synthesis, Synlett 2 (2008) 0151-0163.

[8] K. Jahnisch, V. Hessel, H. Lowe, M. Baerns, Chemistry in microstructured reactors, Angew. Chem. Int. Ed. 43 (2004) 406-446.

[9] Y. Matsushita, S. Kumada, K. Wakabayashi, K. Sakeda, T. Ichimura, Photocatalytic reduction in microreactors, Chem. Lett. 35 (2006) 410-411.

[10] T. Fukuyama, Y. Hino, N. Kamata, I. Ryu, Quick execution of [2+2] type photochemical cycloaddition reaction by continuous flow system using a glass-made microreactor, Chemistry Letters 33 (2004) 1430-1431.

[11] A. Sugimoto, Y. Sumino, M. Takagi, T. Fukuyama, I. Ryub, The barton reaction using a microreactor and black light. Continuous-flow synthesis of a key steroid

intermediate for an endothelin receptor antagonist, Tetrahedron Letters 47 (2006) 6197-6200.

[12] H. Maeda, H. Mukae, K. Mizuno, Enhanced efficiency and regioselectivity of intramolecular ($2\pi+2\pi$) photocycloaddition of 1-cyanonaphthalene derivative using microreactors, Chemistry Letters 34 (2005) 66-67.

[13] R.C.R. Wootton, R. Fortt, A.J.d. Mello, A Microfabricated Nanoreactor for Safe, Continuous Generation and Use of Singlet Oxygen, Org. Process Res. Dev. 6 (2002) 187-189.

[14] H. Ehrich, D. Linke, K. Morgenschweis, M. Baerns, K. Jahnisch, Application of Microstructured Reactor Technology for the Photochlorination of Alkylaromatics, Chimia 56 (2002) 647-653.

[15] K. Jahnisch, U. Dingerdissen, Photochemical Generation and [4+2]-Cycloaddition of Singlet Oxygen in a Falling Film Microreactor, Chem Eng. Technol. 28 (2005) 4.

[16] S. Meyer, D. Tietze, S. Rau, B. Schäfer, G. Kreisel, Photosensitized Oxidation of Citronellol in Microreactors, J. of Photochem. Photobiol. A: Chemistry 186 (2007) 248-253.

[17] K. Ueno, F. Kitagawa, N. Kitamura, Photocyanation of Pyrene Across an Oil/Water Interface in a Polymer Microchannel Chip, Lab. Chip 2 (2002) 231-234.

[18] G. Takei, T. Kitamori, H.-B. Kim, Photocatalytic Redox-Combined Synthesis of L-Pipecolinic Acid with a Titania-Modified Microchannel Chip, Catalysis Communications 6 (2005) 357-360.

[19] Y. Matsushita, N. Ohba, S. Kumada, K. Sakeda, T. Suzuki, T. Ichimura, Photocatalytic Reactions in Microreactors, Chemical Engineering Journal 135S (2007) S303-S308.

[20] N. Kitamura, K. Yamada, K. Ueno, S. Iwata, Photodecomposition of Phenol by Silica-Supported Porphyrin Derivative in Polymer Microchannel Chips, Journal of Photochemistry and Photobiology A: Chemistry 184 (2006) 170-176.

[21] R. Gorges, S. Meyer, G. Kreisel, Photocatalysis in Microreactors, Photochem. Photobiol. A: Chemistry 167 (2004) 95-99.

[22] A.G. Griesbeck, N. Maptue, S. Bondock, M. Oelgemöller, The Excimer Radiation System: a Powerful Tool for Preparative Organic Photochemistry. A technical note, Photochem. Photobiol. Sci 2 (2003) 450-451.

[23] A.A. Lapkin, V. Boddu, G.N. Aliev, B. Goller, S. Polisski, D. Kovalev, Photooxidation by Singlet Oxygen Generated on Nanoporous Silicon in a LED-Powered Reactor, Chem. Eng. J. 136 (2008) 331-336.

[24] M.C. DeRosa, R.J. Crutchley, Photosensitized Singlet Oxygen and its Applications, Coord. Chem. Rev. 233 (2002) 351-371.

[25] D.L. Gilbert, C.A. Colton, Reactive Oxygen Species in Biological System, Plenum (1999).

[26] J.G. Moser, Photodynamic Tumor Therapy: 2nd and 3rd Generation Photosensitizers, Gordon and Breach, London (1998).

[27] A.P. Schaap, A.L. Thayer, E.C. Blossey, D.C. Neckers, Polymer-based sensitizers for photooxidations, J. Am. Chem. Soc. 97 (1975) 3741-3745.

[28] R. Gerdes, O. Bartels, G. Schneider, D. Wohrle, G. Schulz-Ekloff, Photooxidations of phenol, cyclopentadiene and citronellol with photosensitizers ionically bound at a polymeric ion exchanger, Polym. Adv. Technol. 12 (2001) 152-160.

[29] J.L. Bourdelande, J. Font, G. Marques, A.A. Abdel-Shafi, F. Wilkinson, D.R. Worrall, On the efficiency of the photosensitized production of singlet oxygen in water suspensions of a tris(bipyridyl)ruthenium(II) complex covalently bound to an insoluble hydrophilic polymer, J. Photochem. Photobiol. A: Chem. 138 (2001) 65-68.

[30] R. Sasai, D. Sugiyama, S. Takahashi, Z. Tong, T. Shichi, H. Itoh, K. Takagi, The removal and photodecomposition of n-nonylphenol using hydrophobic clay incorporated with copper-phthalocyanine in aqueous media, J. Photochem. Photobiol. A: Chem. 155 (2003) 223-229.

[31] A.G. Griesbeck, A. Bartoschekstry, Sustainable photochemistry: solvent-free singlet oxygen-photooxygenation of organic substrates embedded in porphyrin-loaded polystyrene beads, Chem. Commun. (2002) 1594-1595.

[32] V. Iliev, A. Ileva, L. Bilyarska, Oxidation and photooxidation of sulfur-containing compounds in the presence of immobilized phthalocyanine complexes, J. Mol. Catal. 126 (1997) 99-108.

[33] M. Fujii, M. Usui, S. Hayashi, E. Gross, D. Kovalev, N. Kunzner, J. Diener, V.Y. Timoshenko, Chemical Reaction Mediated by Excited States of Si Nanocrystals: Singlet Oxygen Formation in Solution, J. Appl. Phys. 95 (2004) 3689-3693.

[34] D. Kovalev, M. Fujii, Silicon Nanocrystals: Photosensitizers for Oxygen Molecules, Adv. Mater. 17 (2005) 1-15.

[35] M. Prein, W. Adam, The Schenck Ene Reaction: Diastereoselective Oxyfunctionalization with Singlet Oxygen in Synthetic Applications, Angew. Chem. Int. Ed. Engl. 35 (1996) 477-494.

[36] A.V. Malkov, M. Bell, M. Orsini, D. Pernazza, A. Massa, P. Herrmann, P. Kocovsky, New Lewis-Basic N-Oxides as Chiral Organocatalysts in Asymmetric Allylation of Aldehydes, J. Org. Chem. 68 (2003) 9659-9668.

[37] A.V. Malkov, M. Orsini, D. Pernazza, K.W. Muir, V. Langer, P. Meghani, P. Kocovsky, Chiral 2,2'-Bipyridine-Type N-Monoxides as Organocatalysts in the Enantioselective Allylation of Aldehydes with Allyltrichlorosilane, Org. Lett. 4 (2002) 1047-1049.

[38] A.V. Malkov, M. Bell, F. Castelluzzo, P. Kocovsky, METHOX: A new pyridine N-oxide organocatalyst for the asymmetric allylation of aldehydes with allyltrichlorosilanes, Org. Lett. 7 (2005) 3219-3222.

[39] A.V. Malkov, A. Mariani, K.N. MacDougal, P. Kocovsky, Role of noncovalent interactions in the enantioselective reduction of aromatic ketimines with trichlorosilane, Org. Lett. 6 (2004) 2253-2256.

[40] A.V. Malkov, S. Stoncius, K.N. MacDougal, A. Mariani, G.D. McGeoch, P. Kocovsky, Formamides derived from N-methyl amino acids serve as new chiral organocatalysts in the enantioselective reduction of aromatic ketimines with trichlorosilane, Tetrahedron, Symposium-in-print on organocatalysis 62 (2006) 264-284.

[41] A.V. Malkov, D. Pernazza, M. Bell, M. Bella, A. Massa, P. Teply, P. Meghani, P. Kocovsky, Synthesis of new chiral 2,2'-bipyridine ligands and their application in the copper-catalyzed asymmetric allylic oxidation and cyclopropanation, J. Org. Chem. 68 (2003) 4727-4742.

[42] L. Cointeaux, J.-F. Berrien, J. Mahuteau, M.E.T. Huu-Dâu, L. Cicéron, M. Danis, J. Mayrargue, A Short Synthesis of Antimalarial Peroxides, Bioorganic & Medicinal Chemistry 11 (2003) 3791-3794.

[43] W. Adam, S.R. Saha-Moller, K.C. Schmid, Preparation of optically active allylic hydroperoxy alcohols and 1,3-diols by enzyme-catalyzed kinetic resolution and photooxygenation of chiral homoallylic alcohols, J. Org. Chem 65 (2000) 1431-1433.

[44] J.C. Morales, E.T. Kool, Minor Groove Interactions between Polymerase and DNA: More Essential to Replication than Watson-Crick Hydrogen Bonds?, J. Am. Chem. Soc. 121 (1999) 2323-2324.

[45] H. Liu, J. Gao, L. Maynard, D. Satio, E.T. Kool, Toward a new genetic system with expanded dimensions: size-expanded analogues of deoxyadenosine and thymidine, J. Am. Chem.Soc. 126 (2004) 1102-1109.

[46] A.H.F. Lee, E.T. Kool, A new four-base genetic helix, yDNA, composed of widened benzopyrimidine-purine pairs, J. Am. Chem. Soc. 127 (2005) 3332-3338.

[47] H. Lu, K. He, E.T. Kool, yDNA: a new geometry for size-expanded base pairs, Angew. Chem. Int. Ed. 43 (2005) 5834-5836.

[48] L.D. Landau, E.M. Lifshits, Quantum Mechanics (Nonrelativistic Theory), Moscow: Nauka V 3 (1989).

[49] P.W. Atkins, R.S. Friedman, Molecular Quantum Mechanics, New York: Oxford University Press (2005).

[50] G. Wypych, Handbook of Material Weathering (4th Edition), ChemTec Publishing (2008).

[51] Y.A. Zolotov, Foundations of Analytical Chemistry. Methods of Chemical Analysis, Moscow, Vysshaya Shkola (2002).

[52] J.-C. Andre, M.-L. Viriot, J. Villermaux, New Developments in Photochemical Technology, Pure & Appl. Chem. 58 (1986) 907-916.

[53] A.F. Carey, R.J. Sundberg, Advanced Organic Chemistry-Part A: Structure and Mechanisms (5th Edition), Springer-Verlag (2007) 1073-1112.

[54] F. Wilkinson, W.P. Helman, A.B. Ross, Quantum Yields for the Photosensitized Formation of the Lowest Electronically Excited Singlet State of Molecular Oxygen in Solution, J. Phys. Chem. Ref. Data 22 (1993) 113-262.

[55] N.J. Turro, Modern Molecular Photochemistry, University Science Books, Sausalito, CA (1991).

[56] C. Schweitzer, R. Schmidt, Physical Mechanisms of Generation and Deactivation of Singlet Oxygen, Chem. Rev. 103 (2003) 1685-1757.

[57] W.H.J. Childs, R.Z. Mecke, Intensity measurements in the atmospheric oxygen band at 7600 A, Z. Phys. 68 (1931) 344-361.

[58] L. Wallace, D.M. Hunten, Dayglow of the Oxygen A Band, J. Geophys. Res. 73 (1968) 4813-4834.

[59] L. Villen, F. Manjon, D. Garcıa-Fresnadillo, G. Orellana, Solar Water Disinfection by Photocatalytic Singlet Oxygen Production in Heterogeneous Medium, Applied Catalysis B: Environmental 69 (2006) 1-9.

[60] T. Maisch, J. Baier, B. Franz, M. Maier, M. Landthaler, R. Szeimies, W. Baumler, The Role of Singlet Oxygen and Oxygen Concentration in Photodynamic Inactivation of Bacteria, PNAS 104 (2007) 7223-7228.

[61] L. Packer, H. Sies, Methods in Enzymology, Singlet Oxygen, UV-A, and Ozone, Academic, London (2000) 319.

[62] D.B. Min, J.M. Boff, Chemistry and reaction of singlet oxygen in foods, Compr. Rev. Food Sci. Food Saf. 1 (2002) 58-72.

[63] I.E.Kochevar, M.C. Lynch, S. Zhuang, C.R. Lambert, Singlet oxygen, but not oxidizing radicals, induces apoptosis in HL-60 cells, Photochem. Photobiol. 72 (2000) 548-553.

[64] F. Wilkinson, W.P. Helman, A.B. Ross, Rate Constants for the Decay and Reactions of the Lowest Electronically Excited Singlet State of Molecular Oxygen in Solution. An Expanded and Revised Compilation, J. Phys. Chem. Ref. Data 24 (1995) 663-1021.

[65] H. Tsubomura, R.S. Mulliken, Molecular Complexes and their Spectra. XII. Ultraviolet Absorption Spectra Caused by the Interaction of Oxygen with Organic Molecules, J. Am. Chem. Soc. 82 (1960) 5966-5974.

[66] S.L. Logunov, M.A.J. Rodgers, Laser flash photolysis studies of the contact complex between molecular oxygen and 1-methylnaphthalene, J. Phys. Chem. 97 (1993) 5643-5648.

[67] D.J. McGarvey, F. Wilkinson, D.R. Worrall, J. Hobley, W. Shaikh, Picosecond absorption studies on the role of charge transfer interactions in the mechanism of quenching of triplet states by molecular oxygen, Chem. Phys. Lett. 202 (1993) 528-534.

[68] D.J. Carlsson, T. Suprunchuk, D.M.Wiles, The Quenching of Singlet Oxygen ($^1\Delta_g$) by Transition Metal Chelates, Can. J. Chem. 52 (1974) 3728-3737.

[69] C.S. Foote, Photosensitized oxygenations and the role of singlet oxygen, Acc. Chem. Res. 1 (1968) 104-110.

[70] D.R. Kearns, Physical and Chemical Properties of Singlet Molecular Oxygen, Chemical Reviews 71 (1971) 395-427.

[71] A.A. Gorman, G. Lovering, M.A.J. Rodgers, A pulse radiolysis study of the triplet sensitized production of singlet oxygen: determination of energy transfer efficiencies, J. Am. Chem. Soc. 100 (1978) 4527-4532.

[72] R. Schmidt, Photosensitized Generation of Singlet Oxygen, Photochemistry and Photobiology 82 (2006) 1161-1177.

[73] R. Schmidt, F. Shafii, C. Schweitzer, A.A. Abdel-Shafi, F. Wilkinson, Charge Transfer and Non-Charge Transfer Processes Competing in the Sensitization of Singlet Oxygen: Formation of $O_2(^1\Sigma)$, $O_2(^1\Delta)$, and $O_2(^3\Sigma)$ During Oxygen Quenching of Triplet Excited Naphthalene derivatives, J. Phys. Chem. A 105 (2001) 1811-1817.

[74] C. Schweitzer, Z. Mehrdad, A. Noll, E.W. Grabner, R. Schmidt, Mechanism of photosensitized generation of singlet oxygen during oxygen quenching of triplet states and the general dependence of the rate constants and efficiencies of $O_2(^1\Sigma)$, $O_2(^1\Delta)$, and $O_2(^3\Sigma)$ formation on sensitizer triplet state energy and oxidation potential, J. Phys. Chem. A 107 (2003) 2192-2198.

[75] D. Rehm, A. Weller, Kinetics of fluorescence quenching by electron and H-atom transfer, Isr. J. Chem. 8 (1970) 259.

[76] S.L. Mattes, S. Farid (Eds.), Organic Photochemistry, Marcel Dekker, New York, 1983.

[77] C. Schweitzer, Z. Mehrdad, A. Noll, E.W. Grabner, R. Schmidt, Oxygen Quenching of nπ* Triplet Phenyl Ketones: Local Excitation and Local Deactivation, Helv. Chim. Acta 84 (2001) 2493-2507.

[78] R. Schmidt, Quantitative Determination of $^1\Sigma$ and $^1\Delta$ Singlet Oxygen in Solvents of Very Different Polarity. General Energy Gap Law for Rate Constants of Electronic Energy Transfer to and From O_2 in the Absence of Charge Transfer Interactions, J. Phys. Chem. A 110 (2006) 2622-2628.

[79] F. Wilkinson, D.J. McGarvey, A.F. Olea, Factors Governing the Efficiency of Singlet Oxygen Production During Oxygen Quenching of Singlet and Triplet States of Anthracene Derivatives in Cyclohexane Solution, J. Am. Chem. Soc. 115 (1993) 12144-12151.

[80] D. Kovalev, E. Gross, N. Kunzner, F. Koch, V.Y. Timoshenko, M. Fujii, Efficient Resonant Electronic Energy Transfer from Excitons Confined in Silicon Nanocrystals to Oxygen Molecules, Phys. Rev. Lett. 89 (2002) 1-4.

[81] M. Fujii, D. Kovalev, B. Goller, S. Minobe, S. Hayashi, V.Y. Timoshenko, Time-Resolved Photoluminescence Studies of the Eenergy Transfer From Excitons Confined in Si Nanocrystals to Oxygen Molecules, Phys. Rev. B 72 (165321) (2005) 1-8.

[82] E. Gross, D. Kovalev, N. Kunzner, J. Diener, F. Koch, V.Y. Timoshenko, M. Fujii, Spectrally Resolved Electronic Energy Transfer From Silicon Nanocrystals to Molecular Oxygen Mediated by Direct Electron Exchange, Phys. Rev. B 68 (115405) (2003) 1-11.

[83] M. Fujii, S. Minobe, M. Usui, S. Hayashi, E. Gross, J. Diener, D. Kovalev, Generation of Singlet Oxygen at Room Temperature Mediated by Energy Transfer from Photoexcited Porous Si, Phys. Rev. B 70(085311) (2004) 1-5.

[84] D. Kovalev, E. Gross, J. Diener, V.Y. Timoshenko, M. Fujii, Photodegradation of Porous Silicon Induced by Photogenerated Singlet Oxygen Molecules, Appl. Phys. Lett. 85 (2004) 3590-3592.

[85] M. Fujii, M. Usui, S. Hayashi, E. Gross, D. Kovalev, N. Künzner, J. Diener, V.Y. Timoshenko, Singlet Oxygen Formation by Porous Si in Solution, Phys. Stat. Sol. A 202 (2005) 1385-1389.

[86] D. Kovalev, E. Gross, J. Diener, V. Timoshenko, M. Fujii, Photoluminescence Fatigue Effect in Luminescent Porous Silicon, Phys. Sstat. Sol. C 2 (2005) 3188-3192.

[87] M. Fujii, N. Nishimura, H. Fumon, S. Hayashi, D. Kovalev, B. Goller, J. Diener, Dynamics of Photosensitized Formation of Singlet Oxygen by Porous Silicon in Aqueous Solution, J. Appl. Phys. 100 (2006) 124302.

[88] D. Neiner, H.W. Chiu, S.M. Kauzlarich, Low-Temperature Solution Route to Macroscopic Amounts of Hydrogen Terminated Silicon Nanoparticles, J. Am. Chem. Soc. 128 (2006) 11016-11017.

[89] H. Foll, M. Christophersen, J. Carstensen, G. Hasse, Formation and Application of Porous Silicon, Materials Science and Engineering: R 39 (2002) 93-141.

[90] S. Limaye, S. Subramanian, B. Goller, J. Diener, D. Kovalev, Scaleable synthesis route for silicon nanocrystal assemblies, Phys. Stat. Sol. A. 204 (2007) 1297-1301.

[91] V. Lehmann, U. Gsele, Porous silicon formation: a quantum wire effect, Appl. Phys. Lett. 58 (1991) 856-858.

[92] D. Kovalev, H. Heckler, M. Ben-Chorin, G. Polisski, M. Schwartzkopff, F. Koch, Breakdown of the k-conservation rule in Si nanocrystals, Phys. Rev. Lett. 81 (1998) 2803-2806.

[93] D. Kovalev, H. Heckler, G. Polisski, F. Koch, Optical properties of silicon nanocrystals, Phys. Status Solidi B 215 (1999) 871-932.

[94] A.G. Cullis, L.T. Canham, P.D.J. Calcott, The structural and luminescence properties of porous silicon, J. Appl. Phys. 82 (1997) 909-965.

[95] B. Goller, S. Polisski, D. Kovalev, Spin-flip Excitation of Molecules Mediated by Photoexcited Silicon Nanocrystalls, Phys. Rev. B 75 (2007) 073403.

[96] S. Polisski, B. Goller, A. Lapkin, S. Fairclough, D. Kovalev, Synthesis and catalytic activity of hybrid metal/silicon nanocomposites
Phys. Status Solidi (RRL) 2:3 ((2008)) 132-134

[97] R. Schmidt, M. Bodesheim, Radiationless Deactivation of the Second Excited Singlet State $^1\Sigma$ of O_2 in Solution, J. Phys. Chem. A 102 (1995) 4769-4774.

[98] C.S. Foote, Mechanisms of Photosensitized Oxidation, Science 162 (1968) 963-970.

[99] K. Gollnick, Type II Photooxygenation Reactions in Solution, Adv. Photochem. 6 (1968) 1-122.

[100] E.L. Clennan, Synthetic and mechanistic aspects of 1,3-diene photooxidation, Tetrahedron 47 (1991) 1343-1382.

[101] E.L. Clennan, K. Nagraba, Additions of singlet oxygen to alkoxy-substituted dienes. The mechanism of the singlet oxygen 1,2-cycloaddition reaction, J. Am. Chem. Soc. 110 (1988) 4312-4318.

[102] M. Bobrowski, A. Liwo, S. Oldziej, D. Jeziorek, T. Ossowski, CAS MCSCF/CAS MCQDPT2 Study of the Mechanism of Singlet Oxygen Addition to 1,3-Butadiene and Benzene, J. Am. Chem. Soc. 122 (2000) 8112-8119.

[103] E.L. Clennan, Oxygenated Processes 1, JAI Press, Greenwich, Connecticut (1988) 85-122.

[104] F. Ohloff, Singlet oxygen: A reagent in organic synthesis, Pure Appl. Chem. 43 (1975) 481-502.

[105] H.H. Wasserman, J.L. Ives, Singlet oxygen in organic synthesis, Tetrahedron 37 (1981) 1825-1852.

[106] W. Adam, M. Braun, A. Griesbeck, V. Lucchini, E. Staab, B. Will, Photooxygenation of Olefins in the Presence of Titanium (IV) Catalyst: A Convenient One-Pot Synthesis of Epoxy Alcohols, J. Am. Chem. Soc. 111 (1989) 203-212.

[107] W. Adam, M.J. Richter, Metal-Catalyzed Direct Hydroxy-Epoxidation of Olefins, Acc. Chem. Res. 27 (1994) 57-62.

[108] E.D. Mihelich, D.J. Eickhoff, One-pot Conversion of Olefins to α, β-unsaturated Carbonyl Compounds. An Easy Synthesis of 2-cyclopentenone and related compounds, J. Org. Chem. 48 (1983) 4135-4137.

[109] W. Adam, M.J. Richter, One-Pot Synthesis of Trimethylsilyl Enones from Vinylsilanes Synthesis, Synthesis (1994) 176-180.

[110] W. Adam, P. Klug, A Convenient Stereoselective Synthesis of α-Tributylstannyl Enones by Photooxygenation of Vinylstannanes and Dehydration of the Resulting Hydroperoxides, Synthesis (1994) 557-559.

[111] M. Pape, Industrial Applications of Photochemistry, Pure Appl. Chem. 41 (1975) 535-558.

[112] A.M. Braun, M.T. Maurette, E. Oliveros, Photochemical Technology, Wiley, Chichester (1991).

[113] M. Bass, Handbook of Optics, Fundamentals, Techniques and Design (2nd Edition), McGraw-Hill 1 (1995).

[114] M.A. Laughton, D.F. Warne, Electrical Engineer's Reference Book, Elsevier (2003).

[115] D.A. Snow, Plant Engineer's Reference Book, Elsevier (2002).

[116] http://www.lamptech.co.uk (Accessed on 10 November 2008).

[117] J.C. Scaiano, Handbook of Organic Photochemistry, CRC Press Inc., Boca Raton II (1989).

[118] Glossary of terms used in photochemistry, (2005).

[119] D.R. Wulfinghoff, Energy Efficiency Manual, Energy Institute Press (1999).

[120] M. Köfferlein, T. Döhring, H.D. Payer, H.K. Seidlitz, Xenon Lighting Adjusted to Plant Requirements, in: T.W. Tibbitts (Ed.), International Lighting in Controlled Environments Workshop, 1994.

[121] G. Courret, L. Calame, A. Meyer, Environmental Friendly High Efficient Light Source Plasma Lamp-Final Report, Swiss Federal Office of Energy, Available from: http://www.bfe.admin.ch (Accessed on 10 November 2008). 2007.

[122] M. Siminovitch, C. Gould, E. Page, A High-Efficiency Indirect Lighting System Utilizing the Solar 1000 Sulfur Lamp, Proceedings of the Right Light, 4 Conference in Copenhagen, Denmark, 1997.

[123] http://www.rp-photonics.com/light_emitting_diodes.html (Accessed on 10 November 2008).

[124] J. Han, A.V. Nurmikko, Advances in AlGaInN blue and ultraviolet light emitters, IEEE J. Sel. Top. Quant. Electron. 8 (2002) 289-297.

[125] K. Streubel, N. Linder, R. Wirth, A. Jaeger, High Brightness AlGaInP Light-Emitting Diodes, IEEE J. Sel. Top. Quantum Electron 8 (2002) 321-332.

[126] J.M. Phillips, M.E. Coltrin, M.H. Crawford, A.J. Fischer, M.R. Krames, R. Mueller-Mach, G.O. Mueller, Y. Ohno, L.E.S. Rohwer, J.A. Simmons, J.Y. Tsao, Research Challenges to Ultra-Efficient Inorganic Solid-State Lighting, Laser & Photon. Rev. 1 (2007) 307-333.

[127] N. Zheludev, The Life and Times of the LED - a 100-year history, Nat. Photonics 1 (2007) 189.

[128] R.H. Horng, P. Han, D.S. Woo, Phosphor-Free White Light from InGaN Blue and Green Light-Emitting Diode Chips Covered with Semiconductor-Conversion AlGaInP Epilayer, IEEE Photon. Technol. Lett. 20 (2008) 1139-1141.

[129] D.A. Steigerwald, J.C. Bhat, D. Collins, R.M. Fletcher, M.O. Holcomb, M.J. Ludowise, P.S. Martin, S.L. Rudaz, Illumination With Solid State Lighting Technology, IEEE Journal on selected topics in quantum electronics 8 (2002) 310-320.

[130] D. Morita, M. Yamamoto, K. Akaishi, K. Matoba, K. Yasutomo, Y. Kasai, M. Sano, S. Nagahama, T. Mukai, Watt-Class High-Output-Power 365nm Ultraviolet Light-Emitting Diodes, Japanese Journal of Applied Physics 43 (2004) 5945-5950.

[131] E.F. Schubert, Light Emitting Diodes, Cambridge University Press (2006).

[132] www.heraeus-noblelight.com (Accessed on 10 November 2008).

[133] J.A.G. Williams, K. Mullen, U. Scherf, Organic Light-Emitting Devices: Synthesis, Properties and Applications, Platinum Metals Rev. 51 (2007) 85-86.

[134] N.K. Patel, S. Cinà, J.H. Burrows, High-Efficient Organic Light-Emitting Diodes, IEEE J. Sel. Top. Quantum Electron. 8 (2002) 346-361.

[135] G. Schenk, Multi-chamber photoreactor, US 4296066 (1981).

[136] http://www.photochemicalreactors.co.uk/immersion.htm (Accessed on 10 November 2008).

[137] F. Duttil, Photobioreactor, US 6602703 (2003).

[138] H. Wedekamp, Device and Method of UV Irradiation, Especially for Disinfecting, Flowing Liquids with Reduced UV-Transmission, US 6500312 (2002).

[139] M.F.J. Dijkstra, H. Buwalda, A.W.F.d. Jong, A. Michorius, J.G.M. Winkelman, A.A.C.M. Beenackers, Experimental Comparison of Three Reactor Designs for Photocatalytic Water Purification, Chemical Engineering Science 56 (2001) 547-555.

[140] N.J. Peill, M.R. Hoffmann, Development and Optimization of a TiO_2-Coated Fiber Optic Cable Reactor: Photocatalytic Degradation of 4-Chlorophenol, Environ. Sci. Technol. 29 (1995) 2974-2981.

[141] N.J. Peill, M.R. Hoffmann, Mathematical Model of Photocatalytic Fiber-Optic Cable Reactor for Heterogeneous Photocatalysis, Environ. Sci. Technol. 32 (1998) 398-404.

[142] J.C.S. Wu, H.M. Lin, Photo Reduction of Carbon Dioxide to Methanol Via TiO_2 Photocatalyst, Int. J. of Photoenergy 7 (2005) 116-119.

[143] J.A. Cooke, G.D. Austin, M.J. McGarritty, Flow-through Photochemical Reactor, US 5696380 (1997).

[144] H.I.D. Lasa, J. Valladares, Photocatalytic reactor, US 5683589 (1997).

[145] P. Gao, W.H. Ching, M. Herrmann, C.W. Chan, P.L. Yue, Photooxidation of a Model Pollutant in an Oscillatory Flow Reactor with Baffles, Chem. Eng. Sci. 58 (2003) 1013-1020.

[146] S. Dezhi, C. Sheng, J.S. Chung, D. Xiaodong, Z. Zhibin, Photocatalytic Degradation of Toluene Using a Novel Flow Reactor with Fe-doped TiO_2 Catalysts on Porous Nickel Sheets, Photochem. Photobiol. 81 (2005) 352-357.

[147] M.A. Anderson, S. Tunesi, Q. Xu, Degradation of Organic Chemicals with Titanium Ceramic Membranes, US 5035784 (1991).

[148] A. Muller-Fuega, Method of Improving the Performance of Photobioreactor, US 6492149 (2002).

[149] A.K. Ray, A.A. Beenackers, Development of a New Photocatalytic Reactor for Water Purification, Catal. Today 40 (1998) 73 - 80.

[150] H. Lin, K.T. Valsaraj, Development of an Optical Fiber Monolith Reactor for Photocatalytic Wastewater Treatment, Journal of Applied Electrochemistry 35 (2005) 699-708.

[151] D. Meissner, Patent W02/062465 A1, (2002).

[152] N.J. Peill, M.R. Hoffmann, Chemical and physical characterization of a TiO_2 - coated fiber optic cable reactor, Environ. Sci. Technol. 30 (1996) 2806-2812.

[153] J. Hutson, R.S. Logan, Development of a commercial photochlorlnation reactor, Chem. Eng. Prog. 68 (1972) 76.

[154] A.R. Tymoschuk, O.M. Alfano, A.E. Cassano, The Multitubular Photoreactor, Ind. Eng.Chem. Res. 32 (1993) 1328-1341.

[155] http://www.mikroglas.com (Accessed on 10 November 2008).

[156] A. Sugimoto, T. Fukuyama, Y. Sumino, M. Takagi, I. Ryu, Microflow photo-radical reaction using a compact light source: application Barton reaction leading to a key intermediate for myriceric acid A, Tetrahedron 65 (2009) 1593-1598.

[157] B.D.A. Hook, W. Dohle, P.R. Hirst, M. Pickworth, M.B. Berry, K.I. Booker-Milburn, A Practical Flow Reactor for Continuous Organic Photochemistry, J. Org. Chem. 70 (2005) 7558-7564.

[158] T. Carofiglio, P. Donnola, M. Maggini, M. Rossetto, E. Rossi, Fullerene-Promoted Singlet-Oxygen Photochemical Oxygenations in Glass-Polymer Microstructured Reactors, Adv. Synth. Catal. 350 (2008) 2815-2822.

[159] R.A. Bourne, X. Han, M. Poliakoff, M.W. George, Cleaner Continuous Photo-Oxidation Using Singlet Oxygen in Supercritical Carbon Dioxide, Angew. Chem. Int. Ed. 48 (2009) 5322-5325.

[160] L.J. Governale, J.T. Clarke, Chem. Eng. Prog. 52 (1956) 281.

[161] C. Beermann, Normal Paraffins Supplement, Eur. Chem. News 2 (1966) 36.

[162] G.O. Schenck, German Patent 933925, (1943).

[163] P. Esser, B. Pohlmann, H.-D. Scharf, The Photochemical Synthesis of Fine Chemicals with Sunlight, Angew. Chem. Int. Ed. Engl 33 (1994) 2009-2023.

[164] F. Ohloff, E. Klein, G.O. Schenck, Darstellung von Rosenoxyden und anderen Hydropyran-Derivaten über Photohydroperoxyde, Angew. Chem. 73 (1961) 578.

[165] K. Gollnik, Photooxygenation and its Application in Industry, Chem. Industr. 64 (1982) 156-166.

[166] N. Monnerie, J. Ortner, Economic Evaluation of the Industrial Photosynthesis of Rose Oxide via Lamp or Solar Operated Photooxidation of Citronellol, Journal of Solar Energy Engineering 123 (2001) 171-175.

[167] http://www.lumigen.com/documents/LumigenPPD.shtml (Accessed on 10 November 2008).

[168] A.P. Schaap, U.S. patent 887139.

[169] P. Schaap, R.S. Handley, B.P. Giri, Chemical and Enzymatic Triggering of 1,2-Dioxetanes. 1: Aryl Esterase-Catalyzed Chemiluminescence from a Naphthyl Acetate-Substituted 1,2-Dioxetane, Tetrahedron Lett. (1987) 935-938.

[170] A.P. Schaap, M.D. Sandison, R.S. Handley, Chemical and Enzymatic Triggering of 1,2-Dioxetanes. 3: Alkaline Phosphatase-Catalyzed Chemiluminescence from an Aryl Phosphate-Substituted Dioxetane, Tetrahedron Lett. (1987) 1159-1163.

[171] D.C. Neckers, E.C. Blossey, A.P. Schaap, Polymer Based Photosensitizers, U.S. Patent No. 4315998, Canadian Patent No 1044639 (1979).

[172] J. Lehr, J. Keeley, J. Lehr, Photocatalytic Membrane Reactors in Water Purification, Water Encyclopedia, John Wiley & Sons 1-5 (2005) 791-797.

[173] Field Testing of a Solar Assisted System for Detoxification of Water http://es.epa.gov/ncerqa_abstracts (Accessed on 10 November 2008).

[174] J.C. Ireland, P. Klostermann, E.W. Rice, R.M. Clark, Inactivation of Escheria Coli by Titanium Dioxide Photocatalytic Oxidation, Applied and Environmental Microbiology 59 (1993) 1668-1670.

[175] Purifics, http://www.purifics.com/technology/index.html (Accessed on 10 November 2008).

[176] AirOasis, http://www.airoasis.com (Accessed on 10 November 2008).

[177] Biozone PureWare, Biozone Air Purifiers Technology (2007).

[178] Heaven Fresh, http://www.heavenfresh.co.uk (Accessed on 10 November 2008).

[179] C.G. Hatchard, C.A. Parker, A New Sensitive Chemical Actinometer. II. Potassium Ferrioxalate as a Standard Chemical Actinometer, Proc. Roy. Soc. Lond. A 235 (1956) 518-536.

[180] PhotochemCAD Spectra http://omlc.ogi.edu/spectra/PhotochemCAD/html/rhodamine6G.html (Accessed on November 2008).

[181] http://fosterandsmithaquatics.com/Product/prod_display.cfm?pcatid=4511& (Accessed on 12 January, 2011).

[182] https://iquaticsonline.co.uk/components/com_virtuemart/shop_image/product/10k250wspec.jpg (Accessed January, 27).

[183] R.J. Abraham, M.A. Cooper, H. Indyk, T.M. Siverns, D. Whittaker, The NMR spectra and conformations of cyclic compounds-VII: The conformations of β-pinene, pinocarvone and the *cis*- and *trans*-pinocarveols, Organic Magnetic Resonance 5 (1973) 373-377.

[184] F. Kiuchi, Y. Itano, N. Uchiyama, G. Honda, A. Tsubouchi, J. Nakajima-Shimada, T. Aoki, Monoterpene hydroperoxides with trypanocidal activity from *Chenopodium ambrosioides*, J. Nat. Prod. 65 (2002) 509-512.

[185] D.A. Johnson, Handbook of Optical Through the Air Communications, Imagineering E-Zine, 2008.

[186] J.S. Miller, Rose bengal-sensitized photooxidation of 2-chlorophenol in water using solar simulated light, Water Research 39 (2005) 412-422.

[187] I. Willner, Y. Eichen, E. Joselevich, Photosensitized Electron-Transfer Reactions and H_2 Evolution in Organized Microheterogeneous Environments: Separation of Ground-State Xanthene-Bipyridinium Complexes by SiO_2 Colloids, J. Phys. Chem. 94 (1990) 3092-3098.

[188] G.D. Luca, A. Romeo, L.M. Scolaro, G. Ricciardi, A. Rosa, Evidence for Tetraphenylporphyrin Monoacids, Inorganic Chemistry 46 (2007) 5979-5988.

[189] E. Austin, M. Gouterman, Porphyrins. XXXVII. Absorption and Emission of Weak Complexes with Acids, Bases, and Salts, Bioinorganic chemistry 9 (1978) 281-298.

[190] V.S. Chirvony, A.v. Hoek, V.A. Galievsky, I.V. Sazanovich, T.J. Schaafsma, D. Holten, Comparative Study of the Photophysical Properties of Nonplanar Tetraphenylporphyrin and Octaethylporphyrin Diacids, J. Phys. Chem B 104 (2000) 9909-9917.

[191] D. Gryglik, M. Lach, J.S. Miller, The aqueous photosensitized degradation of butylparaben, Photochem. Photobiol. Sci. 8 (2009) 549-555.

[192] M. Ferrer, F. Sanchez-Baeza, A. Messeguer, W. Adam, D. Golsch, F. Görth, W. Kiefer, V. Nagel, The Release of Singlet Oxygen in the Reaction of Dioxiranes with Amine N-Oxides, Eur. J. Org. Chem. (1998) 2527-2532.

[193] W. Adam, M. Schwarm, How mechanistically equivalent are singlet oxygen and triazolinedione? Regiochemical and Stereochemical Differences in Their Ene Reactions with Allylsilanes. , J. Org. Chem. 53 (1988) 3129-3130.

[194] K. Shirono, T. Morimatsu, F. Takemura, Gas Solubilities (CO_2, O_2, Ar, N_2, H_2, and He) in Liquid Chlorinated Methanes, J. Chem. Eng. Data 53 (2008) 1867-1871.

[195] C.B. Kretschmer, J. Nowakowska, R. Wiebe, Solubility of Oxygen and Nitrogen in Organic Solvents from -25° to 50° C, Industrial and Engineering Chemistry 38 (1946) 506-509.

[196] S. Waelchli, P.R.v. Rohr, Two-phase flow characteristics in gas-liquid microreactors, International Journal of Multiphase Flow 32 (2006) 791-806.

[197] D.M. Fries, S. Wälchli, P.R.v. Rohr, Gas-liquid two-phase flow in meandering microchannels, Chemical Engineering Journal 135 (2008) 37-45.

[198] N. Kim, Multiphase Flows in Polymer Microfluidic Systems, Department of Mechanical Engineering, Louisiana State University, 2009. p. 159.

[199] B.A. Wilhite, B. Blackwell, J. Kacmar, A. Varma, M.J. McCready, Origins of Pulsing Regime in Cocurrent Packed-Bed Flows, Ind. Eng. Chem. Res. 44 (2005) 6056-6066.

[200] L.D. Anadon, A.J. Sederman, L.F. Gladden, Mechanism of the Trickle-to-Pulse Flow Transition in Fixed-Bed Reactors, AIChE Journal 52 (2006) 1522-1532.

[201] F. Trachsel, C. Hutter, P.R.v. Rohr, Transparent silicon/glass microreactor for high-pressure and high-temperature reactions, Chemical Engineering Journal 135 (2008) 309-316.

[202] P.K. Plucinski, D.V. Bavykin, S.T. Kolaczkowski, A.A. Lapkin, Liquid-Phase Oxidation of Organic Feedstock in a Compact Multichannel Reactor, Ind. Eng. Chem. Res. 44 (2005) 9683-9690.

[203] A.K. Mogalicherla, D. Kunzru, Effect of Gas and Liquid Superficial Velocities on the Performance of Monolithic Reactors, Ind. Eng. Chem. Res. 49 (2010) 1631-1641.

[204] G. Berčič, A. Pintar, Chemical Engineering Science, The role of gas bubbles and liquid slug lengths on mass transport in the Taylor flow through capillaries 52 (1997) 3709-3719.

[205] I.B.C. Matheson, D.A. Lightner, Oxodipyrromethenes as Reactive Singlet Oxygen Acceptors. Measurement of their Chemical Reaction Rates by a Laser Flash Photolysis Technique, Photochem. Photobiol. 29 (1979) 933-935.

[206] J.L. Coffer, S.C. Lilley, R.A. Martin, L.A. Files-Sesler, The effect of Lewis base chemisorption on the luminescence of porous silicon, Mat. Res. Soc. Symp. Proc. 283 (1993) 305-310.

[207] J.L. Coffer, S.C. Lilley, R.A. Martin, L.A. Files-Sesler, Surface activity of luminescent porous silicon, J. Appl. Phys. 74 (1993) 2094-2096.

[208] W.G. Herkstroeter, P.B. Merkel, The triplet state energies of rubrene and diphenylisobenzofuran, J. Photochem. 16 (1981) 331-342.

[209] B.M. Monroe, Rate constants for the reaction of singlet oxygen with conjugated dienes, J. Am. Chem. Soc. 103 (1981) 7253-7256.

[210] R. Schmidt, The Influence of Heavy Atoms on the Deactivation of Singlet Oxygen (Delta) in Solution, J. Am. Chem. Soc. 111 (1989) 6983-6987.

[211] A.U. Khan, Singlet molecular oxygen: a new kind of oxygen, J. Phys. Chem. 80 (1976) 2219-2228.

[212] I.B. Afanas'ev, Superoxide Ion: Chemistry and Biological Implications, CRC Press (1989).

[213] L.W. Aurand, N.H. Boone, G.G. Giddings, Superoxide and Singlet Oxygen in Milk Lipid Peroxidation, J. of Dairy Science 60 (1976) 363-369.

[214] L.C.P.M.d. Smet, Covalently Bound Organic Monolayers on Silicon Surfaces. Visible Light Attachment, Characterization, and Electrical Properties, 2006. p. 174.

[215] M. Rosso-Vasic, Synthesis and Photophysics of Functionalized Silicon Nanoparticles, 2008. p. 118.

[216] N. Shirahata, A. Hozumi, T. Yonezawa, Monolayer-Derivative Functionalization of Non-oxidized Silicon Surfaces, The Chemical Record 5 (2005) 145-159.

[217] S. Wei, J. Wang, D.-J. Guo, Y.-Q. Chen, S.-J. Xiao, Grafting Organic and Biomolecules on H-Terminated Porous Silicon from a Diazirine, Chemistry Letters 35 (2006) 172-173.

[218] K. Padmaja, L. Wei, J.S. Lindsey, D.F. Bocia, A Compact All-Carbon Tripodal Tether Affords High Coverage of Porphyrins on Silicon Surfaces, J. Org. Chem. 70 (2005) 7972-7978.

[219] B. Fabre, Ferrocene-Terminated Monolayers Covalently Bound to Hydrogen-Terminated Silicon Surfaces. Toward the Development of Charge Storage and Communication Devices, Accounts of Chemical Research 43 (2010) 1509-1518.

[220] G. Lucovsky, Chemical effects on the frequencies of Si-H vibrations in amorphous solids, Solid State Commun. 29 (1979) 571.

[221] H. Fritzsch, Characterization of Glow-Discharge Deposited a-Si:H, Solar Energy Materials 3 (1980) 447-501.

[222] J. Bartella, U. Herwig, Comparison of the long time stability of some SiC_xO_y: H films and related compounds with respect to postdeposition incorporation of OH groups, Fresenius J. Anal. Chem. 346 (1993) 351-354.

[223] J.M. Buriak, M.J. Allen, Lewis Acid Mediated Functionalization of Porous Silicon with Substituted Alkenes and Alkynes, J. Am. Chem. Soc. 120 (1998) 1339-1340.

[224] E.M.A. Khalil, F.H. ElBatal, Y.M. Hamdy, H.M. Zidan, M.S. Aziz, A.M. Abdelghany, Infrared absorption spectra of transition metals-doped soda lime silica glasses, Physica B, 405 (2010) 1294-1300.

[225] Y. Catherine, G. Turban, Infrared absorption of hydrogenated amorphous Si---C and Ge---C films, Thin Solid Films 70 (1980) 101-104.

[226] R. Murri, N. Pinto, S. Giuliodori, G. Ambrosone, U. Coscia, Infrared absorption of a-SiC:H as a function of the annealing temperature, Journal of Materials Science: Materials in Electronics 14 (2003) 341-344.

[227] R.D. Tilley, J.H. Warner, K. Yamamoto, I. Matsui, H. Fujimori, Micro-emulsion synthesis of monodisperse surface stabilized silicon nanocrystals, Chem. Commun. 14 (2005) 1833-1835.

[228] G. Socrates, Infrared and Raman Characteristic Group Frequencies: Tables and Charts, John Wiley & Sons, 2001.

[229] L. Wei, D. Syomin, R.S. Loewe, J.S. Lindsey, F. Zaera, D.F. Bocian, Structural and Electron-Transfer Characteristics of Carbon-Tethered Porphyrin Monolayers on Si(100), J. Phys. Chem. B 109 (2005) 6323-6330.

[230] S.M. Ribeiro, A.C. Serra, A.M.d.A.R. Gonsalves, Immobilised porphyrins in monoterpene photooxidations, Journal of Catalysis 256 (2008) 331-337.

[231] S.M. Ribeiro, A.C. Serra, A.M.d.A.R. Gonsalves, Covalently immobilized porphyrins on silica modified structures as photooxidation catalysts, Journal of Molecular Catalysis A: Chemical 326 (2010) 121-127.

[232] M. Pineiro, S.M. Ribeiro, A.C. Serra, The influence of the support on the singlet oxygen quantum yields of porphyrin supported photosensitizers, ARKIVOC 2010 (2010) 51-63.

[233] K.-K. Iu, J.K. Thomas, Quenching of singlet molecular oxygen ($^1\Delta_gO_2$) in silica gel-solvent heterogeneous system II. A direct time-resolved study, J. Photochem. Photobiol. A: Chem. 71 (1993) 55-60.

[234] K. Takahashi, Y. Takano, T. Yamaguchi, J. Nakamura, C. Yokoe, K. Murata, Porphyrin dye-sensitization of polythiophene in a conjugated polymer/TiO_2 p-n hetero-junction solar cell, Synthetic Metals 155 (2005) 51-55.

[235] S. Kang, M. Yasuda, H. Miyasaka, H. Hayashi, M. Kawasaki, T. Umeyama, Y. Matano, K. Yoshida, S. Isoda, H. Imahori, Light Harvesting and Energy Transfer in Multiporphyrin-Modified CdSe Nanoparticles, Chem. Sus. Chem 1 (2008) 254-261.

[236] L. Wen, X. Liu, N. Yang, J. Zhai, C. Huang, Y. Li, L. Jiang, Photoelectric conversion behavior based on direct interfacial charge-transfer from porphyrin derivative to silicon nanowires, Applied physics letters 97 (2010) 253111.

[237] Y. Harima, K. Yamashita, H. Ishii, K. Seki, Energy structures of molecular semiconductors contacting metals under air studied by the diffusion potential measurements and the Kelvin probe technique, Thin Solid Films 366 (2000) 237-248.

[238] T.v. Buuren, T. Tiedje, J.R. Dahn, B.M. Way, Photoelectron spectroscopy in porous silicon, Appl. Phys. Lett 63 (1993) 2911-2913.

[239] X.Y. Hou, F.L. Zhang, X. Wang, P.H. Hao, Energy band lineup at the porous-silicon/silicon by electron spectroscopy, Appl. Phys. Lett 1994(3602-3604) (64).